HEAT TRANSPORT CHARACTERISTICS IN THIN FILMS

BY

HAIDER ALI

A Dissertation Presented to the
DEANSHIP OF GRADUATE STUDIES

KING FAHD UNIVERSITY OF PETROLEUM & MINERALS

DHAHRAN, SAUDI ARABIA

In Partial Fulfillment of the
Requirements for the Degree of

DOCTOR OF PHILOSOPHY

In

MECHANICAL ENGINEERING

NOVEMBER, 2014

KING FAHD UNIVERSITY OF PETROLEUM & MINERALS
DHAHRAN, SAUDI ARABIA

DEANSHIP OF GRADUATE STUDIES

This thesis, written by **HAIDER ALI** under the direction of his thesis advisor and approved by his thesis committee, has been presented to and accepted by the Dean of Graduate Studies, in partial fulfillment of the requirements for the degree of **DOCTOR OF PHILOSOPHY** in **MECHANICAL ENGINEERING**.

Dr. Bekir Sami Yilbas
(Advisor)

Ahmet

Dr. Ahmet Ziyaettin Sahin
(Co-Advisor)

Dr. Habib I. Abuallhamayel
(Member)

Dr. Shahzada Zaman Shuja
(Member)

Zaman

Dr. Fiazuddin Zaman
(Member)

Dr. Zuhair M. Gasem
Department Chairman

Dr. Salam A. Zummo
Dean of Graduate Studies

7/12/14

Date

Dedicated to

my family for their love and support.

and

Dr. Yilbas for his kind attitude

ACKNOWLEDGEMENT

All praise and thanks are due to Almighty Allah, Most Gracious and Most Merciful, for his immense beneficence and blessings. He bestowed upon me health, knowledge and patience to complete this work. May Allah accept my efforts and help me in my future endeavors and grant me place in Paradise, which is the ultimate success.

I would like to acknowledge King Fahd University of Petroleum and Minerals for providing me with the facilities to accomplish my research objectives. I would also like to acknowledge the support Deanship of Scientific Research under a project RG 1301 in conducting this research.

I acknowledge, with deep gratitude and appreciation, the inspiration, encouragement, valuable time and continuous guidance given to me by Dr. Bekir S. Yilbas, my dissertation advisor. I also appreciate his caring attitude, supportive nature and continuous advices which led to my professional growth.

I am thankful to my dissertation co-advisor Dr. Ahmet Sahin for his valuable guidance and suggestions. I am highly grateful to Dr. Shahzada Shuja for his guidance and support specifically for software Tecplot learning. I am also grateful to my committee members, Dr. Habib Abulhamayel and Dr. Fiazuddin Zaman for their constructive guidance and support.

I want to acknowledge the support from Dr. Saad Bin Mansoor in MATLAB programing. He has always guided and supported me in all programming related problems, especially in the modeling of dispersion relation.

My heartfelt gratitude goes to my parents, for all their prayers, tireless efforts and struggle, in guiding me to this status. My parents' advice, to strive for excellence has made all this work possible. I am very grateful to my wife for her support and care throughout my research work.

Special thanks to my brothers and sister for their help, support and for sharing all the precious moments of life with me.

I also acknowledge the help and support of Osman Kaleem, Ahmer Ali, Arbab Latif, Umar Siddiqui, Omer Qureshi, Asim Akhter, Furqan Tahir and Yasir Jameel. I also appreciate all my fellow colleagues and friends who made my time in KFUPM memorable.

TABLE OF CONTENTS

ACKNOWLEDGEMENT .... **v**

TABLE OF CONTENTS .... **vii**

LIST OF TABLES .... **xiii**

LIST OF FIGURES .... **xiv**

NOMENCLATURE .... **xxix**

ABSTRACT .... **xxxii**

ABSTRACT ARABIC .... **xxxiv**

CHAPTER 1 INTRODUCTION **1**

1.1 Motivation 2

1.2 Microscale Heat Transport 5

1.3 Energy Transport Models 8

1.3.1 Fourier Law 8

1.3.2 Single Phase Lagging Model 9

1.3.3 Dual Phase Lagging Model 10

1.3.4 Kinetic Theory Approach 10

1.3.5 Schrödinger Wave Equation 11

1.3.6 Molecular Dynamics Simulation 12

1.3.7 Boltzmann Transport Equation 13

1.4 Limitation and Application of the Energy Transport Models 13

1.5 Basic Concepts from Statistical Mechanics Relevant to the Microscale Modeling of Heat Transport 15

1.6 Boltzmann Transport Equation (BTE) 19

1.7 Relaxation Time Approximation....21
1.8 Phonons as an Ideal Gas....23
1.9 Scope of Work....26
1.10 Outline....27

CHAPTER 2 LITERATURE REVIEW....28

2.1 Introduction....28
2.2 Literature Review....28
2.3 Current Work and Literature Review....65

CHAPTER 3 MATHEMATICAL ANALYSIS....67

3.1 Introduction....67
3.2 Equation of Phonon Radiative Transfer (EPRT)....67
3.2.1 Energy Transport Properties of a Dielectric Material....69
3.2.2 Boltzmann Transport Equation....70
3.2.3 Equation of Phonon Radiative Transfer....72
3.2.4 Heat Fluxes....81
3.2.5 Equilibrium Intensity Calculation....83
3.2.6 Physical Significance of Each Term in EPRT....85
3.2.7 Polarization and Modes of Phonons....86
3.2.8 Equilibrium Equivalent Temperature....87
3.3 Equation of Phonon Radiative Transfer (EPRT) for One Dimensional Dielectric Thin Films....88
3.3.1 Definition of Temperature....89
3.3.2 Heat Flux....89
3.3.3 Entropy Generation....90
3.3.4 Frequency Independent EPRT....90
3.4 Equation of Phonon Radiative Transfer (EPRT) for One Dimensional Metallic Films....94

3.4.1 EPRT and Two Equation Model 96

3.4.2 Frequency Dependent EPRT for Metallic film....103

3.4.3 Definition of Temperature....105

3.4.4 Heat Flux....106

3.5 Mathematical Formulation for Two Dimensional Dielectric Thin Films....108

3.5.1 Steady State Heat Transport Including the Effects of Heat Source Size and Silicon Film Dimension ..109

3.5.2 Transient Heat Transport Including the Effect of Temperature Oscillation in Silicon and Diamond Thin Films....113

3.5.3 Transient Heat Transport Including the Effects of Pulse Duration of Heat Source in Silicon and Diamond Thin Films 119

3.5.4 Transient Heat Transport Including the Effects of Thickness and Temperature Oscillations in Diamond Thin Film....119

3.5.5 Transient Heat Transport Including the Effects of Heat Source Size and Temperature Oscillation in Silicon Thin Film 120

3.5.6 Transient Heat Transport in Silicon and Diamond Thin Films Pair Including the Thermal Boundary Resistance....120

3.5.7 Transient Heat Transport Including Quantum Dot in Silicon Thin Film....137

3.6 Mathematical Formulation for One Dimensional Dielectric Thin Films 154

3.6.1 Steady State Heat Transport Including the Effect of Film Thickness on Entropy Generation Rate....154

3.6.2 Transient Heat Transport Including the Effect of Minute Vacuum Gap in between the Films 158

3.7 Mathematical Formulation for One Dimensional Metallic Thin Films....166

3.7.1 Transient Heat Transport in Aluminum Thin Film....166

3.7.2 Transient Heat Transport Including the Effect of Thermal Oscillation in Aluminum Thin Film...171

3.7.3 Transient Heat Transport Including the Effects of Thermal Oscillation and Film Thickness in Aluminum Thin Film 173

CHAPTER 4 NUMERICAL SOLUTION.... 174

4.1 EPRT for Two Dimensional Dielectric Films....175

4.1.1 Domain Discretization....177

4.1.2 Discretization of Governing Equation 179

4.1.3 Solution of Discretized Equation 187

4.2 EPRT for One Dimensional Dielectric Films 192

4.2.1 Domain Discretization 192

4.2.2 Discretization of Governing Equation 193

4.2.3 Solution of Discretized Equation 197

4.3 EPRT for One Dimensional Metallic Films 200

4.3.1 Lattice Sub-System 200

4.3.2 Electron Sub-System 204

4.3.3 Solution of Governing Equations for Metallic Films 208

CHAPTER 5 RESULTS AND DISCUSSION 212

5.1 Two dimensional Dielectric Thin Films 212

5.1.1 Steady State Heat Transport Including the Effects of Heat Source Size and Silicon Film Dimension ..213

5.1.2 Transient Heat Transport Including the Effect of Temperature Oscillation in Silicon and Diamond Thin Films 223

5.1.3 Transient Heat Transport Including the Effects of Pulse Duration of Heat Source in Silicon and Diamond Thin Films 235

5.1.4 Transient Heat Transport Including the Effects of Thickness and Temperature Oscillations in Diamond Thin Film 246

5.1.5 Transient Heat Transport Including the Effects of Heat Source Size and Temperature Oscillation in Silicon Thin Films 254

5.1.6 Transient Heat Transport in Silicon and Diamond Thin Film Pair Including the Thermal Boundary Resistance 264

5.1.7 Transient Heat Transport Including Quantum Dot in Silicon Thin Films 284

5.2 One Dimensional Dielectric Thin Films 293

5.2.1 Steady State Heat Transport Including the Effect of Film Thickness on Entropy Generation Rate 293

5.2.2 Transient Heat Transport Including the Effect of Minute Vacuum Gap in between the Films 301

5.3 One Dimensional Metallic Thin Films 316

5.3.1 Transient Heat Transport in Aluminum Thin Films 316

5.3.2 Transient Heat Transport Including the Effect of Thermal Oscillation in Aluminum Thin Film...333

5.3.3 Transient Heat Transport Including the Effects of Thermal Oscillation and Film Thickness in Aluminum Thin Film 348

CHAPTER 6 CONCLUSIONS.... 365

6.1 Two Dimensional Dielectric Thin Films 365

6.1.1 Steady State Heat Transport Including the Effects of Heat Source Size and Silicon Film Dimension ..365

6.1.2 Transient Heat Transport Including the Effect of Temperature Oscillation in Silicon and Diamond Thin Films 366

6.1.3 Transient Heat Transport Including the Effects of Pulse Duration of Heat Source in Silicon and Diamond Thin Films 368

6.1.4 Transient Heat Transport Including the Effects of Thickness and Temperature Oscillation in Diamond Thin Film....369

6.1.5 Transient Heat Transport Including the Effects of Heat Source Size and Temperature Oscillation in Silicon Thin Film 370

6.1.6 Transient Heat Transport in Silicon and Diamond Thin Films Pair Including the Thermal Boundary Resistance....372

6.1.7 Transient Heat Transport Including Quantum Dot in Silicon Thin Film 373

6.2 One Dimensional Dielectric Thin Films 374

6.2.1 Steady State Heat Transport Including the Effect of Film Thickness on Entropy Generation Rate 374

6.2.2 Transient Heat Transport Including the Effect of Gap in between the Films....375

6.3 One Dimensional Metallic Thin Films 377

6.3.1 Transient Heat Transport in Aluminum Thin Films 377

6.3.2 Transient Heat Transport Including the Effect of Thermal Oscillation in Aluminum Thin Film...379

6.3.3 Transient Heat Transport Including the Effects of Thermal Oscillation and Film Thickness in Aluminum Thin Film 380

6.4 Future Work 381

REFERENCES 383

VITAE 396

LIST OF TABLES

Table 1.1 Equilibrium Probability Distribution 25

Table 3.1 Properties of Silicon the used in the numerical simulations of the frequency-independent solution of the phonon radiative transport equation. Thermal conductivity can be determined from the kinetic theory formula $k = {Cv\Lambda}/{3}$ .. 93

Table 3.2 Properties of Aluminum the used in the numerical simulations 107

Table 5.1 Thermal boundary resistance predicted from the present simulations using diffusive mismatch model (DMM) and cut-off mismatch model (CMM) and obtained from the previous studies [140], [141] 272

LIST OF FIGURES

Figure 1.1 Comparison of propagation methods a) Diffusive transport b) Ballistic Transport and c) Ballistic Diffusive transport. 7

Figure 3.1 A schematic showing the coordinate systems for two dimensional thin films.... 75

Figure 3.2 Dispersion Relation for Silicon [130] 79

Figure 3.3 Dispersion Relation for Diamond [131] 80

Figure 3.4 Dispersion relations of aluminum used in the simulations [134]. 104

Figure 3.5 A schematic view of the heat source locations at the top edges of the film and the boundary conditions for study the effect of Heat Source Size and Silicon Film Dimensions 110

Figure 3.6 A schematic view of two-dimensional thin film and the heat source location 114

Figure 3.7 Temporal variation of temperature oscillation (pulsation) at the left edge of the film. It should be noted that $T(\mathrm{t}) = \begin{cases} 301\,K & 0 < t < \tau_h \\ 300\,K & otherwise \end{cases}$ where, $T\left(t+\tau_{cycle}\right) = T\left(t\right)$ $T\left(t+\tau_{cycle}\right) = T\left(t\right)$. 115

Figure 3.8 Schematic view of silicon-diamond film pair and boundary conditions. Λ is the mean free path of silicon corresponding to the gray medium 122

Figure 3.9 Schematic view of emitted, transmitted, and reflected phonon intensities at the boundaries. 127

Figure 3.10 Dispersion relations for silicon and diamond films and wavevectors for cut-off mismatch [112] and [113]. 133

Figure 3.11 Schematic view of quantum dot of aluminum in silicon film, where Λ is the mean free path of silicon corresponding to the gray medium 139

Figure 3.12 Schematic diagram showing all the sub-domain used in computation 140

Figure 3.13 Temporal variation at the edges of quantum dot (aluminum edges). 141

Figure 3.14 A schematic view of silicon thin film and temperature disturbance at the film edges. 155

Figure 3.15 Schematic view of thin silicon films pair consist of two silicon films separated by a small gap. Λ is the mean free path of silicon correspondent gray medium. 159

Figure 3.16 Schematic view of gap located in between two-silicon films pair and heat flux vectors (*k* is wavenumber and, $i = T$ represents the transverse mode of phonons, $i = L$ stands for longitudinal mode of phonons, $j = A$ corresponds to acoustic and $j = O$ stands for optical phonons). The space between $x_A = 3\Lambda$ and $x_B = 3\Lambda$ corresponds to the gap size. 163

Figure 3.17 A schematic view of aluminum film and the temperature settings at the film edges. 167

Figure 4.1 A schematic diagram showing the intensity in first, second, third and fourth quadrant for two dimensional EPRT in dielectric thin films. 176

Figure 4.2 Algorithm which incorporated to solve the two dimensional EPRT in dielectric thin films 191

Figure 4.3 Algorithm which is incorporated for the solution of EPRT for one dimensional dielectric thin films. 199

Figure 4.4 Algorithm which incorporated to solve the EPRT in metallic thin films.... 211

Figure 5.1 Equivalent equilibrium temperature along the normalized film width for different locations of the heat source and two film thicknesses................ 218

Figure 5.2 Equivalent equilibrium temperature contours in the film for different sizes of heat source and for the film thickness of $L = 0.1\mu m$ 219

Figure 5.3 Equivalent equilibrium temperature contours in the film for different sizes of heat source and for the film thickness of $L = 0.1\mu m$ 220

Figure 5.4 Equivalent equilibrium temperature along the normalized film thickness for different locations of the heat source and two film thicknesses. 221

Figure 5.5 Effective thermal conductivity variation with the dimensionless heat source size for two film thicknesses... 222

Figure 5.6 Temporal variation of equivalent equilibrium temperature at location Lx = 0.5L and Lz = 0.05L where L is the film width for three different pulse lengths of temperature oscillation at the film edge.................................... 228

Figure 5.7 Temporal variation of equivalent equilibrium temperature for the time domain 40–60 ps at location Lx = 0.5L and Lz = 0.05L where L is the film width due to three different pulse lengths of temperature oscillation at the film edge. 229

Figure 5.8 Temporal variation of equivalent equilibrium temperature at location Lx = 0.5L and Lz = 0.25L where L is the film width for three different pulse lengths of temperature oscillation at the film edge.................................... 230

Figure 5.9 Temporal variation of equivalent equilibrium temperature for the time domain 40–60 ps at location Lx=0.5L and Lz=0.25L where L is the film width due to three different pulse lengths of temperature oscillation at the film edge. ... 231

Figure 5.10 Temporal variation of equivalent equilibrium temperature at location Lx = 0.5L and Lz = 0.5L where L is the film width for three different pulse lengths of temperature oscillation at the film edge. 232

Figure 5.11 Equivalent equilibrium variation along the film width for heating duration of 15 ps and three different pulse lengths of temperature oscillation at the film edge. Lx = 0.5L, where L is the film width.. 233

Figure 5.12 Equivalent equilibrium variation along the film width for heating duration of 45 ps and three different pulse lengths of temperature oscillation at the film edge. Lx = 0.5L, where L is the film width... 234

Figure 5.13 Equivalent equilibrium temperature along the film width for silicon and diamond films. $\tau_{cycle} = 6ps\ and\ 10ps$,t = 15 ps, and $L_x = 0.5L, where\ L = 0.1\mu m$ 240

Figure 5.14 Equivalent equilibrium temperature along the film width for silicon and diamond films. $\tau_{cycle} = 6ps\ and\ 10ps$,t = 45 ps, and $L_x = 0.5L, where\ L = 0.1\mu m$ 241

Figure 5.15 Temporal variation of equivalent equilibrium temperature for silicon and diamond films. $\tau_{cycle} = 6ps\ and\ 10ps$, $L_x = 0.5L\ and\ L_z = 0.25L$ $where\ L = 0.1\mu m$ 242

Figure 5.16 Temporal variation of equivalent equilibrium temperature for silicon and diamond films. $\tau_{cycle} = 6ps\ and\ 10ps$, $L_x = 0.5L\ and\ L_z = 0.25L$ $where\ L = 0.1\mu m$. 243

Figure 5.17 Close view of temporal variation of equivalent equilibrium temperature for silicon and diamond films. $\tau_{cycle} = 6ps\ and\ 10ps$, $L_x = 0.5L\ and\ L_z = 0.05L$, $where\ L = 0.1\mu m$. 244

Figure 5.18 Close view of temporal variation of equivalent equilibrium temperature for silicon and diamond films. $\tau_{cycle} = 6ps\ and\ 10ps$, $L_x = 0.5L\ and\ L_z = 0.25L$, $where\ L = 0.1\mu m$. 245

Figure 5.19 Temporal variation of equivalent equilibrium temperature for two frequencies of temperature oscillation and various film thicknesses. Temperature is located at $x = 0.5L_x$ and $z = 0.05L_z$ in the film........ 251

Figure 5.20 Temporal variation of equivalent equilibrium temperature for two frequencies of temperature oscillation and various film thicknesses. Temperature is located at $x = 0.5L_x$ and $z = 0.05L_z$ in the film........ 252

Figure 5.21 Equivalent equilibrium temperature variation along the film width for two frequencies of temperature oscillation and various film thicknesses. Temperature is presented for heating time t = 15 ps. 253

Figure 5.22 Temporal variation of equivalent equilibrium temperature for different heat source sizes and two cycles of temperature oscillation. The location in the film is $L_x = 0.5L$ and $L_z = 0.05L$, where $L = 0.1\mu m$ 259

Figure 5.23 Temporal variation of equivalent equilibrium temperature difference due to two consecutive maximum and minimum temperature differences for different heat source sizes and two cycles of temperature oscillation. 260

Figure 5.24 Temporal variation of equivalent equilibrium temperature for different heat source sizes and two cycles of temperature oscillation. The location in the film is $L_x = 0.5L$ and $L_z = 0.25L$, where $L = 0.1\mu m$ 261

Figure 5.25 Equivalent equilibrium temperature variation along the film width for different heat source sizes and two cycles of temperature oscillation. The location in the film is $L_x = 0.5L$ and heating duration is 15 ps. 262

Figure 5.26 Equivalent equilibrium temperature variation along the film width for different heat source sizes and two cycles of temperature oscillation. The location in the film is $L_x = 0.5L$ and heating duration is 45 ps. 263

Figure 5.27 Temporal variation of thermal boundary resistance for diffusive mismatch and cut-off mismatch models for silicon-diamond film pair interface...... 273

Figure 5.28 Equivalent equilibrium temperature contours in the silicon and diamond films due to diffusive mismatch and cut-off mismatch models for 25 ps heating duration. 274

Figure 5.29 Thermal boundary resistance due to diffusive mismatch (DMM) and cut-off mismatch (CMM) models at the silicon-diamond film pair interface along the film thickness for different heating periods. 275

Figure 5.30 Ratio of phonon intensities due to longitudinal acoustic branches $\left(\eta_{LA}\right)$ in silicon film for different heating periods. Ratio is determined from $\eta_{LA} = \frac{\left(I_{Si,LA}^{0}\right)_{CMM}}{\left(I_{Si,LA}^{0}\right)_{DMM}}$, where I^{0} is the equilibrium phonon intensity............ 276

Figure 5.31 Ratio of phonon intensities due to transverse acoustic branches $\left(\eta_{TA}\right)$ in silicon film for different heating periods. Ratio is determined from $\eta_{TA} = \frac{\left(I_{Si,TA}^{0}\right)_{CMM}}{\left(I_{Si,TA}^{0}\right)_{DMM}}$, where I^{0} is the equilibrium phonon intensity. 277

Figure 5.32 Ratio of phonon intensities due to longitudinal acoustic branches $\left(\eta_{LA}\right)$ in diamond film for different heating periods. Ratio is determined from $\eta_{LA} = \frac{\left(I_{Si,LA}^{0}\right)_{CMM}}{\left(I_{Si,LA}^{0}\right)_{DMM}}$, where I^{0} is the equilibrium phonon intensity............ 278

Figure 5.33 Ratio of phonon intensities due to transverse acoustic branches $\left(\eta_{TA}\right)$ in diamond film for different heating periods. Ratio is determined from $\eta_{TA} = \frac{\left(I_{Si,TA}^{0}\right)_{CMM}}{\left(I_{Si,TA}^{0}\right)_{DMM}}$, where I^{0} is the equilibrium phonon intensity............ 279

Figure 5.34 Temporal variation of ratio of phonon intensities due to longitudinal acoustic branches $\left(\eta_{LA}\right)$ in silicon film for different heating periods. Ratio is determined from $\eta_{LA} = \frac{\left(I_{Si,LA}^{0}\right)_{CMM}}{\left(I_{Si,LA}^{0}\right)_{DMM}}$, where I^{0} is the equilibrium phonon intensity.. 280

Figure 5.35 Temporal variation of ratio of phonon intensities due to transverse acoustic branches (η_{TA}) in silicon film for different heating periods. Ratio is determined from $\eta_{TA} = \frac{\left(I^0_{Si,TA}\right)_{CMM}}{\left(I^0_{Si,TA}\right)_{DMM}}$, where I^0 is the equilibrium phonon intensity. 281

Figure 5.36 Temporal variation of ratio of phonon intensities due to longitudinal acoustic branches (η_{LA}) in diamond film for different heating periods. Ratio is determined from $\eta_{LA} = \frac{\left(I^0_{Si,LA}\right)_{CMM}}{\left(I^0_{Si,LA}\right)_{DMM}}$, where I^0 is the equilibrium phonon intensity. 282

Figure 5.37 Temporal variation of ratio of phonon intensities due to transverse acoustic branches (η_{TA}) in diamond film for different heating periods. Ratio is determined from $\eta_{TA} = \frac{\left(I^0_{Si,TA}\right)_{CMM}}{\left(I^0_{Si,TA}\right)_{DMM}}$, where I^0 is the equilibrium phonon intensity. 283

Figure 5.38 Equivalent equilibrium temperature along the z-axis for different heating periods. The x-axis location is x = 3.7 Λ. The x-axis is normalized with the averaged mean free path (Λ). 288

Figure 5.39 Equivalent equilibrium temperature contours in the silicon film for two heating periods. 289

Figure 5.40 Equivalent equilibrium temperature along the x-axis for different heating periods. The z-axis location is z = 1.48 Λ. The x-axis is normalized with the averaged mean free path (Λ). 290

Figure 5.41 Temporal variation of equivalent equilibrium temperature for different z-axis locations. The axis location is x = 3.7Λ. 291

Figure 5.42 Temporal variation of equivalent equilibrium temperature for different x -axis locations. The z-axis location is z = 1.48Λ. 292

Figure 5.43 Comparison of normalized temperature along the film thickness predicted from the present study and obtained from the previous study [3]............. 297

Figure 5.44 Normalized entropy generation along the normalized film thickness for different film thicknesses. The predictions are obtained for frequency independent case. 298

Figure 5.45 Normalized entropy generation along the normalized film thickness for different film thicknesses. The predictions are obtained for frequency dependent case... 299

Figure 5.46 Total entropy generation with the film thicknesses for frequency dependent and frequency independent cases. 300

Figure 5.47 Thermal conductivity predicted and obtained from the previous study [142]... 309

Figure 5.48 Equivalent equilibrium temperature along the thickness of films pair for heating duration of 100 ps. Section *A* represents the first film and section *B* is the second film. The gap is located in between two films. Λ is the mean free path of silicon corresponding to gray medium.................................. 310

Figure 5.49 Equivalent equilibrium temperature along the thickness of films pair for heating duration of 500 ps. Section A represents the first film and section B is the second film. The gap is located in between two films. Λ is the mean free path of silicon corresponding to gray medium.................................. 311

Figure 5.50 Temporal variation of dimensionless equivalent equilibrium temperature $\left(\frac{T_A - T_{Low}}{T_{High} - T_{Low}}\right)$ at the first film edge $\left(x_A = 3\Lambda\right)$ for different values of gap sizes. Λ is the mean free path of silicon corresponding to gray medium. 312

Figure 5.51 Temporal variation of dimensionless equivalent equilibrium temperature $\left(\frac{T_A - T_{Low}}{T_{High} - T_{Low}}\right)$ at the second film edge $\left(x_B = 0\right)$ for different values of gap sizes. Λ is the mean free path of silicon corresponding to gray medium. 313

Figure 5.52 Equivalent equilibrium temperature difference between the first film edge $\left(x_A = 3\Lambda\right)$ and the second film edge $\left(x_B = 0\right)$ with dimensionless gap length (L_{Gap} / Λ, where L_{Gap} is the gap size in between the films and Λ is the mean free path of silicon corresponding to gray medium.)................ 314

Figure 5.53 Thermal conductivity ratio (k_{eff}/k_{Bulk}) with dimensionless gap length (L_{Gap}/Λ, where L_{Gap} is the gap size in between the films and Λ is the mean free path of silicon in gray medium). 315

Figure 5.54 Dimensionless temperature distribution in the lattice sub-system for different film thicknesses. Temperatures are presented for steady state solutions due to the frequency dependent and the frequency independent solutions of the radiative transport equation, and the solution of the two-equation model. 324

Figure 5.55 Dimensionless temperature distribution along the film length in the lattice sub-system for different film thicknesses and 30 ps of the heating duration. The solutions are presented for the frequency dependent and the frequency independent solutions of the radiative transport equation. 325

Figure 5.56 Surface plot of dimensionless equivalent equilibrium temperature with dimensionless length and dimensionless time for different film thicknesses. Distance is normalized through the film thickness $\mathit{Dimensionless}\ \text{Distance} = x / Lx$, and tine is normalized by $\mathit{Dimensionless\ Time} = t / \tau$ where $\tau = Ce / G$ and $\tau = 8.94\text{x}10^{-14}\ s$ 326

Figure 5.57 Dimensionless temperature distribution along the film length in the lattice sub-system for different film thicknesses and 90 ps of the heating duration. The solutions are presented for the frequency dependent and the frequency independent solutions of the radiative transport equation. 327

Figure 5.58 Dimensionless temperature distribution along the film length in the electron sub-system for different film thicknesses and 30 ps of the heating duration. The solutions are presented for the frequency dependent and the frequency independent solutions of the radiative transport equation. 328

Figure 5.59 Dimensionless temperature distribution along the film length in the electron sub-system for different film thicknesses and 90 ps of the heating duration. The solutions are presented for the frequency dependent and the frequency independent solutions of the radiative transport equation. 329

Figure 5.60 Temporal variation of dimensionless temperature distribution in the lattice sub-system for different film thicknesses and x-axis location is x = Lx/4, where Lx is the film thickness. The solutions are presented for the frequency dependent and the frequency independent solutions of the radiative transport equation. 330

Figure 5.61 Temporal variation of dimensionless temperature distribution in the electron sub-system for different film thicknesses and x-axis location is x = Lx/4, where Lx is the film thickness. The solutions are presented for the frequency dependent and the frequency independent solutions of the radiative transport equation. 331

Figure 5.62 Lattice thermal conductivity with normalized film thickness. Lx represents the film thickness and L = 0.1 μm. The solutions are presented for the frequency dependent and the frequency independent solutions of the radiative transport equation. 332

Figure 5.63 Comparison of dimensionless temperature due the frequency dependent, frequency independent solutions of phonon radiative transport equation and modified two-equation model. 340

Figure 5.64 Dimensionless equivalent equilibrium temperature, in the lattice sub-system, along the film thickness for the frequency dependent and independent solutions of phonon radiative transport equation for different duration of high temperature in the temperature oscillation and heating duration of 8 ps. 341

Figure 5.65 3-dimensional view of equivalent equilibrium temperature, obtained from frequency dependent solution of radiative transport equation, with time and distance along the film thickness for different duration of high temperature in temperature oscillation at the film edge. $Dimensionless\ Time = t / \tau_d$ where $\tau_d = C_e / G$ and $\tau_d = 8.94\text{x}10^{-14}\ s$ 342

Figure 5.66 3-dimensional view of equivalent equilibrium temperature, obtained from frequency independent solution of radiative transport equation, with time and distance along the film thickness for different duration of high temperature in temperature oscillation at the film edge. $Dimensionless\ Time = t / \tau_d$ where $\tau_d = C_e / G$ and $\tau_d = 8.94\text{x}10^{-14}\ s$ 343

Figure 5.67 Dimensionless temperature, in the electron sub-system, along the film thickness for the frequency dependent and independent solutions of phonon radiative transport equation for different duration of high temperature in the temperature oscillation and heating duration of 8 ps. 344

Figure 5.68 Temporal variation of dimensionless temperature, in the lattice sub-system, for the frequency dependent and independent solutions of phonon radiative transport equation for different duration of high temperature (τ_h) in the temperature oscillation and heating duration of 8 ps. The location is x = 0.05L (L = 0.1μm) in the film. 345

Figure 5.69 Temporal variation of dimensionless temperature, in the lattice sub-system, for the frequency dependent and independent solutions of phonon radiative transport equation for different duration of high temperature (τ_h) in the temperature oscillation and heating duration of 8 ps. The location is x = 0.1L (L = 0.1μm) in the film. 346

Figure 5.70 Temporal variation of dimensionless temperature, in the electron sub-system, for the frequency dependent and independent solutions of phonon radiative transport equation for different duration of high temperature (τ_h) in the temperature oscillation and heating duration of 8 ps. The location is x = 0.05L (L = 0.1μm) in the film. 347

Figure 5.71 Dimensionless equivalent equilibrium temperature in the lattice sub-system for different film thicknesses and frequency dependent and independent solutions of phonon radiative transport equation. Heating time is 8 ps. ... 356

Figure 5.72 Dimensionless equivalent equilibrium temperature in the lattice sub-system for different film thicknesses and frequency dependent and independent solutions of phonon radiative transport equation. Heating time is 22 ps..................... 357

Figure 5.73 Dimensionless temperature in the electron sub-system for different film thicknesses and frequency dependent and independent solutions of phonon radiative transport equation. Heating time is 8 ps. 358

Figure 5.74 Dimensionless temperature in the electron sub-system for different film thicknesses and frequency dependent and independent solutions of phonon radiative transport equation. Heating time is 22 ps. 359

Figure 5.75 Temporal variation of dimensionless equivalent equilibrium temperature in the lattice sub-system for different film thicknesses and frequency dependent and independent solutions of phonon radiative transport equation. Location is x = 0.05Lx, where Lx is the film thickness. 360

Figure 5.76 Surface plot of dimensionless equivalent equilibrium temperature, in the lattice sub-system for different film thicknesses and frequency dependent and independent solutions of phonon radiative transport equation. $Dimensionless\ Time = t/\tau_d$ where $\tau_d = C_e/G$ and $\tau_d = 8.94\text{x}10^{-14}\ s$ ... 361

Figure 5.77 Temporal variation of dimensionless equivalent equilibrium in the lattice sub-system for different film thicknesses and frequency dependent and independent solutions of phonon radiative transport equation. Location is x = 0.1Lx, where Lx is the film thickness. 362

Figure 5.78 Temporal variation of electron temperature in the lattice sub-system for different film thicknesses and frequency dependent and independent solutions of phonon radiative transport equation. Location is x = 0.05Lx, where Lx is the film thickness.. 363

Figure 5.79 Surface plot of dimensionless electron temperature in the lattice sub-system for different film thicknesses and frequency dependent and independent solutions of phonon radiative transport equation $Dimensionless\ Time = t/\tau_d$ where $\tau_d = C_e/G$ and $\tau_d = 8.94\text{x}10^{-14}\ s$ 364

NOMENCLATURE

C	Volumetric specific heat capacity of the dielectric material.
D	Density of state.
f	Probability distribution function in phase space
f^0	Equilibrium probability distribution function in phase space.
G	Electron-phonon coupling constant.
$\hbar$	Reduced Planck's constant.
I	Phonon intensity.
I^+	Forward intensity.
I^-	Backward intensity.
I^{++}	Phonon intensity in the first quadrant.
I^{-+}	Phonon intensity in the second quadrant.
I^{+-}	Phonon intensity in the third quadrant.
I^{--}	Phonon intensity in the fourth quadrant.
I^o	Equilibrium phonon intensity.
k	Wavenumber.
k_B	Boltzmann Constant.
k_{Bulk}	Thermal conductivity of bulk material.
$k_{eff.}$	Effective thermal conductivity.
L_{Gap}	Length of gap between two thin films.
L_x	Thickness of the dielectric material film.

L_z	Width of the dielectric material film.
p	Momentum.
$q_x^{"}$	Heat flux in the *x*-direction.
$q_z^{"}$	Heat flux in the *z*-direction.
$q"$	Heat flux vector.
S_{gen}	Entropy generation.
t	Time
T	Equivalent equilibrium phonon temperature.
u	Internal energy density of phonon.
v	Speed of phonons.
w_s	Heat source thickness
x	Cartesian coordinate *x*-direction .
z	Cartesian coordinate *z*-direction.
Δx	Grid spacing in the *x*-direction.
Δz	Grid spacing in the *z*-direction.

Greek Symbols

Λ	Phonon mean-free-path.
θ	Polar angle.
ϕ	Azimuthal angle.
τ	Relaxation time.
σ	Stefan Boltzmann Contants.

Ω	Solid angle.
μ	Cosine of polar angle.
λ	Wavelength.
ω	Frequency.

Subscript

A	Acoustic
e	Electron
k	Wavenumber
L	Longitudinal
O	Optical
ph	Phonon
T	Transverse
x	x-axis
z	z-axis

ABSTRACT

Full Name: HAIDER ALI

Thesis Title: HEAT TRANSPROT CHARACTERSITIC IN THIN FILMS

Major Field: MECHANICAL ENGINEERING

Date of Degree: NOVEMBER 2014

Heat transport in thin films is one of the current research areas in mechanical engineering discipline due to the fast growth of solar and thermoelectric applications in domestic and industry. The small size devices require modification of the conventional methods to formulate the multi-physics problems involved during design and operation. Conventional methods which are based on continuum hypothesis to formulate such problems become invalid as the characteristic size of thin film are comparable to the mean free path of the heat carriers. In such situation, a sub-continuum method needs to be incorporated to model energy transport in small size device and thin films. Boltzmann Transport Equation (BTE), which is one of sub-continuum methods, can be used to assess the energy transport characteristics in thin films. Consequently, the mathematical model is introduced to develop frequency dependent transient phonon transport in two-dimensional micro-domains while incorporating thermal boundary resistance. In the dissertation work, the ballistics effects of phonons have been considered for the assessment of the thermal properties of thin films. The heat source size on the transport

characteristics has also been accounted for quantification of thermal properties. Although two-equation model is well established for thermal energy transport in lattice and electron sub-systems, the re-formulation of the problem has accommodated by using the BTE for metallic thin films at micro-scales. The findings and validity of the mathematical formulation has been discussed within the frame of the experimental data presented in the open literature.

ملخص الرسالة

الاسم الكامل: حيدر علي

عنوان الرسالة: خصائص انتقال الحرارة في الأغشية الرقيقة

التخصص: الهندسة الميكانيكية

تاريخ الدرجة العلمية: نوفمبر 2014

يعتبر انتقال الحرارة في الأغشية الرقيقة من أهم مجالات البحث في الهندسة الميكانيكية نظرا للتطور السريع في تطبيقات المحلية والصناعية للأجهزة العاملة بالطاقة الشمسية والأجهزة الحرارية. الحجم الصغير لهذه الأجهزة يتطلب تعديلا في الطرق التقليدية لصياغة المشكلة متعددة الفيزياء أثناء عمليتي التصميم والتشغيل. الطرق التقليدية لصياغة هذه المشكلة، والتي تعتمد على فرضية المادة المتصلة، أصبحت غير صالحة نظرا لأن الحجم المميز للغشاء الرقيق قابل للمقارنة بالمسار الحر للوسيط الحراري الناقل. في هذه الحالة يتوجب استخدام الطرق دون-المتصلة لتدمج في معادلة انتقال الطاقة للأجهزة الصغيرة. يمكن استخدام معادلة بولتزمان للانتقال، والتي تعتبر من الطرق دون-المتصلة، لتقييم خصائص عملية الانتقال في الأغشية الرقيقة. تبعا لذلك يتم تقديم نموذج رياضي لعملية انتقال الفونون غير الترددية لنطاق صغير بحجم المايكرو مع دمج مقاومة الطبقة الجدارية الحرارية. في هذه الأطروحة، تم الأخذ في الاعتبار الأثر المقذوفات للفونون وذلك لتقييم الخواص الحرارية للأغشية الحرارية. أيضا، تم اعتبار حجم المصدر الحراري في خصائص عملية الانتقال. بالرغم من أن النموذج ثنائي-المعادلة تم تقريره لعملية الانتقال في الأنظمة الفرعية الالكترونية والشعرية، تمت إعادة صياغة المعادلة باستخدام معادلة بولتزمان للانتقال للأغشية المعدنية الرقيقة على مستوى المايكرو الدقيق. تمت مناقشة النتائج وصحة وفعالية النموذج الرياضي في إطار النتائج التجريبية المتوفرة.

CHAPTER 1

INTRODUCTION

In the last four decades, there has been an increasing focus on miniaturization of devices by scientists and engineers. Nowadays micro and nano-scale technologies have become one of the major research areas in academia. In the micro and nano-scale analysis, some of the physical effects, which can be ignored at the macroscale analysis, become important while resulting in the error in estimations due to the differences in the properties of bulk, and micro and nano-scale material. In order to design high efficiency micro and nano-scale devices and to achieve desirable performances from these devices, a deep physical understanding of the transport process becomes necessary.

Energy transport at micro and nano-scale is one of the important aspects of the process; therefore, it is the essential part of the area of the research. The knowledge of thermal characteristics including energy transport and properties that can help in determining the performance of micro and nano-scale devices; for example, effective thermal management of heat sources can improve the performance of devices, such as transistors on computer microprocessor.

Numerous researchers have concentrated their efforts towards the proper modeling and the solution of energy transport processes at micro and nano scale levels for such devices. The researchers face the problems in modeling of micro and nano scale energy transport mainly due to the transport properties of the small size devices. When device sizes are comparable to the mean free path of the heat carriers, conventional methods of modeling, which are based on continuum hypothesis, may no longer be applicable. Fourier law, which is quite accurate common engineering situations [1] and bases on the continuum hypothesis, becomes invalid for energy transport at micro and nano scale. It is now well established that conventional Fourier analysis leads to large erroneous thermal predictions when the mean free path of heat carriers is comparable to or larger than the device size [2].

1.1 Motivation

The motivation to investigate the transport process at micro and nano-scale comes from a several practical industrial problems associated with electronic, solar, and thermoelectric applications in industry.

Thin films of dielectric materials of thickness with in the range of 10 nm to 100 μm are used extensively in semiconductor electronic devices. These films form barrier layers between electrically conducting regions, and also have to conduct the heat generated in the devices. Since the performance of an electronic device depends on the device temperature, therefore, the study into energy transport characteristics in dielectric thin films becomes crucial [3]. A design methodology based on the Fourier law of heat conduction does not provide desirable accuracy since the transport characteristics do not match with the experimental data.

In solar energy technology, for direct conversion of solar energy into electrical energy, the photovoltaic (PV) cells are commercially used. Silicon is commonly used as a photoactive material in the manufacturing of PV cells. Since the absorption depth for solar radiation in silicon is large; therefore, thick layer of material is required for sufficient absorption of solar radiation making the PV cells expensive. In an effort to make solar technology economically viable, quantum dots are placed on the solar cells. Quantum dots with their high absorption characteristics are a promising solution for significantly reducing the absorber material requirement. In this regard, the physical understanding of energy transport in silicon thin film with the presence of quantum dots is of vital importance.

Thermoelectric generators (TEG) are cost effective solid-state devices, which are used to convert thermal energy into electrical energy. The TEG efficiency depends upon the operating temperature, figure of Merit, and design configuration of the device. A material with high electrical conductivity and low thermal conductivity is required in order to increase the figure of Merit and efficiency of TEG. In metals, at moderate temperatures, the ratio of the thermal conductivity to that of the electrical conductivity is directly proportional to the temperature, with the proportionality constant being independent of any particular metal. Therefore, improvements in the efficiency of thermoelectric elements using metals are difficult. As the thermal conductivities of dielectric thin films are often smaller than those of their corresponding bulk materials; therefore, in micro-sized semiconductors, it may be possible to reduce the thermal conductivity without reducing the electrical conductivity. This in fact increases the Figure of Merit and efficiency of a thermoelectric device. In this case, the heat is mainly transported by phonons in a semiconductor whereas the electricity is transported by the electrons. Hence, it is important to have a thorough understanding of the transport processes in thin films.

Dielectric thin films are often in contact with a substrate material which may be a dielectric or a metal. Continuum hypothesis becomes invalid, if the mean free path for heat carrier is comparable or higher than the film and substrate thickness. Thermal energy transport between a dielectric film and a metal film is further complicated due to the non-equilibrium energy transfer between the electron and phonon sub-systems in the metallic film, near the interface. As a result of this effect, thermal boundary resistance increases. It is important in such situations, to explore a basic understanding of the thermal transport mechanisms.

Net heat flux for two solids, which are at small distance apart by vacuum gap, is much greater than that predicted by the Stefan–Boltzmann law between two blackbodies [4]. Since, energy transport between surfaces at close vicinity has important applications in nano-scale energy conversion devices and near-field scanning thermal microscopy [5]; therefore, investigation of energy transport in thin films pair with the presence of minute gap is of importance.

Energy transport in dielectric thin films with the combination of metallic/non-metallic films and quantum dots plays an important role for the device performance. The thermal properties of the thin film mainly depend on the film size and heat source location. Therefore, investigation into the energy transport characteristics due to the films size and heat source location becomes necessary. Since the model study provides useful information on the transport characteristics, research focusing on the model study is essential.

1.2 Microscale Heat Transport

There are two important size parameters, which govern the energy transport in a thin film: mean free path (Λ) and characteristic dimension of the material (L).

In dielectric materials, thermal energy is transported by means of lattice vibration about their equilibrium position. Among these vibrations, only certain frequencies of waves are responsible for carrying energy due to quantization. These waves can travel from one surface of thin film towards the other surface, which results in the energy transport between surfaces. These lattice vibrations are called phonons.

The interaction of the two phonon waves is termed as collision and average distance traveled between two successive interactions of phonon wave is known as mean free path of phonon [6].

In the diffusive transport, the characteristics dimension of the materials is much larger than the mean free path that is $(L \gg \Lambda)$, the energy transport is said to be macroscopic, as shown in Figure 1.1. In this case, Fourier Law is applicable and the transport is governed by a purely diffusive nature.

When the mean free path is much greater than the characteristic dimension of the material that is $(\Lambda \gg L)$, the energy transport is said to be microscopic. Since $(\Lambda \gg L)$, the lattice wave reaches another surface without being scattered and is not affected by resistance. This is known as Ballistic Transport. Temperature gradient could not be established inside the film, and according to the Fourier Law, it is impossible to prescribe the thermal conductivity [7]. Ballistic transport is also observed in a specific phonon wave in which the wavelength of phonon (λ) is greater than the distance in x-direction x that is $\lambda > x$. Therefore in thin film at a specific distance it is possible that some of phonon waves are reached by ballistic transport and some diffusive transport.

When the characteristic dimension of the material is comparable with the mean free path, then transport is known as Ballistic Diffusive transport. This is combination of ballistic and diffusive transport. The temperature jump can be observed at the films edges as shown in Figure 1.1.

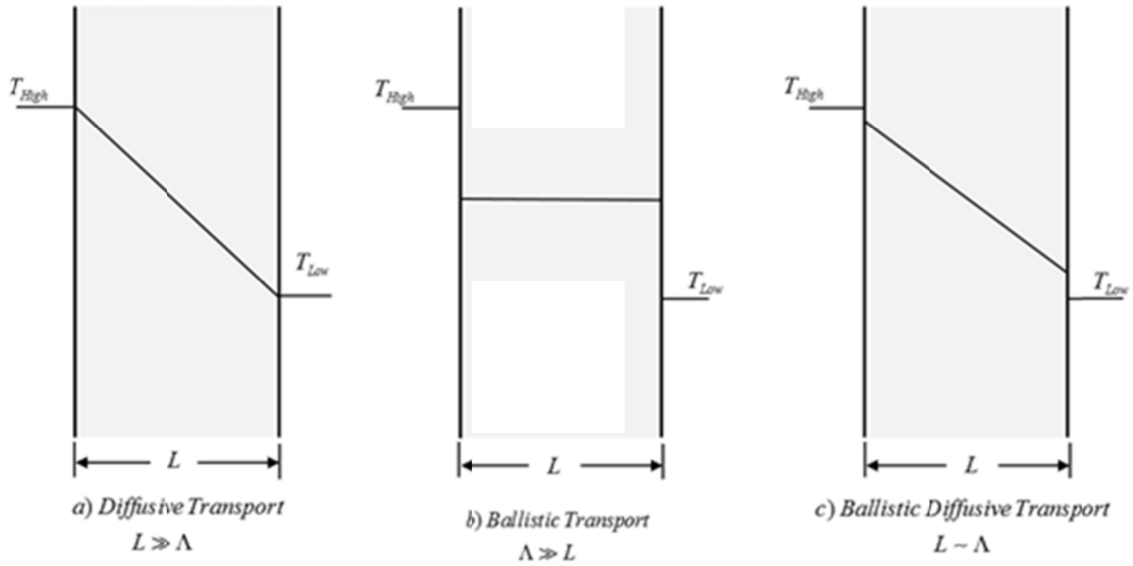

Figure 1.1 Comparison of propagation methods a) Diffusive transport b) Ballistic Transport and c) Ballistic Diffusive transport.

1.3 Energy Transport Models

In this section a brief introduction to different thermal energy transport models, excluding advection and molecular diffusion, are provided. Each of these models can be used to determine the energy transport characteristics for specific situations.

1.3.1 Fourier Law

In 1807, French scientist Joseph Fourier gave the relationship between heat flux q'' and temperature gradient ∇T, which are important thermal quantities in energy transport in solids. For homogeneous and isotropic medium, the Fourier law of heat conduction can be written as:

$$\mathbf{q}'' = -k\nabla T \tag{1.1}$$

where k is the thermal conductivity.

The Fourier law considers that heat flux q'' and temperature gradient ∇T appears at the same time instant; the thermal wave travelled with infinite speed. It means if the thermal disturbance is applied in the material, its effects can be measured at infinite distance from the thermal disturbance with in no time. Although infinite speed of thermal wave is practically imperceptible, but for most common engineering situations the Fourier’s law is quite accurate [1]. However, with the fast development in science and technology creating situations involving temperature near absolute zero, extreme thermal gradients, high heat flux conduction and short time behavior, such as laser–material interaction, under such situations the Fourier's law becomes invalid [2].

1.3.2 Single Phase Lagging Model

In 1992, Tzou [8] proposed the single phase lagging model, it considers the lagging behavior in heat flux, which is given by,

$$\mathbf{q}''(r,t+\tau_0) = -k\nabla T(r,t) \tag{1.2}$$

where, r is the position vector, t is time and τ_0 represents the time lag. According to this model for a particular position vector r, temperature gradient established at time t whereas heat flux appear at some later time $t+\tau_0$. Time lag (τ_0) is the relaxation time which physically represents the time difference needed to establish the heat flux at a position when a temperature gradient is applied. The first order expansion of τ_0 in equation (1.2) with respect to t bridges all the physical quantities at the same instant of time. This results in the expression

$$\mathbf{q}''(r,t) + \tau_0 \frac{\partial \mathbf{q}''}{\partial t}(r,t) \cong -k\nabla T(r,t) \tag{1.3}$$

which is the Cattaneo-Vernotte(CV) model provided by Cattaneo [9] and Vernotte [10]. The above equation is reduced to Fourier law as τ_0 approaches to zero. Analysis of single lagging model indicates that higher $\partial \mathbf{q}'' / \partial t$ results in a large derivation from the Fourier law.

1.3.3 Dual Phase Lagging Model

Many experiments have showed that single lagging model provides more accurate predications when compared with Fourier Law. However, some of the predications by single lagging model are not in good agreement with the experimental results [1, 11-12]. In detailed study, it has been revealed that single lagging model does not consider size effects and only accounts for fast transients. To consider the size effect and fast transition dual phase lag model is presented [12].

$$\mathbf{q}''(r,t+\tau_0)=-k\nabla T(r,t+\tau_T) \tag{1.4}$$

In the above expression, τ_T is the time lag in temperature gradient. It is the time delay due to the size effect and the micro structural interaction such as the phonon-electron interaction or phonon scattering in temperature gradient. τ_0 is the time lag of the heat flux, it incorporates fast transient effects. τ_T and τ_0 are intrinsic thermal properties of the bulk material.

1.3.4 Kinetic Theory Approach

Kinetic theory approach can be used for the analysis of non-equilibrium energy transport processes in metallic substrate. One of non-equilibrium energy transport process is heating of a metallic substrate when the heating time approaches the electron-phonon energy relaxation time. In this case, the Fourier heating model fails to predict the correct temperature distribution in the surface vicinity of the substrate [13]. In such situation, kinetic theory approach can be used to estimate the energy transport characteristics [14]–

[16]. The electron kinetic theory approach considers the electron-phonon collision mechanism through which the energy exchange between the electrons and lattice site atoms occur. For ultrafast external pulse heating application the electron kinetic theory approach gives [17],

$$\rho C_p \frac{\partial T}{\partial t} = k\frac{\partial^2 T}{\partial x^2} + f\frac{{\Lambda_e}^2 \partial^2}{\partial x^2}\left(\rho C_p \frac{\partial T}{\partial t}\right) - \rho C_p \tau_s \frac{\partial^2 T}{\partial t^2} + I_0 \delta \exp\left(-\delta\left|x\right|\right) \tag{1.5}$$

where ρ is density, C_p is the specific heat, x is the spatial coordinate corresponding to x axis, f is the fraction of excess energy exchange, Λ_e is the mean free path of electrons, τ_s is the thermal relaxation time, I_0 is the peak power intensity, δ is the absorption coefficient. When the second and third terms of right hand side in the above equation are neglected, the equation results in the Fourier conduction equation with external heating term.

1.3.5 Schrödinger Wave Equation

The wave particle duality of light, motivated de Broglie [18] to postulate that a material particle also have wave properties. In continuation to wave nature of material particle, Schrödinger introduced the equation in the form of the wave functions that govern the motion of small particles and specify how these waves are altered by external influence. Schrödinger states that the wave function of any material obeys the following [19]:

$$-\frac{\hbar}{2m}\nabla^2\psi_t + U\,\psi_t = i\hbar\frac{\partial\psi_t}{\partial t} \tag{1.6}$$

m is mass, t is the time ,U is the potential energy constraint and ψ_t is the wave function.

In 1926, Born defined the wave function [6]. He stated that the product of wave function and its complex conjugate is the probability density function. Schrödinger equation can be solved for the analysis of energy transport characteristics for some simple cases [20].

1.3.6 Molecular Dynamics Simulation

Molecular Dynamics (MD) simulations can be used to calculate the energy transport characteristics in nano-size devices. These simulations calculate the motion of atoms in a molecular assembly using Newtonian dynamics to determine the net force and acceleration experienced by each particle. For i^{th} particle with a mass m_i at r_i MD simulation solved the following equation [6],

$$m_i\frac{d^2r_i}{dt^2} = \sum_{\substack{j=1 \\ j\neq i}}^{N} F_{ij} \tag{1.7}$$

where N is the number of particles in the system and F_{ij} denotes the force exerted on particle i by particle j.

MD simulation predicts the position and momentum of particles in the system, which can be used to investigate the transport characteristics in the system.

1.3.7 Boltzmann Transport Equation

Boltzmann transport equation (BTE), which is one of the sub-continuum methods, can also be incorporated to examine the non-equilibrium energy transport characteristics in micro and nano scale devices. The BTE predicts the non-equilibrium probability distribution, which can be used to determine the energy transport characteristics in nano and micro scale devices. The BTE can be written as [21],

$$\frac{\partial f}{\partial t}+\frac{p}{m}.\nabla_r f+\dot{p}.\nabla_p f=\left(\frac{\partial f}{\partial t}\right)_{collision} \qquad (1.8)$$

where f is the non-equilibrium probability distribution function and p denotes momentum.

1.4 Limitation and Application of the Energy Transport Models

Fourier law, which is commonly used in macro scale energy transport analysis, does not provide the accurate estimation of transport characteristics at micro and nano-scale level. Although, single phase lagging models overcomes the deficiency of Fourier law regarding the infinite speed thermal wave, but some of predications by single lagging model are not in good agreement with the experimental results [1, 11-12]. Dual phase lagging model considers the micro structural interaction, which was neglected in single phase model. This model can only be used for the predication of energy transport in metallic thin film [22]. Kinetic theory approach can be used for the analysis of non-equilibrium energy transport processes in metallic substrate [14]–[16], but as the solution requires electron and lattice sub-systems, therefore, it cannot be used for the analysis of dielectric thin films. Schrödinger equation, is used for estimation of electrical characteristics in thin films [23-24], but for the analysis of energy transport characteristics in thin films it becomes very complicated to obtained proper solution. A molecular dynamics simulation overcomes the major limitation of BTE methods, which is that they invariably require experiments to determine fitting parameters for the models. Therefore, for new and novel nano-scale materials for which no experiments have been performed or for cases where experiments are too difficult to perform, BTE approaches cannot be electively used. Despite the fact that MD simulation can be used to determine the energy transport characteristics in thin films, it requires excessive computational power and can become unphysical due to periodic boundary conditions implemented in the solution. Thin films are too large to yield to atomistic-level simulation and estimation of the energy transport characteristic must rely on solutions of the BTE [25]. Therefore, in this dissertation Boltzmann transport equation, which is one of sub-continuum methods, is used to assess the energy transport characteristics in thin films including the ballistic effects.

In statistical mechanics, no-equilibrium processes are described by using the BTE which is a semi-classical approach. The BTE is a non-classical approach as it does not consider the matter as a continuum, but is considered to be composed of an extremely large number of particles, atoms, molecules, electrons, etc. Therefore, this models the microscopic behavior of the material and macroscopic properties are comprehended from microscopic behavior. The BTE is classical in the sense that the particles are assumed to obey the laws of classical mechanics and no quantum mechanical effect is assumed. This may not be entirely true because some results from the quantum theory may be needed to model the scattering terms in the BTE. However, the wave mechanics formulation is never used directly and hence one may assume a classical treatment. Hamiltonian mechanics formulation of classical mechanics is usually used in the derivation of the relevant equations [26].

1.5 Basic Concepts from Statistical Mechanics Relevant to the Microscale Modeling of Heat Transport

Statistical mechanics is the modern form of the kinetic theory of matter and was developed mainly by the scientists Clausius, Maxwell, Boltzmann and Gibbs. In this section, a summary of the statistical mechanical approach of modeling is presented as applied to an ideal gas.

Consider a dilute, ideal, monatomic gas. This gas is composed of an extremely large number of exactly identical particles that are travelling in all directions, at tremendous speeds. During their motion, these particles undergo elastic collisions with one another. In each second there are an enormous number of collisions occurring within the gas. These collisions are assumed to be instantaneous and they change the momentum of the particles discontinuously, without changing their spatial positions. Furthermore, it is assumed that only two particles take part in any given collision and three or more particles collisions are extremely rare. In between the collisions, the particles travel in a straight trajectory, obeying the second law of motion or equivalently, obeying the laws of Hamiltonian mechanics. At any given time, different particles have different speeds and travelling directions. It is this microscopic picture of the gas, which has to be used to deduce the macroscopic properties of it. Two points should be noted at this juncture. The first is that to theoretically describe the exact dynamics of such a large number of particles that are also undergoing elastic collisions is virtually impossible. Even by employing modern numerical computations, the problem is without solution. The second thing to note is that the main goal is not to determine the exact dynamics of the particles but to determine the macroscopic manifestations of such a dynamics. This comes about in the form of a few macroscopic properties of the gas, such as its total energy, entropy, density, temperature, etc. In fact, it is these properties which can measure experimentally and not the exact speed of a particular atom or molecule. It is clear therefore that statistical behavior of the collection of a large number of particles having the dynamical characteristics is the main interest. Even in experiments conducted on the gas, it is the time averaged and space averaged quantities that one can measure, since the measurement time and the dimensions of the probe are much larger than the characteristic time of the dynamics of the gas particles and the size of these particles, respectively. Hence, it becomes necessary to apply statistical techniques to the motion of the gas particles and this is the domain of the subject of Statistical Mechanics.

Phase Space:

A single particle, moving in three dimensions and thus having three degrees of freedom, has associated with it three momentums. If the three coordinates of the particle along with the three momentums are prescribed at any given time then the dynamics of the particle is completely prescribed. If these six quantities are given as functions of time then the complete dynamical history of the particle is known. A Cartesian coordinate system with each single axis assign to each of the six quantities. There are three axes for the three position variables and three axes for the three momentum variables. This is called the phase space of the particle. The space consisting of only three position axes is called the configuration space. And the space consisting of only three momentum axes is called the velocity/momentum space.

A single point in a phase space, completely determines the dynamics of the particle at any given time. A trajectory in such a phase space completely determines the dynamical time history of the particle. This trajectory is obviously parameterized by the time variable.

Ensemble:

In order to describe the dynamical behavior of a single particle statistically, one may assume that the phase point corresponding to the dynamics of a particle can be anywhere in the phase space, but with a certain probability. That is, there is a certain probability associated with each location in the phase space. The magnitude of this probability tells the likelihood of the particle's phase point to be in that location. The probability can be defined through the probability distribution function that is $f = f(x, y, z, p_x, p_y, p_z, t)$.

Another view of looking at this feature of statistical mechanics is by means of the concept of an ensemble. An ensemble is the name given to the collection of a large number of identical 'mental' copies of a single particle. Each 'mental' copy of a particle differs from the other 'mental' copies in position, or momentum or both. Then, the density of this ensemble in phase space can be defined function by probability distribution function, which is defined above. Now, the minimum and maximum values of the position variables that any particle can take are dictated by the size of the container in which the particle is confined. The maximum value of the momentum is fixed by the total energy of the single particle. The probability density function, will then give the number of phase points per unit 'infinitesimal volume' of the phase space around any location (x, y, z, p_x, p_y, p_z) (where p_x, p_y, p_z are the momentums) in the phase space and at any given time. The point (x, y, z, p_x, p_y, p_z), for which this density is maximum, is the most probable point to which the dynamics of a single particle is assumed to correspond to at that time. This is in turn will give the most probable position and the most probable momentums of a single particle at any given time. It turns out that the function attains sharp peak at the most probable values of the phase variables and therefore the most probable values of the phase variables are also equal to their corresponding expectation values that are calculated with respect to the probability distribution function. These are given by the expressions, $\overline{r}(t) = \int rf(r, p, t)dr\, dp$ and $\overline{p}(t) = \int pf(r, p, t)dr\, dp$ (where r and p are the position and momentum vectors, respectively). Hence, the actual trajectory of a single particle may now be given as the expectation values of the dynamical variables, corresponding to the time-dependent probability distribution function f.

1.6 Boltzmann Transport Equation (BTE)

For N number of particles, the phase space is actually a $6N$ dimensional space. $3N$ axes correspond to the position variables and the other $3N$ corresponds to the momentum variables. Any point in the phase space completely specifies the dynamics of the N particles. If these N particles are those of our previously described collection of particles, then the dynamics of that collection is also completely prescribed at any given time. The probability density function can be defined as $f = f(x_i, y_i, z_i, p_{xi}, p_{yi}, p_{zi}, t)$ [6], which is now a function of the $6N$ variables as well as that of time t. It can be shown that the function f satisfies a 'continuity' equation in phase space which is given as [21],

$$\begin{aligned} &\frac{\partial f}{\partial t} + \frac{1}{m}\sum_{i=1}^{N}\frac{\partial(p_{xi}f)}{\partial x_i} + \frac{1}{m}\sum_{i=1}^{N}\frac{\partial(p_{yi}f)}{\partial y_i} + \frac{1}{m}\sum_{i=1}^{N}\frac{\partial(p_{zi}f)}{\partial z_i} + \\ &\qquad \sum_{j=1}^{N}\frac{\partial(\dot{p}_{xj}f)}{\partial p_{xj}} + \sum_{j=1}^{N}\frac{\partial(\dot{p}_{yj}f)}{\partial p_{yj}} + \sum_{j=1}^{N}\frac{\partial(\dot{p}_{zj}f)}{\partial p_{zj}} = \left(\frac{\partial f}{\partial t}\right)_{collision} \end{aligned} \tag{1.9}$$

In vector notation the above equation is written as,

$$\frac{\partial f}{\partial t} + \frac{1}{m}\sum_{i=1}^{N}\nabla_{r_i}(p_i f) + \sum_{j=1}^{N}\nabla_{p_j}(\dot{p}_j f) = \left(\frac{\partial f}{\partial t}\right)_{collision} \tag{1.10}$$

The above equation, when expanded using the product rule and simplified using the Hamilton's' equations of motion yield the Liouville's equation. These derivations are given below.

$$\frac{\partial f}{\partial t}+\frac{1}{m}\sum_{i=1}^{N} f\nabla_{r_i} p_i+\frac{1}{m}\sum_{i=1}^{N} p_i\nabla_{r_i} f+\sum_{j=1}^{N} f\nabla_{p_j}\dot{p}_j+\sum_{j=1}^{N}\dot{p}_j\nabla_{p_j} f=\left(\frac{\partial f}{\partial t}\right)_{collision} \tag{1.11}$$

The Hamilton's equation of motion for the N particles are,

$$\dot{x}_i=\frac{\partial H}{\partial p_{x_i}},\quad \dot{y}_i=\frac{\partial H}{\partial p_{y_i}},\quad \dot{z}_i=\frac{\partial H}{\partial p_{z_i}}\ \text{ or }\ \frac{p_i}{m}=\nabla_{p_i} H \tag{1.12}$$

$$\dot{p}_{x_j}=-\frac{\partial H}{\partial x_j},\quad \dot{p}_{y_j}=-\frac{\partial H}{\partial y_j},\quad \dot{p}_{z_j}=-\frac{\partial H}{\partial z_j}\ \text{ or }\ \dot{p}_j=-\nabla_{r_i} H \tag{1.13}$$

The above equation is the Liouville equation. It describes the time dependent behavior of the probability distribution function in the $6N$ dimensional phase space. In particular it can describe the dynamics of previously described collection of N particles.

Due to the assumption that the particles are completely identical, the Liouville's equation can be applied in an extremely simplified form to a collection of particles. For identical particles, the function $f=f(x,y,z,p_x,p_y,p_z,t)$ will be exactly same for each particle; therefore, it is only necessary to consider a single particle and a six-dimensional phase space. However, the consequences of the collision processes between the particles have to be explicitly accounted for. This is done by adding a collision term on the right hand-side of the simplified Liouville's equation. It is this equation which is referred as Boltzmann Transport Equation [27]. The three-dimensional form of the BTE is presented below [21].

$$\frac{\partial f}{\partial t}+\frac{p}{m}.\nabla_r f+\dot{p}.\nabla_p f=\left(\frac{\partial f}{\partial t}\right)_{collision} \tag{1.14}$$

1.7 Relaxation Time Approximation

In dielectric material, the term $\left(\partial f/\partial t\right)_{collision}$ describes phonon scattering (collision) rate. There are two categories of phonon scattering: elastic and inelastic scattering. In the elastic scattering, the phonon interacts with the lattice imperfection: crystal defects, dislocation and the grain boundaries. However, the energy is conserved and frequency of incident phonon is unchanged during an elastic scattering. Inelastic scattering occurs because of the interaction of three or more phonons. This is also known as intrinsic process [3] as it takes place because of the deviation from periodicity in perfect crystal, due to the thermal lattice vibrations [27]. Inelastic event which involves four or more phonons are only important at higher temperatures [28]; therefore, it is neglected in the present study because of low temperature involvement ($300 \leq T \leq 301$ K).

Scattering term solution of the energy transport equation, in its rigorous form, is very complicated as one need to solve the Schrodinger equation for all particles system (i.e. electron and phonons). One way is to use perturbation method [29] to solve the scattering term, but this also results in the complicated integral-differential equation which is difficult to solve [6]. The other ways to treat the scattering term is the relaxation time approximation. This approximation based on the observation that scattering or collision of electron or phonon tends to restore the equilibrium. Scattering term based on the relaxation time approximation which is given as [30]:

$$\left(\frac{\partial f}{\partial t}\right)_{collision} = \frac{f^0 - f}{\tau} \tag{1.15}$$

where, τ is the relaxation time, f^0 and f are the equilibrium and the non-equilibrium probability distribution functions. For different particles the equilibrium probability distrubtion f^0 defined by different distribution function which are given in Table 1.1.

In order to quantify the relaxation time τ, the understanding of elastic and inelastic phonon scattering process and their relaxation times are required. The elastic scattering relaxation τ_i time can be obtained from the kinetic theory approach [31]. Inelastic three phonon scattering are having two types: the *N* process and *U* process. In both processes, the energy conversation takes place with alteration in the frequencies. In the *N* process, momentum conservation takes place therefore it does not directly contribute to the resistance in the energy flow [27]. However, due to frequencies alteration during the *N* process, it indirectly imposes the resistance in the heat flow [3]. In *U* process, energy flow encountered the direct resistance as the momentum is not conserved during the scattering. The expressions for *U* process relaxation time τ_U and *N* process relaxation time τ_N are available in the open literature [32]. When the scattering processes are independent of each other, the relaxation time τ can be calculated using the Matthiessen's Rule as following:

$$\frac{1}{\tau}=\frac{1}{\tau_i}+\frac{1}{\tau_U}+\frac{1}{\tau_N} \qquad (1.16)$$

where, τ_i is the elastic scattering relaxation, τ_U is the U process relaxation time, τ_N is the N process relaxation time and τ is the relaxation time.

The assumption of independent scattering processes, in Matthiessen's Rule, is not valid for inelastic scattering. But error involved in applying the Matthiessen rule is usually very small [27], and it gives correct results for most situations [6]. Therefore, it can be used in the measurement of relaxation time.

In this dissertation the relaxation time approximation is adopted for the simplification of the scattering term in Boltzmann transport equation. The BTE can be written as,

$$\frac{\partial f}{\partial t}+\frac{p}{m}.\nabla_r f+\dot{p}.\nabla_p f=\frac{f^0-f}{\tau} \qquad (1.17)$$

1.8 Phonons as an Ideal Gas

In a dielectric material, thermal energy is stored as the kinetic and potential energies of vibrating atoms or molecules. In crystalline materials, these particles are arranged in the shape of a periodic crystal lattice. Long chains of atoms and molecules vibrate with different frequencies, in longitudinal as well as transverse polarizations. Thermal energy is also transported through these lattice vibrations. According to quantum mechanics, the vibrational energy of an oscillator is quantized and is proportional to the frequency of vibration. Hence, only certain frequencies are allowed due to the specified distribution of energy. It is beneficial to regard a single quantum of vibrational energy as a particle called the phonon. This is analogous to the electromagnetic energy quantum, the photon. However, the phonons and photons are not completely equivalent. According to this picture one may assume that thermal energy is stored and transported by the motion of phonons and since the number of phonons is very large one may conceive of a phonon 'gas' permeating the dielectric material. To this phonon gas the statistical mechanics concepts developed for the particles of an ideal gas can be applicable. To obtain the equilibrium properties, an equilibrium probability distribution function may be used, whereas to compute the transport properties BTE has to be used. In this respect, it is important to realize that the phonons do not obey the Maxwell-Boltzmann distribution function like the gases. This is because the number of phonons is not conserved. Furthermore, they do not obey the Pauli Exclusion Principle. Hence, one may consider the phonons as a type of boson, just as the photons are. The correct equilibrium distribution to use in this case is the Bose-Einstein distribution. Based on this distribution and using the BTE, one may compute the thermal conductivity of the dielectric material under a Fourier law assumption or without it. Usually the Fourier law breaks down in that direction along which the material dimension is of the order of the phonon mean free path.

Table 1.1 Equilibrium Probability Distribution

f^0	Application
Maxwell-Boltzmann Distribution	Ordinary or ideal gas
Fermi-Dirac Distribution	Fermion particles (Such as Electron)
Bose-Einstein Distribution	Boson particles (Such as Phonons)

1.9 Scope of Work

In this dissertation energy transport characteristics are theoretically investigated in one and two dimensional thin films when subjected to thermal distortion.

Thermal transport in two dimensional dielectric thin films is investigated; in which case the influences of film size, heat pulsation and heat source size on energy transport characteristics are examined. In addition, the cross plane energy transport in the silicon and diamond thin films pair is studied. The diffusive mismatch and cut-off mismatch models for the assessment of thermal boundary resistance across the interface is introduced. The study is extended to include the effect of aluminum quantum dot on energy transport characteristics in the silicon thin film.

Entropy generation in one dimensional dielectric thin films is studied. This study is extended to include the effect of film thickness on entropy generation rate. Energy transport characteristics are investigated across the silicon thin films pair separated by the minute gap. In addition, thermal transport in one dimensional metallic films is also studied to examine the influence of film size and heat pulsation on energy transport characteristics.

Since the analysis of energy transport at such small spatial scale requires the techniques of sub-continuum transport processes, the Equation of Phonon Radiative Transfer (EPRT) is incorporated for this purpose. EPRT is a modified form of the Boltzmann Transport Equation, which has been solved numerically using the finite-difference method. For time-marching, an implicit scheme has been used.

1.10 Outline

The dissertation is comprised of five chapters.

Chapter 1 introduced the dissertation topic, motivation of work, introduction of energy transport models and scope of this dissertation.

Chapter 2 provides literature review in the area of micro and nano-scale heat transport. The literature review covers the theoretical as well as experimental studies which have been done previously.

Chapter 3 describes the detailed mathematical models which include the derivation of EPRT; the initial, boundary and interface conditions for all studies considered. The diffuse mismatch and frequency mismatch model also discussed for two dimensional dielectric thin films pair. It also includes the EPRT for metallic thin films.

Chapter 4 gives an account of the numerical method employed in the analysis. Domain discretizations as well as the finite-difference discretization of the governing equations are explained. Algorithms are presented for the solution of the various equations.

In chapter 5, the results of the theoretical investigations are presented for all the considered case studies. This chapter also includes the discussion on the energy transport characteristics for the all considered situation and their significance.

Chapter 6 includes the conclusions drawn from the investigations of all case studies.

CHAPTER 2

LITERATURE REVIEW

2.1 Introduction

Considerable research studies have been carried out since the last three decades in the field of micro and nano-scale energy transport. The researchers have performed theoretical studies to investigate the heat transport characteristics at micro and nano-scale. Experimental research has advanced in parallel to theoretical investigations. In the last two decades, researchers incorporated different models to examine the energy transport characteristics at micro and nano-scale. Scientists and researchers are faced with difficulties in micro and nano-scale modeling of energy transport as continuum hypothesis breaks down. In the absence of this hypothesis, a variety of competing alternatives exist and a single approach does not stand out. In this chapter an overview of the current state of affairs of the micro and nano-scale energy transport research is presented by summarizing the findings of various research papers.

2.2 Literature Review

Mansour and Yilbas [33] studied the heat transfer across the silicon and aluminum thin films. In this study, heat transfer was examined in silicon film using frequency dependent Phonon Radiative Transport Equation (EPRT) while the modified two equation model was used for energy transport in the aluminum film. Thermal boundary layer was also introduced across the silicon and aluminum films. They also included the electron-phonon resistance at the interface of aluminum film. Transient analysis was performed at the temperature difference of 1 K between the edges of silicon and aluminum films. It was found that, the phonon temperature was higher than electron temperature at aluminum interface. In addition, frequency dependent solution of EPRT resulted in sharper decay of equivalent equilibrium temperature than that corresponding to frequency independent solution of the phonon transport in the silicon film.

Chen [34] studied the heat transport characteristics in the perpendicular direction of superlattices and in the periodic thin-film structures. He used the Boltzmann transport equation in his numerical study to obtain a set of integral equations describing the distribution of temperature gradient with in each layer while incorporating the thermal boundary resistance at interfaces. The governing equations were solved numerically. He found that the effective thermal conductivity of the structure in the perpendicular direction was influenced by both the film size effects on heat transfer within each layer and the thermal boundary resistance at different layer interfaces. He also indicated that the thermal boundary resistance become no longer an intrinsic property of the interface, but also depends on the layer thickness as well as the phonon mean free path.

Yilbas et al. [35] analytically solved BTE for laser short pulse heating of solid surface. They derived the hyperbolic heat conduction equation from the Boltzmann transport equation. Their analytical solution provided the equation, which is appropriate for laser short-pulse heating of a solid surface. In modeling, absorption of the incident laser energy was modeled as the time exponentially decaying pulse, which was incorporated as a volumetric heat source in the hyperbolic equation. They incorporated the Fourier transformation for simplification of equation, and then solved the simplified equation using the Laplace transformation method. They solved their developed equation to predict the transient temperature distribution, for laser short-pulse heating in steel. They found that internal energy gain from the irradiated field, due to the presence of the volumetric heat source in the hyperbolic equation, result in rapid rise of temperature in the surface region during the early heating period. They also indicated that temperature decay was gradual in the surface region and as the depth below the absorption depth, temperature decay became sharp.

Nika et al. [36] performed the review study for two dimensional phonon transport in graphene. They reviewed experimental and simulation work done in literature, and discussed different techniques available for the calculation of thermal conductivity. In Raman experiments, it was found that acoustic phonons were the main heat carriers in the graphene, while optical phonons were used for counting the number of atomic plane. They concluded on the basis of recent computational studies that, the thermal conductivity of graphene strongly depended on the concentration of defects, strain distribution, sample size and geometry.

Jeong et al. [37] studied the thermal conductivity of bulk and thin film silicon using the Landauer approach. They numerical results were in good agreement with

Molecular Dynamic (MD) simulations results. They found that for in-plane silicon films, 50% of the heat was carried by phonons with shorter mean free paths as compared to the bulk. They also studied the cross plane thermal conductivity of the thin films. Their study revealed that Landauer approach provided a new simple computational approach to predict the thermal conductivity for in-plane and cross plane in bulk and thin silicon films.

Ju et al. [38] performed the experimental study to investigate the impact of micro and nano-scale heat transfer in silicon substrates on thermal interface resistance characterization. They indicated that sub-continuum heat conduction and spatial non-equilibrium between electrons and phonons in a metal may resulted in overestimation of the thermal interface resistance. In addition, they found that the use of an erroneous substrate thermal conductivity could cause significant systematic errors in steady- and quasi-steady state measurements of the thermal interface resistance.

Donadio et al. [39] studied the effect of temperature on the thermal conductivity of silicon nanowire using the molecular dynamics simulation. Their simulation results for silicon wire with amorphous surface indicated that; the thermal conductivity value reached close to that of amorphous silicon and this value remained almost constant between the range 200 and 600 K. They also developed a parameter free model to account for the temperature dependency, which observed in their simulation and provided a qualitative explanation of recent experiments.

Hao et al. [40] examined the thermal conductivities of the aligned porous silicon structures. They performed the frequency dependent, 2-D transient analysis using Monte Carlo to investigate the porous silicon structure. In the simulations, they introduced the periodic heat flux boundary condition with a constant virtual wall temperature. They observed that this boundary condition resulted in the good estimation of thermal conductivities. In addition, they also found that frequency dependent simulation provided the better estimate of thermal conductivities as compared to frequency independent simulation.

Wong et al. [41] studied the effect of nano-scale phonon transport in the thin silicon films of different aspect ratios using Monte Carlo simulation tool. In their simulation, they considered the external heat source in the silicon films. They developed a new Monte Carlo algorithm to execute the simulation while reducing the requirements of memory storage and computational resources. The simulation results were compared with the results of the heat diffusion equation. They found that the heat diffusion equation significantly underestimated temperature distribution at nanoscale with external heat source. In addition, the diffusion equation was not providing the correct temperature distribution even if it was solved with reduced thermal conductivity values, calculated from the Monte Carlo simulation.

Dames et al. [42] studied the phonon specific heat of titanium dioxide nanotubes. They conducted experiments to measure the phonon specific heat of multi walled titanium dioxide nanotubes from the temperature range of 1.5 to 95 K. They found that at high temperatures the nanotube specific heat approached that of the bulk material; however, below about 50 K the nanotube specific heat showed large enhancements compared to bulk, which was due to the transition to low-dimensional behavior. They also found the second transition in specific heat below about 3 K and the nanotube specific heat became nearly constant while exceeding the bulk material value by an order of magnitude or more at 1.5 K.

Chen et al. [43], considered the thermal conductivity and heat transfer processes in superlattice structure. They modeled the heat transfer processes by means of the Boltzmann transport equation. They found that existing experimental results could be explained on the basis of this model for both the in-plane and cross-plane directions and suggested a possibility for further reduction of the thermal conductivity.

Xu et al. [44] experimentally investigated the microscale boiling heat transfer in microchannels. They conducted experiments with ten parallel microchannels using acetone as the working fluid at high heat flux. Infrared radiator image system was used for the chip temperature measurement while an optical system combining a microscope and high speed camera was used for transient flow pattern identification. They found that all microchannels displayed transient flow pattern behavior in milliseconds.

Avci et al. [45] carried out a second law analysis of heat and fluid flow in microscale geometries. In the analysis, the hydrodynamically and thermally developed flows were considered for the microtube and microduct, microscale effects were included in terms of viscous dissipation, velocity slip and temperature jump. They also conducted a parametric study to determine the effects of the Brinkman number and the Knudsen number on entropy generation. They found that entropy generation deceased with an increase in the Knudsen number while increasing the Brinkman number resulted in increasing entropy generation.

Chu et al. [46] performed the numerical study to investigate the heat transfer, which included the conduction and thermal radiations, in absorbing, emitting and isotropically scattering medium. For conductive heat transfer modeling, they used the non-Fourier equation with lag time between heat flux and temperature disturbance, which predicted the finite speed of temperature disturbance. They performed the steady and transient analysis to study the effect of radiation and optical thickness of the medium. It was found that wave nature was significantly influenced by internal radiation in the medium. They found that the thermal wave nature in the combined non-Fourier heat conduction with thermal radiation was more observable for large values of conduction-to-radiation ratio, small values of optical thickness and higher scattering medium. They also compared the results of Non-Fourier model with Fourier model, which indicated that non-Fourier effect became insignificant as either time increased or the effect of radiation increased.

Pisipati et al.[47] studied heat transfer characteristics in several applications, such as silicon on Insulator transistors, silicon thin films with heat pulsation, and silicon thin film sandwiched between two bulk layers of silicon dioxide. In the analysis, they incorporated the BTE with diffusion term, while introducing the reflectance and transmittance of phonons at the interface. The numerical simulations were performed on COMSOL Multiphysics. The numerical simulations were also carried out for the BTE model without diffusion for multilayers. They compared their numerical analysis results with existing published results for Si/Si, Si/Diamond layers and were found to be in good agreement.

Chen [48] examined the effects of nanoscale heat transfer on the device performance. He presented the review of the some recent development in the area of nanoscale heat transport. He studied the effect of thermal conductivity reduction in superlattices as the case study. He performed the numerical analysis using Boltzmann Transport Equation with appropriate boundary conditions. He found that thermal conductivity reduced with the reduction in film thickness. He indicated that the reduced thermal conductivity of superlattices greatly impacted the temperature rise of photonic devices. On the other hand, the same size effect could be exploited to increase the efficiency of thermoelectric energy conversion devices.

Xiang et al. [49] carried out a study to investigate the thermal conduction across the micro contact points and thermal contact resistances. They used non-equilibrium molecular dynamics simulations with the consideration of the near field radiation. They found that the thermal contact resistance increased with decreasing the area of the micro contact point, and with the increasing micro contact layer thickness.

Bayazitoglu et al. [50] studied the microscale heat transfer with extended slip boundary conditions. They developed these boundary conditions systematically to be used beyond the slip flow regime. They found that the slip velocities calculated from the stress boundary conditions agreed well with linearized Boltzmann results.

Yilbas and Mansoor [51] studied the heat transport characteristics in two dimensional silicon thin films. The steady, frequency independent numerical analysis was performed incorporating the BTE. They simulated the two dimensional silicon films for different boundary conditions and different film sizes. They found that for square films both the longitudinal and transverse phonon radiative transport becomes important. They also indicated that the phonons emitted from low temperature edges do not contribute notably on the overall phonon transport in the film.

Lervik at al. [52] investigated the heat transfer through nano-scale interfaces consisting of n-decane droplets in water. They carried out a computer simulation using the transient non-equilibrium molecular-dynamics method. They calculated the thermal conductivity, the interfacial conductance of the droplet, and the droplet/water interface respectively. They found that the thermal conductivity of the droplets was insensitive to its size, whereas the interfacial conductance shows a strong dependence on the droplet radius.

Srinivasan et al. [53] examined the microscale heat transfer in multilayered thin films using parallel computation. In the analysis, the BTE is solved for 1-D and 2-D silicon and silicon dioxide thin films. They governing equation were discretized using finite difference method. They extended their work to investigate the effects of film thickness, grain boundary scattering and interfacial boundary conditions on the energy transport characteristics.

Shen et al. [54] studied energy transfer across a nanoscale gaps between a microsphere and a flat surface. They conducted the experiments to evaluate the radiation heat transfer between the two surfaces. They found that the heat transfer coefficients at nanoscale gaps were at 3 orders of magnitude larger than that of the black body radiation limit.

Lefèvre et al. [55] studied heat transfer characteristics between hot tips and substrate, which could be used in the application of scanning thermal microscopes. They performed the experimental and numerical study to analyzed the three heat transfer modes; solid-solid conduction, conduction through ambient air and through the water meniscus. They found that the all considered three modes contribute in a similar manner to the thermal contact conductance.

Yilbas and Mansoor [56] examined the effect of ballistic phonons on the energy transport in silicon thin films. In the analysis, they incorporated the frequency dependent EPRT to investigate the energy transport characteristics while introducing a spatially varying temperature source at the film edge. In addition, they examined the influence of film thickness on energy transport. They found that the Gaussian parameter, defining the spatial distribution of temperature at the film edge, significantly influenced equivalent equilibrium temperature variation in the film. They concluded that the equivalent equilibrium temperature reduced sharply across the film as the film thickness reduced.

Bunzendahl et al. [57] studied the heat transfer properties in thin diamond films. They experimentally measured the in-plane thermal diffusivity and thermal conductivity of a 1.75 micron CVD diamond film over a wide temperature range by employing a thermal wave technique. They found that a significant reduction in the thermal diffusivity and thermal conductivity compared to their values in the bulk material. They also indicated that peak diffusivity shifted significantly at high temperatures.

Wang et al. [58] investigated the thermoelectric performance of nanostructured n-type silicon germanium bulk alloy. They conducted several experiments to study the performance of thermoelectric. They observed significant enhancement in figure of merit (ZT) due to large reduction in the thermal conductivity while maintaining the power factor. They found that the peak ZT value was about 1.3 at 900^{o}C, which was because of the significant reduction in the thermal conductivity caused by the enhanced phonons scattering off the increased density of nanograin boundaries.

Chou et al. [59] studied the effect of size on the micro fin performance, particularly in the cryogenic region. They indicated that the heat flow choking could be observed in simple plate fins or pin fins in the microscale regime. The use of micro-plate-fin arrays was found to yield higher heat transfer enhancement than the use of micro-pin-fin arrays. They also established an equation for the optimum fin thickness.

Balasubramanian et al. [60] examined the nanoscale thermal transport across a solid-liquid interface. They incorporated molecular dynamics technique in simulations. Lennard-Jones potential parameter was used to model the fluid-fluid and solid-fluid interaction where as embedded atom method was used to describe the interactions between solid molecules. They found that the averaged Kapitza resistance varies with the initial temperature difference between the wall and the fluid.

Kalisik et al. [61] investigated the thermal conductivity for Cubic C (diamond), with consideration of the heat flow resistance mechanisms of boundary scattering, Umklapp processes, normal processes and presence of impurities. They developed a model, which was based on the effect of curvature of phonon dispersion curves. They found that the curvature of the dispersion curves dramatically affected the thermal conductivity.

Fu et al. [62], investigated the near-field radiative heat transfer between two semi finite media separated by a vacuum gap. They used fluctuational electrodynamics to calculate the net heat flux between high-temperature silicon and room temperature silicon or silicon carbide or aluminum. They found that the net radiative energy flux between two media could be greatly enhanced in the near field.

Tien et al. [63] discussed the challenges in the field of microscale radiative and conductive heat transfer in their study. Microlength scale heat transfer involved thermal energy transport processes in which heat carrier characteristic lengths became comparable to the characteristic device dimension. They presented the review of theoretical approaches available for the assessment of the energy transport characteristics. In addition, they also presented the challenges faced by the researcher to perform the experimental analysis.

Yilbas and Mansoor [64] examined the energy transport characteristics in two dimensional silicon thin film. They performed the numerical study using the BTE with incorporating the variation in phonon mean free path with frequency. They also investigated the influence of the film thickness on the phonon transport characteristics. They compared their results with frequency independent solution and found that ballistic phonons suppressed equivalent equilibrium temperature in the film. Their finding revealed that when the film width became more than double of the film thickness, the two-dimensional phonon transport reduced to one-dimensional transport in film.

Majumdar [65] examined the microscale heat conduction in dielectric thin films, where Fourier law was not applicable. He used the BTE to derive EPRT for steady-state and transient energy transport. He showed that in the limit, when the film thickness was much larger than the phonon-scattering mean free path, the EPRT reduced to the hyperbolic heat equation. In addition, he indicated that at lower temperature with the film thickness smaller than or comparable to the phonon mean free, the EPRT reduced to the black-body radiation law.

Gao et al. [66], studied the heat conduction mechanisms in fluids seeded with nanoparticles. They measured the thermal conductivity experimentally and carried out structural analysis for the same material in both liquid and solid states. They found that the thermal conductivity enhancement of nanofluids was related to clustering.

Mansoor et al. [67] studied the phonon transport characteristics in layered thin film with the consideration of boundary layer resistance. They examined silicon-silicon and silicon-diamond films numerically using the EPRT. Thermal boundary resistance was modeled by diffusive mismatch method. Transient and steady analysis was carried out on the two layered thin films. They found that the temperature slips occurs at interface in Silion-Silion film which happened because the transmittance and reflectance of phonons at the interface of the films. Their finding revealed that the equilibrium, emitted and gray body temperatures was higher at the interface of the silicon films during the heating period 36<t<72 ps which was because of the small mean free path of silicon; in which case, phonons reach the interface at higher rates. In addition, they found that silicon-diamond film pair showed the higher temperature slip at the interface which was due to the thermal boundary resistance and large mean free path of diamond.

McGaughey et al. [68] investigated the phonon thermal conductivity of the argon face centered cubic crystal. They incorporated the BTE with the Single-Mode relaxation

Time Approximation (SMTA) in their analysis. They performed their simulation at 20 K and 80 K. The estimated values of phonon thermal conductivity from their analysis were in good agreement with the MD simulations. Their suggested approach eliminated the need for experimental fitting parameters. They concluded that predictions of thermal conductivity were strongly effected by frequency dependent the modeling of the of the phonon and relaxation times.

Dai et al. [69] investigated a compact finite-difference scheme for a 1-D heat transport equation at microscales. They numerically solved a heat transport equation involving second-order time derivatives as well as mixed derivatives of temperature. They showed that their scheme was unconditionally stable.

Narumanchi et al. [70] proposed a model based on the BTE. In their model, they considered transverse acoustic and longitudinal acoustic phonons as well as optical phonons by incorporating realistic phonon dispersion curves for silicon. The interactions among the different phonon branches and different phonon frequencies were considered, and their proposed model satisfies energy conservation. They solved BTE numerically using finite volume approach for steady and transient cases. Their simulation results were in good agreement with the experimental data over the wide range of temperature.

Yilbas and Mansoor [71] perfumed the numerical study to investigate the energy transport characteristics in two dimensional silicon thin films. Frequency dependent EPRT has been incorporated in the simulations. They performed their simulations while providing of 1 K temperature difference across the surfaces of thin film. They introduced the generalized logistic curve to analyze the logistic characteristic of temporal behavior of averaged heat flux. They also examined the influence of film width on the average heat flux. Their result indicated that temporal behavior of averaged heat flux followed the logistic S curve. They observed sigmoid variation between the averaged heat flux and the heating time on while plotting on log scale. In addition, they found that increasing the film width resulted in the increment of average heat flux.

Joshi and Majumdar [72] studied the transient heat transport in thin films. They developed an equation of phonon radiative transfer (EPRT) from the BTE which showed the correct limiting behavior for both purely ballistic and diffusive transport. They solved the EPRT for thin diamond films. In steady state analysis for thick films (10 μm), they found the same temperature predication from EPRT, Fourier law and hyperbolic heat equation (HHE). In thin films steady state analysis, EPRT showed the temperature jumps at wall (due to ballistic transport) which was much different temperature profile as compare to the Fourier law and HHE. They concluded that as the Fourier law represented the diffusive transport with infinite speed of thermal wave it could not be used for short time and spatial scale, whereas HHE indicated wave like behavior but not predicted the temperature jump under the ballistic transport therefore, it could be used for short time. They concluded that EPRT could be used for short duration and small spatial scale.

Che et al. [73] performed molecular dynamics (MD) simulations to study the thermal conductivity of diamond and related materials. They examined the role of quantum corrections to the classical thermal conduction and concluded that these effects were small for fairly harmonic systems such as diamond. They calculated the thermal conductivities for bulk crystalline materials using the classical MD. Their finding showed that vacancies sharply decrease the thermal conductivity of diamond. Their simulation results for isotopically perfect diamond were in well agreement with the experimental results.

Ju [74] performed the experiments to study the phonon transport characteristics in silicon nano structures. He presented the results of thermal conductivity of silicon, at room temperature, with variation of silicon layer thickness to get more insight into heat conduction in silicon. At room temperature, there was significant reduction in the thermal conductivity of the silicon layer with the film thickness less than 100 nm due to phonon boundary scattering. His experimental results were in consistent with the previous studies.

Narumanchi et al. [75] studied the comparison of different heat transport models for the predication of heat condition in submicron silicon-on-insulator transistor. They developed model based on the BTE incorporating full phonon dispersion effect. They validated full BTE against the experimental thermal conductivity values of silicon. They used the structured finite volume approach for the solution of BTE. They compared their results with the Fourier diffusion model, gray and semi gray BTE published results; which indicated that Fourier diffusion under-predicted the temperature by 350% with respect to prediction from the full phonon dispersion model. They found that for the full phonon dispersion model, the longitudinal acoustic modes carried majority of the energy flux.

Escombar and Amon [76] performed the numerical study to investigate the phonon dispersion influence on the thermal response of Silicon on insulator (SOI) transistor. They solved 1D and 2D computational models using Lattice Boltzmann method (LBM). Their study extended to examine the effects of hotspot size and heat pulse duration on energy transport. Their results revealed that sub continuum effects in SOI Joule heating were important when the heat pulse was shorter than the phonon relaxation time and/or when the hotspot region was smaller than the phonon mean free path. They also indicated that the sub continuum effects were characterized by the appearance of boundary effects, as well as by the propagation of thermal energy in the form of multiple, superimposed phonon waves.

Rashidi-Huyeh et al. [77] studied the non-Fourier heat transport in metal-dielectric core-shall nanoparticles under ultrafast laser pulse excitation. They performed the simulation using the Ballistic-diffusive equation, which was based on the BTE under the relaxation time approximation. They numerically determined the electron and lattice temperature in a spherical gold nanoparticle core under picosecond pulsed excitation as well as in the surrounding shell dielectric medium. They used the electron-phonon coupling equation in the particle with a source term linked with the laser pulse absorption and the ballistic-diffusive equations for heat conduction in the medium. Their results indicated that the lattice temperature values predicted from Fourier's law were smaller than estimated values from Ballistic diffusive equation.

Chen et al. [78] examined the structural, phonon, and thermodynamic properties of the ternary carbides in the Ti–Al–C system using first-principles calculations. They investigated the phonon dispersion curves and partial density of states. They found the different Ti–C bond characteristics between Ti_3AlC and the two other compounds. They predicated the values of the Gibbs energy, entropy, heat capacity, and thermal expansion coefficient of the compounds using the quasi-harmonic approximation. They also included the thermal electronic contribution in the thermodynamic properties. Their obtained results were in good agreement with experimental data.

Etessam-Yazdani et al. [79] performed the numerical analysis to study the ballistic phonon transport and self- heating effects in strained silicon transistor. They incorporated two dimensional BTE to study the phonon transport in Si and SiGe alloy while considering of acoustic mismatch model at the interface. Their results showed that lateral thermal conductivity of a 10 nm strained Si layer was order of magnitude smaller than the bulk silicon and, strongly dependent on the level of specularity at the interface of the strained-Si and SiGe layers. Their calculated temperature distribution in the device could be used to predict the impact of self-heating on the performance of future generation strained-Si devices.

Shakouri [80] performed the review study for nano-scale thermal and thermoelectric transport properties. They reviewed the experimental and numerical studies available for the thermal conductivity, thermoelectric effects, quantum dot and thermo tunneling. He compared the various experimental results for the thermal conductivities. He found that the thermal conductivity of silicon reduced with the reduction in film thickness. He mentioned some studies about the thermal transport in Nanowire and CNTs. In addition, he discussed about the Figure of Merit of low dimensions thermoelectric device.

Thouy et al. [81] numerically studied the phonon transport characteristics in electronic devices. They incorporated the Lattice Boltzmann model to study the phonon transport in silicon based film. They performed simulation with consideration of the gray body assumption in two dimensional cases. Their results of thermal conductivities were in good agreement with experimental data.

Asheghi et al. [82] studied the thermal conduction in a doped single crystal silicon thin films. In their study, they calculated the thermal conductivities of thin silicon layers doped with boron and phosphorus at temperatures between 15 and 300 K. They used the secondary ion mass spectroscopy to measure the impurity concentrations. The thermal conductivity data were interpreted using phonon transport theory accounting for scattering on impurities, free electrons and the layer boundaries. They concluded that a large fraction of the reduction in thermal conductivity of bulk doped silicon samples were due to the contamination of samples by oxygen atoms and unintentional impurities.

Sinha and Goodson [83] performed the review study on multiscale thermal modeling in nanoelectronics. They reviewed the sub-continuum thermal modeling focusing on the silicon field effect transistor. They discussed about the about the BTE, Monte Carlo and MD simulation modeling. In BTE, they further discussed about EPRT, energy, moment and ballistic diffusive equation. They concluded that the Monte Carlo simulation required more theoretical development, specifically in terms of improved treatment of phonon-phonon scattering and energy conservation schemes. They also mentioned that measurement of phonon dispersion relation in ultrathin film was important.

Alkhairy [84] performed the numerical study for the solution of Dual phase lag heat equation. He utilized the generalized green function to solve the dual lag model in homogenous materials. He treated the higher order derivate in special manner in order to get the general solution of dual phase lag heat transfer equation, higher order derivative terms represents the lagging behavior in dual phase lag heat equation. His proposed solution could be applicable for wide range of dual lag phase heat transfer problem. His results were in good agreement with literature.

Gutiérrez et al. [85] studied about the thermal conductivity and phonon transport characteristics in thin silicon films. They computed the scattering term in the linearized phonon BTE through perturbation theory without the use of any parameter fitting. The three-phonon and isotope scattering mechanisms were simulated using the Perturbation theory. They computed the thermal conductivities of Bulk silicon across a range of temperatures which were in good agreement with the experimental data. Their study revealed that about 96% of the heat transport in bulk silicon was by acoustic modes, in which about two-thirds was carried by the transverse acoustic modes.

Karamitaheri et. al. [86] studied the ballistic phonon transport characteristics in ultra-thin film. Their numerical study included the effect of confinement and orientation on the ballistic phonon conductance for thin silicon layer with thickness between 1 nm and 16 nm. They modeled lattice dynamics employing modified valence force field and the ballistic Landauer transport formalism was used to calculate the thermal conductance. They studied the thermal conductance in four surface orientations {100}, {110}, {111} and {112}. They found that the ballistic conductance of thin layers with {100} and {111} surface orientations was almost isotropic for all transport orientations. They also reported that an anisotropy in the transport orientation of the order of 60% and 40% was observed for {112} and {110} channels, respectively, due to the asymmetry in their phonon mode structure.

Brown and Hensel [87] developed the statistical phonon transport (SPT) model to study the thermal transport from nano-scale to bulk semiconductor materials. SPT model was a full three dimensional probabilistic model that solves the BTE in a statistical framework, which could be used to model phonon transport in crystalline materials across multiple length scales. They indicated that SPT model was not required any random number for the solution of BTE. Their model employed a fully anisotropic dispersion model and also provides a flexible framework that permits incorporation of additional scattering mechanisms and various scattering models. Their model could be used to simulate the complex three-dimensional geometric domains necessary for simulating thermal transport in semiconductor devices.

Brown and Hensel [88] performed verification and validation of their previously developed SPT model. They evaluated the three-phonon scattering model by considering populations of phonons interacting within an enclosed volume of silicon. Validation of the SPT model against analytical test cases showed that the SPT model was capable of predicting thermal transport in the diffuse, mixed and ballistic regimes. They validated steady-state and transient results from SPT model with analytical solutions, results from Monte Carlo models, and experimental data for homogeneous silicon. They found that SPT model predicted the higher values of thermal conductivity.

Yamada et al. [89] numerically studied the diffusive ballistic heat transport in thin film using the dissipative particle dynamics (DPDe). They performed simulation for two dimensional domains, introducing two edges with constant temperature and two were the periodic boundary condition. They used the relation of cut-off radius of energy interaction in the modeling of the phonon mean free path while utilizing the existing phonon scattering model to obtain the cut-off radius. For the validation of the model, they solved one dimensional thin film with in the range of 0.1 to 10 Knudsen number and compared their results with the semi-analytical solution of EPRT, the maximum difference was found to be 15%. They indicated that results improved with the modification of effective mean free path based on the phonon-boundary scattering.

Yilbas and Mansoor [90] examined the phonon transport characteristics in the two dimensional silicon thin film. They carried out the transient analysis while incorporating the Boltzmann Transport Equation. Their findings revealed that the time required to reach steady temperature was faster in the vicinity of the high temperature edge of the film than the low temperature edge.

Kuleyev et al. [91] studied the phonon thermal conductivity in cubic crystals. Their study included the effect of phonon focusing on the phonon relaxation characteristics in the boundary scattering regime for rod shaped and thin plate samples. Their results indicated that relaxation times could be represented by piecewise smooth functions for different intervals of angle; which was defined by the relation between components of the phonon group velocity and geometrical parameters. Silicon mean free path and thermal conductivity was calculated with different orientation of the temperature gradient and side faces in the anisotropic continuum model. Their finding indicated that anisotropies of thermal conductivity and phonon mean free paths for silicon changed strongly with the aspect ratio. In addition, they found that thermal conductivity and phonon mean path were having steep dependence on the orientation of temperature gradient.

Liu et al. [92] developed the model for determination of effective thermal conductivity for micro and nano porous silicon. In their model, they included the effects of the pore size, the pore shape (square, rectangular, and triangular cylinders), and the porosity. They also introduced the geometry dependent view factor and porosity function.

They validated their model for some reference cases with the Monte Carlo simulation. They found that the phonon transport characteristics in micro and nano porous silicon were influenced by pore shape, the pore alignment, and the pore size.

Pattamatta et al. [93] performed the modeling of thermal resistance in carbon nanotube(CNT) contacts, as it is having significant effect on the heat transfer ability of carbon nanotube. They performed three dimensional simulations for CNT/Si and CNT/SiO_2 incorporating the BTE for phonon. They introduced dispersion relation of graphite to calculate the properties of CNT. Simulation results for CNT/SiO_2 were good agreement with theory but its two orders of magnitude smaller than experimental results due to the imperfect contact at interface in experiments. They found that CNT/Si contact resistance one order higher than Debye model. Their finding showed that the CNT and substrate do not have a significant effect on the thermal contact resistance. They found that thermal contact resistances were decreased with increasing values of the CNT diameter and thickness.

Clancy et al. [94] performed the modeling for thermal conductivity of polymer and carbon nano-composites. They performed MD simulation to calculate the interfacial thermal resistance between nanoparticles and amorphous and crystalline polymer matrices. They also estimated the thermal conductivity of nano-composites using an established effective medium approach. They found that functionalization of edges and faces of plate-like graphite nanoparticles reduced the interfacial thermal resistance and increased the composite thermal conductivity.

Lam and Fong [95] performed the analytical study to compare the classical parabolic heat conduction equation based on Fourier's law of heat conduction and the hyperbolic heat conduction equation based on the Cattaneoe-Vernotte (CV) constitutive relation. In their investigation, they included the effect of thermal diffusion and wave propagation in finite slab subjected to a spatially-decaying laser source incidence at the surface. Laser irradiation was considered as internal heat generation inside the medium. Their results indicated that the thermal lagging behavior had a pronounced effect on the energy transport. They also indicated that the temperature distribution based on classical diffusion theory, under-predicted the peak temperature at small times and over-predicted at larger times. They concluded that due to the lagging behavior, the hyperbolic model predicted a wave front in the direction of propagation and caused a large concentration of energy in a localized area; whereas, the parabolic model predicted an instantaneous diffusion of heat into the medium.

Donmezer and Graham [96] presented the multiscale thermal modeling approach for ballistic and diffusive heat transport. As the heat transport modeling required much detailed information about the physics of heat transfer carrier and it was computationally expensive. Therefore, they suggested that for large domains, multiscale modeling approach could be resulted in less computational requirement. They incorporated the BTE to investigate the energy transport characteristics in the region where ballistic-diffusive transport was dominant. They used a Finite Volume Discrete Ordinates Model (FVDOM) for the numerical solution of governing equations. The approach showed that it was possible to create a coupled multiscale model. Their finding indicated that physical dimensions, the size of the heat generation region, mean free path of carriers were important parameters affecting the nature of heat transport in the domain.

Lee et al. [97] conducted the experimental study to examine the thermal conductivity of nano-scale aluminum films, with variation of mechanical strain. The mechanical strain was developed during the fabrication of the thin film. They investigated the effect of mechanical strain in 125 nm aluminum films with average grain size of 50 nm. Their experimental results showed that the strain–thermal conductivity coupling caused almost 50% reduction in thermal conductivity at around 0.25% strain. Their analysis showed that mechanical strain decreased the mean free path of the thermal conduction electrons, primarily through enhanced scattering at the moving grain boundaries.

Sim et al. [98] studied the effect of femtosecond pulse laser interactions in silicon thin films. They used the two-temperature model (2TM) and the three-temperature model (3TM) along with BTE. They used the relaxation time approximation for simplification of scattering term in BTE. They performed the transient analysis to estimate the electron temperatures and phonon temperatures. Their finding revealed that longitudinal optical phonon and acoustic phonon were nearly in thermal equilibrium state for picosecond pulse laser. In case of femtosecond pulse lasers, there was nonequilibrium exist between longitudinal optical phonon and acoustic phonon, as the longitudinal optical phonon–acoustic phonon energy relaxation time was larger than the pulse duration.

Ma et al. [99] performed experiments to study the electron–phonon relaxation time for metallic thin films. They calculated relaxation time in thin gold and aluminum films by using the transient thermoreflectance technique. Their measurement indicated that optical properties of the thin metallic films were different from those of bulk metal. Their measurement revealed that relaxation time was independent of film thickness and interface.

Xu and Cheng [100] studied the temperature enhancement through interaction of thermal waves for phonon transport in silicon thin films. They incorporated the Lattice Boltzmann equation in their study to investigate the phonon transport in silicon thin film with constant temperature at two surfaces. Their results indicated that the interaction of the two thermal waves initiated from the two surfaces, make the temperature in the inner part of the thin film significantly high at some time, which could not be predicted by Fourier heat conduction theory. They also mentioned that the interaction of the thermal waves induced by two hot spots, separated by a nanoscale distance, significantly enhanced the temperature in some inner parts of the thin film. They concluded that the Fourier law may severely underestimated the temperature in some inner regions of the silicon thin film.

Cheng et al. [101] derived the single phase lagging (SPL) heat conduction equation form the BTE. In order to derive the SPL, they solved the BTE, with the assumptions of no external forces acting on the heat transfer media and the quasi-equilibrium. They analytically established occurrence of thermal oscillation in SPL heat conduction. They concluded that SPL heat conduction equation was not addressed the spatial nonlocal effect, which was important in the ballistic heat transport.

Xu and Wang [102] analytically derived the dual phase lagging (DPL) heat conduction equation from the Boltzmann transport equation. They assumed the local quasi-equilibrium state of system with no external forces act on the heat transfer medium along with relaxation times which were independent on the energy of the system. They mathematically formulated the initial–boundary problem, which was solved by separation of variables method. They also analytically established condition under which the thermal oscillation occurred.

Fang and Pilon [103] studied the thermal conductivity of crystalline nanoporous silicon using the molecular dynamics simulation. They reported that effective thermal conductivity of crystalline nanoporous silicon was strongly affected not only by the porosity and the system's length but also by the pore interfacial area concentration. They also developed physics based model by combining kinetic theory and the coherent potential approximation. Their molecular dynamics simulations results of thermal conductivity of nanoporous silicon were in excellent agreement with literature.

Wang and Murthy [104] developed the model incorporating the phonon BTE with consideration of full scattering term. Their developed model based on the BTE in the energy form with consideration of phonon dispersion and polarization. They also considered the anisotropy of silicon dispersion curves to capture the realistic shape of the first Brillouin zone. They discretized physical space and the first Brillouin zone into finite volumes for solution of the developed model. They solved their developed model for thermal conductivity of silicon which was comparable with experimental data.

Hua and Minnich [105] performed the experiments to study the transport regimes in quasiballistic heat conduction. They analyzed the thermal transport regimes in transient thermal grating (TTG) using a new analytical solution of the frequency-dependent BTE. Their suggested analytical solution accurately described thermal transport from the diffusive to ballistic regimes. They indicated that thermal decay time relative to the relaxation times as a key nondimensional parameter, which separated the two quasiballistic transport regimes. Their results demonstrated more accurate measurement of MFP spectra and an improved understanding of heat conduction in solids.

Sellan et al. [106] studied the cross-plane phonon thermal conductivity of silicon thin films. They performed their simulation using the lattice Boltzmann method. They modeled thin films using bulk phonon properties obtained from harmonic and anharmonic lattice dynamics calculations. They specified that the frequency-dependent contributions to thermal conductivity changes, as the film thickness were reduced. They found that the cross-plane thermal conductivities were less than the in-plane value for all film thicknesses. Their predictions of cross plane thin film thermal conductivity were in good agreement with those predicted from the Matthiessen rule.

Turney et al. [107] performed a numerical study to calculate in-plane phonon thermal conductivities of argon and silicon thin films, while incorporating the Boltzmann transport equation with the relaxation time approximation. They modeled the thin films using bulk phonon properties obtained from harmonic and an-harmonic lattice dynamics calculations. The input required for the lattice dynamics calculations was obtained from interatomic potentials. They found that the average of the bulk phonon mean free path was an inadequate metric to use when modeling the thermal conductivity reduction in thin films. They concluded that knowledge of the phonon properties could also be used to gain insight into the mechanisms of phonon transport through nanostructures and quantified the contribution of individual phonon modes.

Minnich et. al. [108] performed the one dimensional transient study for silicon and aluminum thin films. They indicated that phonon transport characteristics were modified at interfaces of the films because of the thermal boundary resistance created during the transmittance of phonons at the film-pair interface. Their study indicated that transmittance of phonons across the interface was mainly governed by the phonon frequencies. Phonons were having the frequencies less or equal to the cut-off frequency at the interface could not be transmitted across the interface. Therefore, transmittance and reflectance of the phonons at the interface highly depended on the mode and braches of the phonons reaching at the interface; which formed the bases for the cut-off mismatch model. This method can be used for those phonons, which could possibly transmitted across the interface; provided that no interfacial scattering takes place and phonons propagated elastically across the interface, while the energy balance across the interface satisfied.

Wong et al. [109] investigated the temperature distribution in an n-doped silicon thin film subjected to near-field thermal radiative heating in the three dimensional rectangular geometry. In their study, they considered the near-field radiative heating as a volumetric phenomenon within the thin film and solved using the Maxwell equations combined with fluctuational electrodynamics. They incorporated the BTE to examine the phonon transport characteristics. Their finding indicated that for continuous heating the temperature gradient was insignificant in thin films, whereas for pulse heating the temperature gradient established in thin films.

Bulusu and Walker [110] investigated the phonon transport in one-dimensional thin-film with heat generation. They incorporated the one dimensional BTE and diffusion equation, to perform the comparison between the continuum and non-continuum models. In the analysis, they carried out numerical simulations for various Kundsen numbers and heat generation region. They suggested that non-continuum distributions were similar to continuum distributions except at boundaries, where the jump condition resulted due to the ballistic transport. Their comparative study revealed that peak energy in a device predicted using the non-continuum formulation was always less than that of the continuum model, regardless of Knudsen number.

Wang et al. [111] studied the thermal boundary resistance and temperature dependent phonon conduction in multiwall carbon nanotube (MWCNT) structures. They found that the large thermal interface resistances in MWCNT array, which were related to the incomplete contact at the MWCNT free ends and the interface resistances of individual contacts at the nano-scale. They found large discrepancy between the measured and theoretical results of the thermal boundary conductance.

Ruiqiang and Huang [112] examined the thermal transport in nanoporous silicon, while introducing anisotropy and junction effects. They investigated the thermal transport using nonequilibrium and equilibrium molecular dynamics simulations together with lattice dynamics calculations. The major thermal resistance was from the channel region, while ballistic phonon transport was important for the other regions. They also indicated that additional scattering caused by the junctions led to an effective thermal conductivity considerably lower than that predicted via considering diffusive boundary scattering only.

Prasher [113] developed the general framework for the calculation of thermal boundary resistance between a substrate and a composite. He showed that when the particle size became large; the thermal boundary resistance between the substrate and the composite was the same as, the substrate and the host matrix of the composite. He concluded that due to multiple and dependent scattering of phonons, thermal boundary resistance of composites get modified, which was more dominant for nanocomposites at low temperatures.

Tzou [114] investigated the nonlocal behavior in phonon transport. He performed the steady analysis which showed that effective thermal conductivity was linearly depended on the radius of nanowire. He demonstrated by transient study that a new type of thermal wave resulted from the first order nonlocality and, a localized zone with a finite width was observed due to phonon scattering. He also specified that the temperature level established in the affected region was much higher than predicted by Fourier's law or Cattaneo–Vernotte thermal wave model, due to the nonlocal effect in heat propagation.

Hida et al. [115] performed the molecular dynamics simulation to investigate the thermal resistance and phonon scattering at the interface, between carbon nanotube (CNT) and amorphous polyethylene. Their result indicated that the thermal boundary conductance increased moderately with temperature and decreased noticeably as CNT becomes softer. Interfacial interaction reduced thermal conductivity of CNT by 28%. In the mode-dependent phonon transport analysis, they found that the phonon boundary scattering rate increased with decreasing frequency.

Wang et al. [116] investigated the thermal transport across interfaces between semiconductor and adjacent layers. They incorporated the modified diffuse mismatch model (DMM) to interpret the data and extract the phonon transmissivity at the interface. They showed that over a wide phonon velocity; phonon intensity decreased with increasing average phonon velocity. In addition, the vibration mismatch and changes in the localized phonon transport near the interface contributed to the reduction in thermal boundary conductance.

Liang and Tsai [117] examined thermal boundary resistance alteration via inserting an interlayer in between the films. They found that for the two solids with very close crystal structure and lattice constant; more than 50% reduction of the thermal boundary resistance could be achieved by inserting a 1- to 2-nm-thick interlayer. The inserted layer Debye temperature was approximately equal to the square root of the product of two solids Debye temperatures. They indicated that the reduction in thermal boundary resistance was mainly due to more phonon states participating in the boundary transport by inserting an interlayer.

Barisik and Beskok [118] performed molecular dynamics (MD) simulations to investigate the energy transport characteristics in water-silicon system. Their results showed that the interface thermal resistance between a liquid and solid was dominated by the liquid structure formed on the surface under high wetting conditions. They further indicated that under high wetting conditions changed in temperature; altered the phonon transport and, created different coupling between liquid and solid molecules which was due to the variation of liquid ordering near the surface. That resulted in interface resistance increment with increased temperature. They found the opposite behavior for low wetting surfaces, where the density structure near the surface was independent of the surface temperature. They also indicated that under low wetting condition, change of surface temperature only affected the phonon transport.

Dong et al. [119] studied the size dependent thermal conductivity of silicon nano-systems. They derived the constitutive equation for a phonon gas flow in a porous medium based on phonon gas dynamics. The effective phonon gas viscosity was proportional to the system size in nanoscale based on the rarefied gas dynamics. They indicated that the explicit expression could be developed for the size dependent thermal conductivity of silicon nano-systems.

Zhou et al. [120] examined phonon transport in indium-arsenide nanowires for different sizes and growth directions. They performed their study incorporating the nonequilibrium MD methods. They found anisotropy for the thermal conductivity of InAs nanowires. They demonstrated that the thermal conductivity along [110] growth direction was about three times larger than that along [100] or [111] direction and, the thermal conductivity along [110] direction decreased significantly with the incensement in temperature. In addition, they indicated that the thermal conductivity along [100] or [111] direction was not sensitive to temperature. The anisotropy of thermal conductivity in InAs nanowires was due to their different phonon group velocities, which originates from their different phonon-boundary and phonon–phonon scattering.

Hua and Cao [121] studied phonon ballistic-diffusive heat conduction in silicon nano-films. They carried out their simulations using the efficient Monte Carlo (MC) method while introducing a model of phonon scattering processes to simulate the ballistic-diffusive heat conduction in silicon nano-films. Their calculated size dependent thermal conductivity agreed well with the experimental data. They observed the boundary temperature jump, caused by the ballistic phonons, was increases with the Knudsen number (Kn). They also derived the theoretical models for predicting the boundary temperature jumps from the Boltzmann transport equation.

Stevens et al. [122] investigated the effects of temperature and disorder on thermal boundary conductance at solid–solid interfaces. They incorporated the nonequilibrium molecular dynamics approach to investigate thermal transport across solid–solid interfaces. They showed that for large lattice mismatches, resulted in numerous defects at the interface, the thermal interfacial conductance dramatically decreased. They also found that interfacial thermal transport was dependent on temperature at solid-solid interfaces. In addition, they found linear dependency of interface conductance on temperature; which was indicating that interfacial transport directly related to occupancy of vibration states, because of that inelastic scattering played a critical role in the interfacial thermal transport.

Chen et al. [123] carried out a sub-continuum thermal transport modeling, incorporating the lattice Boltzmann transport equation. Effective thermal conductivity trace for each BTE model was presented and showed nearly 400 times difference from the ballistic to the diffusive region. They compared the results from the original semi-gray Lattice Boltzmann model and the simplified model, for a wide range of sizes and time scales. Their study revealed that the semi-gray lattice Boltzmann model with a diffusion term successfully recovered the size-dependent data of effective thermal conductivity and, agreed well with the diffusive solution at large scales.

Yilbas and Mansoor [124] examined energy transport characteristics in the silicon-diamond thin film pair while introducing the thermal boundary resistance at the interface. In their study, they incorporated the frequency dependent EPRT to perform the transient analysis on thin film pair. They predicted the equilibrium temperature to investigate the contribution of the ballistic phonons on energy transport. Their finding revealed that the ballistic phonons were significant influenced on heat transport across the thin film pair. They indicated that the effect ballistic phonons were pronounced with the progressing heat duration. They concluded that for the frequency dependent case, the equilibrium temperature changed sharply as compared to frequency independent case, as the ballistic phonons suppressed the rise in equilibrium temperature in both films.

2.3 Current Work and Literature Review

Literature review indicated that many research studies have been carried in the area of micro and nano scale energy transport. Researchers have used different models for the assessment of energy transport at micro and nano scale. In this case, Boltzmann transport equation was found to be appropriate for the analysis of transport characteristics in dielectric thin films.

Many researchers incorporated the Boltzmann transport equation for the analysis of energy transport in thin films. Most of studies were carried out using the gray body assumption in BTE. Although, in some studies the frequency dependent BTE was introduced; there were so many applications such as formulation of thermal boundary resistance, vacuum gap in between films, and quantum dots etc.; where energy transport characteristics not examined incorporating the frequency dependent BTE. Therefore, in this dissertation; the dielectric thin films are investigated for the applications, which are not thoroughly investigated, using the frequency dependent BTE. Some researchers indicated the large values of heat transport took place between two films with the presence of nano scale size gaps when compared to that obtained from the Stefan Boltzmann law of heat radiation. However, the effect of nano scale gap sizes were not investigated using the BTE. Therefore, the energy transport characteristics in dielectric thin films with the presence of minute gap in between the films are also investigated while incorporating the frequency dependent BTE.

Many researchers investigated the metallic thin films using the two-equation model, which was established for energy transport in lattice and electron sub-systems. In this dissertation, thermal transports in the metallic thin films are examined by tailoring the BTE in line with the lattice and the electron sub-systems; in which case, the frequency dependency is introduced in lattice sub-system.

CHAPTER 3

MATHEMATICAL ANALYSIS

3.1 Introduction

In this chapter the relevant mathematical arrangements are described for energy transport in thin films pertinent to the various simulations conditions. To model energy transport in the thin films, the Equation of Phonon Radiative Transfer, hereafter referred to as the EPRT, has been introduced. As in the dielectric thin film mainly the phonons considered to be responsible for energy transport; therefore, EPRT has been incorporated to account for the phonons transport. In metals, the thermal transport involves the electron and lattice sub-systems; therefore, modified version of EPRT is incorporated in both sub-systems through introducing the coupling term in the governing equations. The models used and the associated initial, boundary and interface conditions are discussed in details for all the studies considered in the present study.

3.2 Equation of Phonon Radiative Transfer (EPRT)

In 1993 the Equation of Phonon Radiative Transfer was presented by Majumdar [3]. The basic idea behind the derivation is that, the phonons are similar to the photons; therefore the transfer of phonons between two parallel faces of a thin film may be modeled as a type of radiation exchange between the two surfaces, exactly analogous to the radiation heat transfer between two heated surfaces which are separated either by a vacuum or by a participating medium, such as a semi-transparent gas.

When the thin film thickness approaches to the atomic spacing or less than the mean free path of the carriers, the steady-state 'radiation exchange of phonons between the two faces of the thin film approaches the limit of radiation exchange between two surfaces separated by a vacuum. This is the Casimir limit [125] and in this case the phonon radiative heat transfer for low temperatures is given by [126],

$$q'' = \sigma\left(T_1^4 - T_2^4\right) \tag{3.1}$$

This is similar to the Stefan-Boltzmann law. In the above equation, σ is the Stefan-Boltzmann constant for phonons [127], T_1 and T_2 are the surface temperatures in Kelvin. The above equation implies that during the transfer of phonons from one surface to the other, there is no scattering of the phonons. The phonons will only be scattered at the surfaces, where they may be scattered completely diffusely or completely specularly or in some combination of the two.

In the case when the film thickness is comparable to the mean free path of the phonons, the space between the two faces of the thin film cannot be considered as a vacuum. The phonon radiation exchange now has to be modeled analogous to the photon radiation exchange between two surfaces with an absorbing, transmitting and scattering medium in between them, such as a semi-transparent gas. In this case, the intensity distribution inside the gas is calculated from the Equation of Radiative Transfer [128].

For the case of the phonon radiative transfer a similar equation can be derived from the Boltzmann Transport Equation, resulting in the Equation of Phonon Radiative Transfer.

3.2.1 Energy Transport Properties of a Dielectric Material

In order to calculate the energy transport properties of a dielectric material in local thermodynamic equilibrium; it is assumed that the atoms or molecules are arranged in a regular lattice structure and vibrating about their mean positions in the lattice at different frequencies. Among these vibrations, only certain frequencies of waves are responsible for carrying energy due to quantization. These waves are actually responsible for the storage and transport of thermal energy. According to quantum mechanics, waves can also be treat of as particles with momentum according to the relation $p = h / \lambda$ [18]. The particles associated with the lattice vibrations are phonons and they obey the Bose-Einstein statistics [129]. In a thick dielectric material, these phonons experience considerable scattering during their motion and hence produce a local thermodynamic equilibrium inside the material and a temperature gradient may be defined at each location. On the basis of these assumptions the energy transport properties of a dielectric material in local thermodynamic equilibrium may be calculated through the methods of statistical mechanics. Specifically, one may use the relaxation time approximation of the Boltzmann Transport Equation, together with the Bose-Einstein distribution as the equilibrium phonon distribution in phase space, to calculate the non-equilibrium probability distribution function. The non-equilibrium probability distribution function can be used to comprehend the energy transport properties.

In thin dielectric films, in which the film dimensions are comparable to or smaller than the mean-free-path of the phonons, the phonons do not experience enough scattering events and hence local thermodynamic equilibrium does not prevail. It may happen that some phonons, which originate at a boundary, may reach the other boundary without being scattered. In these situations, temperature cannot be defined in the usual sense. It therefore becomes necessary to solve the Boltzmann Transport Equation (BTE) to calculate the correct energy transport characteristics as well as the correct transport properties. The BTE may be used to analyze equilibrium as well as non-equilibrium transport [26].

3.2.2 Boltzmann Transport Equation

The Boltzmann Transport Equation was originally developed to model a dilute gas in which the gas particles interact only through two-particle collisions and do not interact through the attractive/repulsive forces [26]. This representation implies a straight-line trajectory of the gas particles through relatively empty space interrupted occasionally by abrupt collisions. The BTE is derived from the Liouville Equation, which governs the time evolution of the N particle distribution function of a collection of particles in $6N$ dimensional phase space [6]. The distribution function $f(x_1 ... x_N, y_1 ... y_N, z_1 ... z_N, p_{x1} ... p_{xN}, p_{y1} ... p_{yN}, p_{z1} ... p_{zN}, t)$ (where x, y and z are the space coordinates and p_x, p_y and p_z are the momentum coordinates) is related to the density of the phases in an ensemble. This is the normalized density function in phase space and the total number of particles in the collection is N. Moreover, Liouville Equation is applicable to a solid, liquid or a gas. For a gas, if it is dilute, only two particle collisions are the only mode of energy and momentum transfer, it is possible to simplify the Liouville Equation. Suppose that the gas consists of a single particle. In this case the one particle distribution function becomes $f^{(1)}(x, y, z, p_x, p_y, p_z, t)$. It is now assumed that the N particles are completely identical and they all have the same single particle distribution function. It is then possible to simply find $f^{(1)}(x, y, z, p_x, p_y, p_z, t)$ and derive the relevant transport properties from this function. The Liouville equation can be modified to yield an equation for $f^{(1)}(x, y, z, p_x, p_y, p_z, t)$ and this is actually the Boltzmann Transport Equation [27]. Due to the assumption that a single distribution function represents the N particles, it becomes necessary to include the scattering or collision term in the modified Liouville equation. The three-dimensional Boltzmann Transport Equation is described below [21],

$$\frac{\partial f}{\partial t}+\frac{1}{m}\left(p_x\frac{\partial f}{\partial x}+p_y\frac{\partial f}{\partial y}+p_z\frac{\partial f}{\partial z}\right)+\left(\dot{p}_x\frac{\partial f}{\partial p_x}+\dot{p}_y\frac{\partial f}{\partial p_y}+\dot{p}_z\frac{\partial f}{\partial p_z}\right)=\left(\frac{\partial f}{\partial t}\right)_{collision} \tag{3.2}$$

$$\frac{\partial f}{\partial t}+\frac{p}{m}.\nabla_r f+\dot{p}.\nabla_p f=\left(\frac{\partial f}{\partial t}\right)_{collision} \tag{3.3}$$

where f is the distribution function; x, y and z are the space coordinates; p_x, p_y and p_z are the momentum coordinates, t is time, m is the mass; $\dot{p}_x$, $\dot{p}_y$ and $\dot{p}_z$ are rate of momentum.

The collision term is a complicated expression accounting for the effects of collisions between the particles. It may be replaced by a simpler expression by assuming the relaxation time approximation, which was explained in chapter 1. The above equation may then be written as,

$$\frac{\partial f}{\partial t} + \frac{p}{m} . \nabla_r f + \dot{p} . \nabla_p f = - \frac{\left(f - f^0 \right)}{\tau} \tag{3.4}$$

where f^0 is the equilibrium probability distribution defined by different distribution functions which are given in Table 1.1.

3.2.3 Equation of Phonon Radiative Transfer

A thin two dimensional dielectric film has a thickness and its width is very small as compared to its other third dimension. These lengths are comparable to or less than the phonon mean-free-path in the film. For the two dimensional the thin dielectric films as shown in Figure 3.1, the frequency dependent BTE with relaxation time approximation simplifies to,

$$\frac{\partial f_\omega}{\partial t} + v_{x,\omega} \frac{\partial f_\omega}{\partial x} + v_{z,\omega} \frac{\partial f_\omega}{\partial z} + \dot{p}_{x,\omega} \frac{\partial f_\omega}{\partial p_{x,\omega}} + \dot{p}_{y,\omega} \frac{\partial f_\omega}{\partial p_{y,\omega}} + \dot{p}_{z,\omega} \frac{\partial f_\omega}{\partial p_{z,\omega}} = - \frac{\left(f_\omega - f_\omega^0 \right)}{\tau_\omega} \tag{3.5}$$

In the above equation, f is the single-particle distribution function of the phonons in the phase space and ω in subscript showing the frequency dependency. f_ω^0 is the frequency dependent equilibrium intensity distribution and τ_ω is the frequency dependent relaxation time. Here f is considered as function of all the three momentum variables because phonons travel in all directions [26].

The momentums (p) for a single phonon using de-Broglie formula can written as [18]:

$$p_{\omega} = \frac{h}{\lambda_{\omega}} = \hbar k(\omega) \tag{3.6}$$

In the above equation λ_{ω} is the frequency dependent wave length, $k(\omega)$ is called the wave number ($k(\omega) = 2\pi / \lambda_{\omega}$), which is the function of frequency and $\hbar$ is the reduced Planck's constant ($\hbar = h / 2\pi$). In three dimensions the three components of the momentum are related to the wave vector k. These are given as,

$$p_{x,\omega} = \hbar k_x(\omega),\ p_{y,\omega} = \hbar k_y(\omega),\ p_{z,\omega} = \hbar k_z(\omega) \text{ or } p_{\omega} = \hbar k(\omega) \tag{3.7}$$

also, $k(\omega) = \left(2\pi / \lambda_{\omega}\right) \hat{n}$,where, $\hat{n}$ is the unit vector in the direction of propagation of the wave. The momentum and the wave vector may be used interchangeably. It is assumed that the phonons are not under the influence of any attractive/repulsive force ,therefore [26],

$$\dot{p}_{x,\omega} = \dot{p}_{y,\omega} = \dot{p}_{z,\omega} = 0 \tag{3.8}$$

Substituting the above equations in equation (3.5) yield,

$$\frac{\partial f_{\omega}}{\partial t} + v_{x,\omega} \frac{\partial f_{\omega}}{\partial x} + v_{z,\omega} \frac{\partial f_{\omega}}{\partial z} = -\frac{\left(f_{\omega} - f_{\omega}^{0}\right)}{\tau_{\omega}} \tag{3.9}$$

where, $f_\omega(x, y, z, p_{x,\omega}, p_{y,\omega}, p_{z,\omega}, t)$ may also write equivalently, $f_\omega(x, y, z, k_x, k_y, k_z, t)$. The phonons are pictured as moving among the faces of the thin film. These phonons travel in all directions with a speed and momentum, which is dependent on the corresponding frequency of the lattice vibration. The above picture is exactly that of photons, when they are transferring thermal energy among different faces in a vacuum. This suggests that for radiative energy transport through phonons, an equation completely analogous to the Equation of Radiative Transfer, which is used for radiative energy transport through photons, may be derived. This equation is called the Equation of Phonon Radiative Transfer (EPRT) [3].

In the equation (3.9), $v_{x,\omega}$ and $v_{z,\omega}$ are the frequency dependent velocity components in x and z coordinate respectively. This can be written as,

$$v_{x,\omega} = v_\omega \cos\theta \quad , \quad v_{z,\omega} = v_\omega \sin\theta \sin\phi \tag{3.10}$$

where θ is the polar angle and ϕ is azimuthal angle, as shown in Figure 3.1. The equation (3.9) becomes,

$$\frac{\partial f_\omega}{\partial t} + v_\omega \cos\theta \frac{\partial f_\omega}{\partial x} + v_\omega \sin\theta \sin\phi \frac{\partial f_\omega}{\partial z} = \frac{f_\omega^0 - f_\omega}{\tau_\omega} \tag{3.11}$$

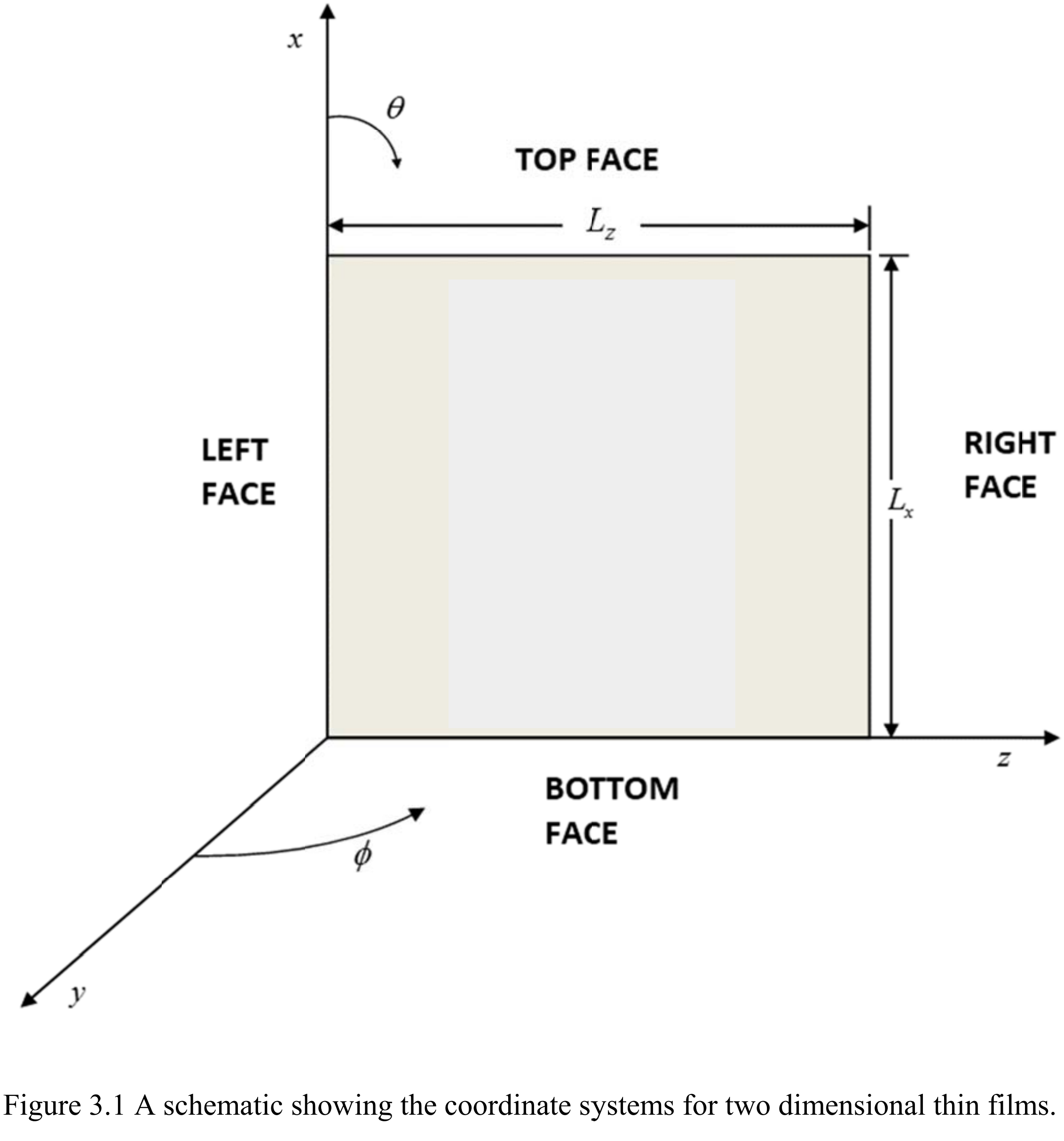

Figure 3.1 A schematic showing the coordinate systems for two dimensional thin films.

Dividing the above equation by v_ω on the both side result in the following:

$$\frac{1}{v_\omega}\frac{\partial f_\omega}{\partial t}+\cos\theta\frac{\partial f_\omega}{\partial x}+\sin\theta\sin\phi\frac{\partial f_\omega}{\partial z}=\frac{f_\omega^0-f_\omega}{v_\omega\tau_\omega} \tag{3.12}$$

Here the product of frequency dependent group velocity and the relaxation time is equal to the frequency dependent mean free path that is $\Lambda_\omega = v_\omega\tau_\omega$. Now equation (3.12) becomes:

$$\frac{1}{v_\omega}\frac{\partial f_\omega}{\partial t}+\cos\theta\frac{\partial f_\omega}{\partial x}+\sin\theta\sin\phi\frac{\partial f_\omega}{\partial z}=\frac{f_\omega^0-f_\omega}{\Lambda_\omega} \tag{3.13}$$

Now, multiplying the equation (3.13) with $v_\omega\hbar\omega D(\omega)/4\pi$ on both side and rearranging:

$$\begin{aligned}&\frac{1}{v_\omega}\frac{\partial v_\omega f_\omega\hbar\omega D(\omega)/4\pi}{\partial t}+\cos\theta\frac{\partial v_\omega f_\omega\hbar\omega D(\omega)/4\pi}{\partial x}\\&+\sin\theta\sin\phi\frac{\partial v_\omega f_\omega\hbar\omega D(\omega)/4\pi}{\partial z}=\frac{v_\omega f_\omega^0\hbar\omega D(\omega)/4\pi-v_\omega f_\omega\hbar\omega D(\omega)/4\pi}{\Lambda_\omega}\end{aligned} \tag{3.14}$$

where, is the $D(\omega)$ density of state, which is the number of phonon / electron per unit volume per in a unit energy interval [6]. It is given by [90]:

$$D(\omega)=\frac{k^2}{2\pi^2}\frac{dk}{d\omega} \tag{3.15}$$

In equation (3.15) frequency is the function of wave number that is $\omega=\omega(k)$, which describe by dispersion relation, which describes the effect of dispersion in a medium on the properties of traveling wave inside the medium. Dispersion relations are obtaining from the experimental studies. Dispersion relations for Silicon and Diamond are shown in Figure 3.2 and Figure 3.3 respectively.

In the theory of thermal radiation transfer, the *Spectral Intensity* is defined as the amount of energy transferred per unit time per unit perpendicular area per unit solid angle per unit wavelength interval, i.e.:

$$I_\lambda = I_\lambda(x, y, z, \theta, \phi, t)$$

A similar spectral intensity may define for the phonons. Note that the dependence on (θ, ϕ) is actually dependence on the solid angle (Ω), which in turn implies dependence on the direction. Similarly dependence on wavelength (λ) implies a dependence on the wave number or the frequency, which in turn implies dependence on the momentum and the energy of the phonons. The phonon spectral intensity may be related to the phonon distribution function, which is given as [124]:

$$I_\omega(x, z, t, \theta, \phi) = \frac{1}{4\pi} f_\omega v_\omega \hbar \omega D(\omega) \tag{3.16}$$

Now equation (3.14) can be written in terms of phonon intensities, which is given by:

$$\frac{1}{v_\omega}\frac{\partial I_\omega}{\partial t} + \cos\theta \frac{\partial I_\omega}{\partial x} + \sin\theta \sin\phi \frac{\partial I_\omega}{\partial z} = \frac{I_\omega^0 - I_\omega}{\Lambda_\omega} \tag{3.17}$$

$$t > 0,\ 0 < x < L_x,\quad 0 < z < L_z,\ 0 < \theta < \pi,\quad 0 < \phi < 2\pi$$

where, ω is frequency (in subscript it shows the frequency dependency), I_ω frequency dependent intensity in phase space, I_ω^0 frequency dependent equilibrium probability distribution function in phase space, t is the time, x is the distance in x-direction, z is the distance in z-direction, θ is polar angle , ϕ is azimuthal angle, τ_ω is the frequency dependent relaxation time, v_ω is the frequency dependent phonon group velocity and $\Lambda_\omega = v_\omega \tau_\omega$ is the frequency dependent mean-free-path. The phonon intensity is a function of five independent variables, $I_\omega = I_\omega\left(x, z, \theta, \phi, t\right)$.

The above equation is known as Equation of Phonon Radiative Transfer (EPRT).

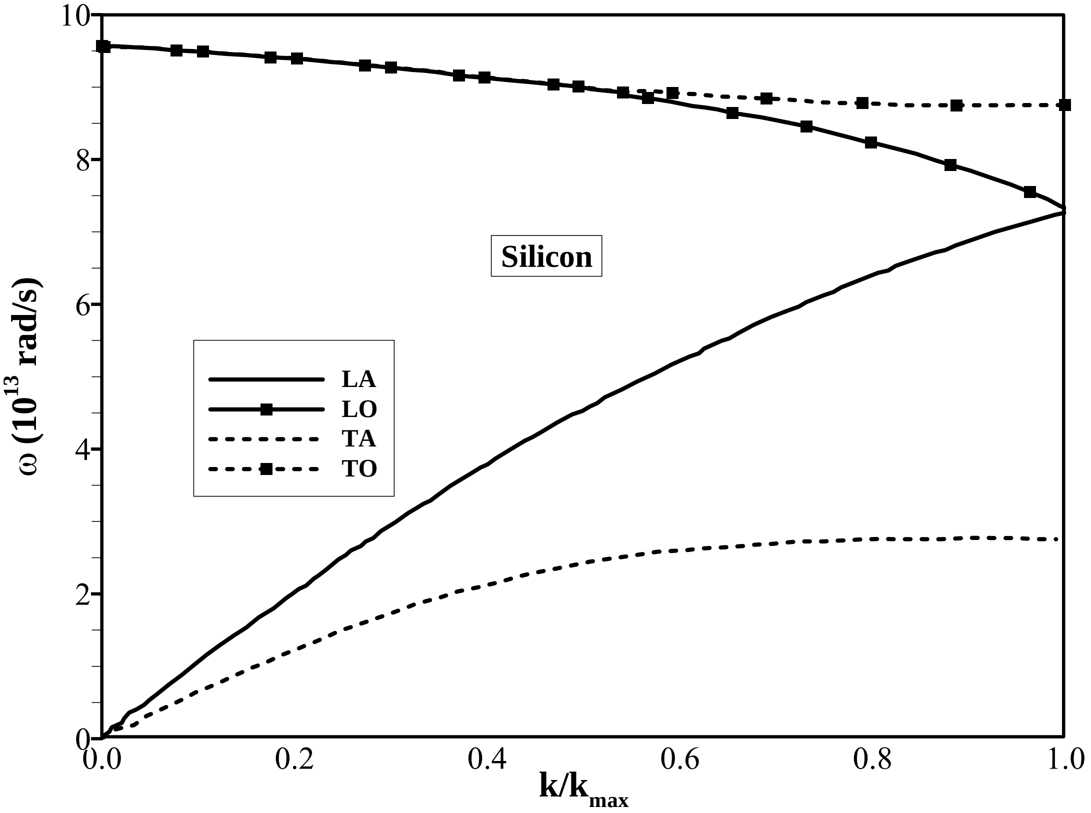

Figure 3.2 Dispersion Relation for Silicon [130]

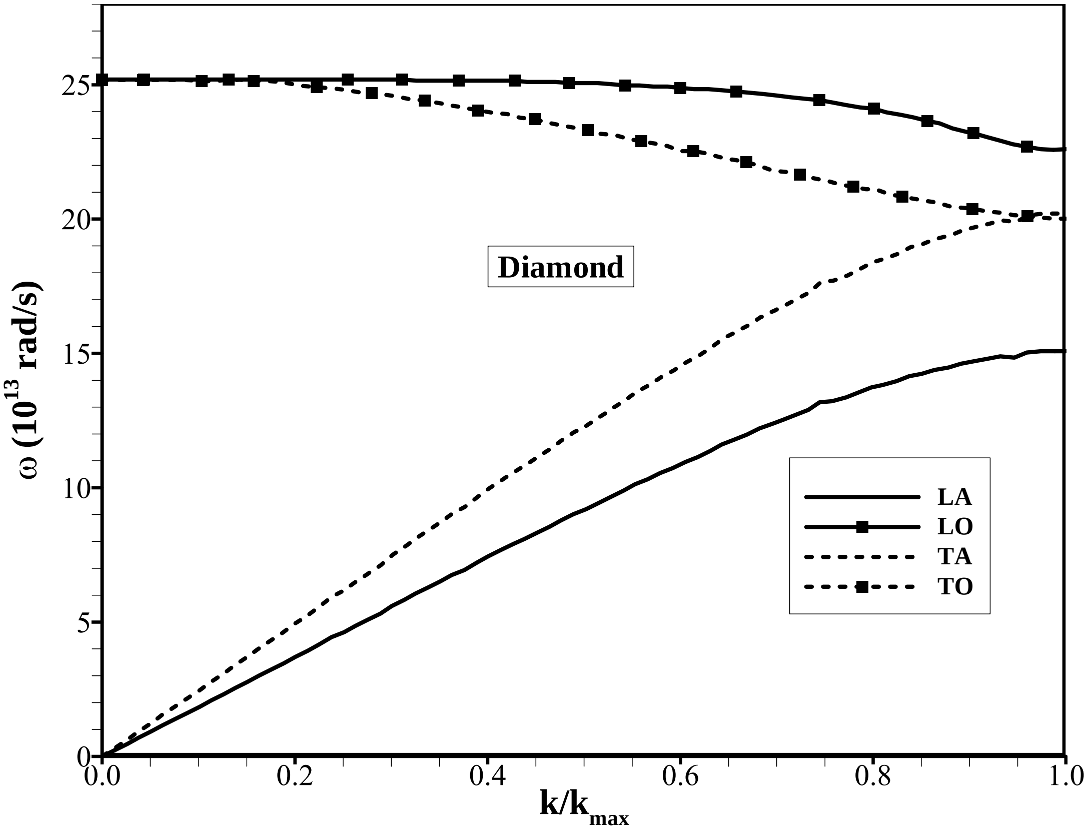

Figure 3.3 Dispersion Relation for Diamond [131]

3.2.4 Heat Fluxes

Heat flux vector of phonon for any frequency can be given as [3]:

$$q''_{\omega}(x,y,z,t) = N\iiint v_{\omega} f_{\omega} \hbar\omega \, dp_x \, dp_y \, dp_z \tag{3.18}$$

In order to find the total heat flux by the all phonon, the above expression needs to be integrated over the whole range of frequencies. Therefore, expression for the total heat flux can be written as:

$$q''(x,y,z,t) = N\int_{0}^{\omega_{\max}} \left(\iiint v_{\omega} f_{\omega} \hbar\omega \, dp_x \, dp_y \, dp_z\right) d\omega \tag{3.19}$$

Instead of the momentum, the frequency and the solid angle can be used as the independent variables. This may then write,

Infinitesimal solid angle $d^2\Omega = sin\theta d\phi d\theta$

$$q''(x,y,z,t) = \int_{0}^{\omega_{\max}} \left(\iiint v_{\omega} f_{\omega} \hbar\omega D(\omega) d\omega d^2\Omega\right) d\omega$$

Heat flux vector

$$q''(x,y,z,t) = \int_{0}^{\omega_{\max}} \left(\iiint v_{\omega} f_{\omega} \hbar\omega D(\omega) sin\theta d\omega d\phi d\theta\right) d\omega$$

In two dimensional domain heat flux in the x-direction and z-direction defined as follows:

Heat Flux in x***-direction*** $\left(q_x^{"}\right)$

$$q_x^{"}(x,y,z,t)=\int_0^{\omega_{\max}}\left(\iiint v_{x,\omega}f_\omega\hbar\omega D(\omega)sin\theta d\omega d\phi d\theta\right)d\omega \tag{3.20}$$

Now using $v_{x,\omega}=v_\omega\cos\theta$ and the definition of frequency dependent phonon intensity (equation(3.16)) the above equations can be written as:

$$q_x^{"}(x,y,z,t)=\int_0^{\omega_{\max}}\int_0^{2\pi}\int_0^{\pi}I_\omega\cos\theta\sin\theta d\theta d\phi d\omega \tag{3.21}$$

Heat Flux in z***-direction*** $\left(q_z^{"}\right)$

$$q_z^{"}(x,y,z,t)=\int_0^{\omega_{\max}}\left(\iiint v_{z,\omega}f_\omega\hbar\omega D(\omega)sin\theta d\omega d\phi d\theta\right)d\omega \tag{3.22}$$

Now using $v_{z,\omega}=v_\omega\sin\theta\sin\phi$ and the definition of frequency dependent phonon intensity (equation (3.16)) the above equations can be written as:

$$q_z^{"}(x,y,z,t)=\int_0^{\omega_{\max}}\int_0^{2\pi}\int_0^{\pi}I_\omega\sin\phi\sin^2\theta d\theta d\phi d\omega \tag{3.23}$$

In the vector form the heat flux is given as:

$$\mathbf{q}''=q_x''\hat{\mathbf{i}}+q_z''\hat{\mathbf{k}} \tag{3.24}$$

3.2.5 Equilibrium Intensity Calculation

I_ω^0 is the equilibrium intensity, corresponding to black body intensity at temperature below the Debye temperature [26]. Debye temperature is the highest temperature that can be achieved in a normal mode of vibration. In order to determine equilibrium intensity I_ω^0 First we multiply the equation (3.17) by $\sin\theta d\theta d\phi$ and integrate over solid angle and over the all range of frequencies.

$$\begin{aligned}&\frac{\partial}{\partial t}\int_0^{\omega_{\max}}\int_0^{2\pi}\int_0^{\pi}\frac{1}{v_\omega}I_\omega \sin\theta d\theta d\phi d\omega+\frac{\partial}{\partial x}\int_0^{\omega_{\max}}\int_0^{2\pi}\int_0^{\pi}I_\omega \cos\theta\sin\theta d\theta d\phi d\omega\\&+\frac{\partial}{\partial z}\int_0^{\omega_{\max}}\int_0^{2\pi}\int_0^{\pi}I_\omega\sin\phi\sin^2\theta d\theta d\phi d\omega=\int_0^{\omega_{\max}}\frac{1}{\Lambda_\omega}\begin{bmatrix}\int_0^{2\pi}\int_0^{\pi}I_\omega^o\sin\theta d\theta d\phi-\\ \int_0^{2\pi}\int_0^{\pi}I_\omega\sin\theta d\theta d\phi\end{bmatrix}d\omega\end{aligned} \tag{3.25}$$

Now using the definition of heat flux from equation (3.21) and (3.23) into above equation results in:

$$\begin{aligned}&\frac{\partial}{\partial t}\int_0^{\omega_{\max}}\int_0^{2\pi}\int_0^{\pi}\frac{1}{v_\omega}I_\omega \sin\theta d\theta d\phi d\omega+\frac{\partial q_x^{"}}{\partial x}+\frac{\partial q_z^{"}}{\partial z}\\&=\int_0^{\omega_{\max}}\frac{1}{\Lambda_\omega}\begin{bmatrix}\int_0^{2\pi}\int_0^{\pi}I_\omega^o\sin\theta d\theta d\phi-\\ \int_0^{2\pi}\int_0^{\pi}I_\omega\sin\theta d\theta d\phi\end{bmatrix}d\omega\end{aligned} \tag{3.26}$$

Now to simply the first term of left hand side, using the definition of phonon intensity from equation (3.16) into it:

$$\int_0^{\omega_{\max}}\int_0^{2\pi}\int_0^{\pi}\frac{1}{v_\omega}I_\omega\sin\theta d\theta d\phi d\omega=\int_0^{\omega_{\max}}\int_0^{2\pi}\int_0^{\pi}\frac{f_\omega\hbar\omega D(\omega)}{4\pi}\sin\theta d\theta d\phi d\omega \tag{3.27}$$

The energy of each phonon is $\hbar\omega$. Therefore, on right hand side of above equation, the product of phonon energy, density of state and nonequilibrium probability distribution, integrated over complete solid angle and frequency spectrum gives the internal energy density of phonons that is.

$$u(x,z,t)=\int_0^{\omega_{\max}}\int_0^{2\pi}\int_0^{\pi}\frac{f_\omega\hbar\omega D(\omega)}{4\pi}\sin\theta d\theta d\phi d\omega \tag{3.28}$$

Therefore, equation (3.27) is represents the internal energy density of phonons. Now utilizing the definition of divergence and above equation into the equation (3.26) results into:

$$\frac{\partial u}{\partial t}+\nabla .q^{"}=\int_0^{\omega_{\max}}\frac{1}{\Lambda_\omega}\begin{bmatrix}\int_0^{2\pi}\int_0^{\pi}I_\omega^o\sin\theta d\theta d\phi- \\ \int_0^{2\pi}\int_0^{\pi}I_\omega\sin\theta d\theta d\phi\end{bmatrix}d\omega \tag{3.29}$$

As the law of energy conservation with no internal heat generation is $\partial u/\partial t+\nabla .q^{"}=0$. Now, as in present dissertation, heat generation is not included, therefore above equation should satisfy the conservation law of energy without internal heat generation, which leads to following:

$$\int_0^{\omega_{\max}}\frac{1}{\Lambda_\omega}\left[\int_0^{2\pi}\int_0^{\pi}I_\omega^o\sin\theta d\theta d\phi-\int_0^{2\pi}\int_0^{\pi}I_\omega\sin\theta d\theta d\phi\right]d\omega=0 \tag{3.30}$$

The equilibrium intensity is only a function of spatial coordinate and time that is $I_\omega^0 = I_\omega^0(x,z,t)$, therefore,

$$\int_0^{\omega_{\max}} \frac{1}{\Lambda_\omega}\left[I_\omega^o - \frac{1}{4\pi}\int_0^{2\pi}\int_0^{\pi} I_\omega \sin\theta d\theta d\phi \right] d\omega = 0 \tag{3.31}$$

Here, assumption is made that radiative equilibrium satisfied at all frequencies therefore at each frequency the integrand in equation (3.31) vanished. This yields,

$$I_\omega^o = \frac{1}{4\pi}\int_0^{2\pi}\int_0^{\pi} I_\omega \sin\theta d\theta d\phi \tag{3.32}$$

Now equation (3.17) can be written as:

$$\frac{1}{v_\omega}\frac{\partial I_\omega}{\partial t} + \cos\theta\frac{\partial I_\omega}{\partial x} + \sin\theta\sin\phi\frac{\partial I_\omega}{\partial z} = \frac{\frac{1}{4\pi}\int_0^{2\pi}\int_0^{\pi} I_\omega \sin\theta d\theta d\phi - I_\omega}{\Lambda_\omega} \tag{3.33}$$

3.2.6 Physical Significance of Each Term in EPRT

Each term of equation of phonon radiative transport has a physical significance, which is given below.

$$\frac{1}{v_\omega}\frac{\partial I_\omega}{\partial t} + \cos\theta\frac{\partial I_\omega}{\partial x} + \sin\theta\sin\phi\frac{\partial I_\omega}{\partial z} = \frac{\frac{1}{4\pi}\int_0^{2\pi}\int_0^{\pi} I_\omega \sin\theta d\theta d\phi - I_\omega}{\Lambda_\omega}$$

The first term on the left hand side $\frac{1}{v_\omega}\frac{\partial I_\omega}{\partial t}$ account for the fact that the thermal energy transport through lattice vibration takes place at a finite speed. Therefore at any point in the film the intensity changes until a steady state is reached. The second and third term on the left hand side is represents the intensity gradient, which is necessary to balance the effect of phonon scattering, emission and transmittance. The right hand side is the scattering term which is associated with the phonon mean free path and film thickness. For the larger values of mean free path as compared to film thickness, scattering becomes smaller.

3.2.7 Polarization and Modes of Phonons

There are three different polarizations and two different modes of vibrations of the phonons. This information collected through the dispersion relations of the dielectric materials. Polarization represents that wave can oscillate in more than one orientation. Waves can propagate in a dielectric crystal in three different polarizations, one longitudinal and two transverse polarizations. The two transverse waves coincide and therefore only one dispersion curve required to represent the two transverse waves for each mode of vibration. As the vibration of two atoms at each lattice point can in-phase or out-of phase; therefore, two modes of lattice in dielectric crystal [6]. The first mode is called the Acoustic waves, represents the in-phase lattice vibration, and the second mode is called the Optical waves, represents the out-of phase vibration. Hence there are six different types of waves but since the transverse waves are identical therefore, actually different types of waves are present and hence four different curves in the dispersion relation as shown in Figure 3.2 and Figure 3.3.

The EPRT given above in equation (3.33) has to be applied to each of these waves individually. These EPRTs are given below.

Longitudinal Acoustic:

$$\frac{1}{v_{LA,\omega}}\frac{\partial I_{LA,\omega}}{\partial t}+\cos\theta\frac{\partial I_{LA,\omega}}{\partial x}+\sin\theta\cos\phi\frac{\partial I_{LA,\omega}}{\partial z}=\frac{\frac{1}{4\pi}\int_0^{2\pi}\int_0^{\pi}I_{LA,\omega}\sin\theta d\theta d\phi-I_{LA,\omega}}{\Lambda_{LA,\omega}} \tag{3.34}$$

Transverse Acoustic:

$$\frac{1}{v_{TA,\omega}}\frac{\partial I_{TA,\omega}}{\partial t}+\cos\theta\frac{\partial I_{TA,\omega}}{\partial x}+\sin\theta\cos\phi\frac{\partial I_{TA,\omega}}{\partial z}=\frac{\frac{1}{4\pi}\int_0^{2\pi}\int_0^{\pi}I_{TA,\omega}\sin\theta d\theta d\phi-I_{TA,\omega}}{\Lambda_{TA,\omega}} \tag{3.35}$$

Longitudinal Optical:

$$\frac{1}{v_{LO,\omega}}\frac{\partial I_{LO,\omega}}{\partial t}+\cos\theta\frac{\partial I_{LO,\omega}}{\partial x}+\sin\theta\cos\phi\frac{\partial I_{LO,\omega}}{\partial z}=\frac{\frac{1}{4\pi}\int_0^{2\pi}\int_0^{\pi}I_{LO,\omega}\sin\theta d\theta d\phi-I_{LO,\omega}}{\Lambda_{LO,\omega}} \tag{3.36}$$

Transverse Optical:

$$\frac{1}{v_{TO,\omega}}\frac{\partial I_{TO,\omega}}{\partial t}+\cos\theta\frac{\partial I_{TO,\omega}}{\partial x}+\sin\theta\cos\phi\frac{\partial I_{TO,\omega}}{\partial z}=\frac{\frac{1}{4\pi}\int_0^{2\pi}\int_0^{\pi}I_{TO,\omega}\sin\theta d\theta d\phi-I_{TO,\omega}}{\Lambda_{TO,\omega}} \tag{3.37}$$

Where *LA* represents the longitudinal acoustic, *TA* corresponds to transverse acoustic, *LO* is the longitudinal optical and *TO* is transverse optical.

3.2.8 Equilibrium Equivalent Temperature

This temperature defined anywhere in the dielectric thin layer is the analog of the usual thermodynamic temperature defined in the diffusive limit in any medium. It represents the average energy of all phonons around a local point and it is equivalent to the equilibrium temperature of phonons when they redistribute adiabatically to an equilibrium state. It is defined as [64],

$$T(x,z,t)=\frac{\int_0^{\omega_{\max}}\int_0^{2\pi}\int_0^{\pi} I_\omega \sin\theta\, d\theta\, d\phi\, d\omega}{\int_0^{\omega_{\max}}\left(C_{LA,\omega}v_{LA,\omega}+2C_{TA,\omega}v_{TA,\omega}+C_{LO,\omega}v_{LO,\omega}+2C_{TO,\omega}v_{TO,\omega}\right)d\omega} \tag{3.38}$$

In the above equation, $C_{LA,\omega}$ is the frequency dependent volumetric specific heat capacity, and $v_{LA,\omega}$ is the frequency dependent phonon group velocity for the longitudinal acoustic branch for the dielectric material. Similar definitions apply for the transverse acoustic, transverse optical and longitudinal optical branches of phonons.

The equation which derived above are equally valid when written as a function of wavenumber (k) instead of frequency(ω).

3.3 Equation of Phonon Radiative Transfer (EPRT) for One Dimensional Dielectric Thin Films

For one dimensional film, the EPRT which derived in equation (3.17) for two dimensional reduces to following.

$$\frac{1}{v_\omega}\frac{\partial I_\omega}{\partial t}+\cos\theta\frac{\partial I_\omega}{\partial x}=\frac{I_\omega^0-I_\omega}{\Lambda_\omega} \tag{3.39}$$

Now, introducing $\mu = \cos\theta$ in the equation (3.39) one can get the following:

$$\frac{1}{v_\omega}\frac{\partial I_\omega}{\partial t} + \mu\frac{\partial I_\omega}{\partial x} = \frac{I_\omega^0 - I_\omega}{\Lambda_\omega}, \qquad t > 0, 0 < x < L, -1 < \mu < 1 \tag{3.40}$$

The equilibrium intensity in one dimensional can be calculated from the following relation [3],

$$I_\omega^0 = \tfrac{1}{2}\int_{-1}^{1} I_\omega \, d\mu \tag{3.41}$$

3.3.1 Definition of Temperature

Equilibrium equivalent temperature for one dimensional dielectric thin film can be written as:

$$T(x,t) = \frac{2\pi\int_0^{\omega_{\max}}\int_{-1}^{1}(I_{LA,\omega} + 2\,I_{TA,\omega} + I_{LO,\omega} + 2\,I_{TO,\omega})\,d\mu\, d\omega}{\int_0^{\omega_{\max}}\left(C_{LA,\omega}v_{LA,\omega} + 2\,C_{TA,\omega}v_{TA,\omega} + C_{LO,\omega}v_{LO,\omega} + 2\,C_{TO,\omega}v_{TO,\omega}\right)d\omega} \tag{3.42}$$

3.3.2 Heat Flux

The total heat flux due to contribution of all branches of the acoustic and optical phonons for one dimensional dielectric thin film is given as:

$$q''(x,t) = 2\pi\int_0^{\omega_{\max}}\int_{-1}^{1} I_\omega \mu d\mu \, d\omega \tag{3.43}$$

3.3.3 Entropy Generation

The entropy generation rate per unit volume is given as [132],

$$S_{gen} = \frac{q}{T^2}(\nabla T) \tag{3.44}$$

Using equations (3.43) and (3.44) yields

$$S_{gen} = 2\pi \frac{1}{T^2(x)} \frac{\partial T(x)}{\partial x} \int_0^{\omega_{\max}} \int_{-1}^{1} I_\omega \mu d\mu \, d\omega \tag{3.45}$$

Using equations (3.43) and (3.44) yields

$$S_{gen} = 2\pi \frac{1}{T^2(x)} \frac{\partial T(x)}{\partial x} \int_0^{\omega_{\max}} \int_{-1}^{1} I_\omega \mu d\mu \, d\omega \tag{3.46}$$

Equation (3.46) can be used to calculate the entropy generation due to the frequency dependent phonon transport in the thin film after integrating over the volume, that is

$$S_{gen,\mathrm{tot}} = \iiint S_{gen}(x) dV = 2\pi A \int_0^L \left(\frac{1}{T^2(x)} \frac{\partial T(x)}{\partial x} \int_0^{\omega_{\max}} \int_{-1}^{1} I_\omega \mu d\mu \, d\omega \right) dx \tag{3.47}$$

where, $S_{gen,\mathrm{tot}}$ is the total entropy generation rate, V is the volume and A is the area normal to the x-direction.

3.3.4 Frequency Independent EPRT

For the frequency independent case, which is the gray medium, EPRT simples to,

$$\frac{1}{v}\frac{\partial I}{\partial t}+\mu\frac{\partial I}{\partial x}=\frac{I^0-I}{\Lambda} \qquad 0<x<L,-1<\mu<1 \tag{3.48}$$

The thermal properties of dielectric materials, which required for the solution of above equation (3.48), are given in Table 3.1.

The equilibrium intensity in one dimensional can be calculated from the following relation [3],

$$I^0=\tfrac{1}{2}\int_{-1}^{1} I\,d\mu \tag{3.49}$$

3.3.4.1 Definition of Temperature

Equilibrium equivalent temperature for one dimensional frequency independent case simplify as:

$$T(x,t)=\frac{2\pi\int_{-1}^{1} I\,d\mu}{Cv} \tag{3.50}$$

3.3.4.2 Heat Flux

The total heat flux for one dimensional frequency independent case can be given as,

$$q''(x,t)=2\pi\int_{-1}^{1} I\mu d\mu \tag{3.51}$$

3.3.4.3 Entropy Generation

The expression for total entropy generation rate which derived in equation (3.47) can be simplify for the frequency independent case, which is given as,

$$S_{gen,\mathrm{tot}} = \iiint S_{gen}\left(x\right)dV = 2\pi A\int_0^L\left(\frac{1}{T^2\left(x\right)}\frac{\partial T\left(x\right)}{\partial x}\int_{-1}^{1} I\mu d\mu\right)dx \tag{3.52}$$

Table 3.1 Properties of Silicon the used in the numerical simulations of the frequency-independent solution of the phonon radiative transport equation. Thermal conductivity can be determined from the kinetic theory formula $k = {}^{Cv\Lambda}\!/_{3}$.

Thermal Conductivity ($Wm^{-1}K^{-1}$)	Volumetric Specific Heat ($Jm^{-3}K^{-1}$)	Phonon Speed (ms^{-1})	Mean Free Path (nm)
157	1.653×10^6	8430	33.8

3.4 Equation of Phonon Radiative Transfer (EPRT) for One Dimensional Metallic Films

In a metallic film, there are two sub-systems present: Electron Sub-System and Lattice Sub-System. Both sub-systems participate in the energy transport in the metallic films. Thermal separation of electron and lattice (phonon) sub-systems exists, which requires incorporating the restructuring of the energy equations in line with the Boltzmann equation. This can be achieved through formulating energy transport in each sub-system using the Boltzmann transport equation. In this case, separate equations for radiate phonon transport (EPRT) for each sub-system needs to be developed. Due to the presence of thermal communication of both subsystems during the energy transport, the electron-phonon coupling term should be included in the EPRTs of each subsystem. The electron-phonon coupling term should be accommodated in such a way that in the diffusive limit, the EPRT should reduce to the standard two-equation model. The resulting EPRTs using the Boltzmann equation for each subsystem are given next.

In this dissertation EPRT is to solve the both sub-systems along with to coupling term to connect the electron and lattice (phonon) sub systems.

Lattice Sub-System

The radiative transport equation for the lattice sub-system can be written as [133]:

$$\frac{1}{v_{ph}}\frac{\partial I_{ph}}{\partial t}+\mu\frac{\partial I_{ph}}{\partial x}=\frac{\frac{1}{2}\int_{-1}^{1}I_{ph}d\mu-I_{ph}}{\Lambda_{ph}}-\frac{G}{2}\left(\frac{1}{C_{ph}v_{ph}}\int_{-1}^{1}I_{ph}d\mu-\frac{1}{C_e v_e}\int_{-1}^{1}I_e d\mu\right) \tag{3.53}$$

where $t>0, 0<x<L, -1<\mu<1$ and ph represents the lattice sub-system. In above equation, $I_{ph}, v_{ph}, \Lambda_{ph}$ *and* C_{ph} are the phonon intensity, speed, mean free path, and volumetric specific heat respectively. G is the electron-phonon coupling constant.

Electron Sub-System

The electron relaxation time is much shorter than the phonon relaxation time, the assumption of grey body is appropriate for the radiative energy transfer in electron sub-system of the thin film. Therefore, the proposed equation for the energy transport in the electron sub-system including the electron-phonon coupling should satisfy the conservation of energy and it can be written as:

$$\frac{1}{v_e}\frac{\partial I_e}{\partial t}+\mu\frac{\partial I_e}{\partial x}=\frac{\frac{1}{2}\int_{-1}^{1}I_e d\mu-I_e}{\Lambda_e}-\frac{G}{2}\left(\frac{1}{C_e v_e}\int_{-1}^{1}I_e d\mu-\frac{1}{C_{ph}v_{ph}}\int_{-1}^{1}I_{ph}d\mu\right) \tag{3.54}$$

where, $t>0, 0<x<L, -1<\mu<1$ and e represents the lattice sub-system. In above equation, I_e, v_e, Λ_e *and* C_e are the electron intensity, speed, mean free path, and volumetric specific heat respectively. G is the electron-phonon coupling constant.

Using the definitions of the phonon and electron temperatures T_{ph} and T_e,which are, $C_{ph}v_{ph}T_{ph}/4\pi = \tfrac{1}{2}\int_{-1}^{1} I_{ph} d\mu$ and $C_e v_e T_e/4\pi = \tfrac{1}{2}\int_{-1}^{1} I_e d\mu$, equation (3.54) and (3.54) become:

$$\frac{1}{v_{ph}}\frac{\partial I_{ph}}{\partial t} + \mu\frac{\partial I_{ph}}{\partial x} = \frac{\tfrac{1}{2}\int_{-1}^{1} I_{ph} d\mu - I_{ph}}{\Lambda_{ph}} - \frac{G}{4\pi}\left(T_{ph} - T_e\right) \tag{3.55}$$

and

$$\frac{1}{v_e}\frac{\partial I_e}{\partial t} + \mu\frac{\partial I_e}{\partial x} = \frac{\tfrac{1}{2}\int_{-1}^{1} I_e d\mu - I_e}{\Lambda_e} - \frac{G}{4\pi}\left(T_e - T_p\right) \tag{3.56}$$

3.4.1 EPRT and Two Equation Model

As it is mentioned above, in the diffusion limit, EPRT for electron and lattice subsystems can be reduced to modified form of the two equation model. This section deals with its derivation.

Multiply equation (3.55) and (3.56) throughout by $2\pi d\mu$ and then integrating from -1 to 1, yields,

$$\begin{aligned}\frac{2\pi}{v_{ph}}\int_{-1}^{1}\frac{\partial I_{ph}}{\partial t} d\mu + 2\pi\int_{-1}^{1}\mu\frac{\partial I_{ph}}{\partial x} d\mu = {} & \frac{2\pi\left(\int_{-1}^{1} d\mu\right)\left(\tfrac{1}{2}\int_{-1}^{1} I_{ph} d\mu\right) - 2\pi\int_{-1}^{1} I_{ph} d\mu}{\Lambda_{ph}} \\ & - 2\pi\frac{G}{4\pi}\left(T_{ph} - T_e\right)\left(\int_{-1}^{1} d\mu\right)\end{aligned} \tag{3.57}$$

and

$$\frac{2\pi}{v_e}\int_{-1}^{1}\frac{\partial I_e}{\partial t}d\mu+2\pi\int_{-1}^{1}\mu\frac{\partial I_e}{\partial x}d\mu=\frac{2\pi\left(\int_{-1}^{1}d\mu\right)\left(\frac{1}{2}\int_{-1}^{1}I_e d\mu\right)-2\pi\int_{-1}^{1}I_e d\mu}{\Lambda_p} \qquad (3.58)$$
$$-2\pi\frac{G}{4\pi}\left(T_e-T_{ph}\right)\left(\int_{-1}^{1}d\mu\right)$$

The phonon and electron heat flux is defined as, $q''_{ph}=2\pi\int_{-1}^{1}\mu I_{ph}d\mu$ and $q''_e=2\pi\int_{-1}^{1}\mu I_e d\mu$ respectively. (These definitions are to be used in the second term on the left hand side of equations (3.57) and (3.58)). Using the definition of heat flux in equations (3.57) and (3.58), the following simplified forms become,

$$C_{ph}\frac{\partial T_{ph}}{\partial t}+\frac{\partial q''_{ph}}{\partial x}=-G\left(T_{ph}-T_e\right) \qquad (3.59)$$

and

$$C_e\frac{\partial T_e}{\partial t}+\frac{\partial q''_e}{\partial x}=-G\left(T_e-T_{ph}\right) \qquad (3.60)$$

In the diffusion limit when the Knudsen number $Kn=\Lambda/L_x\to 0$ (where Λ is the mean free path and L_x is the film thickness), equation (3.55) and (3.56) should reduce to the two-equation model. This is can be verified as follows. After multiplying equation (3.55) and (3.56) throughout by $2\pi\mu d\mu$ and then integrating from -1 to 1, it yields,

$$\frac{2\pi}{v_{ph}}\int_{-1}^{1}\frac{\partial I_{ph}}{\partial t}d\mu+2\pi\int_{-1}^{1}\mu\frac{\partial I_{ph}}{\partial x}d\mu=\frac{2\pi\left(\int_{-1}^{1}d\mu\right)\left(\frac{1}{2}\int_{-1}^{1}I_{ph}d\mu\right)-2\pi\int_{-1}^{1}I_{ph}d\mu}{\Lambda_{ph}} \\ -2\pi\frac{G}{4\pi}\left(T_{ph}-T_e\right)\left(\int_{-1}^{1}d\mu\right) \tag{3.61}$$

and

$$\frac{2\pi}{v_{e}}\int_{-1}^{1}\frac{\partial I_{e}}{\partial t}d\mu+2\pi\int_{-1}^{1}\mu\frac{\partial I_{e}}{\partial x}d\mu=\frac{2\pi\left(\int_{-1}^{1}d\mu\right)\left(\frac{1}{2}\int_{-1}^{1}I_{e}d\mu\right)-2\pi\int_{-1}^{1}I_{e}d\mu}{\Lambda_{p}} \\ -2\pi\frac{G}{4\pi}\left(T_{e}-T_{ph}\right)\left(\int_{-1}^{1}d\mu\right) \tag{3.62}$$

However, the second term on the left-hand-side needs some elaboration. In the diffusive limit, the behavior of $I_{e,ph}\left(x,\mu,t\right)$ is mainly linear in μ. This means that we may neglect the terms of order 2 or higher in the Taylor series expansion of $I_{e,ph}\left(x,\mu,t\right)$ in μ:

$$\begin{aligned} I_{e,ph}\left(x,\mu,t\right)&=I_{e,ph}\left(x,0,t\right)+\mu\left.\frac{\partial I_{e,ph}}{\partial\mu}\right|_{\mu=0}+O\left(\mu\right) \\ &\approx I_{e,ph}^{o}\left(x,t\right)+\mu\left.\frac{\partial I_{e,ph}}{\partial\mu}\right|_{\mu=0} \end{aligned} \tag{3.63}$$

This is because,

$$I_{e,ph}^{o}\left(x,t\right)=\frac{1}{2}\int_{-1}^{1}I_{e,ph}\left(x,\mu,t\right)d\mu\approx I_{e,ph}\left(x,0,t\right)+\frac{1}{2}\left(\int_{-1}^{1}\mu d\mu\right)\left.\frac{\partial I_{e,ph}}{\partial\mu}\right|_{\mu=0}=I_{e,ph}\left(x,0,t\right)$$

Then,

$$
\begin{aligned}
2\pi\int_{-1}^{1}\mu^2\frac{\partial I_{e,ph}}{\partial x}d\mu &= 2\pi\int_{-1}^{1}\mu^2\frac{\partial}{\partial x}\left(I^o_{e,ph}\left(x,t\right)+\mu\frac{\partial I_{e,ph}}{\partial \mu}\bigg|_{\mu=0}\right)d\mu \\
&= 2\pi\int_{-1}^{1}\mu^2\frac{\partial I^o_{e,ph}\left(x,t\right)}{\partial x}d\mu+2\pi\frac{\partial}{\partial x}\left(\frac{\partial I_{e,ph}}{\partial \mu}\bigg|_{\mu=0}\right)\int_{-1}^{1}\mu^3 d\mu \\
&= 2\pi\frac{2}{3}\frac{\partial I^o_{e,ph}\left(x,t\right)}{\partial x}
\end{aligned}
\tag{3.64}
$$

Since,

$$
\frac{C_{e,ph}v_{e,ph}T_{e,ph}}{4\pi}=I^o_{e,ph}\left(x,t\right)=\tfrac{1}{2}\int_{-1}^{1}I_{e,ph}\left(x,\mu,t\right)d\mu
$$

therefore finally:

$$
2\pi\int_{-1}^{1}\mu^2\frac{\partial I_{e,ph}}{\partial x}d\mu=2\pi\frac{2}{3}\frac{dI^o_{e,ph}}{dT_{e,ph}}\frac{\partial T_{e,ph}}{\partial x}
\tag{3.65}
$$

Now the equation (3.61) and (3.62) are now simplified to:

$$
\frac{1}{v_{ph}}\frac{\partial q''_{ph}}{\partial t}+\frac{4\pi}{3}\frac{dI^o_{ph}}{dT_{ph}}\frac{\partial T_{ph}}{\partial x}=\frac{0-q''_{ph}}{\Lambda_{ph}}-0
\tag{3.66}
$$

and

$$
\frac{1}{v_e}\frac{\partial q''_e}{\partial t}+\frac{4\pi}{3}\frac{dI^o_e}{dT_e}\frac{\partial T_e}{\partial x}=\frac{0-q''_e}{\Lambda_e}-0+0
\tag{3.67}
$$

or

$$\frac{\Lambda_{ph}}{v_{ph}}\frac{\partial q''_{ph}}{\partial t}+q''_{ph}=-\frac{C_{ph}v_{ph}\Lambda_{ph}}{3}\frac{\partial T_{ph}}{\partial x} \tag{3.68}$$

and

$$\frac{\Lambda_e}{v_e}\frac{\partial q''_e}{\partial t}+q''_e=-\frac{C_e v_e\Lambda_e}{3}\frac{\partial T_e}{\partial x} \tag{3.69}$$

The kinetic theory formula for the thermal conductivity for phonons and electrons are given as,

$$k_{ph}=\frac{C_{ph}v_{ph}\Lambda_{ph}}{3} \tag{3.70}$$

and

$$k_e=\frac{C_e v_e\Lambda_e}{3} \tag{3.71}$$

Hence, equation (3.68) and (3.69) can be transformed into,

$$\frac{\Lambda_{ph}}{v_{ph}}\frac{\partial q''_{ph}}{\partial t}+q''_{ph}=-k_{ph}\frac{\partial T_{ph}}{\partial x} \tag{3.72}$$

and

$$\frac{\Lambda_e}{v_e}\frac{\partial q''_e}{\partial t}+q''_e=-k_e\frac{\partial T_e}{\partial x} \tag{3.73}$$

To eliminate q''_{ph} and q''_{e} between equation (3.68) and (3.72) as well as equation (3.69) and (3.73), one can proceed as follows. After differentiating (3.72) and (3.73) once with respect to x, it gives:

$$\frac{\Lambda_{ph}}{v_{ph}}\frac{\partial}{\partial t}\left(\frac{\partial q''_{ph}}{\partial x}\right)+\frac{\partial q''_{ph}}{\partial x}=-k_{ph}\frac{\partial^2 T_{ph}}{\partial x^2} \tag{3.74}$$

and

$$\frac{\Lambda_{e}}{v_{e}}\frac{\partial}{\partial t}\left(\frac{\partial q''_{e}}{\partial x}\right)+\frac{\partial q''_{e}}{\partial x}=-k_{e}\frac{\partial^2 T_{e}}{\partial x^2} \tag{3.75}$$

Now, substitute for $\partial q''_{ph}/\partial x$ & $\partial q''_{e}/\partial x$ from equations (3.59) and (3.60) in to equation (3.74) and (3.75) respectively and simplify to obtain:

$$\frac{\Lambda_{p}}{v_{p}}\frac{\partial}{\partial t}\left[C_p\frac{\partial T_p}{\partial t}+G\left(T_p-T_e\right)\right]+C_p\frac{\partial T_p}{\partial t}=k_p\frac{\partial^2 T_p}{\partial x^2}-G\left(T_p-T_e\right) \tag{3.76}$$

and

$$\frac{\Lambda_{e}}{v_{e}}\frac{\partial}{\partial t}\left[C_e\frac{\partial T_e}{\partial t}+G\left(T_e-T_{ph}\right)\right]+C_e\frac{\partial T_e}{\partial t}=k_e\frac{\partial^2 T_e}{\partial x^2}-G\left(T_e-T_{ph}\right) \tag{3.77}$$

Noting that $\tau_{ph}=\Lambda_{ph}/v_{ph}$ & $\tau_{e}=\Lambda_{e}/v_{e}$ are the relaxation times of the phonons and electrons respectively, the above equations may be written as,

$$\tau_{ph}\frac{\partial}{\partial t}\left[C_{ph}\frac{\partial T_{ph}}{\partial t}+G\left(T_{ph}-T_{e}\right)\right]+C_{ph}\frac{\partial T_{ph}}{\partial t}=k_{ph}\frac{\partial^{2}T_{ph}}{\partial x^{2}}-G\left(T_{ph}-T_{e}\right) \tag{3.78}$$

and

$$\tau_{e}\frac{\partial}{\partial t}\left[C_{e}\frac{\partial T_{e}}{\partial t}+G\left(T_{e}-T_{p}\right)\right]+C_{e}\frac{\partial T_{e}}{\partial t}=k_{e}\frac{\partial^{2}T_{e}}{\partial x^{2}}-G\left(T_{e}-T_{ph}\right) \tag{3.79}$$

or

$$\tau_{ph}C_{ph}\frac{\partial^{2}T_{ph}}{\partial t^{2}}+\left(C_{ph}+\tau_{ph}G\right)\frac{\partial T_{ph}}{\partial t}-\tau_{ph}G\frac{\partial T_{e}}{\partial t}=k_{ph}\frac{\partial^{2}T_{ph}}{\partial x^{2}}-G\left(T_{ph}-T_{e}\right) \tag{3.80}$$

and

$$\begin{aligned}\tau_{e}C_{e}\frac{\partial^{2}T_{e}}{\partial t^{2}}+\left(C_{e}+\tau_{e}G\right)\frac{\partial T_{e}}{\partial t}-\tau_{e}G\frac{\partial T_{p}}{\partial t}=k_{e}\frac{\partial^{2}T_{e}}{\partial x^{2}}-G\left(T_{e}-T_{p}\right)\\ \tau_{e}C_{e}\frac{\partial^{2}T_{e}}{\partial t^{2}}+\left(C_{e}+\tau_{e}G\right)\frac{\partial T_{e}}{\partial t}-\tau_{e}G\frac{\partial T_{p}}{\partial t}=k_{e}\frac{\partial^{2}T_{e}}{\partial x^{2}}-G\left(T_{e}-T_{p}\right)\end{aligned} \tag{3.81}$$

It should be noted that when the overall time scale of the heat transfer process is much longer than the relaxation time, then equation (3.80) and (3.81)can be further simplified to,

$$C_{ph}\frac{\partial T_{ph}}{\partial t}=k_{ph}\frac{\partial^{2}T_{ph}}{\partial x^{2}}-G\left(T_{ph}-T_{e}\right) \tag{3.82}$$

and

$$C_{e}\frac{\partial T_{e}}{\partial t}=k_{e}\frac{\partial^{2}T_{e}}{\partial x^{2}}-G\left(T_{e}-T_{ph}\right) \tag{3.83}$$

The above two equations constitute the familiar of modified two-equation model [16].

3.4.2 Frequency Dependent EPRT for Metallic film

In order to account for the frequency dependent formulation of the lattice sub-system, the experimental dispersion relations for aluminum is introduced [134] as shown in Figure 3.4, which provide 3 different polarizations for acoustic mode of vibrations of phonons. However, two transverse waves are degenerate and, therefore, one can have only one dispersion curve for two transverse waves and the other is for the longitudinal wave for aluminum. The constant relaxation time is assumed for all modes in aluminum; the value $\tau = 2.73\, ps$ is chosen to yield the phonon thermal conductivity around 11.3(Wm^{-1}K^{-1}) [135].

Due to the high speed of electrons, the electron sub-system is assumed to be a grey body and the radiative transport is considered to be a frequency independent [16]. Therefore, term contain electron-phonon coupling constant calculated separately and, then, it is redistributed over all polarization and frequency. Hence, the electron-phonon coupling term yields:

$$G_k = \frac{G}{4\pi}\frac{\left(T_{ph} - T_e\right)}{3k_{\max}} \tag{3.84}$$

Therefore, the frequency-dependent, transient phonon radiative transport for lattice sub-system is given by following equations:

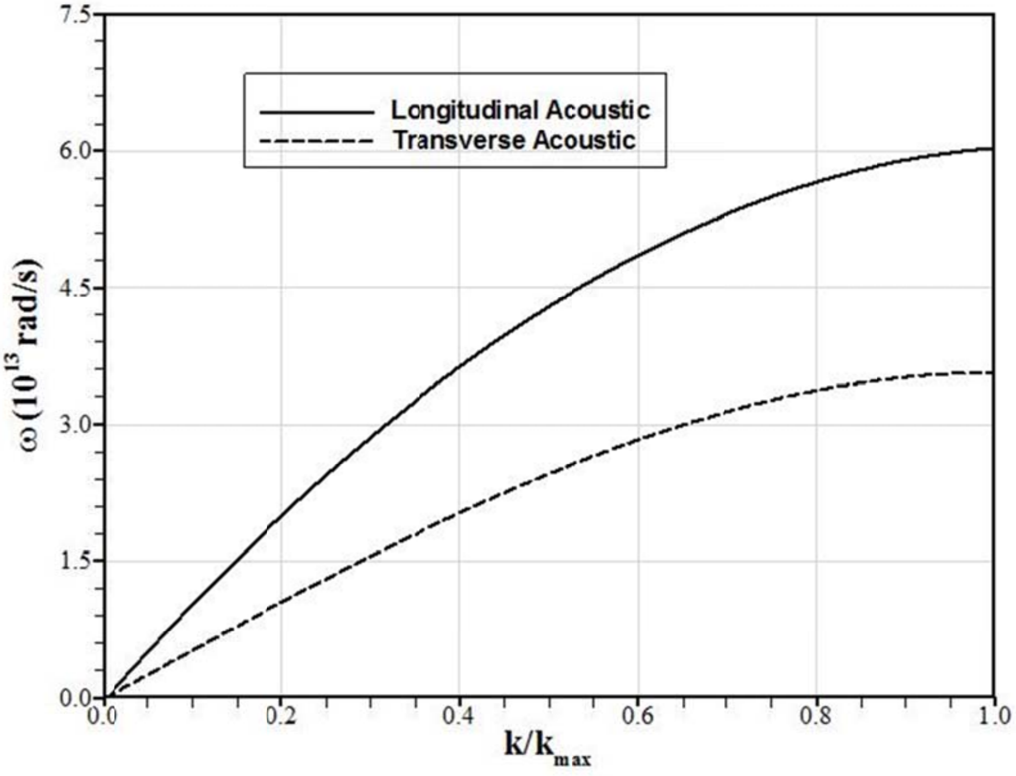

Figure 3.4 Dispersion relations of aluminum used in the simulations [134].

Longitudinal Acoustic:

$$\frac{1}{v_{ph,LA,k}}\frac{\partial I_{ph,LA,k}}{\partial t}+\mu\frac{\partial I_{ph,LA,k}}{\partial x}=\frac{\frac{1}{2}\int_{-1}^{1} I_{ph,LA,k}\,d\mu-I_{ph,LA,k}}{\Lambda_{ph,LA,k}}-G_k \quad (3.85)$$

Transverse Acoustic:

$$\frac{1}{v_{ph,TA,k}}\frac{\partial I_{ph,TA,k}}{\partial t}+\mu\frac{\partial I_{ph,TA,k}}{\partial x}=\frac{\frac{1}{2}\int_{-1}^{1} I_{ph,TA,k}\,d\mu-I_{ph,TA,k}}{\Lambda_{ph,TA,k}}-G_k \quad (3.86)$$

3.4.3 Definition of Temperature

Phonon Temperature

a) Frequency Dependent case

Phonon temperature for frequency dependent case is defined as:

$$T_{ph}(x,t)=\frac{2\pi\int_0^{k_{\max}}\int_{-1}^{1}(2I_{ph,TA,k}+I_{ph,LA,k})\,d\mu\,dk}{\int_0^{k_{\max}}\left(2C_{ph,TA,k}v_{ph,TA,k}+C_{ph,LA,k}v_{ph,LA,k}\right)dk} \quad (3.87)$$

b) Frequency Independent case

Phonon temperature frequency independent can be defined as:

$$T_{ph}(x,t)=\frac{2\pi}{C_{ph}v_{ph}}\int_{-1}^{1} I_{ph}\,d\mu \quad (3.88)$$

Electron Temperature

Electron temperature can be defined as:

$$T_e(x,t)=\frac{2\pi}{C_e v_e}\int_{-1}^{1} I_e\,d\mu \quad (3.89)$$

3.4.4 Heat Flux

Phonon Heat Flux

a) Frequency Dependent case

Heat flux for phonon frequency dependent case is defined as:

$$q''_{ph}(x,t) = 2\pi \int_0^{k_{\max}} \int_{-1}^{1} (2 I_{ph,TA,k} + I_{ph,LA,k})\, \mu d\mu\, dk \tag{3.90}$$

b) Frequency Independent case

Heat flux for phonon frequency independent can be defined as:

$$q''_{ph}(x,t) = 2\pi \int_{-1}^{1} I_{ph}\, \mu d\mu \tag{3.91}$$

Electron Heat Flux

Electron heat flux can be defined as:

$$q''_{e}(x,t) = 2\pi \int_{-1}^{1} I_{e}\, \mu d\mu \tag{3.92}$$

The properties of electron and lattice sub system which are incorporated in the simulation are given in Table 3.2.

Table 3.2 Properties of Aluminum the used in the numerical simulations

	Aluminum, Phonons	Aluminum, Electrons
Thermal Conductivity, ($Wm^{-1}K^{-1}$)	11.3 = .05×k_e	225.7
Volumetric Specific Heat, ($Jm^{-3}K^{-1}$)	2294396.6	23659
Speed (ms^{-1})	6420	2.03×10^{6}
Mean-Free-Path, $\Lambda = 3k/Cv$, (m)	2.3×10^{-9}	14.1×10^{-9}
Relaxation Time $\tau = \Lambda/v$, (s)	3.58×10^{-13}	6.945×10^{-15}
Electron-Phonon Coupling Constant in Aluminum, ($Wm^{-3}K^{-1}$)		2.4642×10^{17}

3.5 Mathematical Formulation for Two Dimensional Dielectric Thin Films

This section presents the complete mathematical formulation for seven different cases studied in relation to thermal heat transport in dielectric films. The relevant formulation consists of the governing equations, their domain of definition, and the associated initial, boundary and interface conditions for the cases considered.

1. Steady State Heat Transport Including the Effects of Heat Source Size and Silicon Film Dimension.
2. Transient Heat Transport Including the Effect of Temperature Oscillation in Silicon and Diamond Thin Films.
3. Transient Heat Transport Including the Effects of Pulse Duration of Heat Source in Silicon and Diamond Thin Films.
4. Transient Heat Transport Including the Effects of Thickness and Temparture Oscillations in Diamond Thin Films.
5. Transient Heat Transport Including the Effects of Heat Source Size and Temparture Oscillations in Silicon Thin films.
6. Transient Heat Transport in Silicon and Diamond Thin Film Pair Including the Thermal Boundary Resistance.
7. Transient Heat Transport Including Quantum Dot in Silicon Thin Film.

3.5.1 Steady State Heat Transport Including the Effects of Heat Source Size and Silicon Film Dimension

In order to the study the effect of heat source size and film dimension a two dimensional silicon film is considered as shown in Figure 3.5. To study the effect of heat source size and silicon film dimension eight different cases are considered. These include two different film length of silicon film and four different sizes of heat source at the top edge of the film.

Boundary Conditions:

Four boundaries of the domain, bottom, top, left and right are introduced, provided that the boundary conditions at the right, left and bottom surfaces remain unchanged at 300 K. However, the top boundary of the silicon layer is assumed to have a step temperature distribution. Along the heat source size, w_s temperature of 301 K is considered at the top edge of the film; else it's taken as 300 K along the other edges of the film. These boundary conditions are given in Figure 3.5 and they are formulated below:

Bottom Boundary:

$$\left.\begin{aligned}
I_{LA,k}\left(x=0,z,\theta,\phi\right) &= \frac{C_{LA,k}v_{LA,k}T_{bottom}}{4\pi} \\
I_{TA,k}\left(x=0,z,\theta,\phi\right) &= \frac{C_{TA,k}v_{TA,k}T_{bottom}}{4\pi} \\
I_{LO,k}\left(x=0,z,\theta,\phi\right) &= \frac{C_{LO,k}v_{LO,k}T_{bottom}}{4\pi} \\
I_{TO,k}\left(x=0,z,\theta,\phi\right) &= \frac{C_{TO,k}v_{TO,k}T_{bottom}}{4\pi}
\end{aligned}\right. \quad 0<z<L_z, \quad 0<\theta<\pi/2, \quad 0<\phi<2\pi \qquad (3.93)$$

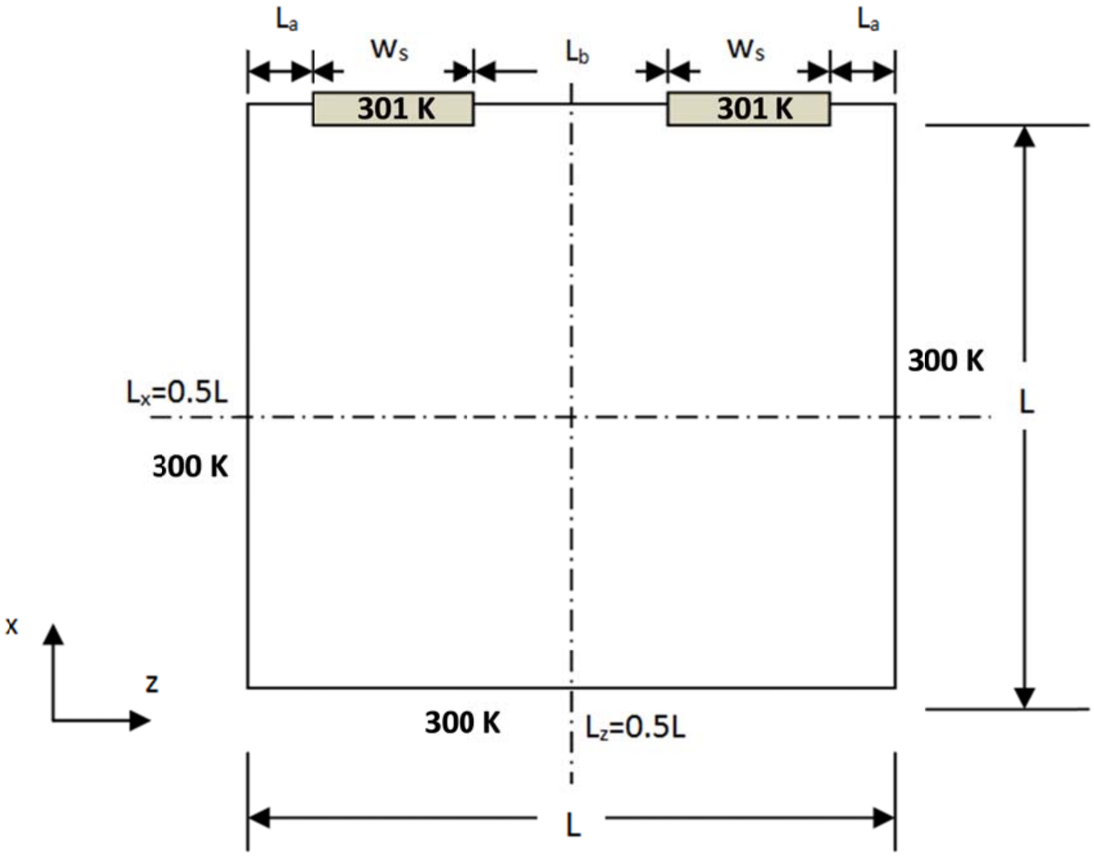

Figure 3.5 A schematic view of the heat source locations at the top edges of the film and the boundary conditions for study the effect of Heat Source Size and Silicon Film Dimensions

Top Boundary:

For the top boundary, there are two temperatures at the face $T_{top,high}$ in the region of w_s and otherwise the temperature is $T_{top,high}$ (Figure 3.5).

Top Boundary with higher temperature

$$
\begin{aligned}
I_{LA,k}\left(x=L,z,\theta,\phi\right) &= \frac{C_{LA,k}v_{LA,k}T_{top,high}}{4\pi} \\
I_{TA,k}\left(x=L,z,\theta,\phi\right) &= \frac{C_{TA,k}v_{TA,k}T_{top,high}}{4\pi} \qquad L_a < z < L_a + w_s \\
&\qquad\qquad\qquad\qquad\quad L_a + w_s + L_b < z < L_a + 2w_s + L_b \\
I_{LO,k}\left(x=L,z,\theta,\phi\right) &= \frac{C_{LO,k}v_{LO,k}T_{top,high}}{4\pi} \qquad \pi/2 < \theta < \pi, 0 < \phi < 2\pi \\
I_{TO,k}\left(x=L,z,\theta,\phi\right) &= \frac{C_{TO,k}v_{TO,k}T_{top,high}}{4\pi}
\end{aligned}
\tag{3.94}
$$

Top Boundary with lower temperature

$$
\begin{aligned}
I_{LA,k}\left(x=L,z,\theta,\phi\right) &= \frac{C_{LA,k}v_{LA,k}T_{top,high}}{4\pi} \\
I_{TA,k}\left(x=L,z,\theta,\phi\right) &= \frac{C_{TA,k}v_{TA,k}T_{top,high}}{4\pi} \qquad 0 < z < L_a \\
&\qquad\qquad\qquad\qquad\quad L_a + w_s < z < L_a + w_s + L_b \\
I_{LO,k}\left(x=L,z,\theta,\phi\right) &= \frac{C_{LO,k}v_{LO,k}T_{top,high}}{4\pi} \qquad L_a + 2w_s + L_b < z < L_z \\
I_{TO,k}\left(x=L,z,\theta,\phi\right) &= \frac{C_{TO,k}v_{TO,k}T_{top,high}}{4\pi}
\end{aligned}
\tag{3.95}
$$

Left Boundary:

$$\left.\begin{aligned}
I_{LA,k}\left(x,z=0,\theta,\phi\right) &= \frac{C_{LA,k}v_{LA,k}T_{left}}{4\pi}\\
I_{TA,k}\left(x,z=0,\theta,\phi\right) &= \frac{C_{TA,k}v_{TA,k}T_{left}}{4\pi}\\
I_{LO,k}\left(x,z=0,\theta,\phi\right) &= \frac{C_{LO,k}v_{LO,k}T_{left}}{4\pi}\\
I_{TO,k}\left(x,z=0,\theta,\phi\right) &= \frac{C_{TO,k}v_{TO,k}T_{left}}{4\pi}
\end{aligned}\right. \quad 0 < x < L_x, 0 < \theta < \pi, 0 < \phi < \pi \tag{3.96}$$

Right Boundary:

$$\left.\begin{aligned}
I_{LA,k}\left(x,z=L,\theta,\phi\right) &= \frac{C_{LA,k}v_{LA,k}T_{right}}{4\pi}\\
I_{TA,k}\left(x,z=L,\theta,\phi\right) &= \frac{C_{TA,k}v_{TA,k}T_{right}}{4\pi}\\
I_{LO,k}\left(x,z=L,\theta,\phi\right) &= \frac{C_{LO,k}v_{LO,k}T_{right}}{4\pi}\\
I_{TO,k}\left(x,z=L,\theta,\phi\right) &= \frac{C_{TO,k}v_{TO,k}T_{right}}{4\pi}
\end{aligned}\right. \quad 0 < x < L_x, 0 < \theta < \pi, 0 < \phi < \pi \tag{3.97}$$

3.5.2 Transient Heat Transport Including the Effect of Temperature Oscillation in Silicon and Diamond Thin Films

The influence of film temperature oscillation at the film edge on the phonon transport characteristics is investigated after considering frequency dependent solution of phonon radiative transport equation in silicon and diamond thin films as shown in Figure 3.6. To study the effect of temperature oscillation (Figure 3.7) three cases are studied for each film considering heating cycles of 3 ps , 5 ps and 7.5 ps.

Initial Conditions:

It is considered the whole domain initially at 300 K. The following initial condition are incorporated in the domain,

$$\begin{aligned}
&I_{LA,k}\left(x,z,\theta,\phi,t=0\right)=\frac{C_{LA,k}v_{LA,k}T_{\text{initial}}}{4\pi} \\
&I_{TA,k}\left(x,z,\theta,\phi,t=0\right)=\frac{C_{TA,k}v_{TA,k}T_{\text{initial}}}{4\pi} \qquad 0<x<L_x, 0<z<L_z \\
&I_{LO,k}\left(x,z,\theta,\phi,t=0\right)=\frac{C_{LO,k}v_{LO,k}T_{\text{initial}}}{4\pi} \qquad 0<\theta<\pi,\ 0<\phi<2\pi \\
&I_{TO,k}\left(x,z,\theta,\phi,t=0\right)=\frac{C_{TO,k}v_{TO,k}T_{\text{initial}}}{4\pi}
\end{aligned} \qquad (3.98)$$

Boundary Conditions:

Four boundaries of the domain, bottom, top, left and right are introduced, provided that the boundary conditions at the top, left and right surfaces remain unchanged at 300 K.

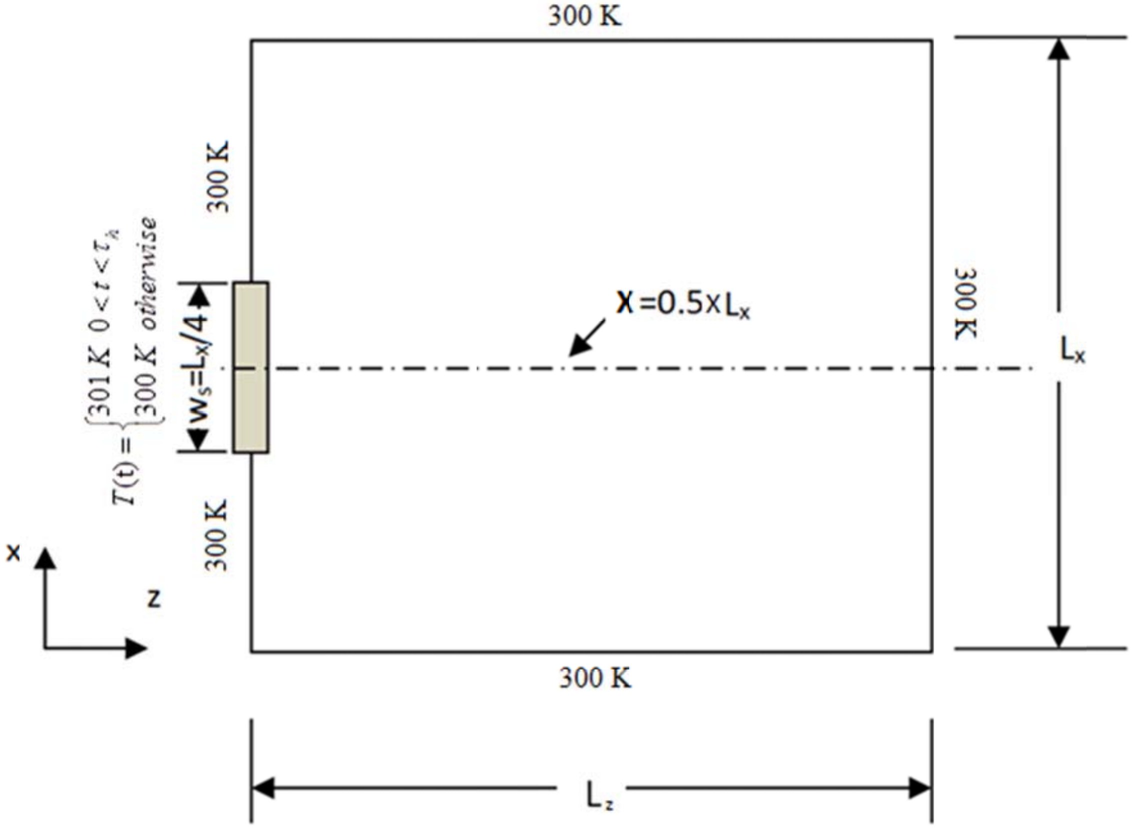

Figure 3.6 A schematic view of two-dimensional thin film and the heat source location

.

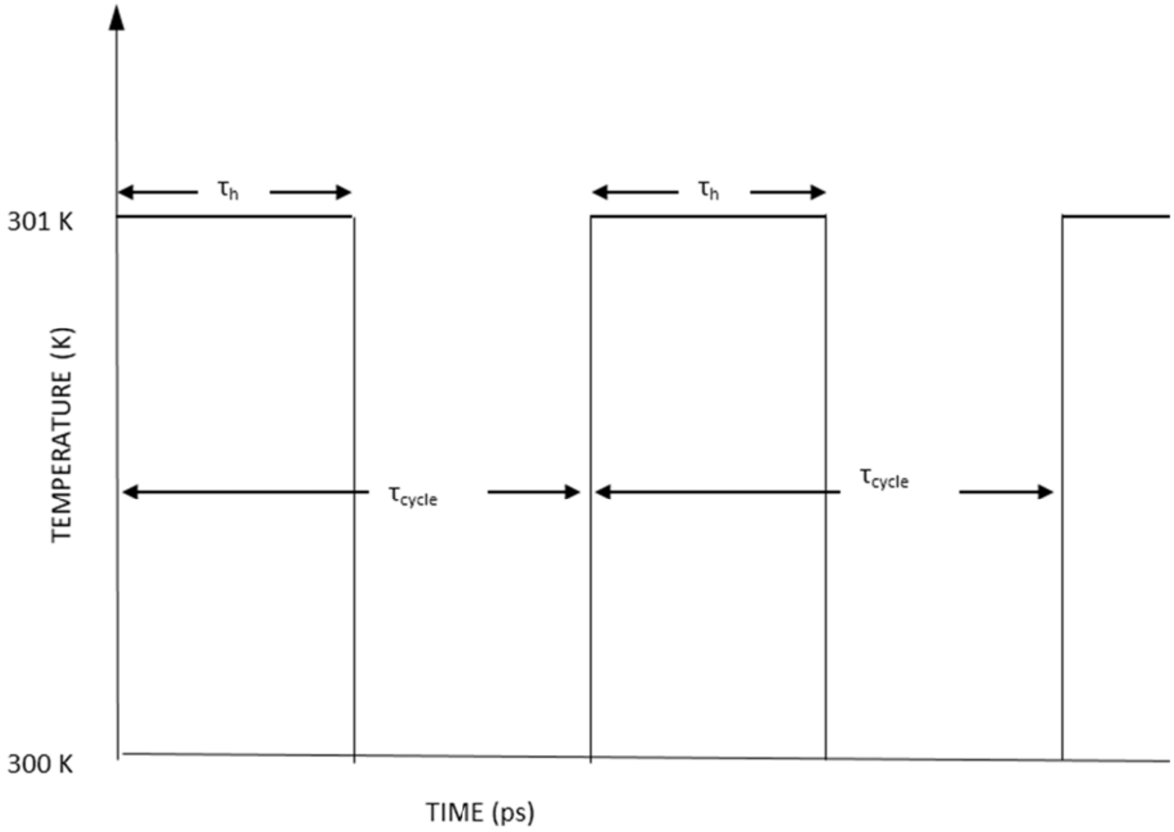

Figure 3.7 Temporal variation of temperature oscillation (pulsation) at the left edge of the film. It should be noted that $T(\mathrm{t}) = \begin{cases} 301\,K & 0 < t < \tau_h \\ 300\,K & otherwise \end{cases}$ where, $T\left(t+\tau_{cycle}\right) = T\left(t\right)$

$T\left(t+\tau_{cycle}\right) = T\left(t\right)$.

However, the left boundary of the silicon and diamond films is assumed to have a periodic temperature oscillation (pulsation) with the minimum and the maximum temperatures of 300 K and 301 K, respectively in according to Figure 3.7. The other edges of the film are considered at 300 K (Figure 3.6). These boundary conditions are formulated below:

Bottom Boundary:

$$\begin{aligned}
I_{LA,k}\left(x=0,z,\theta,\phi,t\right) &= \frac{C_{LA,k}v_{LA,k}T_{bottom}}{4\pi} \\
I_{TA,k}\left(x=0,z,\theta,\phi,t\right) &= \frac{C_{TA,k}v_{TA,k}T_{bottom}}{4\pi} \\
I_{LO,k}\left(x=0,z,\theta,\phi,t\right) &= \frac{C_{LO,k}v_{LO,k}T_{bottom}}{4\pi} \\
I_{TO,k}\left(x=0,z,\theta,\phi,t\right) &= \frac{C_{TO,k}v_{TO,k}T_{bottom}}{4\pi}
\end{aligned}
\qquad
\begin{aligned}
&t>0, 0<z<L_z, \\
&0<\theta<\pi/2, 0<\phi<2\pi
\end{aligned}
\qquad (3.99)$$

Top Boundary:

$$\begin{aligned}
I_{LA,k}\left(x=0,z,\theta,\phi,t\right) &= \frac{C_{LA,k}v_{LA,k}T_{top}}{4\pi} \\
I_{TA,k}\left(x=0,z,\theta,\phi,t\right) &= \frac{C_{TA,k}v_{TA,k}T_{top}}{4\pi} \\
I_{LO,k}\left(x=0,z,\theta,\phi,t\right) &= \frac{C_{LO,k}v_{LO,k}T_{top}}{4\pi} \\
I_{TO,k}\left(x=0,z,\theta,\phi,t\right) &= \frac{C_{TO,k}v_{TO,k}T_{top}}{4\pi}
\end{aligned}
\qquad
\begin{aligned}
&t>0, 0<z<L_z, \\
&0<\theta<\pi, 0<\phi<\pi
\end{aligned}
\qquad (3.100)$$

Left Boundary:

For the left boundary, there are two temperatures at the face. $T_{left,high}$ (which oscillates, Figure 3.7) in the region of w_s and otherwise the temperature is $T_{left,low}$ (Figure 3.6.).

Left Boundary with higher temperature

$$\begin{aligned}
I_{LA,k}\left(x=L_m,z=0,\theta,\phi,t\right)&=\frac{C_{LA,k}v_{LA,k}T_{left,high}}{4\pi}\\
I_{TA,k}\left(x=L_m,z=0,\theta,\phi,t\right)&=\frac{C_{TA,k}v_{TA,k}T_{left,high}}{4\pi}\\
I_{LO,k}\left(x=L_m,z=0,\theta,\phi,t\right)&=\frac{C_{LO,k}v_{LO,k}T_{left,high}}{4\pi}\\
I_{TO,k}\left(x=L_m,z=0,\theta,\phi,t\right)&=\frac{C_{TO,k}v_{TO,k}T_{left,high}}{4\pi}
\end{aligned}
\qquad
\begin{aligned}
&L_a<L_m<L_a+w_s\,,t>0\\
&T_{left,high}\ (\mathrm{t})=\begin{cases}301\,K & 0<t<\tau_h\\ 300\,K\ otherwise\end{cases}\\
&\pi/2<\theta<\pi,\quad 0<\phi<2\pi
\end{aligned}
\tag{3.101}$$

Left Boundary with lower temperature

$$\begin{aligned}
I_{LA,k}\left(x=L_n,z=0,\theta,\phi,t\right)&=\frac{C_{LA,k}v_{LA,k}T_{left,low}}{4\pi}\\
I_{TA,k}\left(x=L_n,z=0,\theta,\phi,t\right)&=\frac{C_{TA,k}v_{TA,k}T_{left,low}}{4\pi}\\
I_{LO,k}\left(x=L_n,z=0,\theta,\phi,t\right)&=\frac{C_{LO,k}v_{LO,k}T_{left,low}}{4\pi}\\
I_{TO,k}\left(x=L_n,z=0,\theta,\phi,t\right)&=\frac{C_{TO,k}v_{TO,k}T_{left,low}}{4\pi}
\end{aligned}
\qquad
\begin{aligned}
&0\le L_n<L_a\ and\\
&L_a+w_s\le L_n<L_x,t>0\\
&T_{left,low}\ (t)=300\,\mathrm{K}\\
&\pi/2<\theta<\pi,\quad 0<\phi<2\pi
\end{aligned}
\tag{3.102}$$

Right Boundary:

$$\left.\begin{aligned}
I_{LA,k}\left(x, z=L_z, \theta, \phi, t\right) &= \frac{C_{LA,k} v_{LA,k} T_{right}}{4\pi} \\
I_{TA,k}\left(x, z=L_z, \theta, \phi, t\right) &= \frac{C_{TA,k} v_{TA,k} T_{right}}{4\pi} \\
I_{LO,k}\left(x, z=L_z, \theta, \phi, t\right) &= \frac{C_{LO,k} v_{LO,k} T_{right}}{4\pi} \\
I_{TO,k}\left(x, z=L_z, \theta, \phi, t\right) &= \frac{C_{TO,k} v_{TO,k} T_{right}}{4\pi}
\end{aligned}\right. \qquad \begin{aligned} &0 < x < L_x, t > 0 \\ &0 < \theta < \pi, \pi < \phi < 2\pi \end{aligned} \qquad (3.103)$$

3.5.3 Transient Heat Transport Including the Effects of Pulse Duration of Heat Source in Silicon and Diamond Thin Films

In order to study the effect of heating pulse duration on the phonon transport, two-dimensional frequency dependent EPRT is solved in the two-dimensional diamond and silicon films as shown schematically in Figure 3.6. Temperature oscillation is introduced at one edge of the film, which is shown in Figure 3.7. Energy transport characteristics in silicon and diamond films are investigated for twelve cases which include two heating pulses ($\tau_h = 6$ ps and $\tau_h = 10$ ps) with three different heating durations ($\tau_h = 0.25\tau_{Cycle}$, $\tau_h = 0.50\tau_{Cycle}$ and $\tau_h = 0.25\tau_{Cycle}$).

In all the simulations the domain initially considered at 300 K. The initial conditions and boundary condition are incorporated in the similar way as described in section 3.5.2.

3.5.4 Transient Heat Transport Including the Effects of Thickness and Temperature Oscillations in Diamond Thin Film

In the study, transient heat transport characteristics are investigated to examine the effect of film thickness for the temperature oscillating boundary condition in diamond thin film. EPRT is incorporated for solution the two-dimensional diamond films as shown in Figure 3.6. Temperature oscillations ($\tau_h = 3$ ps and $\tau_h = 5$ ps) are introduced at left edge of the film, which is shown in Figure 3.7. Simulations are carried out for four different film thicknesses ($L_z = 0.01$ μm, $L_z = 0.05$ μm, $L_z = 0.10$ μm and $L_z = 0.15$μm) for each temperature oscillation. All the cases are solved with the consideration that initial temperature of computational domains is 300 *K*. All the initial conditions and boundary condition are incorporated in the same way as explained in section 3.5.2.

3.5.5 Transient Heat Transport Including the Effects of Heat Source Size and Temperature Oscillation in Silicon Thin Film

The study includes the investigation of the coupling effect of heat source and temperature oscillation on the phonon transport characteristics. A transient frequency dependent EPRT is solved in line with the two-dimensional silicon films as shown schematically in Figure 3.6. At left edge of the film the oscillating heat source is placed as shown in Figure 3.7. Transient analysis is performed for four different heat source sizes (w_s = 0.25L, w_s = 0.50L, w_s = 0.75L and w_s = 1.00L, where L = 0.1 μm). Each of the heat source size is analyzed for two temperature oscillations (τ_h = 6 ps and τ_h = 10 ps). In simulations, the initial and boundary condition are introduced in the similar way which described in section 3.5.2.

3.5.6 Transient Heat Transport in Silicon and Diamond Thin Films Pair Including the Thermal Boundary Resistance

The study is conducted to investigate the phonon transport across the silicon-diamond thin film pairs due to temperature disturbance. The thermal boundary resistance at the interface of the thin film pairs is modeled incorporating the cut-off mismatch and diffusive mismatch models. The transient and frequency dependent EPRT is solved for the silicon and diamond films.

There are four boundaries introduced for the silicon and diamond film pair. These are the bottom, top, left, and right boundaries (Figure 3.8). In addition, the right boundary for the silicon and the left boundary for diamond make a single interface. At this interface an appropriate condition has to be defined, which is derived from the energy balance condition at the interface. The phonon intensity specification at the boundaries, the interface condition and the initial condition should be prescribed to complete the problem specification. In the present study, the geometry of the physical domain and the boundary conditions do not change with time. Initially, the silicon and diamond films are assumed to be at a uniform temperature of 300 K and after that for all times the following boundary conditions are imposed. The left boundary of silicon assumed at 301 K while bottom and top boundaries of the silicon layer are assumed to be at a constant temperature of 300 K. The top, right and bottom boundaries of the diamond layer are assumed to be at a constant temperature at 300 K. At the interface, the temperatures in the silicon and diamond layers are variable and they are determined by means of the interface condition.

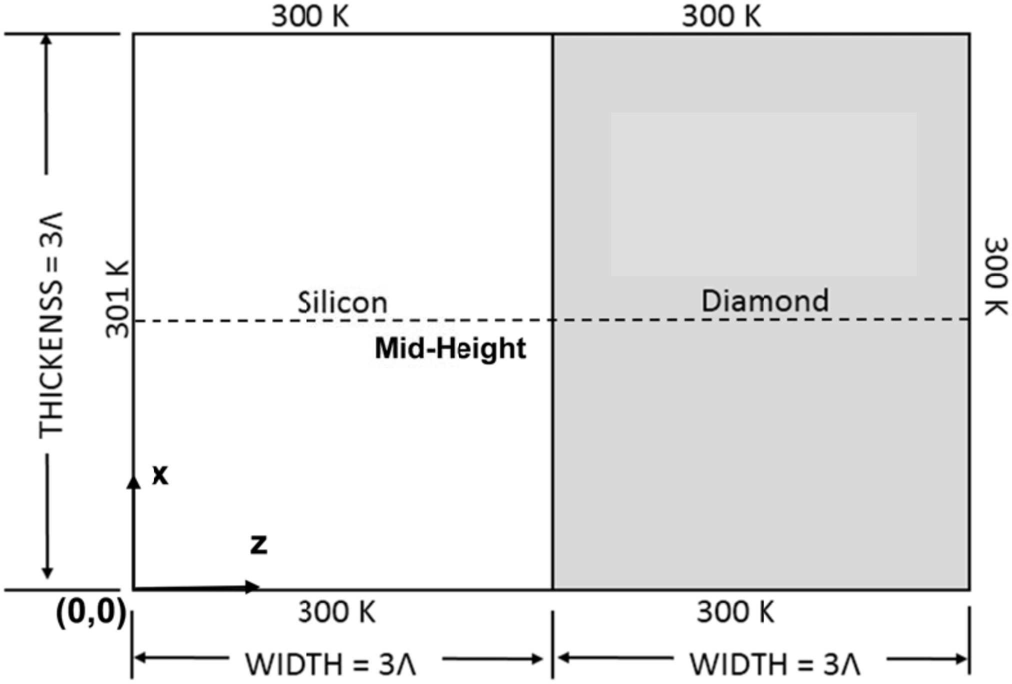

Figure 3.8 Schematic view of silicon-diamond film pair and boundary conditions. Λ is the mean free path of silicon corresponding to the gray medium.

.

The initial, boundary and interface conditions are described below.

Silicon Film:

Initial Conditions:

$$
\begin{aligned}
I_{Si,LA,\omega}\left(x_{Si}, z_{Si}, \theta, \phi, t=0\right) &= \frac{C_{Si,LA,\omega} v_{Si,LA,\omega} T_{initial}}{4\pi} \\
I_{Si,TA,\omega}\left(x_{Si}, z_{Si}, \theta, \phi, t=0\right) &= \frac{C_{Si,TA,\omega} v_{Si,TA,\omega} T_{initial}}{4\pi} \qquad 0 < x_{Si} < L_{x,Si}, 0 < z_{Si} < L_{z,Si}, \\
I_{Si,LO,\omega}\left(x_{Si}, z_{Si}, \theta, \phi, t=0\right) &= \frac{C_{Si,LO,\omega} v_{Si,LO,\omega} T_{initial}}{4\pi} \qquad 0 < \theta < \pi, \quad 0 < \phi < 2\pi \\
I_{Si,TO,\omega}\left(x_{Si}, z_{Si}, \theta, \phi, t=0\right) &= \frac{C_{Si,TO,\omega} v_{Si,TO,\omega} T_{initial}}{4\pi}
\end{aligned}
\qquad (3.104)
$$

In above equation subscript Si indicate the Silicon thin film. For example $v_{Si,LA,\omega}$ represents the frequency dependent phonon group velocity for longitudinal acoustic branch in silicon.

Boundary Conditions:

Bottom Boundary:

$$
\begin{aligned}
I_{Si,LA,\omega}\left(x_{Si}=0, z_{Si}, \theta, \phi, t\right) &= \frac{C_{Si,LA,\omega} v_{Si,LA,\omega} T_{bottom}}{4\pi} \\
I_{Si,TA,\omega}\left(x_{Si}=0, z_{Si}, \theta, \phi, t\right) &= \frac{C_{Si,TA,\omega} v_{Si,TA,\omega} T_{bottom}}{4\pi} \qquad t > 0, \quad 0 < z_{Si} < L_{z,Si}, \\
I_{Si,LO,\omega}\left(x_{Si}=0, z_{Si}, \theta, \phi, t\right) &= \frac{C_{Si,LO,\omega} v_{Si,LO,\omega} T_{bottom}}{4\pi} \qquad \pi/2 < \theta < \pi, 0 < \phi < 2\pi \\
I_{Si,TO,\omega}\left(x_{Si}=0, z_{Si}, \theta, \phi, t\right) &= \frac{C_{Si,TO,\omega} v_{Si,TO,\omega} T_{bottom}}{4\pi}
\end{aligned}
\qquad (3.105)
$$

Top Boundary:

$$\begin{aligned}
I_{Si,LA,\omega}\left(x_{Si}=L_{x,Si},z_{Si},\theta,\phi,t\right)&=\frac{C_{Si,LA,\omega}v_{Si,LA,\omega}T_{top}}{4\pi}\\
I_{Si,TA,\omega}\left(x_{Si}=L_{x,Si},z_{Si},\theta,\phi,t\right)&=\frac{C_{Si,TA,\omega}v_{Si,TA,\omega}T_{top}}{4\pi}\qquad t>0,0<z_{Si}<L_{z,Si},\\
I_{Si,LO,\omega}\left(x_{Si}=L_{x,Si},z_{Si},\theta,\phi,t\right)&=\frac{C_{Si,LO,\omega}v_{Si,LO,\omega}T_{top}}{4\pi}\qquad \pi/2<\theta<\pi,0<\phi<2\pi\\
I_{Si,TO,\omega}\left(x_{Si}=L_{x,Si},z_{Si},\theta,\phi,t\right)&=\frac{C_{Si,TO,\omega}v_{Si,TO,\omega}T_{top}}{4\pi}
\end{aligned}\tag{3.106}$$

Left Boundary:

$$\begin{aligned}
I_{Si,LA,\omega}\left(x_{Si},z_{Si}=0,\theta,\phi,t\right)&=\frac{C_{Si,LA,\omega}v_{Si,LA,\omega}T_{left}}{4\pi}\\
I_{Si,TA,\omega}\left(x_{Si},z_{Si}=0,\theta,\phi,t\right)&=\frac{C_{Si,TA,\omega}v_{Si,TA,\omega}T_{left}}{4\pi}\qquad t>0,\quad 0<x_{Si}<L_{x,Si},\\
I_{Si,LO,\omega}\left(x_{Si},z_{Si}=0,\theta,\phi,t\right)&=\frac{C_{Si,LO,\omega}v_{Si,LO,\omega}T_{left}}{4\pi}\qquad 0<\theta<\pi,\quad 0<\phi<\pi\\
I_{Si,TO,\omega}\left(x_{Si},z_{Si}=0,\theta,\phi,t\right)&=\frac{C_{Si,TO,\omega}v_{Si,TO,\omega}T_{left}}{4\pi}
\end{aligned}\tag{3.107}$$

Diamond Film:

Initial Conditions:

$$\begin{aligned}
I_{Di,LA,\omega}\left(x_{Di},z_{Di},\theta,\phi,t=0\right)&=\frac{C_{Di,LA,\omega}v_{Di,LA,\omega}T_{initial}}{4\pi}\\
I_{Di,TA,\omega}\left(x_{Di},z_{Di},\theta,\phi,t=0\right)&=\frac{C_{Di,TA,\omega}v_{Di,TA,\omega}T_{initial}}{4\pi}\qquad 0<x_{Di}<L_{x,Di},0<\theta<\pi,\\
I_{Di,LO,\omega}\left(x_{Di},z_{Di},\theta,\phi,t=0\right)&=\frac{C_{Di,LO,\omega}v_{Di,LO,\omega}T_{initial}}{4\pi}\qquad 0<z_{Di}<L_{z,Di},0<\phi<2\pi\\
I_{Di,TO,\omega}\left(x_{Di},z_{Di},\theta,\phi,t=0\right)&=\frac{C_{Di,TO,\omega}v_{Di,TO,\omega}T_{initial}}{4\pi}
\end{aligned}\tag{3.108}$$

In above equation subscript Di indicate the Diamond thin film. For example $v_{Di,LA,\omega}$ represents the frequency dependent phonon group velocity for diamond in longitudinal acoustic branch.

Boundary Conditions:

Bottom Boundary:

$$\begin{aligned}
I_{Di,LA,\omega}\left(x_{Di}=0,z_{Di},\theta,\phi,t\right)&=\frac{C_{Di,LA,\omega}v_{Di,LA,\omega}T_{bottom}}{4\pi}\\
I_{Di,TA,\omega}\left(x_{Di}=0,z_{Di},\theta,\phi,t\right)&=\frac{C_{Di,TA,\omega}v_{Di,TA,\omega}T_{bottom}}{4\pi}\\
I_{Di,LO,\omega}\left(x_{Di}=0,z_{Di},\theta,\phi,t\right)&=\frac{C_{Di,LO,\omega}v_{Di,LO,\omega}T_{bottom}}{4\pi}\\
I_{Di,TO,\omega}\left(x_{Di}=0,z_{Di},\theta,\phi,t\right)&=\frac{C_{Di,TO,\omega}v_{Di,TO,\omega}T_{bottom}}{4\pi}
\end{aligned}
\qquad
\begin{aligned}
&t>0,\quad 0<z_{Di}<L_{z,Di},\\
&0<\theta<\pi/2,0<\phi<2\pi
\end{aligned}
\qquad (3.109)$$

Top Boundary:

$$\begin{aligned}
I_{Di,LA,\omega}\left(x_{Di}=L_{x,Di},z_{Di},\theta,\phi,t\right)&=\frac{C_{Di,LA,\omega}v_{Di,LA,\omega}T_{top}}{4\pi}\\
I_{Di,TA,\omega}\left(x_{Di}=L_{x,Di},z_{Di},\theta,\phi,t\right)&=\frac{C_{Di,TA,\omega}v_{Di,TA,\omega}T_{top}}{4\pi}\\
I_{Di,LO,\omega}\left(x_{Di}=L_{x,Di},z_{Di},\theta,\phi,t\right)&=\frac{C_{Di,LO,\omega}v_{Di,LO,\omega}T_{top}}{4\pi}\\
I_{Di,TO,\omega}\left(x_{Di}=L_{x,Di},z_{Di},\theta,\phi,t\right)&=\frac{C_{Di,TO,\omega}v_{Di,TO,\omega}T_{top}}{4\pi}
\end{aligned}
\qquad
\begin{aligned}
&t>0,\quad 0<z_{Di}<L_{z,Di},\\
&\pi/2<\theta<\pi,0<\phi<2\pi
\end{aligned}
\qquad (3.110)$$

Right Boundary:

$$\left.\begin{aligned}
I_{Di,LA,\omega}\left(x_{Di}, z_{Di} = L_{z,Di}, \theta, \phi, t\right) &= \frac{C_{Di,LA,\omega} v_{Di,LA,\omega} T_{top}}{4\pi} \\
I_{Di,TA,\omega}\left(x_{Di}, z_{Di} = L_{z,Di}, \theta, \phi, t\right) &= \frac{C_{Di,TA,\omega} v_{Di,TA,\omega} T_{top}}{4\pi} \\
I_{Di,LO,\omega}\left(x_{Di}, z_{Di} = L_{z,Di}, \theta, \phi, t\right) &= \frac{C_{Di,LO,\omega} v_{Di,LO,\omega} T_{top}}{4\pi} \\
I_{Di,TO,\omega}\left(x_{Di}, z_{Di} = L_{z,Di}, \theta, \phi, t\right) &= \frac{C_{Di,TO,\omega} v_{Di,TO,\omega} T_{top}}{4\pi}
\end{aligned}\right. \quad \begin{aligned} &t > 0, \quad 0 < x_{Di} < L_{x,Di}, \\ &0 < \theta < \pi, \quad \pi < \phi < 2\pi \end{aligned} \qquad (3.111)$$

Interface Conditions*:*

In order to obtain the detailed information about the phonon intensities at interface, it is necessary to specify the incoming/outgoing phonon intensities distribution at interface. Figure 3.9 shows that in the silicon film, I_{Si}^{++} and I_{Si}^{-+} are the phonon intensities which are coming towards the interface and the phonon intensities which are going from the interface are I_{Si}^{--} and I_{Si}^{+-}. And in the diamond film, the I_{Di}^{--} and I_{Di}^{+-} are the phonon intensities which are coming towards the interface and phonon intensities which are going from the interface are I_{Di}^{++} and I_{Di}^{-+}. The heat flux which is coming at the interface due to the incoming phonon intensities from both films is either reflected or transmitted. Boundary conditions at the edges of silicon and diamond film give us the values of the incoming intensities $\left(I_{Si}^{++}, I_{Si}^{-+}, I_{Di}^{--} \; and \; I_{Di}^{+-}\right)$ towards the interface. In order to determine the unknown phonon intensities distribution at the interface i.e. outgoing phonon intensities from the interface $\left(I_{Si}^{+-}, I_{Si}^{--}, I_{Di}^{++} \; and \; I_{Di}^{-+}\right)$, the following methods adopted to model the thermal boundary resistance across the interface. These are: 1) Diffuse Mismatch Model and 2) Cut-off Mismatch Model.

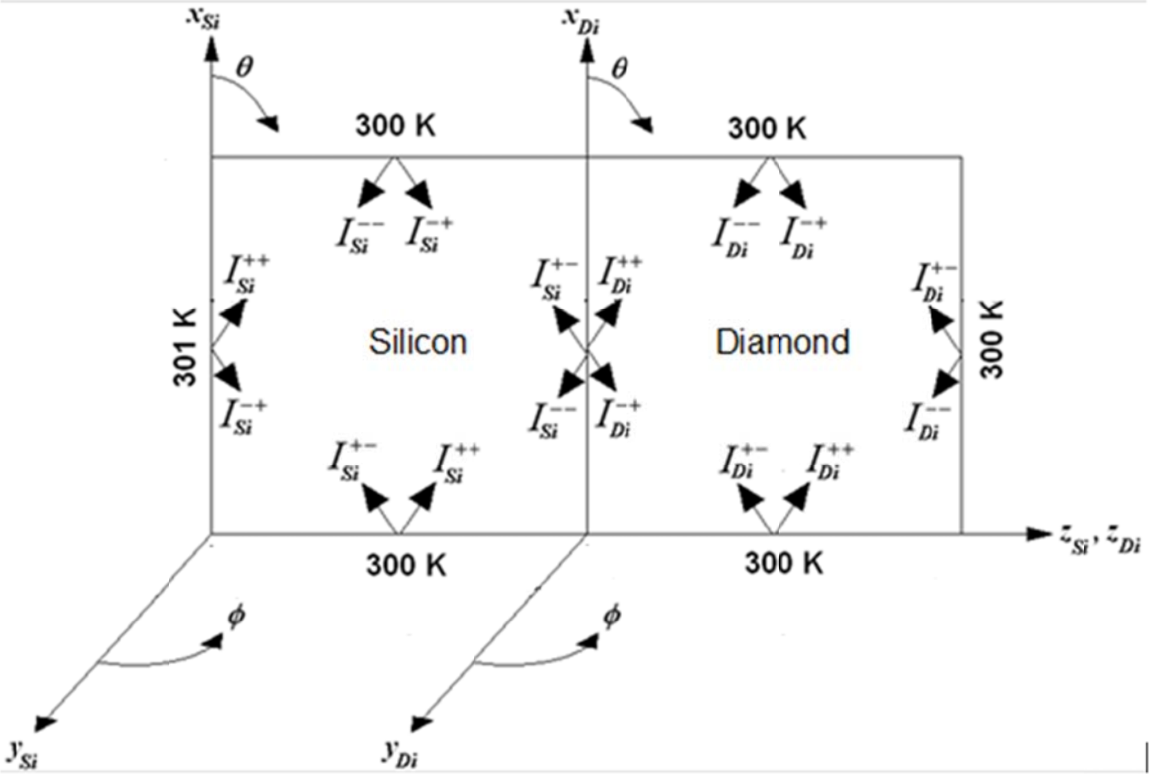

Figure 3.9 Schematic view of emitted, transmitted, and reflected phonon intensities at the boundaries.

Diffuse Mismatch Model:

In the diffuse mismatch model, the intensities are integrated over all frequencies and then applied the energy balance at the interface [126]. In this case, energy transfer is considered independent of frequencies [126]. Therefore, all phonon at the silicon film interface can possibly transfer their energy to the diamond film interface irrespective of the phonon frequency mismatch.

Heat fluxes at the interface can be written as:

$$q''^{+}_{z,Si}(x_{Si}, z_{Si} = L_{z,Si}, t) = \int_0^{\omega_{\max,\mathrm{Si}}} \left(\begin{array}{l} \int_0^{\pi}\int_0^{\pi/2} I^{++}_{Si,\omega} \sin\phi \sin^2\theta d\theta\, d\phi \\ +\int_0^{\pi}\int_{\pi/2}^{\pi} I^{-+}_{Si,\omega} \sin\phi \sin^2\theta d\theta\, d\phi \end{array} \right) d\omega \tag{3.112}$$

and

$$q''^{-}_{z,Si}(x_{Si}, z_{Si} = L_{z,Si}, t) = \int_0^{\omega_{\max,\mathrm{Si}}} \left(\begin{array}{l} \int_{\pi}^{2\pi}\int_0^{\pi/2} I^{+-}_{Si,\omega} \sin\phi \sin^2\theta d\theta\, d\phi \\ +\int_{\pi}^{2\pi}\int_{\pi/2}^{\pi} I^{--}_{Si,\omega} \sin\phi \sin^2\theta d\theta\, d\phi \end{array} \right) d\omega \tag{3.113}$$

and

$$q''^{+}_{z,Di}(x_{Di}, z_{Di} = 0, t) = \int_0^{\omega_{\max,\mathrm{Di}}} \left(\begin{array}{l} \int_0^{\pi}\int_0^{\pi/2} I^{++}_{Di,\omega} \sin\phi \sin^2\theta d\theta\, d\phi \\ +\int_0^{\pi}\int_{\pi/2}^{\pi} I^{-+}_{Di,\omega} \sin\phi \sin^2\theta d\theta\, d\phi \end{array} \right) d\omega \tag{3.114}$$

and

$$q^{''-}_{z,Di}(x_{Di}, z_{Di}=0,t)=\int_0^{\omega_{\max,\mathrm{Di}}}\left(\begin{array}{l}\int_{\pi}^{2\pi}\int_0^{\pi/2} I^{+-}_{Di,\omega}\sin\phi\sin^2\theta d\theta d\phi \\ +\int_{\pi}^{2\pi}\int_{\pi/2}^{\pi} I^{--}_{Di,\omega}\sin\phi\sin^2\theta d\theta d\phi\end{array}\right)d\omega \qquad (3.115)$$

where, $I^{++/--/+-/-+}_{Si/Di,\omega}$ is sum of all frequency branches and modes. For example $I^{++}_{Si,\omega}$ is:

$$I^{++}_{Si,\omega}=I^{++}_{LA,Si,\omega}+2I^{++}_{TA,Si,\omega}+I^{++}_{LO,Si,\omega}+2I^{++}_{TO,Si,\omega} \qquad (3.116)$$

Using the energy balance at the interface, one can write the outgoing heat fluxes at the interface in terms of incoming heat fluxes

$$q^{''-}_{z,Si}=T_{Di-Si}\,q^{''-}_{z,Di}-R_{Si-Di}\,q^{''+}_{z,Si} \qquad (3.117)$$

$$q^{''+}_{z,Di}=T_{Si-Di}\,q^{''+}_{z,Si}-R_{Di-Si}\,q^{''-}_{z,Di} \qquad (3.118)$$

where, T is the transmittance and R is used for the reflectance at the interface. Here, the subscript *Si-Di* indicates from silicon to diamond and *Di-Si* indicates from diamond to silicon.

Considering the diffuse scattering and utilizing the equation (3.117) and equation (3.118) with equation (3.113) and (3.114) one can get the following relations:

$$I^{--}_{Si,\omega}=I^{+-}_{Si,\omega}=\frac{1}{\pi\omega_{\max,Si}}\left[-T_{Di-Si}\,q^{''-}_{z,Di}+R_{Si-Di}\,q^{''+}_{z,Si}\right] \qquad (3.119)$$

and

$$I_{Di,\omega}^{++} = I_{Di,\omega}^{-+} = \frac{1}{\pi\omega_{\max,Di}}\left[T_{Si-Di}\, q_{z,Si}^{"+} - R_{Di-Si}\, q_{z,Di}^{"-}\right] \tag{3.120}$$

The outgoing intensities $I_{Si,\omega}^{--/+-}$ and $I_{Di,\omega}^{++/-+}$, which can be calculated form equation (3.119) and (3.120), are distributed among different frequency modes and branches using:

$$I_{Si,ij,\omega}^{--/+-} = \frac{C_{Si,ij,\omega} v_{Si,ij,\omega} \omega_{\max,Si}}{\left\langle C_{Si} v_{Si} \right\rangle} I_{Si,\omega}^{--/+-} \tag{3.121}$$

where,

$$\left\langle C_{Si} v_{Si} \right\rangle = \int_0^{\omega_{\max}} \begin{pmatrix} C_{Si,LA}(\omega) v_{Si,LA}(\omega) + 2C_{Si,TA}(\omega) v_{Si,TA}(\omega) + \\ C_{Si,LO}(\omega) v_{Si,LO}(\omega) + 2C_{Si,LO}(\omega) v_{Si,LO}(\omega) \end{pmatrix} d\omega \tag{3.122}$$

and

$$I_{Di,ij,\omega}^{++/-+} = \frac{C_{Di,ij,\omega} v_{Di,ij,\omega} \omega_{\max,Di}}{\left\langle C_{Di} v_{Di} \right\rangle} I_{Di,\omega}^{++/-+} \tag{3.123}$$

where,

$$\left\langle C_{Di} v_{Di} \right\rangle = \int_0^{\omega_{\max}} \begin{pmatrix} C_{Di,LA}(\omega) v_{Di,LA}(\omega) + 2C_{Di,TA}(\omega) v_{Di,TA}(\omega) + \\ C_{Di,LO}(\omega) v_{Di,LO}(\omega) + 2C_{Di,LO}(\omega) v_{Di,LO}(\omega) \end{pmatrix} d\omega \tag{3.124}$$

where, in equation (3.121) and(3.123), $i = T$ represents the Transverse mode and $i = L$ stands for Longitudinal mode. In addition, $j = A$ corresponds to Acoustic and $j = O$ stands for and Optical phonons.

The transmittance and reflectance are calculated based on the energy conservation at the interface. In this case, energy conservation gives:

$$T_{Si-Di}\left\langle C_{Si}v_{Si}\right\rangle = T_{Di-Si}\left\langle C_{Di}v_{Di}\right\rangle \tag{3.125}$$

The diffuse mismatch model gives:

$$T_{Si-Di} = 1 - T_{Di-Si} \tag{3.126}$$

Simultaneous solution of the above two equations yields the transmissions:

$$T_{Si-Di} = \frac{\left\langle C_{Di}v_{Di}\right\rangle}{\left\langle C_{Di}v_{Di}\right\rangle + \left\langle C_{Si}v_{Si}\right\rangle} \tag{3.127}$$

and

$$T_{Si-Di} = \frac{\left\langle C_{Si}v_{Si}\right\rangle}{\left\langle C_{Di}v_{Di}\right\rangle + \left\langle C_{Si}v_{Si}\right\rangle} \tag{3.128}$$

The reflectance can be written as:

$$R_{Di-Si} = 1 - T_{Di-Si} \tag{3.129}$$

and

$$R_{Si-Di} = 1 - T_{Si-Di} \tag{3.130}$$

Cut-off Mismatch Model

In the cut-off mismatch model, the mismatch due the frequency and branch is considered. Figure 3.10 is showing the optical branches frequencies of silicon not matching with the optical branches frequencies of diamond. Therefore longitudinal and transverse optical branches phonons of both layers are reflected from the interface i.e. transmittance becomes zero. Similarly, above the cut-off frequency, the transmittance remains zero for longitudinal and transverse acoustic branches of phonons in the diamond thin film, as shown is Figure 3.10. One can, therefore, apply the energy balance at each frequency.

Heat fluxes at the interface can be written as:

$$q''^{+}_{z,Si,ij,\omega}(x_{Si}, z_{Si} = L_{z,Si}, t) = \begin{cases} \int_0^{\pi}\int_0^{\pi/2} I^{++}_{Si,ij,\omega} \sin\phi \sin^2\theta d\theta\, d\phi \\ +\int_0^{\pi}\int_{\pi/2}^{\pi} I^{-+}_{Si,ij,\omega} \sin\phi \sin^2\theta d\theta\, d\phi \end{cases} \tag{3.131}$$

and

$$q''^{-}_{z,Si,ij,\omega}(x_{Si}, z_{Si} = L_{z,Si}, t) = \begin{cases} \int_{\pi}^{2\pi}\int_0^{\pi/2} I^{+-}_{Si,ij,\omega} \sin\phi \sin^2\theta d\theta\, d\phi \\ +\int_{\pi}^{2\pi}\int_{\pi/2}^{\pi} I^{--}_{Si,ij,\omega} \sin\phi \sin^2\theta d\theta\, d\phi \end{cases} \tag{3.132}$$

and

$$q''^{+}_{z,Di,ij,\omega}(x_{Di}, z_{Di} = 0, t) = \begin{cases} \int_0^{\pi}\int_0^{\pi/2} I^{++}_{Di,ij,\omega} \sin\phi \sin^2\theta d\theta\, d\phi \\ +\int_0^{\pi}\int_{\pi/2}^{\pi} I^{-+}_{Di,ij,\omega} \sin\phi \sin^2\theta d\theta\, d\phi \end{cases} \tag{3.133}$$

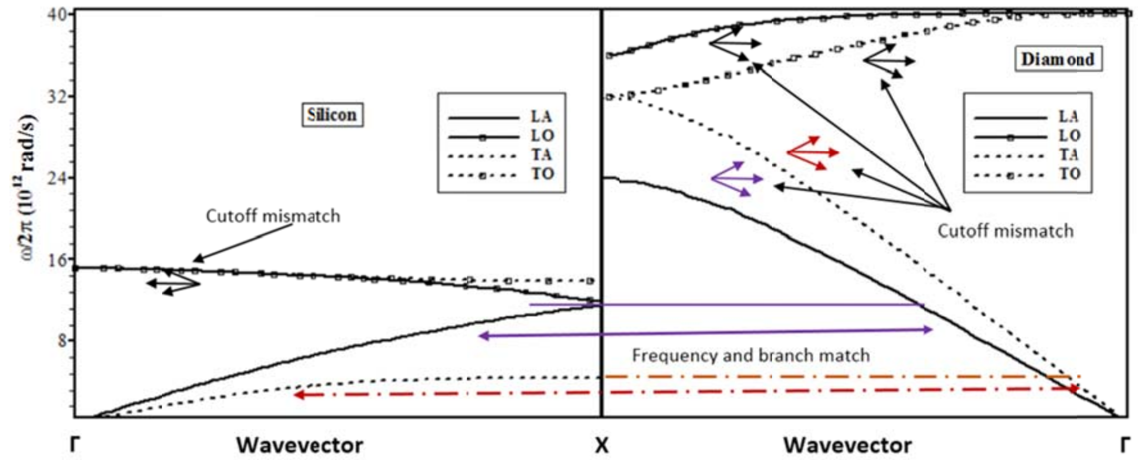

Figure 3.10 Dispersion relations for silicon and diamond films and wavevectors for cut-off mismatch [112] and [113].

.

and

$$q''^{-}_{z,Di,ij,\omega}(x_{Di}, z_{Di} = 0, t) = \begin{cases} \int_{\pi}^{2\pi} \int_{0}^{\pi/2} I^{+-}_{Di,ij,\omega} \sin\phi \sin^2\theta d\theta\, d\phi \\ + \int_{\pi}^{2\pi} \int_{\pi/2}^{\pi} I^{--}_{Di,ij,\omega} \sin\phi \sin^2\theta d\theta\, d\phi \end{cases} \tag{3.134}$$

where, subscript ω is used to indicate that these equation written for each frequency of the phonons, $i = T$ represents the transverse mode and $i = L$ stands for longitudinal mode. In addition, $j = A$ corresponds to acoustic and $j = O$ stands for and optical phonons.

Using the energy balance at the interface, one can write the outgoing heat fluxes at the interface for each frequency in terms of incoming heat fluxes, i.e.

$$q''^{-}_{z,Si,ij,\omega} = T_{Di-Si,ij,\omega} q''^{-}_{z,Di,ij,\omega} - R_{Si-Di,ij,\omega} q''^{+}_{z,Si,ij,\omega} \tag{3.135}$$

and

$$q''^{+}_{z,Di,ij,\omega} = T_{Si-Di,ij,\omega} q''^{+}_{z,Si,ij,\omega} - R_{Di-Si,ij,\omega} q''^{-}_{z,Di,ij,\omega} \tag{3.136}$$

where, T is the transmittance and R is used for the reflectance at the interface. Here, the subscript *Si-Di* indicates from silicon to diamond and *Di-Si* indicates from diamond to silicon.

Considering the diffuse scattering and utilizing the equation (3.135) and equation (3.136) along with equation (3.132) and equation (3.133) one can get the following relations:

$$I^{--}_{Si,ij,\omega} = I^{+-}_{Si,ij,\omega} = \frac{1}{\pi}\left[-T_{Di-Si,ij,\omega}\, q^{''-}_{z,ij,Di,\omega} + R_{Si-Di,ij,\omega}\, q^{''+}_{z,Si,ij,\omega}\right] \tag{3.137}$$

and

$$I^{++}_{Di,ij,\omega} = I^{-+}_{Di,ij,\omega} = \frac{1}{\pi}\left[T_{Si-Di,ij,\omega}\, q^{''+}_{z,Si,ij,\omega} - R_{Di-Si,ij,\omega}\, q^{''-}_{z,Di,ij,\omega}\right] \tag{3.138}$$

The transmittance and reflectance can be calculated form the following relations:

$$T_{Si-Di,ij,\omega} = \frac{C_{Di,ij,\omega} v_{Di,ij,\omega}}{C_{Di,ij,\omega} v_{Di,ij,\omega} + C_{Si,ij,\omega} v_{Si,ij,\omega}} \tag{3.139}$$

and

$$T_{Di-Si,ij,\omega} = \frac{C_{Si,ij,\omega} v_{Si,ij,\omega}}{C_{Di,ij,\omega} v_{Di,ij,\omega} + C_{Si,ij,\omega} v_{Si,ij,\omega}} \tag{3.140}$$

The reflectance can be determined from:

$$R_{Di-Si,ij,\omega} = 1 - T_{Di-Si,ij,\omega} \tag{3.141}$$

and

$$R_{Si-Di,ij,\omega} = 1 - T_{Si-Di,ij,\omega} \tag{3.142}$$

Thermal Boundary Resistance:

The thermal boundary resistance at the interface can be defined as:

$$TBR = \frac{\Delta T_{eq,Si-Di}}{q''_{z,interface}} \tag{3.143}$$

In equation (3.143) $\Delta T_{eq.,Si-Di} = T_{eq.,Si} - T_{eq.,Di}$ which is the equivalent equilibrium temperature difference at the interface for silicon and diamond thin films and $q''_{z,interface}$ is the heat flux at the interface.

$$q''_{z,interface} = q''_{z,Si}(x_{Si}, z_{Si} = L_{z,Si}, t) = q''_{z,Di}(x_{Di}, z_{Di} = 0, t) \tag{3.144}$$

In order to assessment of the phonon transport across thin film pairs incorporating the cut-off mismatch and diffusive mismatch models, a ratio of equilibrium intensities by two models are introduced, which is given by,

$$\eta_{LA} = \frac{\left(I^0_{Si/Di,\,LA}\right)_{CMM}}{\left(I^0_{Si/Di,LA}\right)_{DMM}} \tag{3.145}$$

and

$$\eta_{TA} = \frac{\left(I^0_{Si/Di,TA}\right)_{CMM}}{\left(I^0_{Si/Di,TA}\right)_{DMM}} \tag{3.146}$$

where $I^0_{Si/Di,\,LA}$ represents the equilibrium intensities for longitudinal acoustic branch of phonons for Silicon/Diamond and $I^0_{Si/Diamond\,,TA}$ represents the equilibrium intensities for transverse acoustic branch of phonons for Silicon/Diamond. Equilibrium intensities are calculated as,

$$I^0_{Si/Di,\,LA/TA} = \int_0^{\omega_{\max}} I^0_{Si/Di,\,LA/TA,\omega} d\omega \tag{3.147}$$

3.5.7 Transient Heat Transport Including Quantum Dot in Silicon Thin Film

The study is conducted to investigate the heat transport characteristics in silicon film with the presence quantum dot in the center of the film. The physical domain consists of the aluminum quantum dot in the center region of silicon, as shown in Figure 3.10. In the aluminum quantum dot no spatial variation of temperature is considered. In this study interface thermal resistance between the edges of quantum dot (aluminum) and silicon is neglected. The EPRT is solved for phonon transport in the silicon site of physical domain. In order to get the solution of domain, which is shown in Figure 3.11, it is divided into four sub-domains as appears in Figure 3.12. Each sub-domain can be considers as a rectangular geometry. Therefore, mathematical formulation provided earlier is applicable on each sub-domain.

It is considered the whole domain initially at 300 K. Then, after that all outer edge boundary of computational domain is at 300 K and time dependent exponentially varying temperature disturbance as shown in

Figure 3.13, is introduced at inner surface of computational domain which is attached with quantum dot as shown in Figure 3.12Figure . In order to complete the problem specification, the initial and boundary for each sub domain is provided with interface condition. For the solution of complete silicon domain, interface conditions are incorporated to connect all sub domains. For stable numerical solution of phonon intensity I divided into four portions I^{++}, I^{+-}, I^{-+} *and* I^{--} (details are given in numerical section). Following are the initial boundary and interface conditions which incorporated in computation.

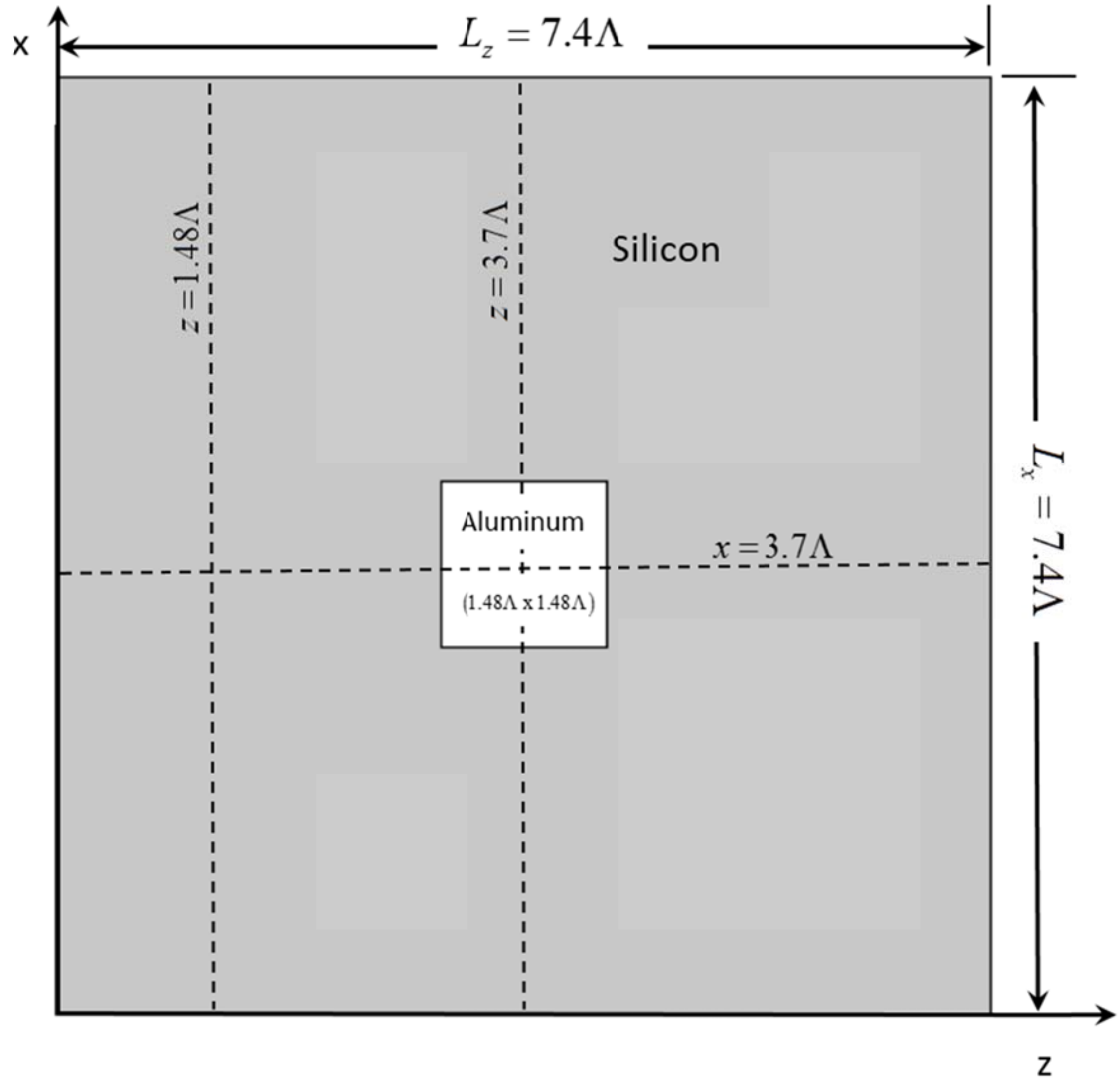

Figure 3.11 Schematic view of quantum dot of aluminum in silicon film, where Λ is the mean free path of silicon corresponding to the gray medium

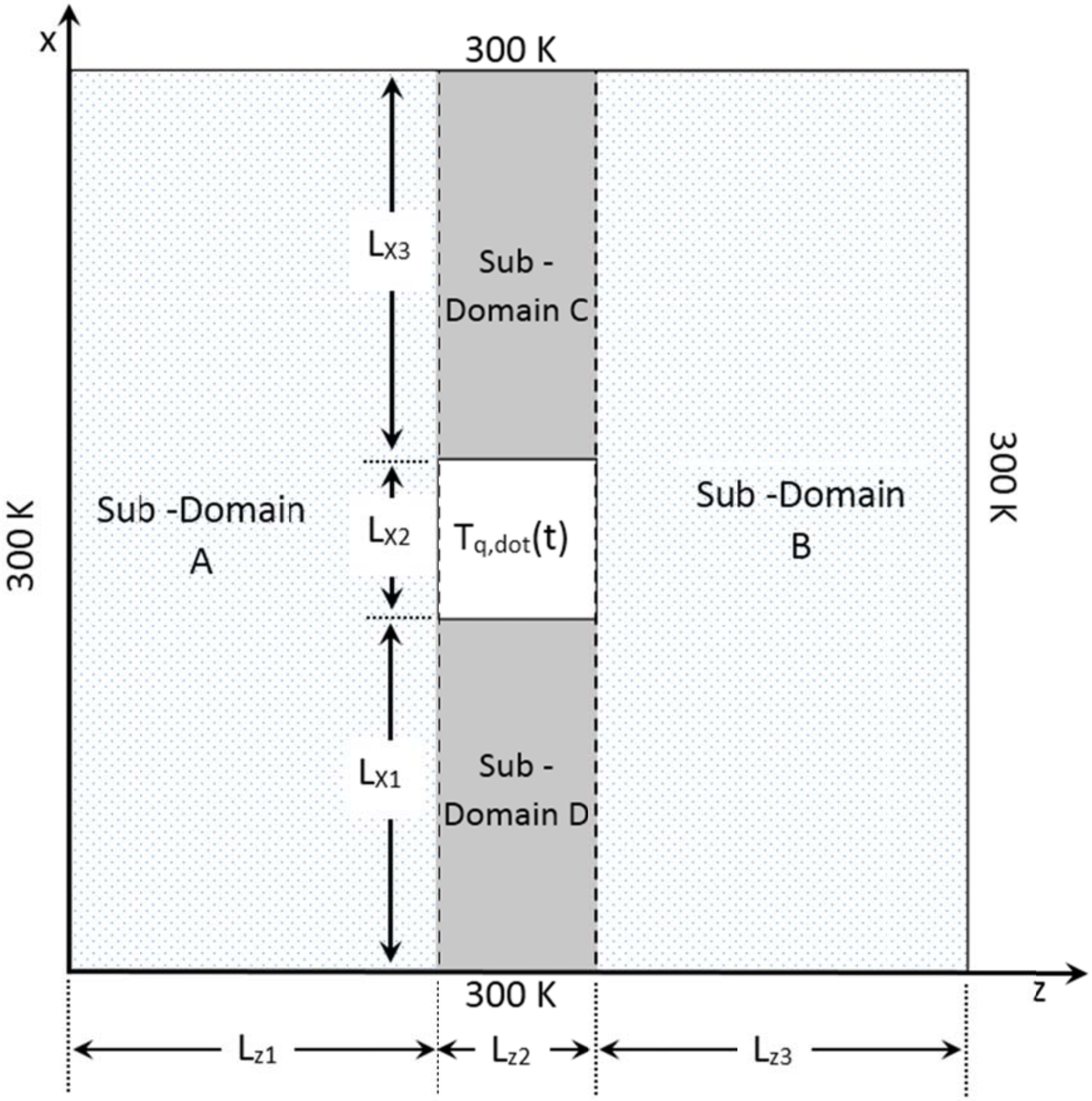

Figure 3.12 Schematic diagram showing all the sub-domain used in computation.

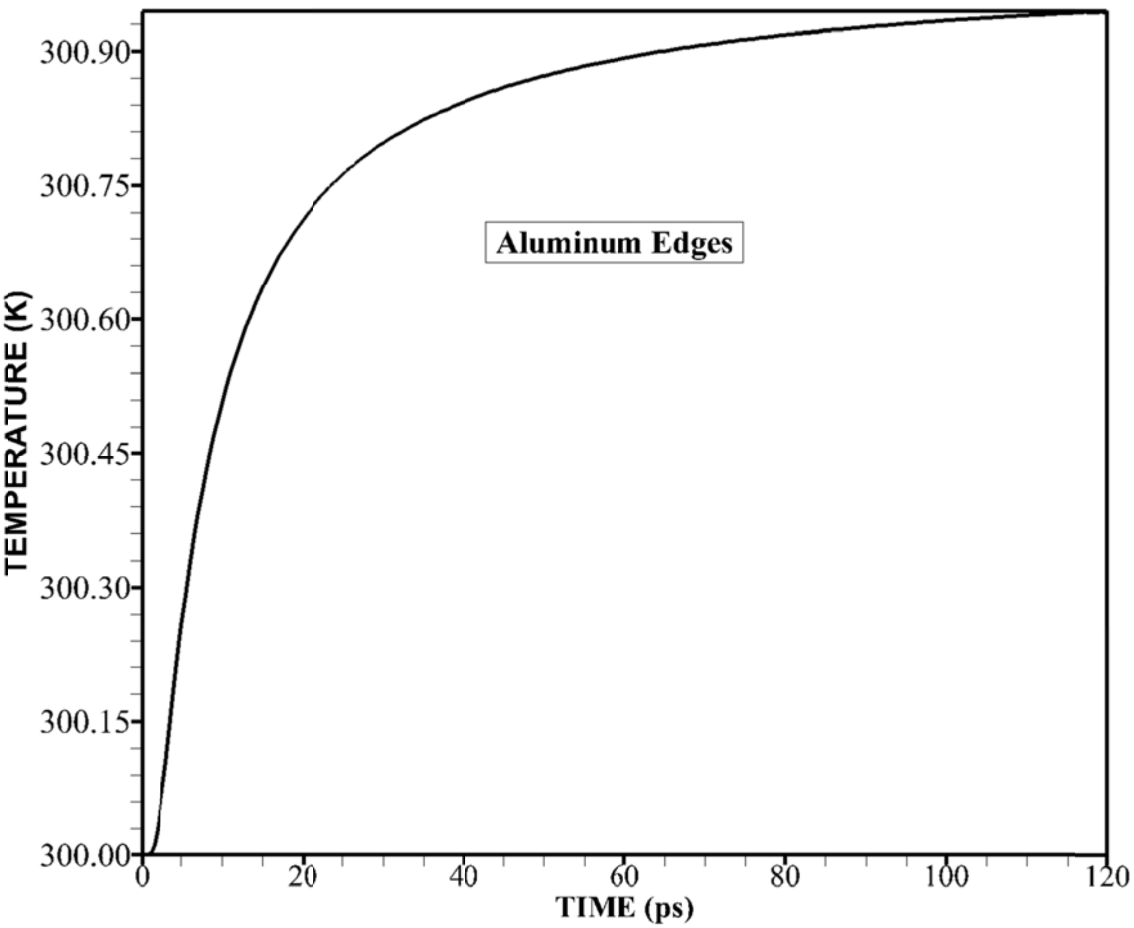

Figure 3.13 Temporal variation at the edges of quantum dot (aluminum edges).

Sub-domain A:

Initial Conditions:

The physical domain initialized at 300 K. The following initial condition are incorporated in the domain,

$$\begin{aligned}
I_{A,LA,k}\left(x_A, z_A, \theta, \phi, t=0\right) &= \frac{C_{LA,k} v_{LA,k} T_{\text{initial}}}{4\pi} \\
I_{A,TA,k}\left(x_A, z_A, \theta, \phi, t=0\right) &= \frac{C_{TA,k} v_{TA,k} T_{\text{initial}}}{4\pi} \qquad 0 < x_A < L_{A,x}, 0 < z_A < L_{A,z}, \\
I_{A,LO,k}\left(x_A, z_A, \theta, \phi, t=0\right) &= \frac{C_{LO,k} v_{LO,k} T_{\text{initial}}}{4\pi} \qquad 0 < \theta < \pi, \quad 0 < \phi < 2\pi \\
I_{A,TO,k}\left(x_A, z_A, \theta, \phi, t=0\right) &= \frac{C_{TO,k} v_{TO,k} T_{\text{initial}}}{4\pi}
\end{aligned} \tag{3.148}$$

Boundary Conditions:

Bottom Boundary:

$$\begin{aligned}
I_{A,LA,k}\left(x_A = 0, z_A,, \theta, \phi, t\right) &= \frac{C_{LA,k} v_{LA,k} T_{bottom}}{4\pi} \\
I_{A,TA,k}\left(x_A = 0, z_A,, \theta, \phi, t\right) &= \frac{C_{TA,k} v_{TA,k} T_{bottom}}{4\pi} \qquad t > 0, \quad 0 < z_A < L_{A,z}, \\
I_{A,LO,k}\left(x_A = 0, z_A,, \theta, \phi, t\right) &= \frac{C_{LO,k} v_{LO,k} T_{bottom}}{4\pi} \qquad 0 < \theta < \pi/2, \quad 0 < \phi < 2\pi \\
I_{A,TO,k}\left(x_A = 0, z_A,, \theta, \phi, t\right) &= \frac{C_{TO,k} v_{TO,k} T_{bottom}}{4\pi}
\end{aligned} \tag{3.149}$$

Top Boundary:

$$\begin{aligned}
I_{A,LA,k}\left(x_A = L_{A,x}, z_A,, \theta, \phi, t\right) &= \frac{C_{LA,k} v_{LA,k} T_{top}}{4\pi} \\
I_{A,TA,k}\left(x_A = L_{A,x}, z_A,, \theta, \phi, t\right) &= \frac{C_{TA,k} v_{TA,k} T_{top}}{4\pi} \\
I_{A,LO,k}\left(x_A = L_{A,x}, z_A,, \theta, \phi, t\right) &= \frac{C_{LO,k} v_{LO,k} T_{top}}{4\pi} \\
I_{A,TO,k}\left(x_A = L_{A,x}, z_A,, \theta, \phi, t\right) &= \frac{C_{TO,k} v_{TO,k} T_{top}}{4\pi}
\end{aligned}
\qquad
\begin{aligned}
&t > 0, \quad 0 < z_A < L_{A,z} \\
&\pi/2 < \theta < \pi, \quad 0 < \phi < 2\pi
\end{aligned}
\qquad (3.150)$$

Left Boundary:

$$\begin{aligned}
I_{A,LA,k}\left(x_A, z_A = 0, \theta, \phi, t\right) &= \frac{C_{LA,k} v_{LA,k} T_{left}}{4\pi} \\
I_{A,TA,k}\left(x_A, z_A = 0, \theta, \phi, t\right) &= \frac{C_{TA,k} v_{TA,k} T_{left}}{4\pi} \\
I_{A,LO,k}\left(x_A, z_A = 0, \theta, \phi, t\right) &= \frac{C_{LO,k} v_{LO,k} T_{left}}{4\pi} \\
I_{A,TO,k}\left(x_A, z_A = 0, \theta, \phi, t\right) &= \frac{C_{TO,k} v_{TO,k} T_{left}}{4\pi}
\end{aligned}
\qquad
\begin{aligned}
&t > 0, \quad 0 < x_A < L_{A,x}, \\
&0 < \theta < \pi, \quad 0 < \phi < \pi
\end{aligned}
\qquad (3.151)$$

Right Boundary:

$$\begin{aligned}
I_{A,LA,k}\left(x_A, z_A = L_{A,z}, \theta, \phi, t\right) &= \frac{C_{LA,k} v_{LA,k} T_{q,dot}(t)}{4\pi} \\
I_{A,TA,k}\left(x_A, z_A = L_{A,z}, \theta, \phi, t\right) &= \frac{C_{TA,k} v_{TA,k} T_{q,dot}(t)}{4\pi} \\
I_{A,LO,k}\left(x_A, z_A = L_{A,z}, \theta, \phi, t\right) &= \frac{C_{LO,k} v_{LO,k} T_{q,dot}(t)}{4\pi} \\
I_{A,TO,k}\left(x_A, z_A = L_{A,z}, \theta, \phi, t\right) &= \frac{C_{TO,k} v_{TO,k} T_{q,dot}(t)}{4\pi}
\end{aligned}
\qquad
\begin{aligned}
&t > 0, L_{x1} < x_A < L_{x1} + L_{x2}, \\
&0 < \theta < \pi, \quad 0 < \phi < \pi
\end{aligned}
\qquad (3.152)$$

where, $T_{q,dot}(t) = \left(300 + e^{(-6.8/t)}\right) K$, t is in ps. The variation of $T_{q,dot}$ is shown in

Figure 3.13.

Interface Conditions:

Right Interface (Upper Portion)

$$\begin{aligned}
I^{+-}_{A,LA,k}\left(x_A, z_A = L_{A,z}, \theta, \phi, t\right) &= I^{+-}_{C,LA,k}\left(x_C, z_C = 0, \theta, \phi, t\right)\\
I^{+-}_{A,TA,k}\left(x_A, z_A = L_{A,z}, \theta, \phi, t\right) &= I^{+-}_{C,TA,k}\left(x_C, z_C = 0, \theta, \phi, t\right)\\
I^{+-}_{A,LO,k}\left(x_A, z_A = L_{A,z}, \theta, \phi, t\right) &= I^{+-}_{C,LO,k}\left(x_C, z_C = 0, \theta, \phi, t\right)\\
I^{+-}_{A,TO,k}\left(x_A, z_A = L_{A,z}, \theta, \phi, t\right) &= I^{+-}_{C,TO,k}\left(x_C, z_C = 0, \theta, \phi, t\right)
\end{aligned} \tag{3.153}$$

and

$$\begin{aligned}
I^{--}_{A,LA,k}\left(x_A, z_A = L_{A,z}, \theta, \phi, t\right) &= I^{--}_{C,LA,k}\left(x_C, z_C = 0, \theta, \phi, t\right)\\
I^{--}_{A,TA,k}\left(x_A, z_A = L_{A,z}, \theta, \phi, t\right) &= I^{--}_{C,TA,k}\left(x_C, z_C = 0, \theta, \phi, t\right)\\
I^{--}_{A,LO,k}\left(x_A, z_A = L_{A,z}, \theta, \phi, t\right) &= I^{--}_{C,LO,k}\left(x_C, z_C = 0, \theta, \phi, t\right)\\
I^{--}_{A,TO,k}\left(x_A, z_A = L_{A,z}, \theta, \phi, t\right) &= I^{--}_{C,TO,k}\left(x_C, z_C = 0, \theta, \phi, t\right)
\end{aligned} \tag{3.154}$$

where, $t > 0, \quad , 0 < x_C < L_{C,x},\ L_{x1} + L_{x2} < x_A < L_{A,x}\ , 0 < \theta < \pi/2, 0 < \phi < 2\pi.$

Right Interface (Lower Portion)

$$\begin{aligned}
I^{+-}_{A,LA,k}\left(x_A, z_A = L_{A,z}, \theta, \phi, t\right) &= I^{+-}_{D,LA,k}\left(x_D, z_D = 0, \theta, \phi, t\right)\\
I^{+-}_{A,TA,k}\left(x_A, z_A = L_{A,z}, \theta, \phi, t\right) &= I^{+-}_{D,TA,k}\left(x_D, z_D = 0, \theta, \phi, t\right)\\
I^{+-}_{A,LO,k}\left(x_A, z_A = L_{A,z}, \theta, \phi, t\right) &= I^{+-}_{D,LOA,k}\left(x_D, z_D = 0, \theta, \phi, t\right)\\
I^{+-}_{A,TO,k}\left(x_A, z_A = L_{A,z}, \theta, \phi, t\right) &= I^{+-}_{D,TO,k}\left(x_D, z_D = 0, \theta, \phi, t\right)
\end{aligned} \tag{3.155}$$

and

$$\begin{aligned}
I^{--}_{A,LA,k}\left(x_A, z_A = L_{A,z}, \theta, \phi, t\right) &= I^{--}_{D,LA,k}\left(x_D, z_D = 0, \theta, \phi, t\right) \\
I^{--}_{A,TA,k}\left(x_A, z_A = L_{A,z}, \theta, \phi, t\right) &= I^{--}_{D,TA,k}\left(x_D, z_D = 0, \theta, \phi, t\right) \\
I^{--}_{A,LO,k}\left(x_A, z_A = L_{A,z}, \theta, \phi, t\right) &= I^{--}_{D,LO,k}\left(x_D, z_D = 0, \theta, \phi, t\right) \\
I^{--}_{A,TO,k}\left(x_A, z_A = L_{A,z}, \theta, \phi, t\right) &= I^{--}_{D,TO,k}\left(x_D, z_D = 0, \theta, \phi, t\right)
\end{aligned} \tag{3.156}$$

where, $t > 0, 0 < x_D < L_{D,x}, 0 < x_A < L_{x1}, 0 < \theta < \pi/2, 0 < \phi < 2\pi.$

<u>Sub-domain B:</u>

<u>Initial Conditions:</u>

$$\begin{aligned}
I_{B,LA,k}\left(x_B, z_B, \theta, \phi, t = 0\right) &= \frac{C_{LA,k} v_{LA,k} T_{\text{initial}}}{4\pi} \\
I_{B,TA,k}\left(x_B, z_B, \theta, \phi, t = 0\right) &= \frac{C_{TA,k} v_{TA,k} T_{\text{initial}}}{4\pi} \\
I_{B,LO,k}\left(x_B, z_B, \theta, \phi, t = 0\right) &= \frac{C_{LO,k} v_{LO,k} T_{\text{initial}}}{4\pi} \\
I_{B,TO,k}\left(x_B, z_B, \theta, \phi, t = 0\right) &= \frac{C_{TO,k} v_{TO,k} T_{\text{initial}}}{4\pi}
\end{aligned} \qquad \begin{aligned} &0 < x_B < L_{B,x}, 0 < z_B < L_{B,z}, \\ &0 < \theta < \pi, \quad 0 < \phi < 2\pi \end{aligned} \tag{3.157}$$

<u>Boundary Conditions:</u>

Bottom Boundary:

$$\begin{aligned}
I_{B,LA,k}\left(x_B = 0, z_B,, \theta, \phi, t\right) &= \frac{C_{LA,k} v_{LA,k} T_{bottom}}{4\pi} \\
I_{B,TA,k}\left(x_B = 0, z_B,, \theta, \phi, t\right) &= \frac{C_{TA,k} v_{TA,k} T_{bottom}}{4\pi} \\
I_{B,LO,k}\left(x_B = 0, z_B,, \theta, \phi, t\right) &= \frac{C_{LO,k} v_{LO,k} T_{bottom}}{4\pi} \\
I_{B,TO,k}\left(x_B = 0, z_B,, \theta, \phi, t\right) &= \frac{C_{TO,k} v_{TO,k} T_{bottom}}{4\pi}
\end{aligned} \qquad \begin{aligned} &t > 0, \quad 0 < z_B < L_{B,z}, \\ &0 < \theta < \pi/2, \quad 0 < \phi < 2\pi \end{aligned} \tag{3.158}$$

Top Boundary:

$$\begin{aligned}
&I_{B,LA,k}\left(x_B = L_{B,x}, z_B,, \theta, \phi, t\right) = \frac{C_{LA,k} v_{LA,k} T_{top}}{4\pi} \\
&I_{B,TA,k}\left(x_B = L_{B,x}, z_B,, \theta, \phi, t\right) = \frac{C_{TA,k} v_{TA,k} T_{top}}{4\pi} \qquad t > 0, \quad 0 < z_B < L_{B,z} \\
&I_{B,LO,k}\left(x_B = L_{B,x}, z_B,, \theta, \phi, t\right) = \frac{C_{LO,k} v_{LO,k} T_{top}}{4\pi} \qquad \pi/2 < \theta < \pi, \quad 0 < \phi < 2\pi \\
&I_{B,TO,k}\left(x_B = L_{B,x}, z_B,, \theta, \phi, t\right) = \frac{C_{TO,k} v_{TO,k} T_{top}}{4\pi}
\end{aligned} \tag{3.159}$$

Left Boundary:

$$\begin{aligned}
&I_{B,LA,k}\left(x_B, z_B = 0, \theta, \phi, t\right) = \frac{C_{LA,k} v_{LA,k} T_{q,dot}(t)}{4\pi} \\
&I_{B,TA,k}\left(x_B, z_B = 0, \theta, \phi, t\right) = \frac{C_{TA,k} v_{TA,k} T_{q,dot}(t)}{4\pi} \qquad t > 0, \quad L_{x1} < x_B < L_{x1} + L_{x2}, \\
&I_{B,LO,k}\left(x_B, z_B = 0, \theta, \phi, t\right) = \frac{C_{LO,k} v_{LO,k} T_{q,dot}(t)}{4\pi} \qquad 0 < \theta < \pi, \quad 0 < \phi < \pi \\
&I_{B,TO,k}\left(x_B, z_B = 0, \theta, \phi, t\right) = \frac{C_{TO,k} v_{TO,k} T_{q,dot}(t)}{4\pi}
\end{aligned} \tag{3.160}$$

where, $T_{q,dot}(t) = \left(300 + e^{(-6.8/t)}\right)K$, t is in ps . The variation of $T_{q,dot}$ is shown in Figure 3.13.

Right Boundary:

$$\begin{aligned}
&I_{B,LA,k}\left(x_B, z_B = L_{B,z}, \theta, \phi, t\right) = \frac{C_{LA,k} v_{LA,k} T_{right}}{4\pi} \\
&I_{B,TA,k}\left(x_B, z_B = L_{B,z}, \theta, \phi, t\right) = \frac{C_{TA,k} v_{TA,k} T_{right}}{4\pi} \qquad t > 0, \quad 0 < x_B < L_{B,x}, \\
&I_{B,LO,k}\left(x_B, z_B = L_{B,z}, \theta, \phi, t\right) = \frac{C_{LO,k} v_{LO,k} T_{right}}{4\pi} \qquad 0 < \theta < \pi, \quad 0 < \phi < \pi \\
&I_{B,TO,k}\left(x_B, z_B = L_{B,z}, \theta, \phi, t\right) = \frac{C_{TO,k} v_{TO,k} T_{right}}{4\pi}
\end{aligned} \tag{3.161}$$

Interface Conditions:

Left Interface (Upper Portion)

$$\begin{aligned}
I^{+-}_{B,LA,k}\left(x_B, z_B = L_{B,z}, \theta, \phi, t\right) &= I^{+-}_{C,LA,k}\left(x_C, z_C = L_{C,z}, \theta, \phi, t\right)\\
I^{+-}_{B,TA,k}\left(x_B, z_B = L_{B,z}, \theta, \phi, t\right) &= I^{+-}_{C,TA,k}\left(x_C, z_C = L_{C,z}, \theta, \phi, t\right)\\
I^{+-}_{B,LO,k}\left(x_B, z_B = L_{B,z}, \theta, \phi, t\right) &= I^{+-}_{C,LO,k}\left(x_C, z_C = L_{C,z}, \theta, \phi, t\right)\\
I^{+-}_{B,TO,k}\left(x_B, z_B = L_{B,z}, \theta, \phi, t\right) &= I^{+-}_{C,TO,k}\left(x_C, z_C = L_{C,z}, \theta, \phi, t\right)
\end{aligned} \tag{3.162}$$

and

$$\begin{aligned}
I^{--}_{B,LA,k}\left(x_B, z_B = L_{B,z}, \theta, \phi, t\right) &= I^{--}_{C,LA,k}\left(x_C, z_C = L_{C,z}, \theta, \phi, t\right)\\
I^{--}_{B,TA,k}\left(x_B, z_B = L_{B,z}, \theta, \phi, t\right) &= I^{--}_{C,TA,k}\left(x_C, z_C = L_{C,z}, \theta, \phi, t\right)\\
I^{--}_{B,LO,k}\left(x_B, z_B = L_{B,z}, \theta, \phi, t\right) &= I^{--}_{C,LO,k}\left(x_C, z_C = L_{C,z}, \theta, \phi, t\right)\\
I^{--}_{B,TO,k}\left(x_B, z_B = L_{B,z}, \theta, \phi, t\right) &= I^{--}_{C,TO,k}\left(x_C, z_C = L_{C,z}, \theta, \phi, t\right)
\end{aligned} \tag{3.163}$$

where, $t > 0, 0 < x_C < L_{C,x}, L_{x1} + L_{x2} < x_B < L_{B,x} 0 < \theta < \pi/2, \quad 0 < \phi < 2\pi..$

Left Interface (Lower Portion)

$$\begin{aligned}
I^{+-}_{B,LA,k}\left(x_B, z_B = L_{B,z}, \theta, \phi, t\right) &= I^{+-}_{D,LA,k}\left(x_D, z_D = L_{D,z}, \theta, \phi, t\right)\\
I^{+-}_{B,TA,k}\left(x_B, z_B = L_{B,z}, \theta, \phi, t\right) &= I^{+-}_{D,TA,k}\left(x_D, z_D = L_{D,z}, \theta, \phi, t\right)\\
I^{+-}_{B,LO,k}\left(x_B, z_B = L_{B,z}, \theta, \phi, t\right) &= I^{+-}_{D,LO,k}\left(x_D, z_D = L_{D,z}, \theta, \phi, t\right)\\
I^{+-}_{B,TO,k}\left(x_B, z_B = L_{B,z}, \theta, \phi, t\right) &= I^{+-}_{D,TO,k}\left(x_D, z_D = L_{D,z}, \theta, \phi, t\right)
\end{aligned} \tag{3.164}$$

and

$$\begin{aligned}
I^{--}_{B,LA,k}\left(x_B, z_B = L_{B,z}, \theta, \phi, t\right) &= I^{--}_{D,LA,k}\left(x_D, z_D = L_{D,z}, \theta, \phi, t\right)\\
I^{--}_{B,TA,k}\left(x_B, z_B = L_{B,z}, \theta, \phi, t\right) &= I^{--}_{D,TA,k}\left(x_D, z_D = L_{D,z}, \theta, \phi, t\right)\\
I^{--}_{B,LO,k}\left(x_B, z_B = L_{B,z}, \theta, \phi, t\right) &= I^{--}_{D,LO,k}\left(x_D, z_D = L_{D,z}, \theta, \phi, t\right)\\
I^{--}_{B,TO,k}\left(x_B, z_B = L_{B,z}, \theta, \phi, t\right) &= I^{--}_{D,TO,k}\left(x_D, z_D = L_{D,z}, \theta, \phi, t\right)
\end{aligned} \qquad (3.165)$$

where, $t > 0, 0 < x_D < L_{D,x}, 0 < x_B < L_{x1}, 0 < \theta < \pi/2, 0 < \phi < 2\pi..$

Sub-domain C:

Initial Conditions:

$$\begin{aligned}
I_{C,LA,k}\left(x_C, z_C, \theta, \phi, t = 0\right) &= \frac{C_{LA,k} v_{LA,k} T_{\text{initial}}}{4\pi}\\
I_{C,TA,k}\left(x_C, z_C, \theta, \phi, t = 0\right) &= \frac{C_{TA,k} v_{TA,k} T_{\text{initial}}}{4\pi}\\
I_{C,LO,k}\left(x_C, z_C, \theta, \phi, t = 0\right) &= \frac{C_{LO,k} v_{LO,k} T_{\text{initial}}}{4\pi}\\
I_{C,TO,k}\left(x_C, z_C, \theta, \phi, t = 0\right) &= \frac{C_{TO,k} v_{TO,k} T_{\text{initial}}}{4\pi}
\end{aligned} \qquad \begin{aligned} &0 < x_C < L_{C,x}, 0 < z_C < L_{C,z},\\ &0 < \theta < \pi, \quad 0 < \phi < 2\pi \end{aligned} \qquad (3.166)$$

Boundary Conditions:

Bottom Boundary:

$$\begin{aligned}
I_{C,LA,k}\left(x_C = 0, z_c, \theta, \phi, t\right) &= \frac{C_{LA,k} v_{LA,k} T_{q,dot}(t)}{4\pi}\\
I_{C,TA,k}\left(x_C = 0, z_c, \theta, \phi, t\right) &= \frac{C_{TA,k} v_{TA,k} T_{q,dot}(t)}{4\pi}\\
I_{C,LO,k}\left(x_C = 0, z_c, \theta, \phi, t\right) &= \frac{C_{LO,k} v_{LO,k} T_{q,dot}(t)}{4\pi}\\
I_{C,TO,k}\left(x_C = 0, z_c, \theta, \phi, t\right) &= \frac{C_{TO,k} v_{TO,k} T_{q,dot}(t)}{4\pi}
\end{aligned} \qquad \begin{aligned} &t > 0, \quad 0 < z_C < L_{C,z},\\ &0 < \theta < \pi/2, \quad 0 < \phi < 2\pi \end{aligned} \qquad (3.167)$$

where, $T_{q,dot}(t) = \left(300 + e^{(-6.8/t)}\right) K$ as shown in

Figure 3.13, t is in ps.

Top Boundary:

$$\begin{aligned}
I_{C,LA,k}\left(x_C = L_{C,x}, z_C, \theta, \phi, t\right) &= \frac{C_{LA,k} v_{LA,k} T_{top}}{4\pi} \\
I_{C,TA,k}\left(x_C = L_{C,x}, z_C, \theta, \phi, t\right) &= \frac{C_{TA,k} v_{TA,k} T_{top}}{4\pi} \\
I_{C,LO,k}\left(x_C = L_{C,x}, z_C, \theta, \phi, t\right) &= \frac{C_{LO,k} v_{LO,k} T_{top}}{4\pi} \\
I_{C,TO,k}\left(x_C = L_{C,x}, z_C, \theta, \phi, t\right) &= \frac{C_{TO,k} v_{TO,k} T_{top}}{4\pi}
\end{aligned}
\qquad
\begin{aligned}
&t > 0, \quad 0 < z_C < L_{C,z} \\
&\pi/2 < \theta < \pi, \quad 0 < \phi < 2\pi
\end{aligned}
\tag{3.168}$$

Interface Conditions:

Left Interface:

$$\begin{aligned}
I^{++}_{C,LA,k}\left(x_C, z_C = 0, \theta, \phi, t\right) &= I^{++}_{A,LA,k}\left(x_A, z_A = L_{A,z}, \theta, \phi, t\right) \\
I^{++}_{C,TA,k}\left(x_C, z_C = 0, \theta, \phi, t\right) &= I^{++}_{A,TA,k}\left(x_A, z_A = L_{A,z}, \theta, \phi, t\right) \\
I^{++}_{C,LO,k}\left(x_C, z_C = 0, \theta, \phi, t\right) &= I^{++}_{A,LO,k}\left(x_A, z_A = L_{A,z}, \theta, \phi, t\right) \\
I^{++}_{C,TO,k}\left(x_C, z_C = 0, \theta, \phi, t\right) &= I^{++}_{A,TO,k}\left(x_A, z_A = L_{A,z}, \theta, \phi, t\right)
\end{aligned}
\tag{3.169}$$

and

$$\begin{aligned}
I^{-+}_{C,LA,k}\left(x_C, z_C = 0, \theta, \phi, t\right) &= I^{-+}_{A,LA,k}\left(x_A, z_A = L_{A,z}, \theta, \phi, t\right) \\
I^{-+}_{C,TA,k}\left(x_C, z_C = 0, \theta, \phi, t\right) &= I^{-+}_{A,TA,k}\left(x_A, z_A = L_{A,z}, \theta, \phi, t\right) \\
I^{-+}_{C,LO,k}\left(x_C, z_C = 0, \theta, \phi, t\right) &= I^{-+}_{A,LO,k}\left(x_A, z_A = L_{A,z}, \theta, \phi, t\right) \\
I^{-+}_{C,TO,k}\left(x_C, z_C = 0, \theta, \phi, t\right) &= I^{-+}_{A,TO,k}\left(x_A, z_A = L_{A,z}, \theta, \phi, t\right)
\end{aligned}
\tag{3.170}$$

where, $t > 0, 0 < x_C < L_{C,x}, L_{x1} + L_{x2} < x_A < L_{A,x}, 0 < \theta < \pi/2, 0 < \phi < 2\pi.$

Right Interface:

$$\begin{aligned}
I^{+-}_{C,LA,k}\left(x_C, z_C = L_{C,z}, \theta, \phi, t\right) &= I^{+-}_{B,LA,k}\left(x_B, z_B = 0, \theta, \phi, t\right) \\
I^{+-}_{C,TA,k}\left(x_C, z_C = L_{C,z}, \theta, \phi, t\right) &= I^{+-}_{B,TA,k}\left(x_B, z_B = 0, \theta, \phi, t\right) \\
I^{+-}_{C,LO,k}\left(x_C, z_C = L_{C,z}, \theta, \phi, t\right) &= I^{+-}_{B,LO,k}\left(x_B, z_B = 0, \theta, \phi, t\right) \\
I^{+-}_{C,TO,k}\left(x_C, z_C = L_{C,z}, \theta, \phi, t\right) &= I^{+-}_{B,TO,k}\left(x_B, z_B = 0, \theta, \phi, t\right)
\end{aligned} \tag{3.171}$$

and

$$\begin{aligned}
I^{--}_{C,LA,k}\left(x_C, z_C = L_{C,z}, \theta, \phi, t\right) &= I^{--}_{B,LA,k}\left(x_B, z_B = 0, \theta, \phi, t\right) \\
I^{--}_{C,TA,k}\left(x_C, z_C = L_{C,z}, \theta, \phi, t\right) &= I^{--}_{B,TA,k}\left(x_B, z_B = 0, \theta, \phi, t\right) \\
I^{--}_{C,LO,k}\left(x_C, z_C = L_{C,z}, \theta, \phi, t\right) &= I^{--}_{B,LO,k}\left(x_B, z_B = 0, \theta, \phi, t\right) \\
I^{--}_{C,TO,k}\left(x_C, z_C = L_{C,z}, \theta, \phi, t\right) &= I^{--}_{B,TO,k}\left(x_B, z_B = 0, \theta, \phi, t\right)
\end{aligned} \tag{3.172}$$

where, $t > 0, 0 < x_C < L_{C,x}, L_{x1} + L_{x2} < x_B < L_{B,x}, 0 < \theta < \pi/2, \quad 0 < \phi < 2\pi.$

<u>Sub-domain D:</u>

<u>Initial Conditions:</u>

$$\begin{aligned}
&I_{D,LA,k}\left(x_D, z_D, \theta, \phi, t=0\right) = \frac{C_{LA,k} v_{LA,k} T_{\text{initial}}}{4\pi} \\
&I_{D,TA,k}\left(x_D, z_D, \theta, \phi, t=0\right) = \frac{C_{TA,k} v_{TA,k} T_{\text{initial}}}{4\pi} \qquad 0 < x_D < L_{D,x}, 0 < z_D < L_{D,z}, \\
&I_{D,LO,k}\left(x_D, z_D, \theta, \phi, t=0\right) = \frac{C_{LO,k} v_{LO,k} T_{\text{initial}}}{4\pi} \qquad 0 < \theta < \pi, \quad 0 < \phi < 2\pi \\
&I_{D,TO,k}\left(x_D, z_D, \theta, \phi, t=0\right) = \frac{C_{TO,k} v_{TO,k} T_{\text{initial}}}{4\pi}
\end{aligned} \tag{3.173}$$

Boundary Conditions:

Bottom Boundary:

$$\begin{aligned}
&I_{D,LA,k}\left(x_D = 0, z_D, \theta, \phi, t\right) = \frac{C_{LA,k} v_{LA,k} T_{bottom}}{4\pi} \\
&I_{D,TA,k}\left(x_D = 0, z_D, \theta, \phi, t\right) = \frac{C_{TA,k} v_{TA,k} T_{bottom}}{4\pi} \qquad t > 0, \quad 0 < z_D < L_{D,z}, \\
&I_{D,LO,k}\left(x_D = 0, z_D, \theta, \phi, t\right) = \frac{C_{LO,k} v_{LO,k} T_{bottom}}{4\pi} \qquad 0 < \theta < \pi/2, \quad 0 < \phi < 2\pi \\
&I_{D,TO,k}\left(x_D = 0, z_D, \theta, \phi, t\right) = \frac{C_{TO,k} v_{TO,k} T_{bottom}}{4\pi}
\end{aligned} \tag{3.174}$$

Top Boundary:

$$\begin{aligned}
&I_{D,LA,k}\left(x_D = L_{D,x}, z_D, \theta, \phi, t\right) = \frac{C_{LA,k} v_{LA,k} T_{q,dot}(t)}{4\pi} \\
&I_{D,TA,k}\left(x_D = L_{D,x}, z_D, \theta, \phi, t\right) = \frac{C_{TA,k} v_{TA,k} T_{q,dot}(t)}{4\pi} \qquad t > 0, \quad 0 < z_D < L_{D,z} \\
&I_{D,LO,k}\left(x_D = L_{D,x}, z_D, \theta, \phi, t\right) = \frac{C_{LO,k} v_{LO,k} T_{q,dot}(t)}{4\pi} \qquad \pi/2 < \theta < \pi, 0 < \phi < 2\pi \\
&I_{D,TO,k}\left(x_D = L_{D,x}, z_D, \theta, \phi, t\right) = \frac{C_{TO,k} v_{TO,k} T_{q,dot}(t)}{4\pi}
\end{aligned} \tag{3.175}$$

where, $T_{q,dot}(t) = \left(300 + e^{(-6.8/t)}\right) K$, t is in ps. The variation of $T_{q,dot}$ is shown in

Figure 3.13.

Interface Conditions:

Left Interface:

$$\begin{aligned}
I_{D,LA,k}^{++}\left(x_D,z_D=0,\theta,\phi,t\right) &= I_{A,LA,k}^{++}\left(x_A,z_A=L_{A,z},\theta,\phi,t\right)\\
I_{D,TA,k}^{++}\left(x_D,z_D=0,\theta,\phi,t\right) &= I_{A,TA,k}^{++}\left(x_A,z_A=L_{A,z},\theta,\phi,t\right)\\
I_{D,LO,k}^{++}\left(x_D,z_D=0,\theta,\phi,t\right) &= I_{A,LO,k}^{++}\left(x_A,z_A=L_{A,z},\theta,\phi,t\right)\\
I_{D,TO,k}^{++}\left(x_D,z_D=0,\theta,\phi,t\right) &= I_{A,TO,k}^{++}\left(x_A,z_A=L_{A,z},\theta,\phi,t\right)
\end{aligned} \tag{3.176}$$

and

$$\begin{aligned}
I_{D,LA,k}^{-+}\left(x_D,z_D=0,\theta,\phi,t\right) &= I_{A,LA,k}^{-+}\left(x_A,z_A=L_{A,z},\theta,\phi,t\right)\\
I_{D,TA,k}^{-+}\left(x_D,z_D=0,\theta,\phi,t\right) &= I_{A,TA,k}^{-+}\left(x_A,z_A=L_{A,z},\theta,\phi,t\right)\\
I_{D,LO,k}^{-+}\left(x_D,z_D=0,\theta,\phi,t\right) &= I_{A,LO,k}^{-+}\left(x_A,z_A=L_{A,z},\theta,\phi,t\right)\\
I_{D,TO,k}^{-+}\left(x_D,z_D=0,\theta,\phi,t\right) &= I_{A,TO,k}^{-+}\left(x_A,z_A=L_{A,z},\theta,\phi,t\right)
\end{aligned} \tag{3.177}$$

where, $t>0, 0<x_D<L_{D,x}, 0<x_A<L_{x1}, 0<\theta<\pi/2, 0<\phi<2\pi.$

Right Interface:

$$\begin{aligned}
I_{D,LA,k}^{+-}\left(x_D,z_D=L_{D,z},\theta,\phi,t\right) &= I_{B,LA,k}^{+-}\left(x_B,z_B=0,\theta,\phi,t\right)\\
I_{D,TA,k}^{+-}\left(x_D,z_D=L_{D,z},\theta,\phi,t\right) &= I_{B,TA,k}^{+-}\left(x_B,z_B=0,\theta,\phi,t\right)\\
I_{D,LO,k}^{+-}\left(x_D,z_D=L_{D,z},\theta,\phi,t\right) &= I_{B,LO,k}^{+-}\left(x_B,z_B=0,\theta,\phi,t\right)\\
I_{D,TO,k}^{+-}\left(x_D,z_D=L_{D,z},\theta,\phi,t\right) &= I_{B,TO,k}^{+-}\left(x_B,z_B=0,\theta,\phi,t\right)
\end{aligned} \tag{3.178}$$

and

$$
\begin{aligned}
I_{D,LA,k}^{--}\left(x_D, z_D = L_{D,z}, \theta, \phi, t\right) &= I_{B,LA,k}^{--}\left(x_B, z_B = 0, \theta, \phi, t\right) \\
I_{D,TA,k}^{--}\left(x_D, z_D = L_{D,z}, \theta, \phi, t\right) &= I_{B,TA,k}^{--}\left(x_B, z_B = 0, \theta, \phi, t\right) \\
I_{D,LO,k}^{--}\left(x_D, z_D = L_{D,z}, \theta, \phi, t\right) &= I_{B,LO,k}^{--}\left(x_B, z_B = 0, \theta, \phi, t\right) \\
I_{D,TO,k}^{--}\left(x_D, z_D = L_{D,z}, \theta, \phi, t\right) &= I_{B,TO,k}^{--}\left(x_B, z_B = 0, \theta, \phi, t\right)
\end{aligned}
\tag{3.179}
$$

where, $t > 0, 0 < x_D < L_{D,x}, 0 < x_B < L_{x1}, 0 < \theta < \pi/2, 0 < \phi < 2\pi$.

3.6 Mathematical Formulation for One Dimensional Dielectric Thin Films

This section presents the complete mathematical formulation for two different cases studied in relation to thermal energy transport in dielectric films. The relevant formulation consists of the governing equations, their domain of definition, and the associated initial, boundary and interface conditions for the cases considered.

1. Steady State Heat Transport Including the Effect of Film Thickness on Entropy Generation Rate.
2. Transient Heat Transport Inculding the Effect of Minute Vacuum Gap in between the Films.

3.6.1 Steady State Heat Transport Including the Effect of Film Thickness on Entropy Generation Rate

Thermodynamic irreversibility gives insight into the thermal transport process taking place in the system. Entropy generation quantifies the amount of thermodynamic irreversibility in the radiative transport in thin films. In order to investigate the in the entropy generation due to phonon transport in thin films for various film thicknesses one dimensional steady state analysis is carried out in silicon thin films as shown in Figure 3.14. The EPRT is incorporated to perform the simulations are performed for four different film thicknesses (L = 0.1 μm, L = 0.2 μm, L = 0.5 μm and L = 1.0μm).

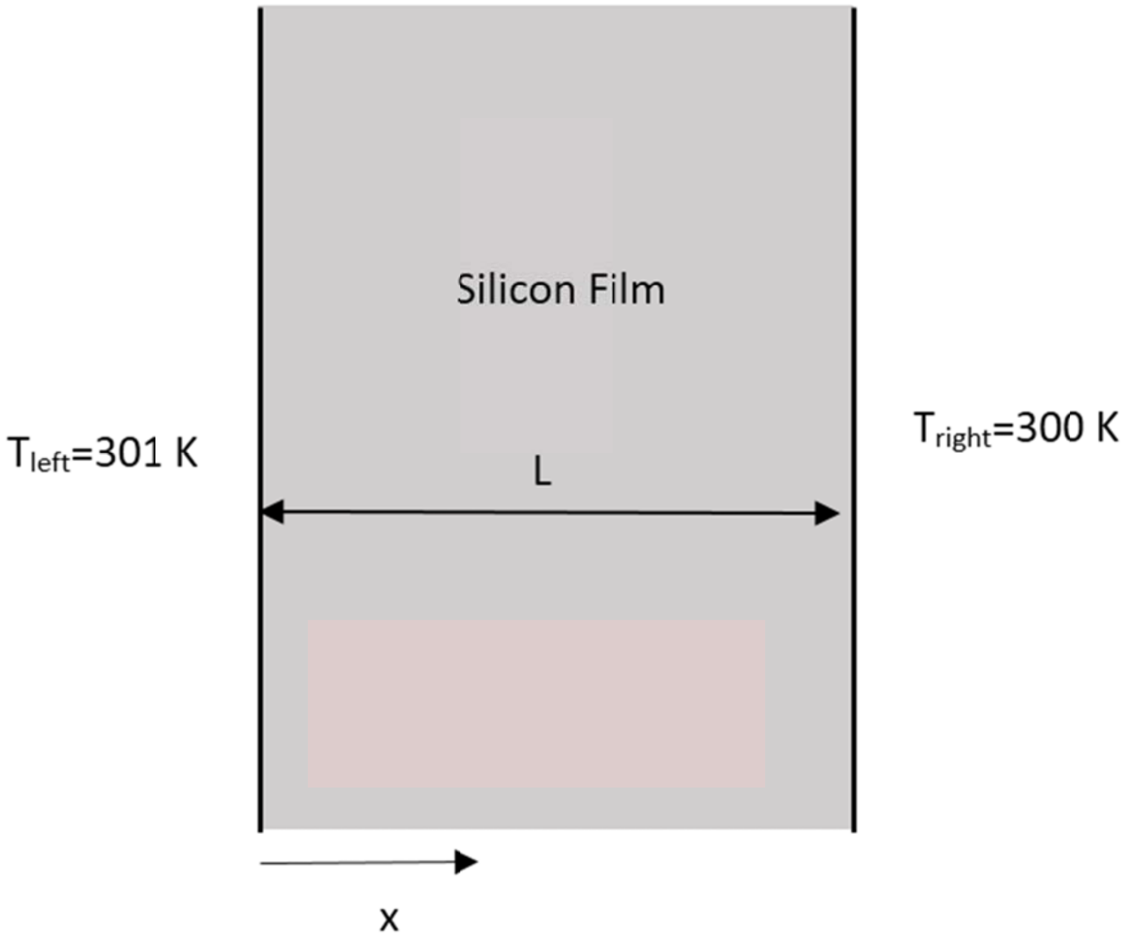

Figure 3.14 A schematic view of silicon thin film and temperature disturbance at the film edges.

Boundary Conditions:

Two boundary conditions are introduced at left and right surfaces in order to account temperature disturbances at the film edges. The left edge of the film is considered at constant temperature of 301 K and the right edge of the film is at 300 K for all eight cases.

Left Boundary:

a) Frequency Dependent Case:

$$\begin{aligned} I_{LA,k}\left(x=0,\mu\right) &= \frac{C_{LA,k}v_{LA,k}T_{left}}{4\pi} \\ I_{TA,k}\left(x=0,\mu\right) &= \frac{C_{TA,k}v_{TA,k}T_{left}}{4\pi} \\ I_{LO,k}\left(x=0,\mu\right) &= \frac{C_{LO,k}v_{LO,k}T_{left}}{4\pi} \\ I_{TO,k}\left(x=0,\mu\right) &= \frac{C_{TO,k}v_{TO,k}T_{left}}{4\pi} \end{aligned} \qquad -1<\mu<1 \qquad (3.180)$$

b) Frequency Independent Case:

$$I\left(x=0,\mu\right)=\frac{CvT_{left}}{4\pi} \qquad -1<\mu<1 \qquad (3.181)$$

Right Boundary:

a) Frequency Dependent Case:

$$
\begin{aligned}
I_{LA,k}\left(x=L,\mu\right) &= \frac{C_{LA,k} v_{LA,k} T_{right}}{4\pi} \\
I_{TA,k}\left(x=L,\mu\right) &= \frac{C_{TA,k} v_{TA,k} T_{right}}{4\pi} \\
I_{LO,k}\left(x=L,\mu\right) &= \frac{C_{LO,k} v_{LO,k} T_{right}}{4\pi} \\
I_{TO,k}\left(x=L,\mu\right) &= \frac{C_{TO,k} v_{TO,k} T_{right}}{4\pi}
\end{aligned}
\qquad -1 < \mu < 1 \qquad (3.182)
$$

b) Frequency Independent Case:

$$
I\left(x=L,\mu\right) = \frac{C v T_{right}}{4\pi} \qquad -1 < \mu < 1 \qquad (3.183)
$$

3.6.2 Transient Heat Transport Including the Effect of Minute Vacuum Gap in between the Films

Phonon transport across the silicon thin films pair with presence of minute gap (Casimir limit) in between the films is studied. The physical domain considered consists of the two silicon thin films (pair) separated by a considerably small gap (Casimir limit) as shown in Figure.3.15. In the analysis, transient, frequency dependent EPRT is incorporated to obtain the phonon intensity distribution in the silicon thin films pair. The boundary conditions used are those of constant temperature (Figure.3.15) resembling temperature disturbance across the films pair at the exterior edges. At the interface of the thin silicon films pair appropriate interface conditions are imposed satisfying the energy balance. The radiation heat transfer is also incorporated at the interface of film pair.

Section A:

Initial Conditions:

The following initial condition $\left(T_{initial} = 300\,\mathrm{K}\right)$ are incorporated in the domain,

$$\begin{aligned}
I_{A,LA,\mathrm{k}}\left(x_A,\mu,t=0\right) &= \frac{C_{LA,k}v_{LA,k}T_{initial}}{4\pi} \\
I_{A,TA,\mathrm{k}}\left(x_A,\mu,t=0\right) &= \frac{C_{TA,k}v_{TA,k}T_{initial}}{4\pi} \\
I_{A,LO,\mathrm{k}}\left(x_A,\mu,t=0\right) &= \frac{C_{LO,k}v_{LO,k}T_{initial}}{4\pi} \\
I_{A,TO,\mathrm{k}}\left(x_A,\mu,t=0\right) &= \frac{C_{TO,k}v_{TO,k}T_{initial}}{4\pi}
\end{aligned} \qquad -1<\mu<1 \qquad (3.184)$$

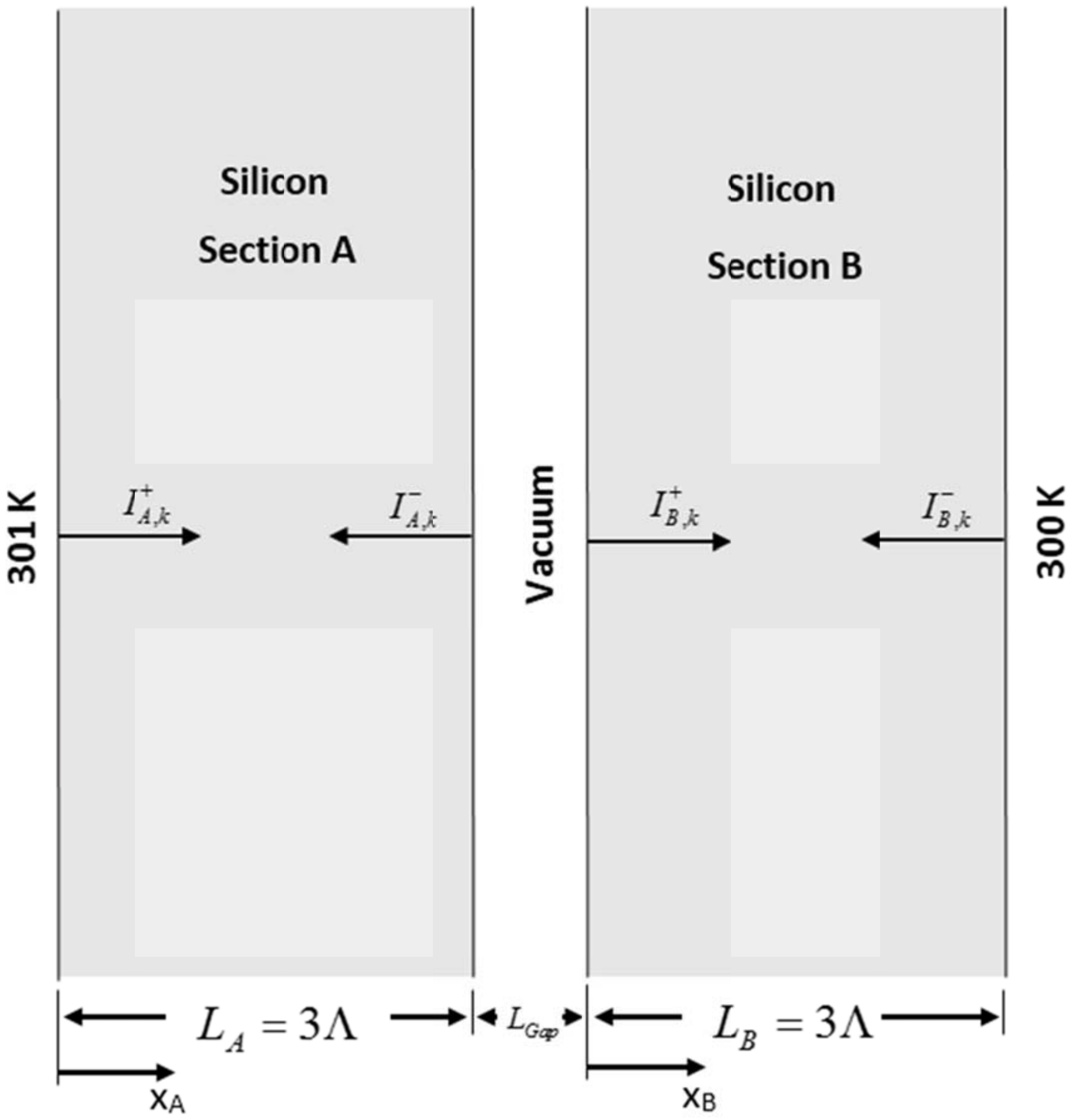

Figure.3.15 Schematic view of thin silicon films pair consist of two silicon films separated by a small gap. Λ is the mean free path of silicon correspondent gray medium.

Boundary Conditions:

Left Boundary:

$$
\begin{aligned}
I_{A,LA,\mathrm{k}}\left(x_A=0,\mu,t\right)&=\frac{C_{LA,k}v_{LA,k}T_{left}}{4\pi}\\
I_{A,TA,\mathrm{k}}\left(x_A=0,\mu,t\right)&=\frac{C_{TA,k}v_{TA,k}T_{left}}{4\pi}\\
I_{A,LO,\mathrm{k}}\left(x_A=0,\mu,t\right)&=\frac{C_{LO,k}v_{LO,k}T_{left}}{4\pi}\\
I_{A,TO,\mathrm{k}}\left(x_A=0,\mu,t\right)&=\frac{C_{TO,k}v_{TO,k}T_{left}}{4\pi}
\end{aligned}
\qquad -1<\mu<1 \qquad (3.185)
$$

Section B:

Initial Conditions:

It is considered the whole domain initially at 300 K. The following initial condition are incorporated in the domain,

$$
\begin{aligned}
I_{B,LA,\mathrm{k}}\left(x_B,\mu,t=0\right)&=\frac{C_{LA,k}v_{LA,k}T_{initial}}{4\pi}\\
I_{B,TA,\mathrm{k}}\left(x_B,\mu,t=0\right)&=\frac{C_{TA,k}v_{TA,k}T_{initial}}{4\pi}\\
I_{B,LO,\mathrm{k}}\left(x_B,\mu,t=0\right)&=\frac{C_{LO,k}v_{LO,k}T_{initial}}{4\pi}\\
I_{B,TO,\mathrm{k}}\left(x_B,\mu,t=0\right)&=\frac{C_{TO,k}v_{TO,k}T_{initial}}{4\pi}
\end{aligned}
\qquad -1<\mu<1 \qquad (3.186)
$$

Boundary Conditions:

Right Boundary:

$$
\begin{aligned}
I_{B,LA,\mathrm{k}}\left(x_B,\mu,t=0\right) &= \frac{C_{LA,k}v_{LA,k}T_{initial}}{4\pi} \\
I_{B,TA,\mathrm{k}}\left(x_B,\mu,t=0\right) &= \frac{C_{TA,k}v_{TA,k}T_{initial}}{4\pi} \\
I_{B,LO,\mathrm{k}}\left(x_B,\mu,t=0\right) &= \frac{C_{LO,k}v_{LO,k}T_{initial}}{4\pi} \\
I_{B,TO,\mathrm{k}}\left(x_B,\mu,t=0\right) &= \frac{C_{TO,k}v_{TO,k}T_{initial}}{4\pi}
\end{aligned}
\qquad -1 < \mu < 1 \qquad (3.187)
$$

In above equation subscript Si indicate the Silicon thin film. For example $v_{Si,LA,\omega}$ represents the frequency dependent phonon group velocity for longitudinal acoustic branch in silicon.

Interface Conditions:

In order to complete the solution of the domain (Figure.3.15), interface conditions should be incorporated. Interface conditions are obtained by applying the energy balance at the interface with consideration of radiation heat transfer (Casimir limit). The radiation heat transfer is incorporated between the section A and B, which is given by:

$$
q_{rad.,total}(t) = \sigma\left(T_A^4(x_{A-Interface},t) - T_B^4(x_{B-Interface},t)\right) \qquad (3.188)
$$

where $x_{A-Interface} = 3\Lambda$ and $x_{B-Interface} = 0$.

Energy transfer from section *A* to section *B* by radiation is disturbed into all the branches of each mode of phonons. This can be expressed as follows:

$$q_{rad.,ij,k}\left(t\right)=\frac{\int\limits_{0}^{1} I_{A,ij,k}^{+}\left(x_{A-Interface},\mu,t\right)d\mu}{I_{A,total}^{+}\left(t\right)}q_{rad.,total}(t) \tag{3.189}$$

where,

$$I_{A,total}^{+}\left(t\right)=\int\limits_{0}^{k_{\max}}\int\limits_{0}^{1}\begin{pmatrix} I_{A,LA,k}^{+}\left(x_{A-Interface},\mu,t\right)+I_{A,TA,k}^{+}\left(x_{A-Interface},\mu,t\right) \\ +I_{A,LO,k}^{+}\left(x_{A-Interface},\mu,t\right)+I_{A,TO,k}^{+}\left(x_{A-Interface},\mu,t\right) \end{pmatrix}d\mu dk \tag{3.190}$$

The heat fluxes $q_{A,ij,k}^{+}, q_{A,ij,k}^{-}, q_{B,ij,k}^{+}\ and\ q_{B,ij,k}^{-}$ (as shown in Figure 3.16) are given as:

$$q_{A,ij,k}^{+}(t)=2\pi\int_{0}^{1} I_{A,ij,k}^{+}\left(x_{A-Interface},\mu,t\right)\mu d\mu \tag{3.191}$$

$$q_{A,ij,k}^{-}(t)=2\pi\int_{-1}^{0} I_{A,ij,k}^{-}\left(x_{A-Interface},\mu,t\right)\mu d\mu \tag{3.192}$$

$$q_{B,ij,k}^{+}(t)=2\pi\int_{0}^{1} I_{B,ij,k}^{+}\left(x_{B-Interface},\mu,t\right)\mu d\mu \tag{3.193}$$

$$q_{B,ij,k}^{-}(t)=2\pi\int_{-1}^{0} I_{B,ij,k}^{-}\left(x_{B-Interface},\mu,t\right)\mu d\mu \tag{3.194}$$

When the phonon wavelength is greater than the gap length $\lambda \geq L_{Gap}$, the phonon wave jumps over the gap from one section to another $(A \rightleftarrows B)$. Here, λ is the phonon wavelength and L_{Gap} is the gap size (length) between the sections *A* and *B*. The wavenumber corresponds to the L_{Gap} is $k_{Cut-off}=2\pi / L_{Gap}$, which works as the cut-off wavenumber. All the phonons having wavenumbers less than the cut-off wavenumber $\left(k<k_{Cut-off}\right)$ can possibly jump from one section to another $(A \rightleftarrows B)$. It should be noted

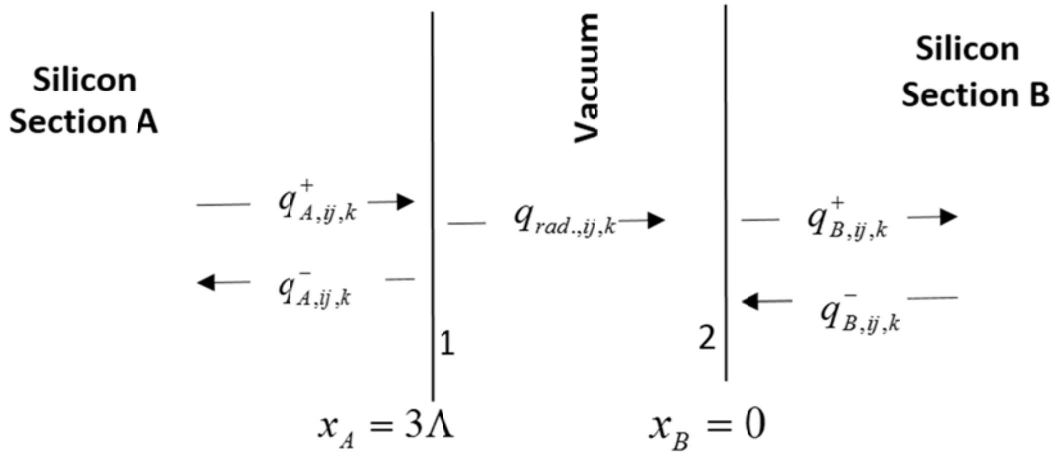

Figure 3.16 Schematic view of gap located in between two-silicon films pair and heat flux vectors (*k* is wavenumber and, *i* = *T* represents the transverse mode of phonons, *i* = *L* stands for longitudinal mode of phonons, *j* = *A* corresponds to acoustic and *j* = *O* stands for optical phonons). The space between $x_A = 3\Lambda$ and $x_B = 3\Lambda$ corresponds to the gap size.

that energy balance has been applied at each wavelength of transverse acoustic, longitudinal acoustic, transverse optical and longitudinal optical branches of phonons waves.

Energy balance at point 1 (Figure 3.16)

Energy balance has to be satisfied at the interface, which requires the following conditions need to be fulfilled.

When $k < k_{Cut-off}$

$$q^{-}_{A,ij,k}(t) = q^{-}_{B,ij,k}(t) + q_{rad.,ij,k}(t) \tag{3.195}$$

Considering the diffusive condition at the inference and incorporating the equation (3.192) into above equation yields the following,

$$I^{-}_{A,ij,k}\left(x_{A-Interface}, \mu, t\right) = \left(-q^{-}_{B,ij,k}(t) - q_{rad.,ij,k}(t)\right)/\pi \tag{3.196}$$

When $k > k_{Cut-off}$

$$q^{-}_{A,ij,k}\left(t\right) = -q^{+}_{A,ij,k}(t) + q_{rad.,ij,k}(t) \tag{3.197}$$

Diffuse boundary condition at interface results into the following equation.

$$I^{-}_{A,ij,k}\left(x_{A-Interface}, \mu, t\right) = \left(q^{+}_{A,ij,k}(t) - q_{rad.,ij,k}(t)\right)/\pi \tag{3.198}$$

Energy balance at point 2 (Figure 3.16)

When $k < k_{Cut-off}$

$$q^{+}_{B,ij,k}(t) = q^{+}_{A,ij,k}(t) + q_{rad.,ij,k}(t) \tag{3.199}$$

Considering the diffuse condition at the boundary that is $I^{+}_{B,ij,k}$ is independent of μ μ and incorporating the equation (3.193) into above equation yields the following.

$$I^{+}_{B,ij,k}\left(x_{B-Interface}, \mu, t\right) = \left(q^{+}_{A,ij,k}(t) + q_{rad.,ij,k}(t)\right)/\pi \tag{3.200}$$

When $k > k_{Cut-off}$

$$q^{+}_{B,ij,k}\left(t\right) = -q^{-}_{B,ij,k}(t) + q_{rad.,ij,k}(t) \tag{3.201}$$

This can be reduced into the following:

$$I^{+}_{B,ij,k}\left(x_{B-Interface}, \mu, t\right) = \left(-q^{-}_{B,ij,k}(t) + q_{rad.,ij,k}(t)\right)/\pi \tag{3.202}$$

In above equations from equation (3.189) to equation (3.202), $i = T$ represents the Transverse mode and $i = L$ stands for Longitudinal mode. In addition, $j = A$ corresponds to Acoustic and $j = O$ stands for and Optical phonons.

3.7 Mathematical Formulation for One Dimensional Metallic Thin Films

This section presents the complete mathematical formulation for three different cases studied in relation to thermal energy transport in metal films. The relevant formulation consists of the governing equations, their domain of definition, and the associated initial and boundary for the cases considered.

1. Transient Heat Transport in Aluminum thin films.
2. Transient Heat Transport Including the Effect of Thermal Oscillation in Aluminum Thin Films.
3. Transient Heat Transport Including the Effects of Thermal Oscillation and Film Thickness in Aluminum thin film.

3.7.1 Transient Heat Transport in Aluminum Thin Film

This study is carried out to investigate the energy transport in aluminum thin film, using the frequency dependent phonon radiative transport equation, due to temperature disturbance at the film edges as shown in Figure 3.17. The effect of aluminum film thickness on the transport characteristics is examined numerically using the discrete ordinate method. The predictions are compared with the findings of the hyperbolic heat equation. The aluminum film consists of electron and lattice sub-systems due to thermal separation of the sub-systems. Therefore, initial and boundary conditions are introduced in both sub-systems.

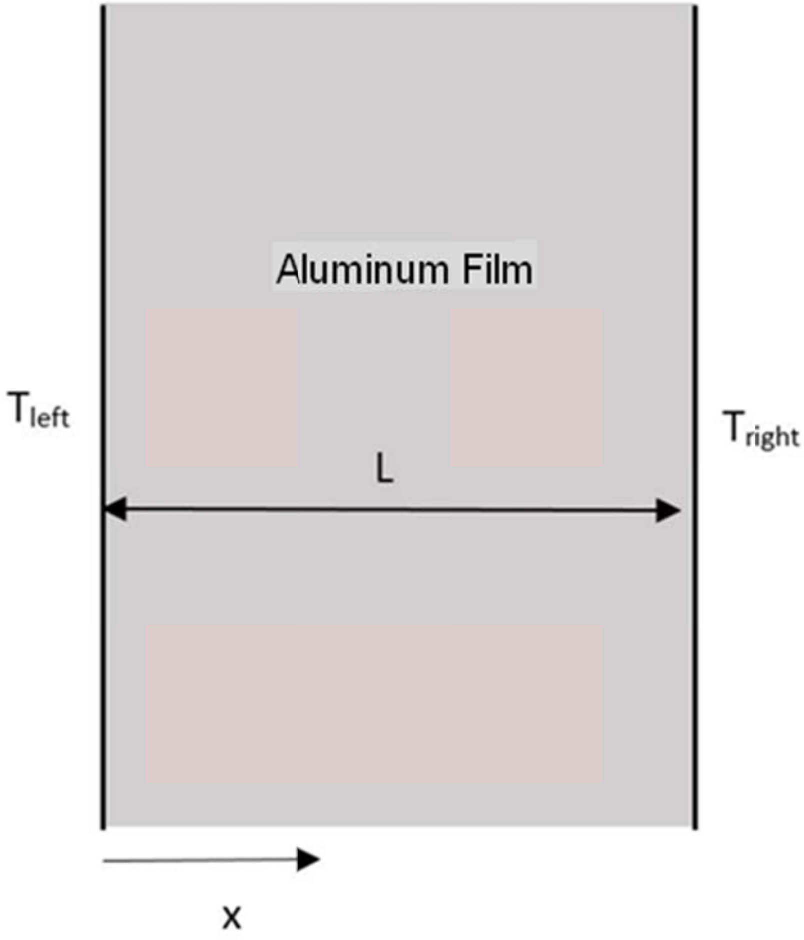

Figure 3.17 A schematic view of aluminum film and the temperature settings at the film edges.

Lattice Sub-System:

Initial Conditions:

The following initial condition are incorporated in the domain,

a) Frequency Independent case:

$$I_p\left(x,\mu,t=0\right)=\frac{C_p v_p}{4\pi}T_{initial} \qquad -1<\mu<1 \qquad (3.203)$$

b) Frequency Independent case:

$$\begin{aligned} I_{p,LA}\left(x,\mu,t=0\right)&=\frac{C_{p,LA}v_{p,LA}}{4\pi}T_{initial} \\ I_{p,TA}\left(x,\mu,t=0\right)&=\frac{C_{p,TA}v_{p,TA}}{4\pi}T_{initial} \end{aligned} \qquad -1<\mu<1 \qquad (3.204)$$

Boundary Conditions:

Left Boundary:

a) Frequency Independent case:

$$I_p\left(x=0,\mu,t\right)=\frac{C_p v_p}{4\pi}T_{left} \qquad -1<\mu<1 \qquad (3.205)$$

b) Frequency Dependent case:

$$\begin{aligned} I_{p,LA,k}\left(x\;=0,\mu,t\right)&=\frac{C_{p,LA,k}v_{p,LA,k}}{4\pi}T_{left} \\ I_{p,TA,k}\left(x\;=0,\mu,t\right)&=\frac{C_{p,TA,k}v_{p,TA,k}}{4\pi}T_{left} \end{aligned} \qquad -1<\mu<1 \qquad (3.206)$$

where, $T_{left}(t)=301\,K$.

Right Boundary:

a) **Frequency Independent Case:**

$$I_p(x = L, \mu, t) = \frac{C_p v_p}{4\pi} T_{right} \qquad -1 < \mu < 1 \qquad (3.207)$$

b) **Frequency Dependent Case:**

$$\begin{aligned} I_{p,LA,k}(x = L, \mu, t) &= \frac{C_{p,LA,k} v_{p,LA,k}}{4\pi} T_{right} \\ I_{p,TA,k}(x = L, \mu, t) &= \frac{C_{p,TA,k} v_{p,TA,k}}{4\pi} T_{right} \end{aligned} \qquad -1 < \mu < 1 \qquad (3.208)$$

where, $T_{right}(t) = 300\, K$.

Electron Sub-System:

Initial Conditions;

It is considered the whole domain initially at 300 K. The following initial condition are incorporated in the domain,

$$I_e(x, \mu, t = 0) = \frac{C_e v_e}{4\pi} T_{initial} \qquad -1 < \mu < 1 \qquad (3.209)$$

Boundary Conditions:

For the case of the electrons, the insulated boundary condition is considered. This is due to the fact that the electrons themselves do not take part in the transfer of thermal energy to, or from, the phonons of a different material. This is true for the case when the bounding surface is exposed to the atmospheric air. When the bounding surface is actually an interface between the metal and the dielectric thin film, then again the electrons do not transfer to, or receive thermal energy from, the phonons of the dielectric material. Hence, one may conclude that the electron sub-system is actually insulated at the boundaries and therefore, the insulated boundary conditions is incorporated in the analysis.

Left Boundary:

$$q_e''\left(x=0,t\right)=2\pi\int_{-1}^{1}\mu I_e\left(x=0,\mu,t\right)d\mu=0 \qquad (3.210)$$

Right Boundary:

$$q_e''\left(x=L,t\right)=2\pi\int_{-1}^{1}\mu I_e\left(x=L,\mu,t\right)d\mu=0 \qquad (3.211)$$

3.7.2 Transient Heat Transport Including the Effect of Thermal Oscillation in Aluminum Thin Film

This study is carried out to investigate the energy transport in one dimensional aluminum thin film as shown in Figure 3.17, using the frequency dependent and frequency independent phonon radiative transport equation, due to temperature oscillations (τ_h = 1.0 ps, τ_h = 1.5 ps, τ_h = 2.0 ps and , τ_h = 2.5 ps) at the film edges as shown in Figure 3.7.

The aluminum film consists of electron and lattice sub-systems due to thermal separation of the sub-systems. Therefore, initial and boundary conditions are introduced according to the sub-systems.

Lattice Sub-System:

Initial Conditions:

The following initial condition are incorporated in the domain,

a) Frequency Independent case:

$$I_p\left(x,\mu,t=0\right)=\frac{C_p v_p}{4\pi}T_{initial} \qquad -1<\mu<1 \qquad (3.212)$$

b) Frequency Independent case:

$$\begin{aligned} I_{p,LA}\left(x,\mu,t=0\right)&=\frac{C_{p,LA}v_{p,LA}}{4\pi}T_{initial} \\ I_{p,TA}\left(x,\mu,t=0\right)&=\frac{C_{p,TA}v_{p,TA}}{4\pi}T_{initial} \end{aligned} \qquad -1<\mu<1 \qquad (3.213)$$

Boundary Conditions:

Left Boundary:

a) Frequency Independent case:

$$I_p\left(x = 0, \mu, t\right) = \frac{C_p v_p}{4\pi} T_{left} \qquad -1 < \mu < 1 \qquad (3.214)$$

b) Frequency Dependent case:

$$\begin{aligned} I_{p,LA,k}\left(x = 0, \mu, t\right) &= \frac{C_{p,LA,k} v_{p,LA,k}}{4\pi} T_{left} \\ I_{p,TA,k}\left(x = 0, \mu, t\right) &= \frac{C_{p,TA,k} v_{p,TA,k}}{4\pi} T_{left} \end{aligned} \qquad -1 < \mu < 1 \qquad (3.215)$$

The $T_{left}(t) = \begin{cases} 301\,K & 0 < t < \tau_h \\ 300\,K & otherwise \end{cases}$ with $T_{left}\left(t + \tau_{cycle}\right) = T_{left}\left(t\right)$.

Right Boundary:

a) Frequency Independent case:

$$I_p\left(x = L, \mu, t\right) = \frac{C_p v_p}{4\pi} T_{right} \qquad -1 < \mu < 1 \qquad (3.216)$$

b) Frequency Dependent case:

$$\begin{aligned} I_{p,LA,k}\left(x = L, \mu, t\right) &= \frac{C_{p,LA,k} v_{p,LA,k}}{4\pi} T_{right} \\ I_{p,TA,k}\left(x = L, \mu, t\right) &= \frac{C_{p,TA,k} v_{p,TA,k}}{4\pi} T_{right} \end{aligned} \qquad -1 < \mu < 1 \qquad (3.217)$$

where, $T_{right}(t) = 300K.$

Electron Sub-System:

The initial and boundary conditions are incorporated in the similar way as explained in section 3.7.1.

3.7.3 Transient Heat Transport Including the Effects of Thermal Oscillation and Film Thickness in Aluminum Thin Film

In the study, energy transfer in an aluminum thin film is considered, due to a temperature disturbance at the film edges. Temperature oscillations (τ_h = 1.5 ps and τ_h = 2.5 ps) are introduced at the high temperature edge of the film. Transient frequency dependent and frequency independent solutions of the EPRT are obtained for aluminum thin film. In addition, the effect of film thickness (L_x= 0.25L, L_x= 0.5L, L_x= 1.0L and L_x= 1.5L, where L = 0.1 μm) on heat transport characteristics is also investigated.

The initial temperature of film considers as 300 K. Initial and boundary conditions are incorporated in the similar way as described in section 3.7.2.

.

CHAPTER 4

NUMERICAL SOLUTION

The previous chapter describes the relevant mathematical models, which includes partial differential equations along with the associated initial, boundary and interface conditions. However, in this chapter numerical method, which incorporated for the solution of governing equation, is presented. Since these equations can not be solved analytically, it becomes unavoidable to obtain an approximate, numerical solution. For this purpose the finite difference method has been used to obtain the numerical solution of all equations. Equation of Phonon Radiative Transfer is solved using the Discrete Ordinates Method is used which is an example of a finite difference method. To solve the transient cases, an implicit scheme is used to ensure accuracy and stability. Moreover, since the equations are coupled, with complex interface conditions, an implicit scheme stands out to be the natural choice. In the following sections various aspects of the numerical method shall be discussed, including the discretization of the domain and of the governing equations, the treatment of the boundary conditions, and the implementation of the interface condition. Solution algorithms are also presented, which are used to solve these equations, as well as to satisfy the boundary and interface conditions. In order to describe numerical method in details, this chapter divided into following three sub-sections.

1. EPRT for Two Dimensional Dielectric Films.
2. EPRT for One Dimensional Dielectric Films.
3. EPRT for One Dimensional Metallic Films.

4.1 EPRT for Two Dimensional Dielectric Films

Consider the phonon radiative transport equation for a particular phonon branch, in the dielectric thin film:

$$\frac{1}{v_\omega}\frac{\partial I_\omega}{\partial t}+\cos\theta\frac{\partial I_\omega}{\partial x}+\sin\theta\cos\phi\frac{\partial I_\omega}{\partial z}=\frac{\frac{1}{4\pi}\int_0^{2\pi}\int_0^{\pi}I_\omega\sin\theta d\theta d\phi-I_\omega}{\Lambda_\omega}\quad \begin{matrix}0<\theta<\pi,\\ 0<\phi<2\pi\end{matrix} \tag{4.1}$$

To facilitate the solution of the phonon radiative transport equation and secure a stable discretization for all values of θ and ϕ, one could partition the complete 4π solid angle in to 4 quadrants as shown in Figure 4.1. In the first quadrant $(0<\theta<\pi/2, 0<\phi<\pi)$ the phonon intensity can be donated as I_ω^{++}; in the second quadrant $(\pi/2<\theta<\pi, 0<\phi<\pi)$ the phonon intensity can be donated as I_ω^{-+}, in the third quadrant $(0<\theta<\pi/2, \pi<\phi<2\pi)$ the phonon intensity can be donated as I_ω^{+-}; finally, in the fourth quadrant $(\pi/2<\theta<\pi, \pi<\phi<2\pi)$, the phonon intensity can be donated as I_ω^{--}.

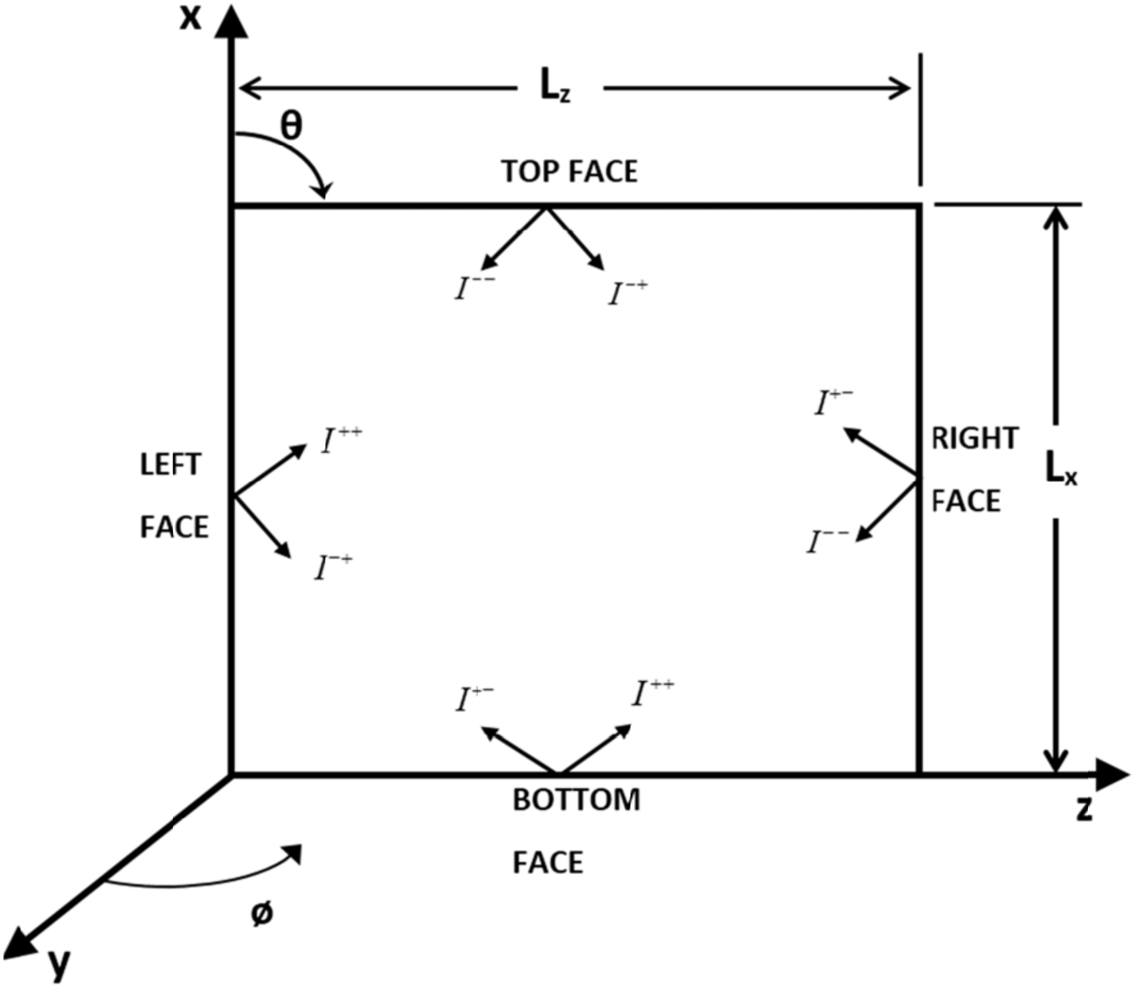

Figure 4.1 A schematic diagram showing the intensity in first, second, third and fourth quadrant for two dimensional EPRT in dielectric thin films.

EPRT in each quadrant can be written as follows:

First Quadrant: $\left(0<\theta<\pi/2,\,0<\phi<\pi\right)$

$$\frac{1}{v_\omega}\frac{\partial I_\omega^{++}}{\partial t}+\cos\theta\frac{\partial I_\omega^{++}}{\partial x}+\sin\theta\cos\phi\frac{\partial I_\omega^{++}}{\partial z}=\frac{\frac{1}{4\pi}\int_0^{2\pi}\int_0^{\pi}I_\omega\sin\theta d\theta d\phi-I_\omega^{++}}{\Lambda_\omega} \tag{4.2}$$

Second Quadrant: $\left(\pi/2<\theta<\pi,\,0<\phi<\pi\right)$

$$\frac{1}{v_\omega}\frac{\partial I_\omega^{-+}}{\partial t}+\cos\theta\frac{\partial I_\omega^{-+}}{\partial x}+\sin\theta\cos\phi\frac{\partial I_\omega^{-+}}{\partial z}=\frac{\frac{1}{4\pi}\int_0^{2\pi}\int_0^{\pi}I_\omega\sin\theta d\theta d\phi-I_\omega^{-+}}{\Lambda_\omega} \tag{4.3}$$

Third Quadrant: $\left(0<\theta<\pi/2,\,\pi<\phi<2\pi\right)$

$$\frac{1}{v_\omega}\frac{\partial I_\omega^{+-}}{\partial t}+\cos\theta\frac{\partial I_\omega^{+-}}{\partial x}+\sin\theta\cos\phi\frac{\partial I_\omega^{+-}}{\partial z}=\frac{\frac{1}{4\pi}\int_0^{2\pi}\int_0^{\pi}I_\omega\sin\theta d\theta d\phi-I_\omega^{+-}}{\Lambda_\omega} \tag{4.4}$$

Fourth Quadrant: $\left(\pi/2<\theta<\pi,\,\pi<\phi<2\pi\right)$

$$\frac{1}{v_\omega}\frac{\partial I_\omega^{--}}{\partial t}+\cos\theta\frac{\partial I_\omega^{--}}{\partial x}+\sin\theta\cos\phi\frac{\partial I_\omega^{--}}{\partial z}=\frac{\frac{1}{4\pi}\int_0^{2\pi}\int_0^{\pi}I_\omega\sin\theta d\theta d\phi-I_\omega^{--}}{\Lambda_\omega} \tag{4.5}$$

4.1.1. Domain Discretization

The film thickness is discretized into n_x number of cells, so that the total number of grid points are n_x+1. The grid points are numbered from 1 to n_x+1. If the grid point index is denoted by i, then $i=1$ indicates the grid point at $x=0$, i.e. at the left face of the film. The grid point situated at $x = L_x$, i.e. at the right face of the film is represented by the grid point index $i = n_x + 1$. The gird points represented by the index numbers $i = 2,3,....n$ lie inside the film. The relation between the coordinate values and the index i is given as, $x_i = (i-1)\Delta x$, where $\Delta x = L_x / n_x$.

The film width is discretized in to n_z number of cells, so that the total number of grid points are $n_z + 1$. The grid points are numbered from 1 to $n_z + 1$. If the grid point index is denoted by j, then $j = 1$ indicates the grid point at $z = 0$, i.e. at the bottom face of the film. The grid point situated at $z = L_z$, i.e. at the top face of the film is represented by the grid point index $j = n_z + 1$. The gird points represented by the index numbers $j = 2,3,....n$ lie inside the film. The relation between the coordinate values and the index j is given as, $z_j = (j-1)\Delta z$, where $\Delta z = L_z / n_z$.

The variable θ is discretized in to $2n_\theta$ number of grid points. Let m be the grid point index, when $m = 1$, $\theta_1 = 0$, when $m = 2n_\theta + 1, \theta_{2n_\theta+1} = \pi$. The index numbers $m = 2,3,...n_\theta + 1$ represent the interval, $0 \le \theta \le \pi / 2$, where as the index numbers $m = n_\theta + 1, n_\theta + 2,...2n_\theta + 1$ represent the interval, $\pi / 2 \le \theta \le \pi$. Notice that the relation between θ_m and m may also be written as, $\theta_m = (m-1)\Delta\theta$, where $\Delta\theta = \pi / 2n_\theta$.

The variable ϕ is discretized in to $2n_\phi$ number of grid points. Let m be the grid point index, when $n = 1$, $\phi_1 = 0$, when $n = 2n_\phi + 1, \phi_{2n_\phi+1} = 2\pi$. The index numbers

$n = 2,3,...n_\phi + 1$ represent the interval, $0 \le \phi \le \pi$, where as the index numbers $n = n_\phi + 1, n_\phi + 2,...2n_\phi + 1$ represent the interval, $\pi \le \theta \le 2\pi$. Notice that the relation between ϕ_n and n may also be written as, $\phi_n = (n-1)\Delta\phi$, where $\Delta\phi = \pi / n_\phi$.

The time variable is discretized in to n_t number of time intervals, so that the total number of time steps are $n_t + 1$. Let be p the time step index, then $p = 1$ represents $t = 0$, where as $p = n_t + 1$ indicates $t = t_{\max}$. The initial condition corresponds to $p = 1$ and it is required to find the intensities at time steps corresponding to the time step indices $p = 2,3,.....n_t + 1$. The relation between the actual time t_p and the index p is given as, $t_p = (\mathrm{p} - 1)\Delta \mathrm{t}$, where $\Delta \mathrm{t} = \mathrm{t}_{\max} / n_t$.

The frequency is discretized in to n_ω number of frequency intervals, so that the total number of frequency steps are $n_\omega + 1$. Let be f the frequency step index, then $f = 1$ represents $\omega = 0$, whereas $f = n_\omega + 1$ indicates $\omega = \omega_{\max}$. The relation between the ω and the index f is given as, $\omega_f = (f-1)\Delta\omega$, where $\Delta\omega = \omega_{\max} / n_\omega$.

4.1.2. Discretization of Governing Equation

The next step is to discretize the governing equations, i.e. the Equation of Phonon Radiative Transfer for two dimensional dielectric thin films. In this relation for all simulation the finite difference method is used. To discretize the EPRT, continuous derivatives replaced by their discrete approximations. The time-derivative is approximated by means of a first-order backward difference. The spatial-derivative is approximated by forward and backward differences. In the first quadrant forward difference formula for both $\partial I_\omega / \partial x$ and $\partial I_\omega / \partial z$. In the second quadrant backward difference applied for $\partial I_\omega / \partial x$. In the third quadrant, backward difference has to be used for $\partial I_\omega / \partial z$. In the fourth quadrant, $\partial I_\omega / \partial x$ and $\partial I_\omega / \partial z$ are discretize with backward difference. This procedure is necessary to ensure stable discretization, which in turn will ensure a converged solution. The integration in the equations in performed by means of the Simpson's Rule. The discretization procedure is described below.

a) Replacement of Derivatives by Algebraic Approximations

First Quadrant: $\left(0 < \theta < \pi/2 \,, 0 < \phi < \pi\right)$

$$\begin{aligned}&\frac{1}{v_f}\frac{I^{++,p}_{f,i,j,m,n} - I^{++,p}_{f,i,j,m,n}}{\Delta t} + \cos\theta_m \frac{I^{++,p}_{f,i,j,m,n} - I^{++,p}_{f,i-1,j,m,n}}{\Delta x} \\ &+ \sin\theta_m \cos\phi_n \frac{I^{++,p}_{f,i,j,m,n} - I^{++,p}_{f,i,j-1,m,n}}{\Delta z} = \frac{\frac{1}{4\pi}\int_0^{2\pi}\int_0^{\pi} I^p_f \sin\theta d\theta d\phi - I^{++,p}_{f,i,j,m,n}}{\Lambda_f}\end{aligned} \tag{4.6}$$

Second Quadrant: $\left(\pi/2 < \theta < \pi, 0 < \phi < \pi\right)$

$$\begin{aligned}&\frac{1}{v_f}\frac{I^{-+,p}_{f,i,j,m,n} - I^{-+,p}_{f,i,j,m,n}}{\Delta t} + \cos\theta_m \frac{I^{-+,p}_{f,i+1,j,m,n} - I^{-+,p}_{f,i,j,m,n}}{\Delta x} \\ &+ \sin\theta_m \cos\phi_n \frac{I^{-+,p}_{f,i,j,m,n} - I^{-+,p}_{f,i,j-1,m,n}}{\Delta z} = \frac{\frac{1}{4\pi}\int_0^{2\pi}\int_0^{\pi} I^p_f \sin\theta d\theta d\phi - I^{-+,p}_{f,i,j,m,n}}{\Lambda_f}\end{aligned} \tag{4.7}$$

Third Quadrant: $\left(0<\theta<\pi/2,\ \pi<\phi<2\pi\right)$

$$\begin{aligned}&\frac{1}{v_f}\frac{I^{+-,p}_{f,i,j,m,n}-I^{+-,p}_{f,i,j,m,n}}{\Delta t}+\cos\theta_m\frac{I^{+-,p}_{f,i,j,m,n}-I^{+-,p}_{f,i-1,j,m,n}}{\Delta x}\\&+\sin\theta_m\cos\phi_n\frac{I^{+-,p}_{f,i,j+1,m,n}-I^{+-,p}_{f,i,j,m,n}}{\Delta z}=\frac{\frac{1}{4\pi}\int_0^{2\pi}\int_0^{\pi}I_f^p\sin\theta d\theta d\phi-I^{+-,p}_{f,i,j,m,n}}{\Lambda_f}\end{aligned}\tag{4.8}$$

Fourth Quadrant: $\left(\pi/2<\theta<\pi,\ \pi<\phi<2\pi\right)$

$$\begin{aligned}&\frac{1}{v_f}\frac{I^{--,p}_{f,i,j,m,n}-I^{--,p}_{f,i,j,m,n}}{\Delta t}+\cos\theta_m\frac{I^{--,p}_{f,i+1,j,m,n}-I^{--,p}_{f,i,j,m,n}}{\Delta x}\\&+\sin\theta_m\cos\phi_n\frac{I^{--,p}_{f,i,j+1,m,n}-I^{++,p}_{f,i,j,m,n}}{\Delta z}=\frac{\frac{1}{4\pi}\int_0^{2\pi}\int_0^{\pi}I_f^p\sin\theta d\theta d\phi-I^{--,p}_{f,i,j,m,n}}{\Lambda_f}\end{aligned}\tag{4.9}$$

In the above equations v_f is the frequency dependent group velocity and Λ_f is the frequency dependent mean free path for a specific frequency corresponding to f that is $\omega_f=(f-1)\Delta\omega$.

b) Simplification of the Algebraic Equaitons

First Quadrant: $\left(0<\theta<\pi/2,\ 0<\phi<\pi\right)$

$$\begin{aligned}&I^{++,p}_{f,i,j,m,n}\left[\frac{1}{v_f\Delta t}+\frac{\cos\theta_m}{\Delta x}+\frac{\sin\theta_m\sin\phi_n}{\Delta z}+\frac{1}{\Lambda_f}\right]\\&=I^{++,p}_{f,i-1,j,m,n}\left[\frac{\cos\theta_m}{\Delta x}\right]+I^{++,p}_{f,i,j-1,m,n}\left[\frac{\sin\theta_m\sin\phi_n}{\Delta z}\right]+\frac{\frac{1}{4\pi}\left(\text{integral}\right)^p_{f,i,j}}{\Lambda_f}+\frac{I^{++,p-1}_{f,i,j,m,n}}{v_f\Delta t}\end{aligned}\tag{4.10}$$

<u>Second Quadrant:</u> $\left(\pi/2 < \theta < \pi,\, 0 < \phi < \pi\right)$

$$\begin{aligned} & I_{f,i,j,m,n}^{-+,p}\left[\frac{1}{v_f\Delta t}-\frac{\cos\theta_m}{\Delta x}+\frac{\sin\theta_m\sin\phi_n}{\Delta z}+\frac{1}{\Lambda_f}\right] \\ & = I_{f,i+1,j,m,n}^{-+,p}\left[-\frac{\cos\theta_m}{\Delta x}\right]+I_{f,i,j-1,m,n}^{-+,p}\left[\frac{\sin\theta_m\sin\phi_n}{\Delta z}\right]+\frac{\frac{1}{4\pi}\left(\text{integral}\right)_{f,i,j}^{p}}{\Lambda_f}+\frac{I_{f,i,j,m,n}^{-+,p-1}}{v_f\Delta t} \end{aligned} \tag{4.11}$$

<u>Third Quadrant:</u> $\left(0 < \theta < \pi/2,\, \pi < \phi < 2\pi\right)$

$$\begin{aligned} & I_{f,i,j,m,n}^{+-,p}\left[\frac{1}{v_f\Delta t}+\frac{\cos\theta_m}{\Delta x}-\frac{\sin\theta_m\sin\phi_n}{\Delta z}+\frac{1}{\Lambda_f}\right] \\ & = I_{k,i-1,j,m,n}^{+-,p}\left[\frac{\cos\theta_m}{\Delta x}\right]+I_{f,i,j+1,m,n}^{+-,p}\left[-\frac{\sin\theta_m\sin\phi_n}{\Delta z}\right]+\frac{\frac{1}{4\pi}\left(\text{integral}\right)_{f,i,j}^{p}}{\Lambda_f}+\frac{I_{f,i,j,m,n}^{+-,p-1}}{v_f\Delta t} \end{aligned} \tag{4.12}$$

<u>Fourth Quadrant:</u> $\left(\pi/2 < \theta < \pi,\, \pi < \phi < 2\pi\right)$

$$\begin{aligned} & I_{f,i,j,m,n}^{--,p}\left[\frac{1}{v_f\Delta t}-\frac{\cos\theta_m}{\Delta x}-\frac{\sin\theta_m\sin\phi_n}{\Delta z}+\frac{1}{\Lambda_f}\right] \\ & = I_{f,i+1,j,m,n}^{--,p}\left[-\frac{\cos\theta_m}{\Delta x}\right]+I_{f,i,j+1,m,n}^{--,p}\left[-\frac{\sin\theta_m\sin\phi_n}{\Delta z}\right]+\frac{\frac{1}{4\pi}\left(\text{integral}\right)_{f,i,j}^{p}}{\Lambda_f}+\frac{I_{f,i,j,m,n}^{--,p}}{v_f\Delta t} \end{aligned} \tag{4.13}$$

where, $\left(\text{integral}\right)_{f,i,j}^{p}=\int_0^{2\pi}\int_0^{\pi} I_f^p \sin\theta d\theta d\phi$.

In the above equations it may be observed that coefficients of all the intensities are positive. This is a necessary condition for convergence. This is evident in the equation for first quadrant. In the second quadrant equation, the coefficient of $I_{f,i+1,j,m,n}^{-+,p}$ is apparently negative but it is to noted that this equation is valid for $\pi/2 < \theta < \pi$ and hence the coefficient $-\cos\theta_m/\Delta x$ turns out to be positive. The coefficient of $I_{f,i,j+1,m,n}^{+-,p}$ appears to be negative in equation of third quadrant, but as it is valid for the range $0<\theta<\pi/2, \pi<\phi<2\pi$, therefore, the coefficient $-\sin\theta_m \sin\phi_n / \Delta z$ become positive. The equation written for fourth quadrant it seems that the coefficient of $I_{f,i+1,j,m,n}^{--,p}$ and $I_{f,i,j+1,m,n}^{--,p}$ are negative since the range of this equation is $\pi/2<\theta<\pi, \pi<\phi<2\pi$, therefore, coefficients $-\cos\theta_m / \Delta x$ and $-\sin\theta_m \sin\phi_n / \Delta z$ are become positive.

c) The Integral Term

The integral term $(\text{integral})_{f,i,j}^{p}$ is given as,

$$(\text{integral})_{f,i,j}^{p} = \begin{bmatrix} \int_0^{\pi}\int_0^{\pi/2} I_f^{++,p} \sin\theta d\theta d\phi + \int_0^{\pi}\int_{\pi/2}^{\pi} I_f^{-+,p} \sin\theta d\theta d\phi \\ \int_{\pi}^{2\pi}\int_0^{\pi/2} I_f^{+-,p} \sin\theta d\theta d\phi + \int_{\pi}^{2\pi}\int_{\pi/2}^{\pi} I_f^{--,p} \sin\theta d\theta d\phi \end{bmatrix} \tag{4.14}$$

It is evaluated into two steps, first step is the integration over the θ and in second step integration is performed over ϕ. Integration is evaluated by means of the Simpson's Rule.

<u>First Step:</u>(Integration over θ)

It is assume that,

$$\begin{aligned} A_f^{++,p} &= \int_0^{\pi/2} I_f^{++,p} \sin\theta d\theta, \quad A_f^{-+,p} = \int_{\pi/2}^{\pi} I_f^{-+,p} \sin\theta d\theta \\ A_f^{+-,p} &= \int_0^{\pi/2} I_f^{+-,p} \sin\theta d\theta, \quad A_f^{--,p} = \int_{\pi/2}^{\pi} I_f^{--,p} \sin\theta d\theta \end{aligned} \tag{4.15}$$

The integration over θ can be evaluated from the following equations,

$$A^{++,p}_{f,i,j,n} = \left(I^{++,p}_{f,i,j,1,n} + 4\text{x}\sum_{l=1}^{n_\theta/2} I^{++,p}_{f,i,j,2l,n} + 2\text{x}\sum_{l=1}^{(n_\theta-2)/2} I^{++,p}_{f,i,j,2l+1,n} + I^{++,p}_{f,i,j,n_\theta+1,n} \right)\text{x}\,\frac{\Delta\theta}{3} \tag{4.16}$$

$$A^{-+,p}_{f,i,j,n} = \left(I^{-+,p}_{f,i,j,n_\theta+1,n} + 4\text{x}\sum_{l=1}^{n_\theta/2} I^{-+,p}_{f,i,j,n_\theta+2l,n} + 2\text{x}\sum_{l=1}^{(n_\theta-2)/2} I^{-+,p}_{f,i,j,n_\theta+2l+1,n} + I^{-+,p}_{f,i,j,2n_\theta+1,n} \right)\text{x}\,\frac{\Delta\theta}{3} \tag{4.17}$$

$$A^{+-,p}_{f,i,j,n} = \left(I^{+-,p}_{f,i,j,1,n} + 4\text{x}\sum_{l=1}^{n_\theta/2} I^{+-,p}_{f,i,j,2l,n} + 2\text{x}\sum_{l=1}^{(n_\theta-2)/2} I^{+-,p}_{f,i,j,2l+1,n} + I^{+-,p}_{f,i,j,n_\theta+1,n} \right)\text{x}\,\frac{\Delta\theta}{3} \tag{4.18}$$

$$A^{--,p}_{f,i,j,n} = \left(I^{--,p}_{f,i,j,n_\theta+1,n} + 4\text{x}\sum_{l=1}^{n_\theta/2} I^{--,p}_{f,i,j,n_\theta+2l,n} + 2\text{x}\sum_{l=1}^{(n_\theta-2)/2} I^{--,p}_{f,i,j,n_\theta+2l+1,n} + I^{--,p}_{f,i,j,2n_\theta+1,n} \right)\text{x}\,\frac{\Delta\theta}{3} \tag{4.19}$$

<u>Second Step:</u>(Integration over ϕ)

It is assume that,

$$\begin{aligned} B_f^{++} &= \int_0^{\pi} A_f^{++,p}\phi d\phi \ , \quad B_f^{-+} = \int_0^{\pi} A_f^{-+,p}\phi d\phi \\ B_f^{+-} &= \int_{\pi}^{2\pi} A_f^{+-,p}\phi d\phi , \quad B_f^{--} = \int_{\pi}^{2\pi} A_f^{--,p}\phi d\phi \end{aligned} \tag{4.20}$$

The integration over ϕ can be evaluated from the following equations

$$B^{++,p}_{f,i,j} = \left(A^{++,p}_{f,i,j,1} + 4\text{x}\sum_{l=1}^{n_\phi/2} A^{++,p}_{f,i,j,2l} + 2\text{x}\sum_{l=1}^{(n_\phi-2)/2} A^{++,p}_{f,i,j,2l+1} + A^{++,p}_{f,i,j,n_\phi+1} \right)\text{x}\,\frac{\Delta\phi}{3} \tag{4.21}$$

$$B^{-+,p}_{f,i,j} = \left(A^{-+,p}_{f,i,j,1} + 4\text{x}\sum_{l=1}^{n_\phi/2} A^{-+,p}_{f,i,j,2l} + 2\text{x}\sum_{l=1}^{(n_\phi-2)/2} A^{-+,p}_{f,i,j,2l+1} + A^{-+,p}_{f,i,j,n_\phi+1} \right)\text{x}\,\frac{\Delta\phi}{3} \tag{4.22}$$

$$B_{f,i,j}^{+-,p} = \left(A_{f,i,j,n_\phi+1}^{+-,p} + 4\text{x}\sum_{l=1}^{n_\phi/2} A_{f,i,j,n_\phi+2l}^{+-,p} + 2\text{x}\sum_{l=1}^{(n_\phi-2)/2} A_{f,i,j,n_\phi+2l+1}^{+-,p} + A_{f,i,j,2n_\phi+1}^{+-,p} \right) \text{x}\,\frac{\Delta\phi}{3} \tag{4.23}$$

$$B_{f,i,j}^{--,p} = \left(A_{f,i,j,n_\phi+1}^{--,p} + 4\text{x}\sum_{l=1}^{n_\phi/2} A_{f,i,j,n_\phi+2l}^{--,p} + 2\text{x}\sum_{l=1}^{(n_\phi-2)/2} A_{f,i,j,n_\phi+2l+1}^{--,p} + A_{f,i,j,2n_\phi+1}^{--,p} \right) \text{x}\,\frac{\Delta\phi}{3} \tag{4.24}$$

The frequency dependent integral term has to be evaluated at each discrete coordinate values of x_i, z_j and time t_p for a specific frequency, can be given by,

$$\left(\text{integral}\right)_{f,i,j}^{p} = B_{f,i,j}^{++,p} + B_{f,i,j}^{-+,p} + B_{f,i,j}^{+-,p} + B_{f,i,j}^{--,p} \tag{4.25}$$

d) Final Form of the Discretized Euqtaions

The final form of the discretized equation may be written in a much simplified form as explained now. The discretized from of EPRT may be written as,

First Quadrant: $\left(0 < \theta < \pi/2\,,\, 0 < \phi < \pi\right)$

$$a_{f,m,n} I_{f,i,j,m,n}^{++,p} = b_m I_{f,i-1,j,m,n}^{++,p} + c_{m,n} I_{f,i,j-1,m,n}^{++,p} + d_{f,i,j,m,n}^{p} \tag{4.26}$$

where, $i = 2,3,\ldots n_x + 1,\ j = 2,\ldots n_z + 1,$
$m = 1,2,\ldots n_\theta + 1, n = 1,2,\ldots n_\phi + 1,\ p = 2,3,\ldots n_t + 1$

Second Quadrant: $\left(\pi/2 < \theta < \pi,\, 0 < \phi < \pi\right)$

$$a_{f,m,n} I_{f,i,j,m,n}^{-+,p} = b_m I_{f,i+1,j,m,n}^{-+,p} + c_{m,n} I_{f,i,j-1,m,n}^{-+,p} + e_{f,i,j,m,n}^{p} \tag{4.27}$$

where, $i = 2,3,\ldots n_x + 1,\ j = 1,2,\ldots n_z,$
$m = n_\theta + 1, n_\theta + 2,\ldots 2n_\theta + 1, n = 1,2,\ldots n_\phi + 1,\ p = 2,3,\ldots n_t + 1$

Third Quadrant: $\left(0 < \theta < \pi/2\,,\ \pi < \phi < 2\pi\right)$

$$a_{f,m,n} I^{+-,p}_{f,i,j,m,n} = b_m I^{+-,p}_{f,i-1,j,m,n} + c_{m,n} I^{+-,p}_{f,i,j+1,m,n} + g^{p}_{f,i,j,m,n} \tag{4.28}$$

where, $i = 1, 2, \ldots n_x,\ j = 2, \ldots n_z + 1,$
$m = 1, 2, \ldots n_\theta + 1, n = n_\phi + 1, n_\phi + 2, \ldots 2n_\phi + 1, p = 2, 3, \ldots n_t + 1$

Fourth Quadrant: $\left(\pi/2 < \theta < \pi,\ \pi < \phi < 2\pi\right)$

$$a_{f,m,n} I^{--,p}_{f,i,j,m,n} = b_m I^{--,p}_{f,i+1,j,m,n} + c_{m,n} I^{--,p}_{f,i,j+1,m,n} + h^{p}_{f,i,j,m,n} \tag{4.29}$$

where, $i = 1, 2, \ldots n_x,\ j = 1, 2, \ldots n_z, m = n_\theta + 1, n_\theta + 2, \ldots 2n_\theta + 1,$
$n = n_\phi + 1, n_\phi + 2, \ldots 2n_\phi + 1, p = 2, 3, \ldots n_t + 1$

The coefficient of above equations can be defined as,

$$\begin{gathered} a_{f,m,n} = \left(\frac{1}{v_f \Delta t} + \frac{\left|\cos\theta_m\right|}{\Delta x} + \frac{\left|\sin\theta_m \sin\phi_n\right|}{\Delta z} + \frac{1}{\Lambda_f} \right) \quad , \\ b_{f,m} = \frac{\left|\cos\theta_m\right|}{\Delta x},\ c_{f,m,n} = \frac{\left|\sin\theta_m \sin\phi_n\right|}{\Delta z} \end{gathered} \tag{4.30}$$

And the last terms of right hand side of above equation can be defined as,

$$\begin{gathered} d^{p}_{f,i,j,m,n} = \frac{\left(\text{integral}\right)^{p}_{f,i,j}}{\Lambda_f} + \frac{I^{++,p-1}_{f,i,j,m,n}}{v_f \Delta t} \quad , e^{p}_{f,i,j,m,n} = \frac{\left(\text{integral}\right)^{p}_{f,i,j}}{\Lambda_f} + \frac{I^{-+,p-1}_{f,i,j,m,n}}{v_f \Delta t}\,, \\ g^{p}_{f,i,j,m,n} = \frac{\left(\text{integral}\right)^{p}_{f,i,j}}{\Lambda_f} + \frac{I^{+-,p-1}_{f,i,j,m,n}}{v_f \Delta t},\ h^{p}_{f,i,j,m,n} = \frac{\left(\text{integral}\right)^{p}_{f,i,j}}{\Lambda_f} + \frac{I^{--,p}_{f,i,j,m,n}}{v_f \Delta t} \end{gathered} \tag{4.31}$$

e) Ingeration over Frequency

Please note that procedure which describe in above equations has to apply on each frequency of all four phonon branches dielectric material that is longitudinal acoustic, transverse acoustic, longitudinal optical and transverse optical. The overall contribution from of all phonon branches at a specific frequency is given by,

$$\left(integral_{f,i,j}^{p}\right)_{total}=\begin{bmatrix}\left(integral_{f,i,j}^{p}\right)_{LA}+2\left(integral_{f,i,j}^{p}\right)_{TA}\\+\left(integral_{f,i,j}^{p}\right)_{LO}+2\left(integral_{f,i,j}^{p}\right)_{TO}\end{bmatrix}\qquad(4.32)$$

where $\left(integral_{f,i,j}^{p}\right)_{total}$ represents the contribution by all six branches, subscript *LA* represents longitudinal acoustic , *TA* indicate transverse acoustic, *LO* indicate longitudinal optical , *TO* represents transverse optical.

The final form of the integral, in terms of the in terms of the grid point values for a specific time can be find out incorporating the Simpson's Rule.

$$\left\langle Integral_{i,j}^{p}\right\rangle=\begin{bmatrix}\left(integral_{1,i,j}^{p}\right)_{total}+\left(4\text{x}\sum_{l=1}^{n_{\omega}/2}\left(integral_{2l,i,j}^{p}\right)_{total}\right)\\+\left(2\text{x}\sum_{l=1}^{(n_{\omega}-2)/2}\left(integral_{2l+1,i,j}^{p}\right)_{total}\right)+\left(integral_{n_{\omega}+1,i,j}^{p}\right)_{total}\end{bmatrix}\text{x}\,\frac{\Delta\omega}{3}\qquad(4.33)$$

4.1.3. Solution of Discretized Equation

The intensities at the end-points of the spatial domain, i.e., at the films boundary, are known then the intensities at different discrete values within the film, at each time step, may be found by starting from the intensities at the surfaces and then 'marching' through the entire spatial domain to obtain all the intensities. This 'marching' has to be done separately in all direction of the discrete θ and ϕ, corresponding to the discrete values θ_m and ϕ_n respectively. The given intensities at the boundary corresponding to the temperature at boundary, are the same in all direction corresponding to θ_m and ϕ_n, at the boundary. The reason for this is that the surfaces are diffuse and scatter phonons diffusely i.e. with out any preferred directions. This aspect of the numerical solution is not difficult. When solving the EPRT within the film, there are no boundary conditions to be satisfied for the $\theta$and ϕ variables and the intensities in each direction are a function of θ_m and ϕ_n. The difficulty arises due to the presence of the integral term. Since, to find the intensities from the discretized EPRT equations the integral should be have to be first guessed at all values of the discrete coordinates $\left(x_i, z_j\right)$, and the variables θ_m and ϕ_n. The most obvious guess values of the intensities are those calculated at the previous time step. These guessed intensities are then used to evaluate the integral term at each $\left(x_i, z_j\right)$ for specific frequency of each branch of phonon. The EPRT equations are then solved to obtain better guesses for the intensities for each frequency of each branch of phonon. Then total integral is calculated from equation (4.33). This procedure is repeated until convergence is obtained. The solution process then proceeds to the next time step.

The algorithm for solving the Equation of Phonon Radiative Transfer, given an initial temperature in the domain and known boundary temperatures is given below.

1. Initialized all the intensity incorpoarting the initial condition.

2. Guess the intensity distribution $I^{p}_{\omega,i,j,m,n}$ at current time step, at all values of indices i, j, m and n, excluding the intensities at the boundary that is index numbers $i = 1, i = n_x + 1,\ j = 1$ and $j = n_z + 1$ because of boundary conditon.
3. Using the first quadrant EPRT equation (4.26) to calculate the intensities $I^{++,p}_{\omega,i,j,m,n}$ at all the values of the indices i, j, m and n except at the index $i = 1$ and $j = 1$ as its known from boundary conditon.
4. Using the second quadrant EPRT equation (4.27) to calculate the intensities $I^{-+,p}_{\omega,i,j,m,n}$ at all the values of the indices i, j, m and n except at the index $i = 1$ and $j = n_z + 1$ as its known from boundary conditon.
5. Using the thrid quadrant EPRT equation (4.28) to calculate the intensities $I^{-+,p}_{\omega,i,j,m,n}$ at all the values of the indices i, j, m and n except at the index $i = n_x + 1$ and $j = 1$ as its known from boundary conditon.
6. Using the fourth quadrant EPRT equation (4.29) to calculate the intensities $I^{--,p}_{\omega,i,j,m,n}$ at all the values of the indices i, j, m and n except at the index $i = n_x + 1$ and $j = n_z + 1$ as its known from boundary conditon.
7. Now calculate the $\left\langle Integral^{p}_{i,j} \right\rangle^{r}$.
8. Now calculate the the residual using the following formula,

$$Residual = \left\langle Integral^{p}_{i,j} \right\rangle^{r-1} - \left\langle Integral^{p}_{i,j} \right\rangle^{r} \qquad (4.34)$$

where, r is the iteration number.

9. Now if $Tolerance > Residual$ moved to next time step.otherwise move to step 3 until the convergance of solution.

Please note the in all the simulation $Tolerance = 1\text{x}10^{-6}$. The flow chart of the algorithm is given in Figure 4.3.

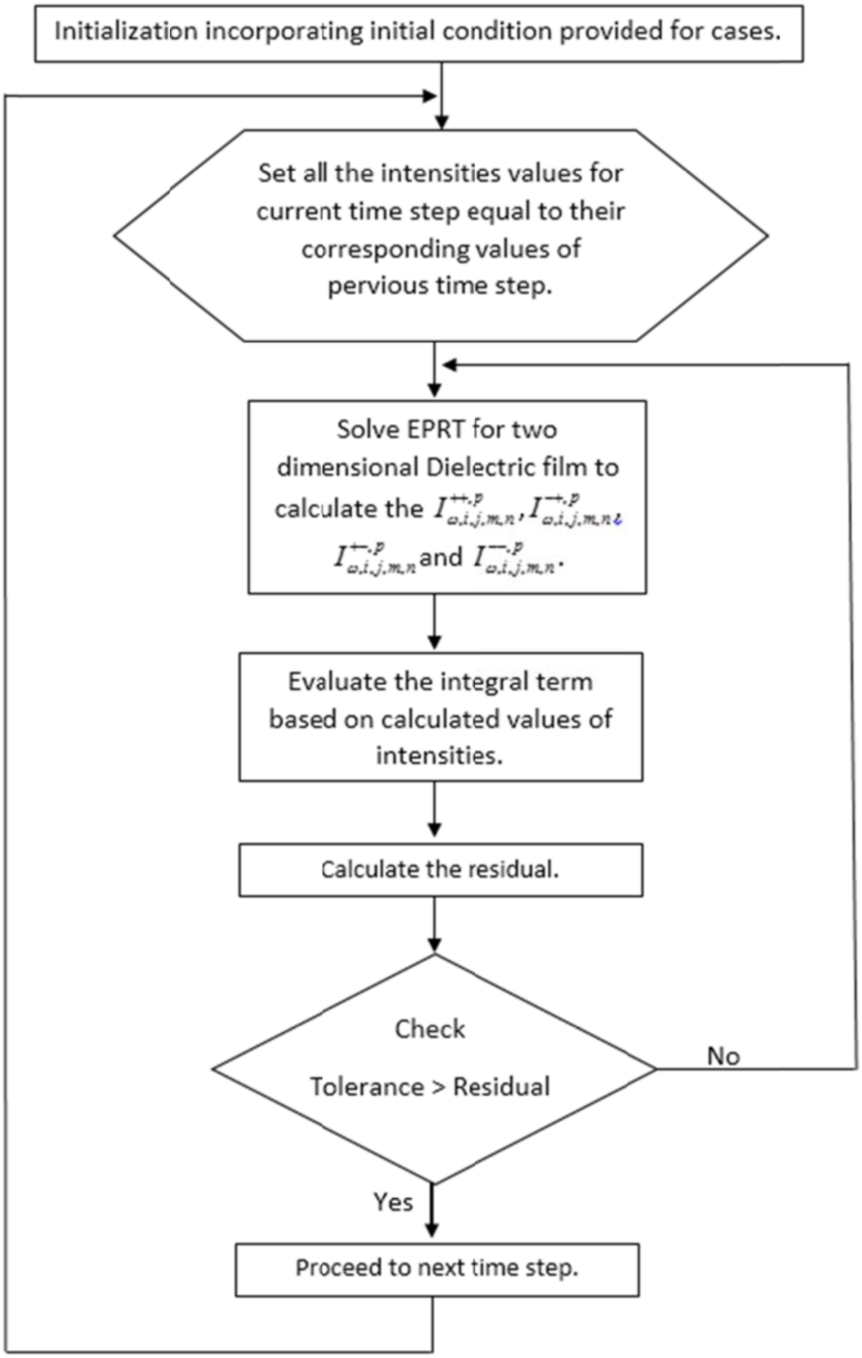

Figure 4.2 Algorithm which incorporated to solve the two dimensional EPRT in dielectric thin films.

4.2 EPRT for One Dimensional Dielectric Films

Consider the phonon radiative transport equation for a particular phonon branch, in the dielectric thin film:

$$\frac{1}{v_\omega}\frac{\partial I_\omega}{\partial t}+\mu\frac{\partial I_\omega}{\partial x}=\frac{\frac{1}{2}\int_{-1}^{1} I_\omega \, d\mu - I_\omega}{\Lambda_\omega} \qquad -1\le\mu\le 1 \tag{4.35}$$

To facilitate the solution of the phonon radiative transport equation, it is customary to break the intensity in to two parts. When $-1\le\mu\le 0, I_\omega = I_\omega^-(x,\mu,t)$ and when $0\le\mu\le 1, I_\omega = I_\omega^+(x,\mu,t)$. Therefore, one may write separate equations for the two intensities. These are given below:

$$\frac{1}{v_\omega}\frac{\partial I_\omega^+}{\partial t}+\mu\frac{\partial I_\omega^+}{\partial x}=\frac{\frac{1}{2}\left(\int_{-1}^{0} I_\omega^- d\mu+\int_{0}^{1} I_\omega^+ d\mu\right)-I_\omega^+}{\Lambda_\omega} \qquad 0\le\mu\le 1 \tag{4.36}$$

$$\frac{1}{v_\omega}\frac{\partial I_\omega^-}{\partial t}+\mu\frac{\partial I_\omega^-}{\partial x}=\frac{\frac{1}{2}\left(\int_{-1}^{0} I_\omega^- d\mu+\int_{0}^{1} I_\omega^+ d\mu\right)-I_\omega^-}{\Lambda_\omega} \qquad -1\le\mu\le 0 \tag{4.37}$$

4.2.1. Domain Discretization

The variable μ is discretized in to $2n_\mu$ number of grid points. Let j be the grid point index, then μ is given as $\mu_j = \left(j - n_\mu - 1\right)/n_\mu$. When $j=1$, $\mu_1=-1$, where as when $j=2n_\mu+1, \mu_{2n_\mu+1}=1$.When we put $j=n_\mu+1$ in the above formula, we obtain, $\mu_{n_\mu+1}=1$. These calculations show that the index numbers $j=2,3,...n_\mu+1$ represent the interval, $-1 \le \mu \le 0$, where as the index numbers $j = n_\mu + 1, n_\mu + 2, ...2n_\mu + 1$ represent the interval, $0 \le \mu \le 1$. Notice that the relation between μ_j and j may also be written as, $\mu_j = \left(j - n_\mu - 1\right)\Delta\mu$, where $\Delta\mu = 1/n_\mu$.

The films thickness, time and frequency are discretized in the same way which described in section 4.1.1.

4.2.2. Discretization of Governing Equation

The discretization of the governing equation which is explained for the two dimensional dielectric films is also applicable for the one dimensional EPRT. Therefore, the governing equation for one dimensional dielectric film is carried out in the similar way which is explained section 4.1.2.

a) Replacement of Derivatives by Algebraic Approximations

$$\frac{1}{v_f}\frac{I_{f,i,j}^{+,p} - I_{f,i,j}^{+,p-1}}{\Delta t} + \mu_j \frac{I_{f,i,j}^{+,p} - I_{f,i-1,j}^{+,p}}{\Delta x} = \frac{\frac{1}{2}\left(\int_{-1}^{0} I_f^{-,p} d\mu + \int_{0}^{1} I_f^{+,p} d\mu\right) - I_{f,i,j}^{+,p}}{\Lambda_f} \tag{4.38}$$

$$\frac{1}{v_f}\frac{I_{f,i,j}^{-,p} - I_{f,i,j}^{-,p-1}}{\Delta t} + \mu_j \frac{I_{f,i+1,j}^{-,p} - I_{f,i,j}^{-,p}}{\Delta x} = \frac{\frac{1}{2}\left(\int_{-1}^{0} I_f^{-,p} d\mu + \int_{0}^{1} I_f^{+,p} d\mu\right) - I_{f,i,j}^{-,p}}{\Lambda_f} \tag{4.39}$$

In the above equations v_f is the frequency dependent group velocity and Λ_f is the frequency dependent mean free path for a specific frequency corresponding to f that is $\omega_f = (f-1)\Delta\omega$.

b) *Simplification of the Algebraic Equaitons*

$$I_{f,i,j}^{+,p}\left(\frac{1}{v_f\Delta t}+\frac{\mu_j}{\Delta x}+\frac{1}{\Lambda_f}\right)=-\frac{\mu_j}{\Delta x}I_{f,i-1,j}^{+,p}+\frac{\frac{1}{2}\left(\int_{-1}^{0}I_f^{-,p}d\mu+\int_0^1 I_f^{+,p}d\mu\right)}{\Lambda_f}+\frac{1}{v_f\Delta t}I_{f,i,j}^{+,p-1} \tag{4.40}$$

$$I_{f,i,j}^{-,p}\left(\frac{1}{v_f\Delta t}-\frac{\mu_j}{\Delta x}+\frac{1}{\Lambda_f}\right)=-\frac{\mu_j}{\Delta x}I_{f,i+1,j}^{-,p}+\frac{\frac{1}{2}\left(\int_{-1}^{0}I_f^{-,p}d\mu+\int_0^1 I_f^{+,p}d\mu\right)}{\Lambda_f}+\frac{1}{v_f\Delta t}I_{f,i,j}^{-,p-1} \tag{4.41}$$

In the above equations it may be observed that coefficients of all the intensities are positive. This is a necessary condition for convergence. In the second equation, the coefficient of $I_{f,i+1,j}^{-,p}$ is apparently negative but it is to noted that this equation is valid for $-1\le\mu\le 0$ and hence the coefficient $-\mu_j/\Delta x$ turns out to be positive.

c) *The Integral Term*

The frequency dependent integral, in terms of the grid point values of the intensities is given below. Notice that the integral has to be evaluated at each coordinate value x_i.

$$\int_0^1 I_f^{+,p}d\mu=\left(I_{f,i,n_\mu+1}^{+,p}+4\text{x}\sum_{l=1}^{n_\mu/2}I_{f,i,n_\mu+2l}^{+,p}+2\text{x}\sum_{l=1}^{(n_\mu-2)/2}I_{f,i,n_\mu+2l+1}^{+,p}+I_{f,i,2n_\mu+1}^{+,p}\right)\text{x}\frac{\Delta\mu}{3} \tag{4.42}$$

$$\int_{-1}^0 I_f^{-,p}d\mu=\left(I_{f,i,1}^{-,p}+4\text{x}\sum_{l=1}^{n_\mu/2}I_{f,i,2l}^{-,p}+2\text{x}\sum_{l=1}^{(n_\mu-2)/2}I_{f,i,2l+1}^{-,p}+I_{f,i,n_\mu+1}^{-,p}\right)\text{x}\frac{\Delta\mu}{3} \tag{4.43}$$

Note that the integral term has to be evaluated at each discrete coordinate values of x_i and time t_p for a specific frequency. Hence, it is useful to write the integral term as,

$$\int_{-1}^{0} I_f^{-,p} d\mu + \int_{0}^{1} I_f^{+,p} d\mu = \text{integral}_{f,i}^{p} \tag{4.44}$$

$$\text{integral}_{f,i}^{p} = \left[\begin{array}{l} \left(I_{f,i,n_\mu+1}^{+,p} + 4\text{x} \sum_{l=1}^{n_\mu/2} I_{f,i,n_\mu+2l}^{+,p} + 2\text{x} \sum_{l=1}^{(n_\mu-2)/2} I_{f,i,n_\mu+2l+1}^{+,p} + I_{f,i,2n_\mu+1}^{+,p} \right) \\ + \left(I_{f,i,1}^{-,p} + 4\text{x} \sum_{l=1}^{n_\mu/2} I_{f,i,2l}^{-,p} + 2\text{x} \sum_{l=1}^{(n_\mu-2)/2} I_{f,i,2l+1}^{-,p} + I_{f,i,n_\mu+1}^{-,p} \right) \end{array} \right] \frac{\Delta\mu}{3} \tag{4.45}$$

d) Final Form of the Discretized Euqtaions

The final form of the discretized equation may be written in a much simplified form as explained now. The discretized from of EPRT may be written as,

$$a_{f,j} I_{f,i,j}^{+,p} = b_j I_{f,i-1,j}^{+,p} + c_{i,j}^{p} \tag{4.46}$$

where, $i = 2,3,...n_x$, $j = 1,2,...n_\mu + 1$, $p = 2,3,...n_t + 1$.

$$a_{f,j} I_{f,i,j}^{-,p} = b_j I_{f,i+1,j}^{-,p} + d_{i,j}^{p} \tag{4.47}$$

where, $i = 2,3,...n_x$, $j = n_\mu + 1, n_\mu + 2, ...2n_\mu + 1$, $p = 2,3,...n_t + 1$.

The coefficient of above equations can be defined as,

$$a_{f,j}=\left(\frac{1}{v_f\Delta t}+\frac{\left|\mu_j\right|}{\Delta x}+\frac{1}{\Lambda_f}\right)\ ,\ b_{f,j}=\frac{\left|\mu_j\right|}{\Delta x} \tag{4.48}$$

And the last terms of right hand side of above equation can be defined as,

$$c_{f,i,j}=\frac{\frac{1}{2}integral_{f,i}^{p}}{\Lambda_f}+\frac{1}{v_f\Delta t}I_{f,i,j}^{+,p-1}\ ,d_{f,i,j}=\frac{\frac{1}{2}integral_{f,i}^{p}}{\Lambda_f}+\frac{1}{v_f\Delta t}I_{f,i,j}^{-,p-1} \tag{4.49}$$

e) Ingeration over Frequency

The overall contribution from of all phonon branches at a specific frequency is given by,

$$\left(integral_{f,i}^{p}\right)_{total}=\begin{bmatrix}\left(integral_{f,i}^{p}\right)_{LA}+2\left(integral_{f,i}^{p}\right)_{TA}\\+\left(integral_{f,i}^{p}\right)_{LO}+2\left(integral_{f,i}^{p}\right)_{TO}\end{bmatrix} \tag{4.50}$$

where $\left(integral_{f,i}^{p}\right)_{total}$ represents the contribution by all six branches, subscript *LA* represents longitudinal acoustic, *TA* indicate transverse acoustic, *LO* indicate longitudinal optical, *TO* represents transverse optical.

The final form of the integral, in terms of the in terms of the grid point values for a specific time is estimated by the Simpson's Rule, which is given as,

$$\left\langle Integral_{i}^{p}\right\rangle=\begin{bmatrix}\left(integral_{1,i}^{p}\right)_{total}+\left(4\text{x}\sum_{l=1}^{n_\omega/2}\left(integral_{2l,i}^{p}\right)_{total}\right)\\+\left(2\text{x}\sum_{l=1}^{(n_\omega-2)/2}\left(integral_{2l+1,i}^{p}\right)_{total}\right)+\left(integral_{n_\omega+1,i}^{p}\right)_{total}\end{bmatrix}\text{x}\frac{\Delta\omega}{3} \tag{4.51}$$

4.2.3. Solution of Discretized Equation

The solution of discretized equation is obtained in the similar way as described in section 4.1.3.

The algorithm for solving the Equation of Phonon Radiative Transfer for one dimensional dielectric film is given below.

1. Initialized all the intensity incorpoarting the initial condition.
2. Guess the intensity distribution $I^{p}_{\omega,i,j}$ at current time step, at all values of indices i and j, excluding the intensities at the boundary that is index numbers $i=1$ and $i=n_x+1$ because of boundary conditon.
3. Using the forward EPRT equation (4.36) or (4.46), calculate the forward intensity $I^{+,p}_{\omega,i,j}$ at all the values of the indices i and j except at the index $i=1$ as its known from boundary conditon.
4. Using the backward EPRT equation (4.37) or(4.47), calculate the backward intensity $I^{-,p}_{\omega,i,j}$ at all the values of the indices i and j except at the index $i=n_x+1$ as its known from boundary conditon.
5. Now again calculate the $\left\langle Integral^{p}_{i}\right\rangle^{r}$.
6. Now calculate the the residual using the following formula,

$$Residual = \left\langle Integral^{p}_{i}\right\rangle^{r+1} - \left\langle Integral^{p}_{i}\right\rangle^{r} \tag{4.52}$$

7. Now if $Tolerance > Residual$ moved to next time step.otherwise move to step 3 until the convergance of solution.

Please note the in all the simulation $Tolerance = 1\text{x}10^{-6}$. The flow chart of the algorithm is given in Figure 4.3.

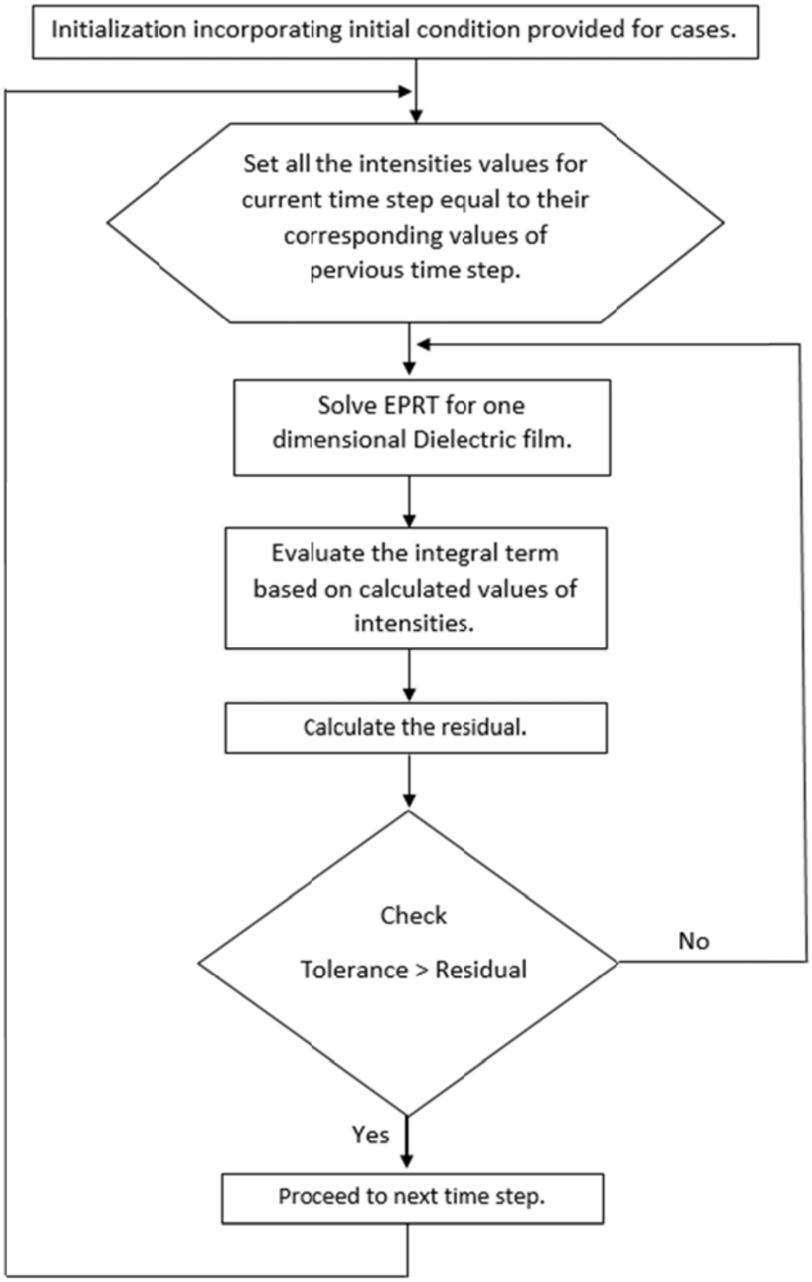

Figure 4.3 Algorithm which is incorporated for the solution of EPRT for one dimensional dielectric thin films.

4.3 EPRT for One Dimensional Metallic Films

The governing equations in the metallic films are the lattice and electron sub-systems EPRTs. In this section numerical method is presented which is used to solve these governing equations.

4.3.1. Lattice Sub-System

Consider the phonon radiative transport equation for lattice sub-system for particular phonon branch, in the metallic thin film:

$$\frac{1}{v_{ph,k}}\frac{\partial I_{ph,k}}{\partial t}+\mu\frac{\partial I_{ph,k}}{\partial x}=\frac{\frac{1}{2}\int_{-1}^{1} I_{ph,k}\,d\mu-I_{ph,k}}{\Lambda_{ph,k}}-G_k \qquad -1\le\mu\le 1 \qquad (4.53)$$

where, $G_k=\frac{G}{4\pi}\frac{\left(T_{ph}-T_e\right)}{3k_{\max}}$. To facilitate the solution of the phonon radiative transport equation, it is customary to break the intensity in to two parts. When $-1\le\mu\le 0$, $I_{ph,k}=I^{-}_{ph,k}(x,\mu,t)$ and when $0\le\mu\le 1$, $I_{ph,k}=I^{+}_{ph,k}(x,\mu,t)$. Therefore, one may write separate equations for the two intensities. These are given below:

$$\frac{1}{v_{ph,k}}\frac{\partial I^{+}_{ph,k}}{\partial t}+\mu\frac{\partial I^{+}_{ph,k}}{\partial x}=\frac{\frac{1}{2}\left(\int_{-1}^{0} I^{-}_{ph,k}d\mu+\int_{0}^{1} I^{+}_{ph,k}d\mu\right)-I^{+}_{ph,k}}{\Lambda_{ph,k}}-G_k \qquad 0\le\mu\le 1 \qquad (4.54)$$

$$\frac{1}{v_{ph,k}}\frac{\partial I^{-}_{ph,k}}{\partial t}+\mu\frac{\partial I^{-}_{ph,k}}{\partial x}=\frac{\frac{1}{2}\left(\int_{-1}^{0} I^{-}_{ph,k}d\mu+\int_{0}^{1} I^{+}_{ph,k}d\mu\right)-I^{-}_{ph,k}}{\Lambda_{ph,k}}-G_k \qquad -1\le\mu\le 0 \qquad (4.55)$$

4.3.1.1. Discretization of Domain and Governing Equation of Lattice Sub-System

The domain and governing equations are discretized in the similar way which is explained in section 4.2.1 and 4.2.2. As the lattice sub-system governing equation contains the electron-phonon coupling term, therefore discretized equations are provided.

a) Replacement of Derivatives by Algebraic Approximations

$$\frac{1}{v_{ph,f}}\frac{I^{+,p}_{ph,f,i,j}-I^{+,p-1}_{ph,f,i,j}}{\Delta t}+\mu_j\frac{I^{+,p}_{ph,f,i,j}-I^{+,p}_{ph,f,i-1,j}}{\Delta x} = \frac{\frac{1}{2}\left(\int_{-1}^{0}I^{-}_{ph,f}d\mu+\int_{0}^{1}I^{+}_{ph,f}d\mu\right)-I^{+,p}_{ph,f,i,j}}{\Lambda_{ph,f}}-G_k \tag{4.56}$$

and

$$\frac{1}{v_{ph,f}}\frac{I^{-,p}_{ph,f,i,j}-I^{-,p-1}_{ph,f,i,j}}{\Delta t}+\mu_j\frac{I^{-,p}_{ph,f,i+1,j}-I^{-,p}_{ph,f,i,j}}{\Delta x} = \frac{\frac{1}{2}\left(\int_{-1}^{0}I^{-}_{ph,f}d\mu+\int_{0}^{1}I^{+}_{ph,f}d\mu\right)-I^{-,p}_{ph,f,i,j}}{\Lambda_{ph,f}}-G_k \tag{4.57}$$

In the above equations $v_{ph,f}$ is the frequency(wavenumber) dependent group velocity of phonon sub-systems and $\Lambda_{ph,f}$ is the frequency (wavenumber) dependent mean free path of phonon sub-systems for a specific frequency corresponding to f that is $k_f=(f-1)\Delta k.$

b) Simplification of the Algebraic Equaitons

$$
\begin{aligned}
&I^{+,p}_{ph,f,i,j}\left(\frac{1}{v_{ph,f}\Delta t}+\frac{\mu_j}{\Delta x}+\frac{1}{\Lambda_{ph,f}}\right)= \\
&-\frac{\mu_j}{\Delta x}I^{+,p}_{ph,f,i-1,j}+\frac{\frac{1}{2}\left(\int_{-1}^{0}I^{-,p}_{ph,f}d\mu+\int_{0}^{1}I^{+,p}_{ph,f}d\mu\right)}{\Lambda_{ph,f}}+\frac{1}{v_{ph,f}\Delta t}I^{+,p-1}_{ph,f,i,j}-G_k
\end{aligned}
\tag{4.58}
$$

and

$$
\begin{aligned}
&I^{-,p}_{ph,f,i,j}\left(\frac{1}{v_{ph,f}\Delta t}-\frac{\mu_j}{\Delta x}+\frac{1}{\Lambda_{ph,f}}\right)= \\
&-\frac{\mu_j}{\Delta x}I^{-,p}_{ph,f,i+1,j}+\frac{\frac{1}{2}\left(\int_{-1}^{0}I^{-,p}_{ph,f}d\mu+\int_{0}^{1}I^{+,p}_{ph,f}d\mu\right)}{\Lambda_{ph,f}}+\frac{1}{v_{ph,f}\Delta t}I^{-,p-1}_{ph,f,i,j}-G_k
\end{aligned}
\tag{4.59}
$$

c) The Integral Term

The frequency dependent integral, in terms of the grid point values of the intensities is given below.

$$
\int_{0}^{1}I^{+,p}_{ph,f}d\mu=\left(\begin{array}{l}
I^{+,p}_{ph,f,i,n_\mu+1}+4\text{x}\sum\limits_{l=1}^{n_\mu/2}I^{+,p}_{ph,f,i,n_\mu+2l} \\
+2\text{x}\sum\limits_{l=1}^{(n_\mu-2)/2}I^{+,p}_{ph,f,i,n_\mu+2l+1}+I^{+,p}_{ph,f,i,2n_\mu+1}
\end{array}\right)\text{x}\frac{\Delta\mu}{3}
\tag{4.60}
$$

and

$$
\int_{-1}^{0}I^{-,p}_{ph,f}d\mu=\left(\begin{array}{l}
I^{-,p}_{ph,f,i,1}+4\text{x}\sum\limits_{l=1}^{n_\mu/2}I^{-,p}_{ph,f,i,2l} \\
+2\text{x}\sum\limits_{l=1}^{(n_\mu-2)/2}I^{-,p}_{ph,f,i,2l+1}+I^{-,p}_{ph,f,i,n_\mu+1}
\end{array}\right)\text{x}\frac{\Delta\mu}{3}
\tag{4.61}
$$

It is useful to write the integral term as,

$$
\int_{-1}^{0}I^{-,p}_{ph,f}d\mu+\int_{0}^{1}I^{+,p}_{ph,f}d\mu=\text{integral}^{p}_{ph,f,i}
\tag{4.62}
$$

$$\text{integral}_{ph,f,i}^{p}=\left[\begin{array}{l}\left(\begin{array}{l}I_{ph,f,i,n_\mu+1}^{+,p}+4\mathrm{x}\sum_{l=1}^{n_\mu/2}I_{ph,f,i,n_\mu+2l}^{+,p}\\ +2\mathrm{x}\sum_{l=1}^{(n_\mu-2)/2}I_{ph,f,i,n_\mu+2l+1}^{+,p}+I_{ph,f,i,2n_\mu+1}^{+,p}\end{array}\right)\\ +\left(I_{ph,f,i,1}^{-,p}+4\mathrm{x}\sum_{l=1}^{n_\mu/2}I_{ph,f,i,2l}^{-,p}+2\mathrm{x}\sum_{l=1}^{(n_\mu-2)/2}I_{ph,f,i,2l+1}^{-,p}+I_{ph,f,i,n_\mu+1}^{-,p}\right)\end{array}\right]\frac{\Delta\mu}{3} \tag{4.63}$$

d) *Final Form of the Discretized Euqtaions*

The discretized from of EPRT may be written as,

$$a_{ph,f,j}I_{ph,f,i,j}^{+,p}=b_{ph,j}I_{ph,f,i-1,j}^{+,p}+c_{ph,i,j}^{p}$$

where, $i=2,3,\ldots n_x,\ j=1,2,\ldots n_\mu+1,\ p=2,3,\ldots n_t+1.$ (4.64)

and

$$a_{ph,f,j}I_{ph,f,i,j}^{-,p}=b_{ph,j}I_{ph,f,i+1,j}^{-,p}+d_{ph,i,j}^{p}$$

where, $i=2,3,\ldots n_x,\ j=n_\mu+1,n_\mu+2,\ldots 2n_\mu+1,\ p=2,3,\ldots n_t+1.$ (4.65)

The coefficient of above equations can be defined as,

$$a_{ph,f,j}=\left(\frac{1}{v_{ph,f}\Delta t}+\frac{|\mu_j|}{\Delta x}+\frac{1}{\Lambda_{ph,f}}\right)\ ,\ b_{ph,f,j}=\frac{|\mu_j|}{\Delta x} \tag{4.66}$$

And the last terms of right hand side of above equation can be defined as,

$$\begin{aligned}c_{ph,f,i,j}&=\frac{\frac{1}{2}\,integral_{ph,f,i}^{p}}{\Lambda_{ph,f}}+\frac{1}{v_f\Delta t}I_{ph,f,i,j}^{+,p-1}-\mathrm{G_k},\\ d_{ph,f,i,j}&=\frac{\frac{1}{2}\,integral_{ph,f,i}^{p}}{\Lambda_{ph,f}}+\frac{1}{v_{ph,f}\Delta t}I_{ph,f,i,j}^{-,p-1}-\mathrm{G_k}\end{aligned} \tag{4.67}$$

e) Ingeration over Frequency

Please note that procedure which describe in above equations has to apply on each frequency of both phonon branches metallic material that is longitudinal acoustic and transverse acoustic. The overall contribution from of all phonon branches at a specific frequency is given by,

$$\left(integral_{ph,f,i}^{p}\right)_{total} = \left[\left(integral_{ph,f,i}^{p}\right)_{LA} + 2\left(integral_{ph,f,i}^{p}\right)_{TA}\right] \tag{4.68}$$

where $\left(integral_{f,i}^{p}\right)_{total}$ represents the contribution by all six branches, subscript *LA* represents longitudinal acoustic and *TA* indicate transverse acoustic.

The final form of the integral is,

$$\left\langle Integral_{ph,i}^{p}\right\rangle = \begin{bmatrix} \left(integral_{ph,1,i}^{p}\right)_{total} + \left(4\text{x}\sum_{l=1}^{n_k/2}\left(integral_{ph,2l,i}^{p}\right)_{total}\right) \\ +\left(2\text{x}\sum_{l=1}^{(n_k-2)/2}\left(integral_{ph,2l+1,i}^{p}\right)_{total}\right) + \left(integral_{ph,n_k+1,i}^{p}\right)_{total} \end{bmatrix} \text{x}\,\frac{\Delta k}{3} \tag{4.69}$$

4.3.2. Electron Sub-System

Consider the phonon radiative transport equation for electron sub-system in the metallic thin film:

$$\frac{1}{v_e}\frac{\partial I_e}{\partial t} + \mu\frac{\partial I_e}{\partial x} = \frac{\frac{1}{2}\int_{-1}^{1} I_e d\mu - I_e}{\Lambda_e} - G_e \qquad -1 \le \mu \le 1 \tag{4.70}$$

where, $G_e = \frac{G}{4\pi}\left(T_e - T_p\right)$. To facilitate the solution of the phonon radiative transport equation, it is customary to break the intensity in to two parts. When $-1 \le \mu \le 0$, $I_e = I_e^-(x,\mu,t)$ and when $0 \le \mu \le 1$, $I_e = I_e^+(x,\mu,t)$. Therefore, one may write separate equations for the two intensities. These are given below:

$$\frac{1}{v_e}\frac{\partial I_e^+}{\partial t} + \mu\frac{\partial I_e^+}{\partial x} = \frac{\frac{1}{2}\left(\int_{-1}^{0} I_e^- d\mu + \int_0^1 I_e^+ d\mu\right) - I_e^+}{\Lambda_e} - G_e \qquad 0 \le \mu \le 1 \tag{4.71}$$

$$\frac{1}{v_e}\frac{\partial I_e^-}{\partial t} + \mu\frac{\partial I_e^-}{\partial x} = \frac{\frac{1}{2}\left(\int_{-1}^{0} I_e^- d\mu + \int_0^1 I_e^+ d\mu\right) - I_e^-}{\Lambda_e} - G_e \qquad -1 \le \mu \le 0 \tag{4.72}$$

4.3.2.1. Discretization of Domain and Governing Equation of Electron Sub-System

The domain and governing equations are discretized in the similar way which is explained in section 4.2.1 and 4.2.2. As the electron sub-system governing equation contains the electron-phonon coupling term, therefore discretized equations are provided.

a) *Replacement of Derivatives by Algebraic Approximations*

$$\frac{1}{v_e}\frac{I_{e,i,j}^{+,p} - I_{e,i,j}^{+,p-1}}{\Delta t} + \mu_j\frac{I_{e,i,j}^{+,p} - I_{e,i-1,j}^{+,p}}{\Delta x} = \frac{\frac{1}{2}\left(\int_{-1}^{0} I_e^- d\mu + \int_0^1 I_e^+ d\mu\right) - I_{e,i,j}^{+,p}}{\Lambda_e} - G_e \tag{4.73}$$

and

$$\frac{1}{v_e}\frac{I^{-,p}_{e,i,j} - I^{-,p-1}_{e,i,j}}{\Delta t} + \mu_j \frac{I^{-,p}_{e,i+1,j} - I^{-,p}_{e,i,j}}{\Delta x} = \frac{\frac{1}{2}\left(\int_{-1}^{0} I_e^{-} d\mu + \int_{0}^{1} I_e^{+} d\mu\right) - I^{-,p}_{e,i,j}}{\Lambda_e} - G_k \tag{4.74}$$

In the above equations v_e is the electron velocity and Λ_e is the electron mean free path.

b) Simplification of the Algebraic Equaitons

$$I^{+,p}_{e,i,j}\left(\frac{1}{v_e \Delta t} + \frac{\mu_j}{\Delta x} + \frac{1}{\Lambda_e}\right) = -\frac{\mu_j}{\Delta x} I^{+,p}_{e,i-1,j} + \frac{\frac{1}{2}\left(\int_{-1}^{0} I_e^{-,p} d\mu + \int_{0}^{1} I_e^{+,p} d\mu\right)}{\Lambda_e} + \frac{1}{v_e \Delta t} I^{+,p-1}_{e,i,j} - G_e \tag{4.75}$$

and

$$I^{-,p}_{e,i,j}\left(\frac{1}{v_e \Delta t} - \frac{\mu_j}{\Delta x} + \frac{1}{\Lambda_e}\right) = -\frac{\mu_j}{\Delta x} I^{-,p}_{e,i+1,j} + \frac{\frac{1}{2}\left(\int_{-1}^{0} I_e^{-,p} d\mu + \int_{0}^{1} I_e^{+,p} d\mu\right)}{\Lambda_e} + \frac{1}{v_e \Delta t} I^{-,p-1}_{e,i,j} - G_e \tag{4.76}$$

c) The Integral Term

The integral, in terms of the grid point values of the intensities is given below.

$$\int_{0}^{1} I_e^{+,p} d\mu = \left(I^{+,p}_{e,i,n_\mu+1} + 4\text{x}\sum_{l=1}^{n_\mu/2} I^{+,p}_{e,i,n_\mu+2l} + 2\text{x}\sum_{l=1}^{(n_\mu-2)/2} I^{+,p}_{e,i,n_\mu+2l+1} + I^{+,p}_{e,i,2n_\mu+1} \right)\text{x}\frac{\Delta\mu}{3} \tag{4.77}$$

and

$$\int_{-1}^{0} I_e^{-,p} d\mu = \left(I^{-,p}_{e,i,1} + 4\text{x}\sum_{l=1}^{n_\mu/2} I^{-,p}_{e,i,2l} + 2\text{x}\sum_{l=1}^{(n_\mu-2)/2} I^{-,p}_{e,i,2l+1} + I^{-,p}_{e,i,n_\mu+1} \right)\text{x}\frac{\Delta\mu}{3} \tag{4.78}$$

It is useful to write the integral term as,

$$\int_{-1}^{0} I_e^{-,p} d\mu + \int_{0}^{1} I_e^{+,p} d\mu = \text{integral}^{p}_{e,i} \tag{4.79}$$

$$\text{integral}_{e,i}^{p}=\left[\begin{array}{l}\left(I_{e,i,n_\mu+1}^{+,p}+4\mathrm{x}\sum_{l=1}^{n_\mu/2}I_{e,i,n_\mu+2l}^{+,p}+2\mathrm{x}\sum_{l=1}^{(n_\mu-2)/2}I_{e,i,n_\mu+2l+1}^{+,p}+I_{e,i,2n_\mu+1}^{+,p}\right)\\+\left(I_{e,i,1}^{-,p}+4\mathrm{x}\sum_{l=1}^{n_\mu/2}I_{e,i,2l}^{-,p}+2\mathrm{x}\sum_{l=1}^{(n_\mu-2)/2}I_{e,i,2l+1}^{-,p}+I_{e,i,n_\mu+1}^{-,p}\right)\end{array}\right]\frac{\Delta\mu}{3} \tag{4.80}$$

d) Final Form of the Discretized Euqtaions

The discretized from of EPRT may be written as,

$$a_{e,j}I_{e,i,j}^{+,p}=b_{e,j}I_{e,i-1,j}^{+,p}+c_{e,i,j}^{p} \tag{4.81}$$

where, $i=2,3,...n_x,\ j=1,2,...n_\mu+1, p=2,3,...n_t+1$.

$$a_{e,j}I_{e,i,j}^{-,p}=b_{e,j}I_{e,i+1,j}^{-,p}+d_{e,i,j}^{p} \tag{4.82}$$

where, $i=2,3,...n_x,\ j=n_\mu+1, n_\mu+2,...2n_\mu+1, p=2,3,...n_t+1$.

The coefficient of above equations can be defined as,

$$a_{e,j}=\left(\frac{1}{v_e\Delta t}+\frac{|\mu_j|}{\Delta x}+\frac{1}{\Lambda_e}\right)\ ,\ b_{e,j}=\frac{|\mu_j|}{\Delta x} \tag{4.83}$$

And the last terms of right hand side of above equation can be defined as,

$$\begin{aligned}c_{e,i,j}&=\frac{\frac{1}{2}integral_{e,i}^{p}}{\Lambda_e}+\frac{1}{v_e\Delta t}I_{e,i,j}^{+,p-1}-\mathrm{G_e},\\ d_{e,i,j}&=\frac{\frac{1}{2}integral_{e,i}^{p}}{\Lambda_e}+\frac{1}{v_e\Delta t}I_{e,i,j}^{-,p-1}-\mathrm{G_e}\end{aligned} \tag{4.84}$$

4.3.3. Solution of Governing Equations for Metallic Films

In order to evaluate the thermal characteristic in metallic thin films it is mandatory to solve both the sub-system simultaneously. Therefore, once each sub systems solved to determine the phonon and electron temperature. Then terms related to the electron-phonon coupling term that is G_k and G_e are updated. After this, both sub-systems are solved incorporating the updated values of G_k and G_e. This procedure is repeated until convergence is obtained. The solution process then proceeds to the next time step.

The algorithm for solving the Equation of Phonon Radiative Transfer for both sub-systems, given an initial temperature in the domain and known boundary temperatures is given below.

1. Initialized all the intensity incorpoarting the initial condition for lattice and electron sub systems.
2. Guess the intensity distribution $I_{ph,\omega,i,j}^{p}$ at current time step, at all values of indices i and j, excluding the intensities at the boundary that is index numbers $i=1$ and $i=n_x+1$ because of boundary conditon.
3. Using the forward EPRT equation (4.64), calculate the forward intensity $I_{ph,\omega,i,j}^{+,p}$ at all the values of the indices i and j except at the index $i=1$ as its known from boundary conditon.

4. Using the backward EPRT equation (4.65), calculate the backward intensity $I^{-,p}_{ph,\omega,i,j}$ at all the values of the indices i and j except at the index $i = n_x + 1$ as its known from boundary conditon.

5. Now again calculate the $\left\langle Integral^{p}_{ph,i} \right\rangle^{r}$.

6. Now calculate the the residual of lattice sub-system using the following formula,

$$\left\langle Residual \right\rangle_{ph} = \left| \left\langle Integral^{p}_{ph,i} \right\rangle^{r+1} - \left\langle Integral^{p}_{ph,i} \right\rangle^{r} \right| \tag{4.85}$$

7. Guess the intensity distribution $I^{p}_{e,i,j}$ at current time step, at all values of indices i and j, excluding the intensities at the boundary that is index numbers $i = 1$ and $i = n_x + 1$ because of boundary conditon (insuated at boundary).

8. Using the forward EPRT equation (4.81), calculate the forward intensity $I^{+,p}_{e,i,j}$ at all the values of the indices i and j except at the index $i = 1$ as it comes from insulated boundary conditon.

9. Using the backward EPRT equation(4.82), calculate the backward intensity $I^{-,p}_{e,i,j}$ at all the values of the indices i and j except at the index $i = n_x + 1$ as it comes from insulated boundary conditon.

10. Now calculate the $\left\langle Integral^{p}_{e,i} \right\rangle^{r+1}$ using the

11. Calculate the the residual of electorn sub-system using the following formula,

$$\left\langle Residual \right\rangle_e = \left| \left\langle Integral_{e,i}^{p} \right\rangle^{r+1} - \left\langle Integral_{e,i}^{p} \right\rangle^{r} \right| \tag{4.86}$$

12. Calculate the phonon and electron temperture.
13. Calcuate the update values of G_k and G_e.
14. Again solve lattice and electron sub-system.
15. Now calculate the residual of comibined systems.

$$\left\langle Residual \right\rangle = \max\left[\left\langle Residual \right\rangle_{ph}, \left\langle Residual \right\rangle_e \right] \tag{4.87}$$

16. Now check ,if $Tolerance > Residual$ and $r > 2$, (where r is the iteration no.) then moved to next time step.otherwise move to step 3 until the convergance of solution.

Please note the in all the simulation $Tolerance = 1\text{x}10^{-6}$. The flow chart of the algorithm is given in Figure 4.4.

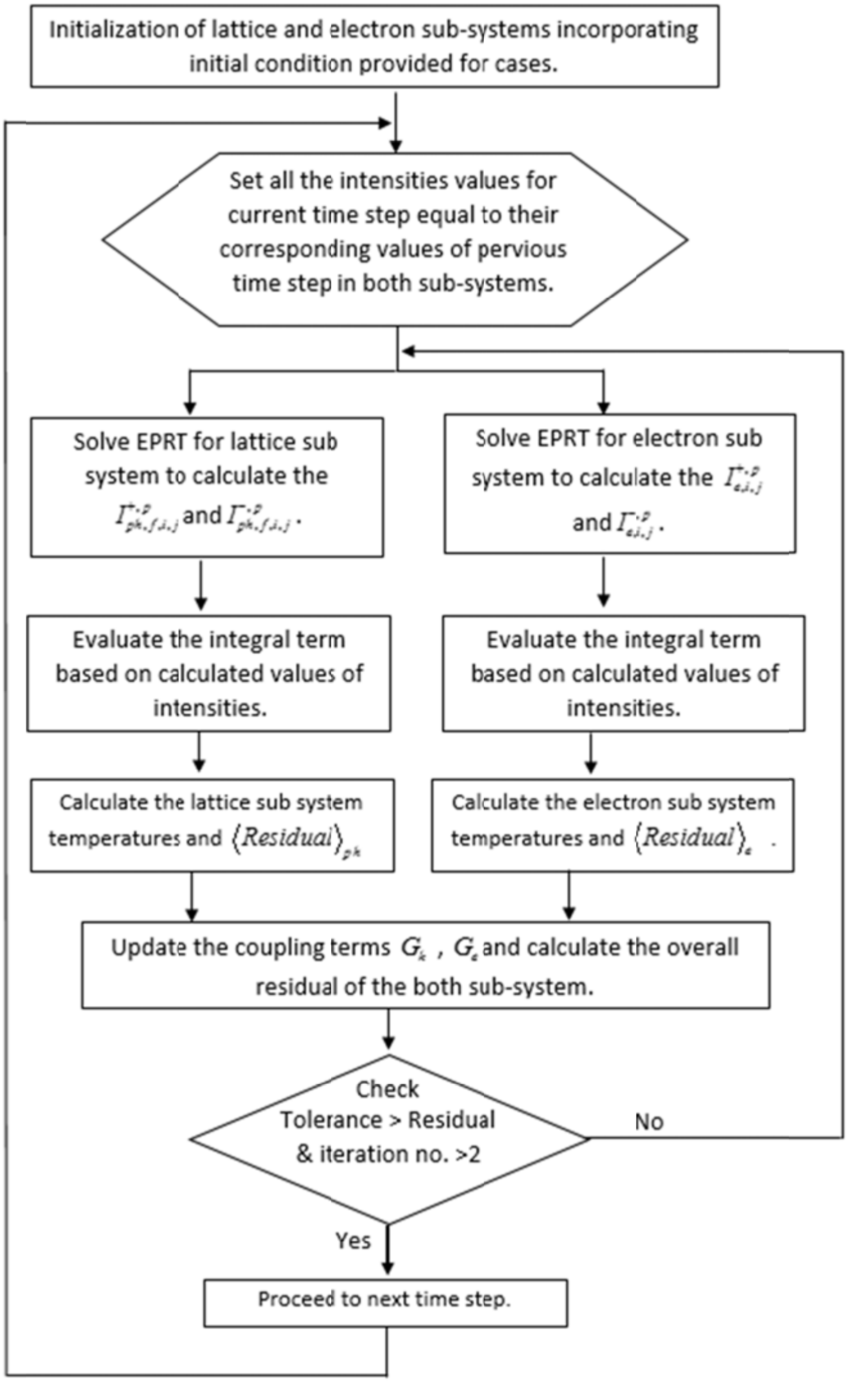

Figure 4.4 Algorithm which incorporated to solve the EPRT in metallic thin films.

CHAPTER 5

RESULTS AND DISCUSSION

This chapter presents the results obtained from all the case studies previously introduced in chapter 3. The chapter consists of three sub-sections. In sub-section 1, results and discussion related to two dimensional dielectric cases are presented. In sub-section 2, results of case studies related to the one dimensional cases are discussed while in sub-section 3, finding of metallic films cases are discussed.

5.1 Two dimensional Dielectric Thin Films

In this section the results of case studies, which are introduced in chapter 3 related to two dimensional dielectric thin films, are presented. All the two dimensional cases are solved incorporating the frequency dependent EPRT along with the initial, boundary and interface conditions which discussed in chapter 3. The case studies are,

1. Steady State Heat Transport Including the Effects of Heat Source Size and Silicon Film Dimension.
2. Transient Heat Transport Including the Effect of Temperature Oscillation in Silicon and Diamond Thin Films.
3. Transient Heat Transport Including the Effects of Pulse Duration of Heat Source in Silicon and Diamond Thin Films.

4. Transient Heat Transport Including the Effects of Thickness and Temparture Oscillations in Diamond Thin Films.
5. Transient Heat Transport Including the Effects of Heat Source Size and Temparture Oscillation in Silicon Thin films.
6. Transient Heat Transport in Silicon and Diamond Thin film Pair Including the Thermal Boundary Resistance.
7. Transient Heat Transport Including Quantum Dot in Silicon Thin Film.

5.1.1 Steady State Heat Transport Including the Effects of Heat Source Size and Silicon Film Dimension

Phonon transport in a two-dimensional silicon thin film with the presence of heat source with different sizes at the film edge is considered and equivalent equilibrium temperature in the film is predicted numerically for various configurations of the heat source locations. The study is extended to include influence of film thickness, due to different arrangements of the heat source size, on phonon transport.

Figure 5.1 shows equivalent equilibrium temperature along the film width (z-axis) for two sizes of the heat source and two-film thicknesses where the x-axis location is the half of the film thickness $\left(L_x = L/2\right)$ while Figure 5.2 and Figure 5.3 shows temperature contours in the film for two heat source sizes and film thicknesses. It should be noted that the film is considered to be square and heat sources are applied from one edge of the film (Figure 3.5).Although the behavior of equivalent equilibrium temperature along the film width is similar, their values differ significantly for two film widths. Equivalent equilibrium temperature attains slightly lower values in the thinner film $(L = 0.1\mu m)$ than that of $1.0\mu m$ thick film. This is associated with the phonon scattering in the film. Since the frequency dependent phonon transport is considered in the analysis, the phonons with large wave lengths do not undergo scattering in the thin film. Consequently, the ballistic phonons do not suffer from the film resistance and do not contribute to temperature increase in the film. The presence of two constant temperature heat sources at one edge of the film modifies temperature distribution in the film, which is more pronounced for the small heat source size (w_s). However, this effect becomes apparent for the thinner film $(L = 0.1\mu m)$ as compared to that of $1.0\mu m$ thick film. This is attributed to the effect of heat source size on the phonon transport; in which case, reducing the heat source suppresses the phonon resistance in the film [56]. Therefore, phonons with large wave length emanating from the heat source do not contribute to the phonon scattering in the film while lowering equivalent equilibrium temperature in the film. As the heat source size increases at the film edge, the spacing between the heat source becomes small and heat source extends over the edge for $w_s = L/2$. In this case, two heat sources reduce to one source alone the edge and the heat source size effect on the phonon transport in the film disappears. Moreover, as the heat source size increases along the film edge, the maximum value of equivalent equilibrium temperature increases and its distribution along z-axis changes. This is associated with the ballistic phonons emanating from the heat source, which modify temperature distribution in the film. This is particularly true for the small heat source size.

Figure 5.4 shows equivalent equilibrium temperature variation along the film thickness (x-axis) for two-film sizes at the z-axis location of $L_z = 0.5L$ (where L is the film size).It should be noted that although the normalized film thickness is presented, the size of each film thickness is different. In addition, the size of the heat source is related to the size of the each film thickness; consequently, the normalized size of the heat source is different for both films. In general, the behavior of equivalent equilibrium temperature is similar for both films, provided that temperature attains low values in thinner film $\left(L = 0.1\,\mu m\right)$. This is attributed to the contribution of the ballistic phonons to energy transport in the film. Since the ballistic phonons do not undergo scattering in the film, the thermal resistance to phonon transport becomes less and temperature increase due to phonon scattering in the film reduces. In addition, temperature jump at the film edges $\left(x = 0\ and\ x = 1\right)$ becomes larger for thinner film than that of $L = 1.0\,\mu m$ thick film. The large wavelength phonons are responsible for the large temperature jump at the edges of the thinner film. In addition, the phonons emitted and reflected, from the low temperature edge of the film, contribute to the temperature jump at low temperature edge of the film $\left(x = 0\right)$.This is more pronounced for the case of the thinner film, i.e. temperature increase (> 300 K) at $x = 0$ is associated with the temperature jump at this edge because of the reflected phonons, which are emitted from the high temperature edge. The effect of the size of the heat source on the phonon transport is considerable; in which case, reducing the heat source size suppresses temperature rise along the x-axis. It should be noted that equivalent equilibrium temperature is presented at z-axis location of $L_z = 0.5L$. Consequently, the spacing between the heat source increases as the heat source size reduces (Figure 3.5). Therefore, phonons emanated from the heat source undergo some scattering prior to reaching the z-axis location $L_z = 0.5L$. This, in turn, suppresses equivalent equilibrium temperature rise along the x-axis at z-axis location of $L_z = 0.5L$.

Figure 5.5 shows effective thermal conductivity $\left(k_{eff}\right)$ variation with the dimensionless heat source size $\left(w_s / L\right)$ for two film thicknesses. The effective thermal conductivity of the film is calculated from the following formula:

$$k_{eff} = \frac{q''_{total} L}{T_{top,high} - T_{bottom}} \tag{5.1}$$

where q''_{total} is the total heat flux, it is the sum of magnitude of heat flux along the mid line of the heated element, L is the length of the silicon of film. q''_{total} can be calculated by taking the first the magnitude of heat flux on every point along the x-axis at $L_{zt} = (L_a + w_s / 2)$.

$$\mathbf{q}''(x) = \sqrt{\left(q''_x(x, z_t)\right)^2 + \left(q''_z(x, z_t)\right)^2} \tag{5.2}$$

q''_{total} is find by integrating the equation (5.2) along the x-axis to get the

$$q''_{total} = \int_{o}^{L} q''(x)dx \tag{5.3}$$

Figure 5.5 showing that reducing film thickness lowers effective thermal conductivity of the film, which is consistent with previous findings [136]. This behavior is related to the ballistic phonons, which do not contribute to the film resistance through scattering during the phonon transport in the film. In the analysis, the heat source size is considered to change with the film size; therefore, the coupling effect of heat source size and the film size influence the effective thermal conductivity behavior, provided that this influence is not significant. This can also be observed when comparing effective thermal conductivity variation along the dimensionless heat source size for two film thicknesses. Moreover, reducing the heat source size modifies the phonon transport in the film, which in turn modifies the thermal resistance of the film and the effective thermal conductivity. Consequently, reducing the heat source size reduces the effective thermal conductivity because of the ballistic phonons which do not undergo scattering in the film. This is particularly true for the thinner film $\left(L_z = 0.5L\right)$, i.e. phonon wavelengths larger than the film thickness do not contribute to the film resistance; however, they contribute to the energy transport from high temperature to the low temperature edges.

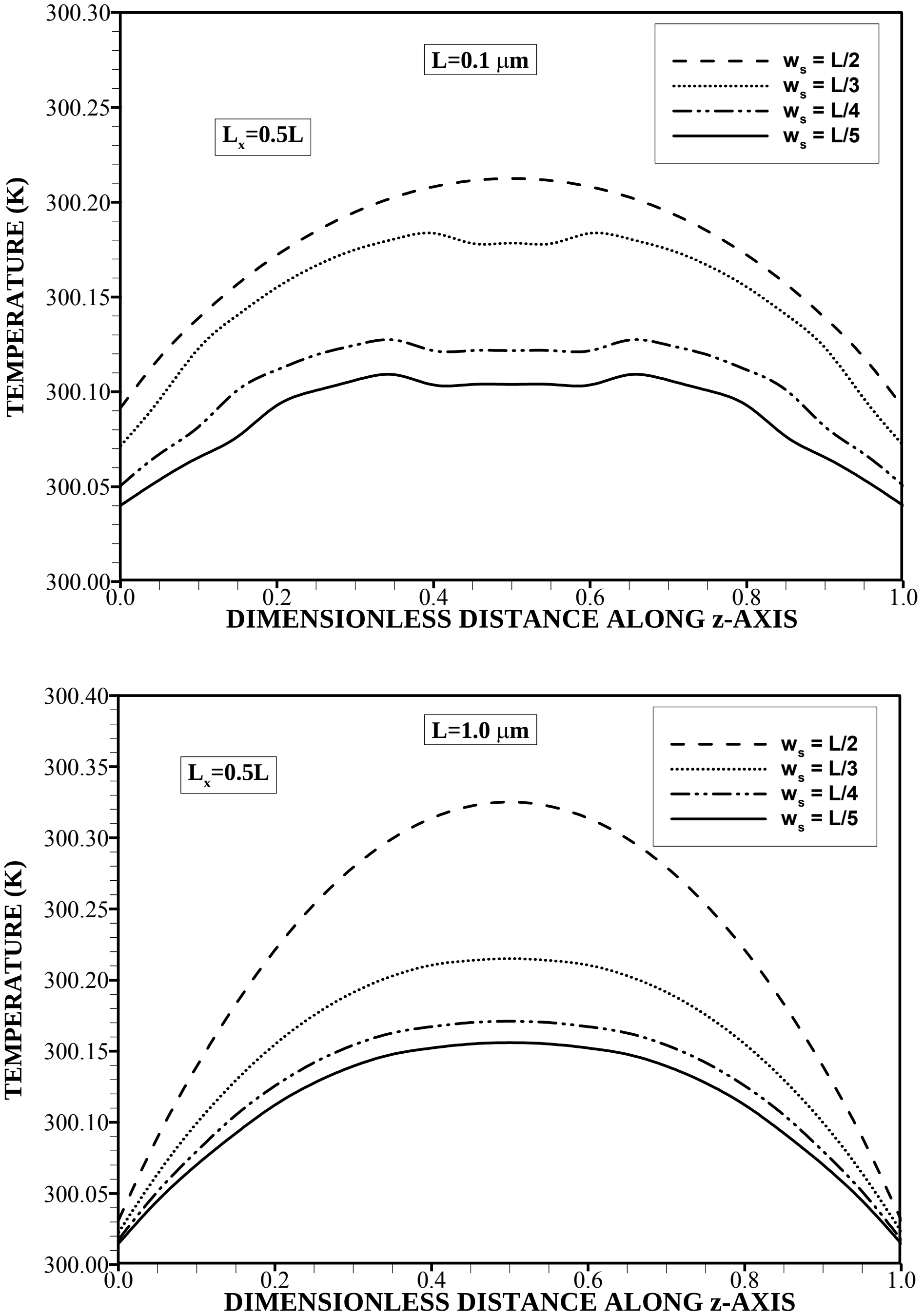

Figure 5.1 Equivalent equilibrium temperature along the normalized film width for different locations of the heat source and two film thicknesses

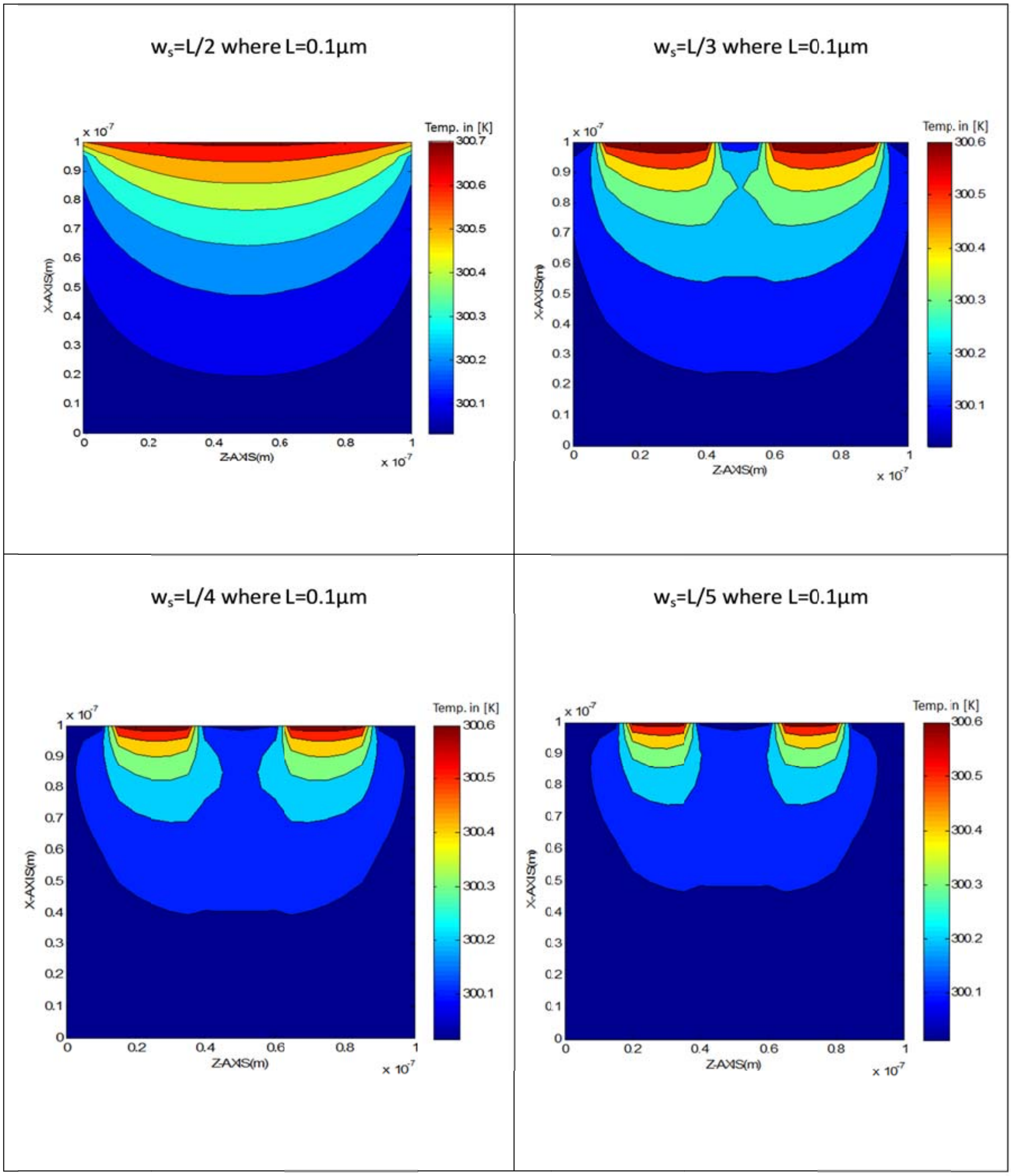
w_s=L/2 where L=0.1μm

w_s=L/3 where L=0.1μm

w_s=L/4 where L=0.1μm

w_s=L/5 where L=0.1μm

Figure 5.2 Equivalent equilibrium temperature contours in the film for different sizes of heat source and for the film thickness of $L = 0.1\mu m$.

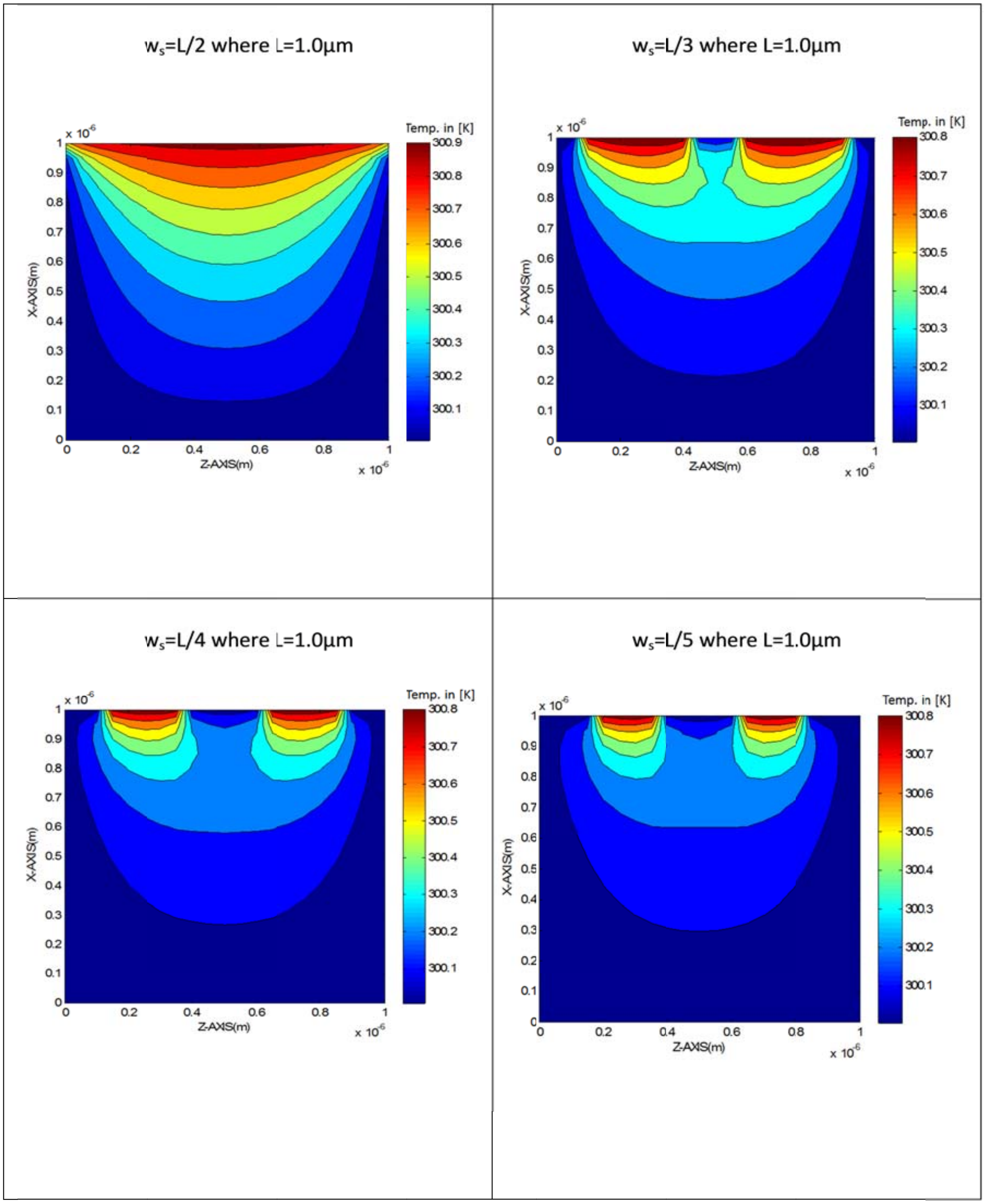

Figure 5.3 Equivalent equilibrium temperature contours in the film for different sizes of heat source and for the film thickness of $L = 0.1\mu m$.

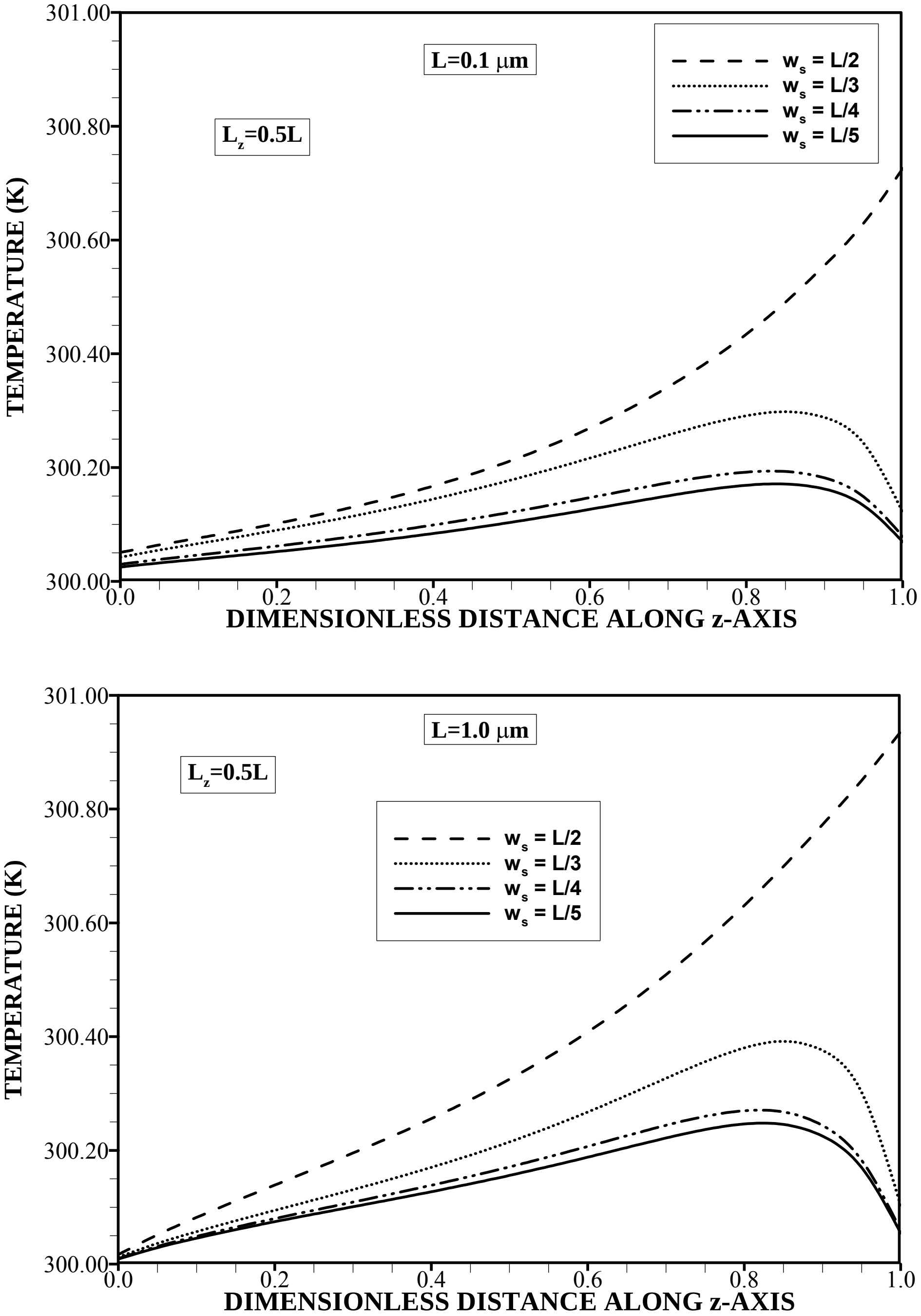

Figure 5.4 Equivalent equilibrium temperature along the normalized film thickness for different locations of the heat source and two film thicknesses.

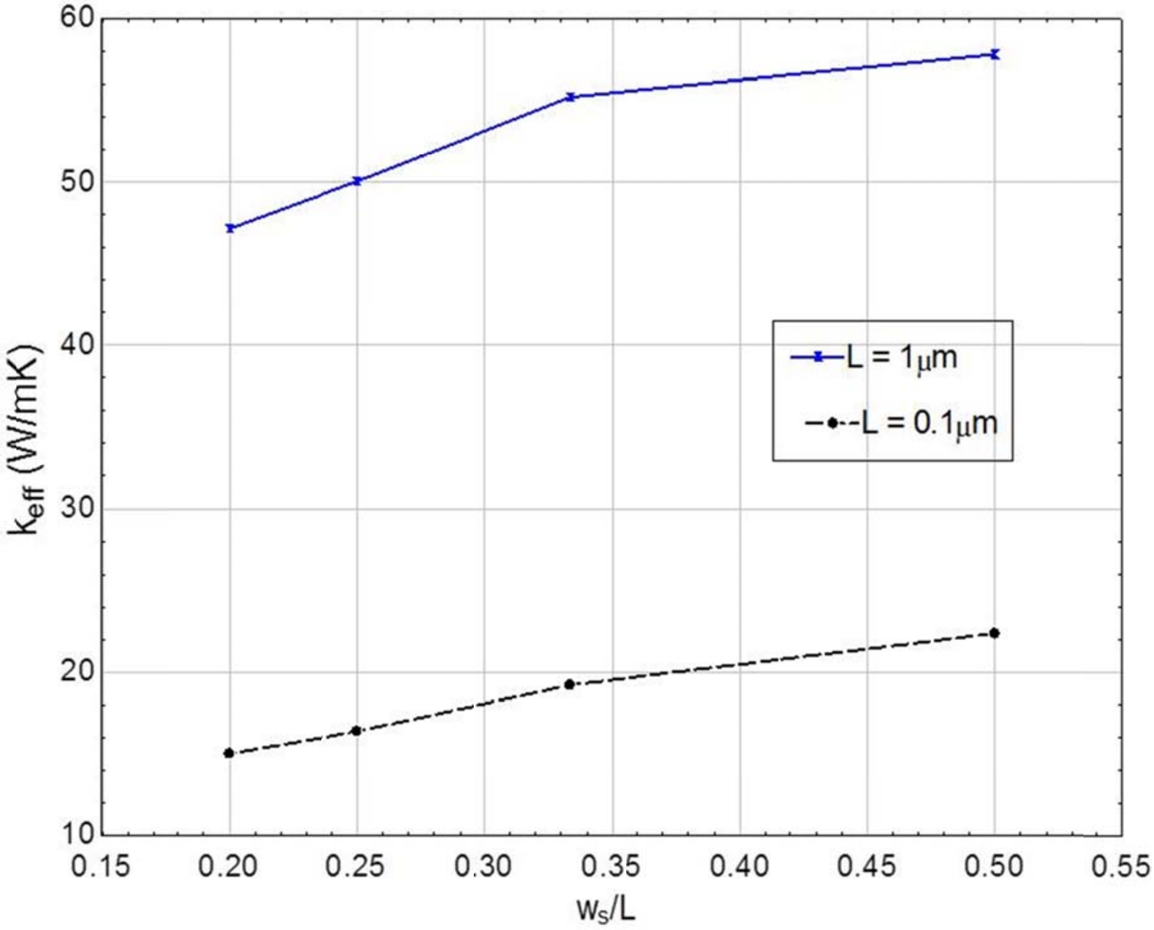

Figure 5.5 Effective thermal conductivity variation with the dimensionless heat source size for two film thicknesses..

5.1.2 Transient Heat Transport Including the Effect of Temperature Oscillation in Silicon and Diamond Thin Films

Phonon transport in two-dimensional silicon and diamond thin films is investigated for temperature pulsation at the film edge. The study is extended to include the effect of pulsing frequency on equivalent equilibrium temperature in the film.

Figure 5.6 shows temporal variation of equivalent equilibrium temperature at x-axis location of x = 0.5L and z-axis location of z = 0.05L, where L is the width of the film, for three different values of the pulse length of the temperature oscillation at the film edge (Figure 3.7). Equivalent equilibrium temperature increases sharply in the early heating period and as the heating period progresses, temperature increase becomes gradual. This is more pronounced for the diamond film. Temperature behavior changes slightly for different pulse lengths of temperature oscillation at the film edge. This behavior is illustrated in small windows in Figure 5.6. Initiation of temperature oscillation occurs in the late heating period; in which case, ripples are observed in the temperature curves. Temperature rippling is more pronounced for the silicon film. The rapid rise of temperature is associated with the phonon intensity at this location, which increases rapidly in the early heating period because of the emitted phonons from the high temperature edge. Although phonon emission from the high temperature film edge follows temperature oscillation, equivalent equilibrium temperature does not oscillate similar to temperature at the film edge during the early heating period $\left(t \le 8ps\right)$. This is attributed to film resistance due to phonon scattering at this location during the early heating period. It should be noted that equivalent equilibrium temperature represents the average energy of all phonons around a local point and it is equivalent to the equilibrium temperature of phonons when they redistribute adiabatically to an equilibrium state. Therefore, adiabatic redistribution of phonon energy to reach equilibrium state does not effect by phonon oscillations at this location during the early heating period. As the time progresses, equivalent equilibrium temperature pulsation (oscillation) becomes visible at this location. This situation can also be seen from Figure 5.7, in which temporal variation of temperature during the period 40 – 80 ps is shown for diamond and silicon films. The time difference (lagging) between the maximum and minimum temperatures in consecutive two temperature oscillations does not follow the pulse duration of temperature oscillation at the film edge. In this case, the time lagging of temperature becomes longer than the pulse length of temperature oscillation at the film edge. This behavior is true for all the pulse lengths incorporated at the film edge. Moreover, as the pulse length of temperature oscillation increases at the film edge, the lagging time of temperature also increases. This behavior is usually observed for the diffusive heat conduction heating situations [137]. Consequently, radiative phonon transport results in similar effect on equilibrium equivalent temperature in the film as it is observed for diffusive transport. Therefore, the consideration of adiabatic redistribution of phonon intensity, in accordance with the definition of the equivalent equilibrium temperature [138], results in diffusive temperature behavior in the film. It should be noted that frequency dependent solution of the radiative phonon transport is considered in the film; therefore, the ballistic phonons do not contribute to the thermal resistance of the film, i.e., their contribution to the diffusive behavior of equivalent equilibrium temperature is not significant. In addition, frequency of phonons, which matches the frequency of temperature oscillation at the film edge, plays important role on the phonon emission from the film edge. Phonons, which are inphase with temperature oscillation frequency at the film edge, do not contribute to the phonon scattering in the film. This, in turn, lowers equivalent equilibrium temperature increase in the film, which can be observed when comparing temperature difference between the maximum and the minimum temperatures along two consecutive equivalent equilibrium temperature at this location in the film. In this case, temperature difference at this location in the film is not the same as the oscillation temperature difference (maximum and minimum temperatures) at the film edge.

Figure 5.8 shows temporal variation of equivalent equilibrium temperature at x-axis location of x = 0.5L and the y-axis location of z = 0.25L, where L is the width of the film, for three different values of the pulse length of temperature oscillation at the film edge (Figure 3.7). Temperature rise in the early heating period is rapid and, then, it becomes gradual as the heating period progresses. As compared to those presented in Figure 5.6 at the location of x = 0.5L and z = 0.05L, temperature rise becomes sharper in Figure 5.8. This is attributed to the location selected in the film, which is x = 0.5L and z = 0.25L; in which case, phonons undergo several scattering prior to reaching this location and the periodic oscillation in equivalent equilibrium temperature, because of temperature oscillation at the film edge, becomes small. This situation can also be seen from Figure 5.9, in which oscillation of equivalent equilibrium temperature is shown during 40–80 ps duration. Although the time lagging of equivalent equilibrium temperature is similar to that is shown in Figure 5.7, the amplitude (the difference between the maximum and the minimum temperature) becomes smaller than that corresponds to Figure 5.7. This behavior is true for all values of the pulse length of temperature oscillation at the film edge. Therefore, as the distance from the film edge increases towards the film center, temperature oscillation almost dies and diffusive behavior of equivalent equilibrium temperature diminishes at this location. This behavior is more pronounced for the silicon film. In the case of diamond film, the different relation time and group velocity, due to dispersion relations, result in slow response of diffusive behavior of equivalent equilibrium temperature in the diamond film. As the distance further increases away from the film edge, time lagging of equivalent equilibrium temperature diminishes in the silicon and the diamond films. This situation can be observed from Figure 5.10, in which temporal variation of equivalent equilibrium temperature is shown at location x = 0.5L and z = 0.5L in the silicon and the diamond films.

Figure 5.11 shows equivalent equilibrium temperature variation along the film width (z-axis) for different values of pulse length of temperature oscillation at the film edge at heating duration t = 15 ps and for the silicon and the diamond thin films. Temperature reduces sharply in the region close to the high temperature edge of the film and temperature decrease becomes gradual as the distance along z-axis increases in the film. In addition, temperature jump is observed at both edges of the film because of emitted and reflected phonons at the film edges [64]. Temperature variation, due to different pulse lengths of temperature oscillation at the film edge, is also shown in a small window in the figure. The variation of equivalent equilibrium temperature along the film width, due to different pulse lengths, is not significant, which is more pronounced for the diamond film. However, small variation is observed in the silicon film, particularly in the near region of the film edge where temperature oscillation takes place. As the depth increases from the film edge, time lagging in equivalent equilibrium temperature disappears. Consequently, phonon scattering in the film creates a damping affect while reducing the temperature lagging in the film. In the case of the heating period t = 45 ps, which is shown in Figure 5.12, similar behavior is observed for equivalent equilibrium temperature along the film width. It should be noted that the amplitude of time lagging of equivalent equilibrium temperature increases slightly in the region close to the film edge at the heating period t = 45 ps. This observation is line with the results shown in Figure 5.12. Consequently, the effect of temperature oscillation on equivalent equilibrium temperature behavior is significant in the near region of the film edge and as the distance increases away from the edge, this effect becomes less significant.

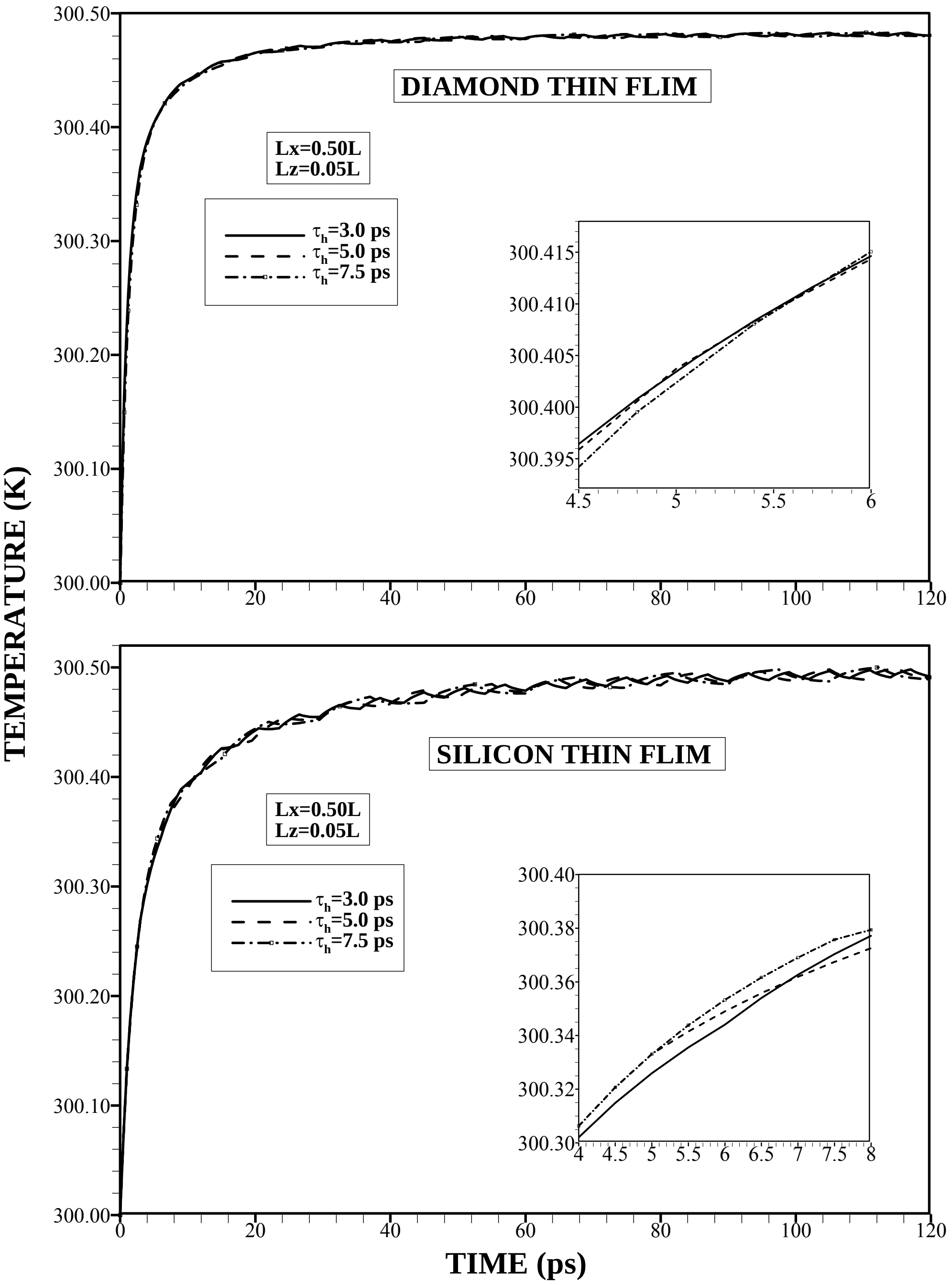

Figure 5.6 Temporal variation of equivalent equilibrium temperature at location Lx = 0.5L and Lz = 0.05L where L is the film width for three different pulse lengths of temperature oscillation at the film edge.

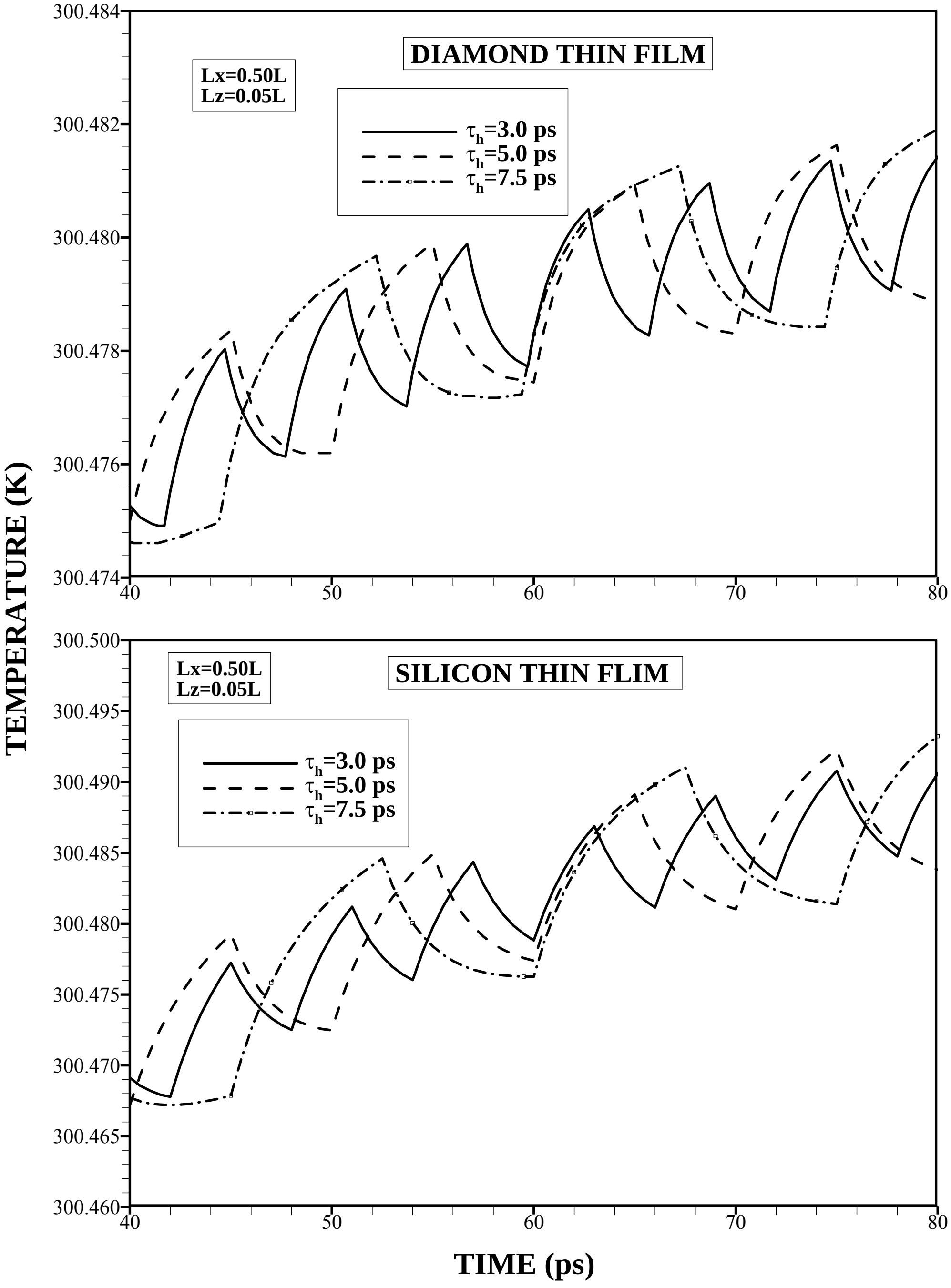

Figure 5.7 Temporal variation of equivalent equilibrium temperature for the time domain 40–60 ps at location Lx = 0.5L and Lz = 0.05L where L is the film width due to three different pulse lengths of temperature oscillation at the film edge.

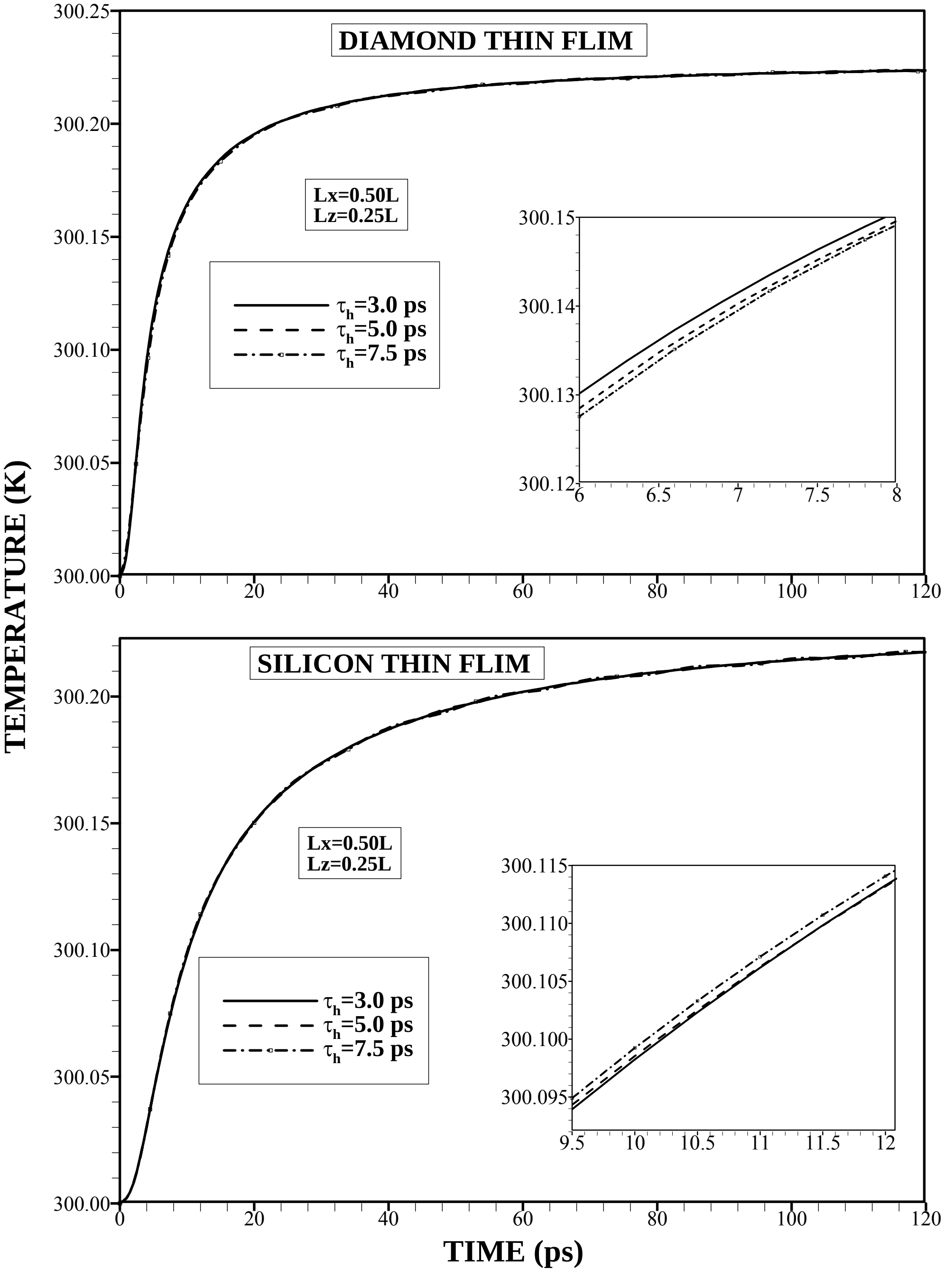

Figure 5.8 Temporal variation of equivalent equilibrium temperature at location Lx = 0.5L and Lz = 0.25L where L is the film width for three different pulse lengths of temperature oscillation at the film edge.

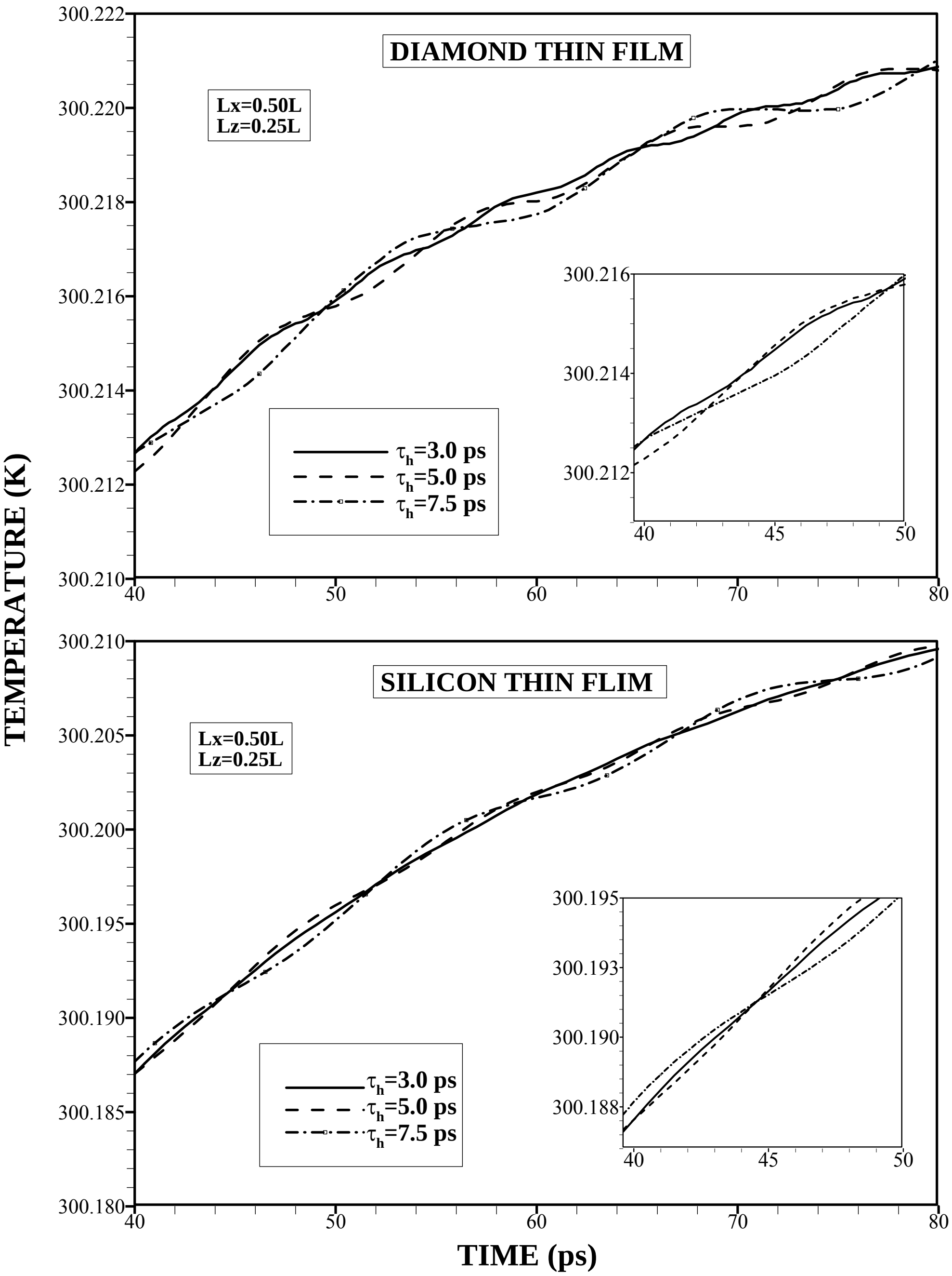

Figure 5.9 Temporal variation of equivalent equilibrium temperature for the time domain 40 – 60 ps at location Lx = 0.5L and Lz = 0.25L where L is the film width due to three different pulse lengths of temperature oscillation at the film edge.

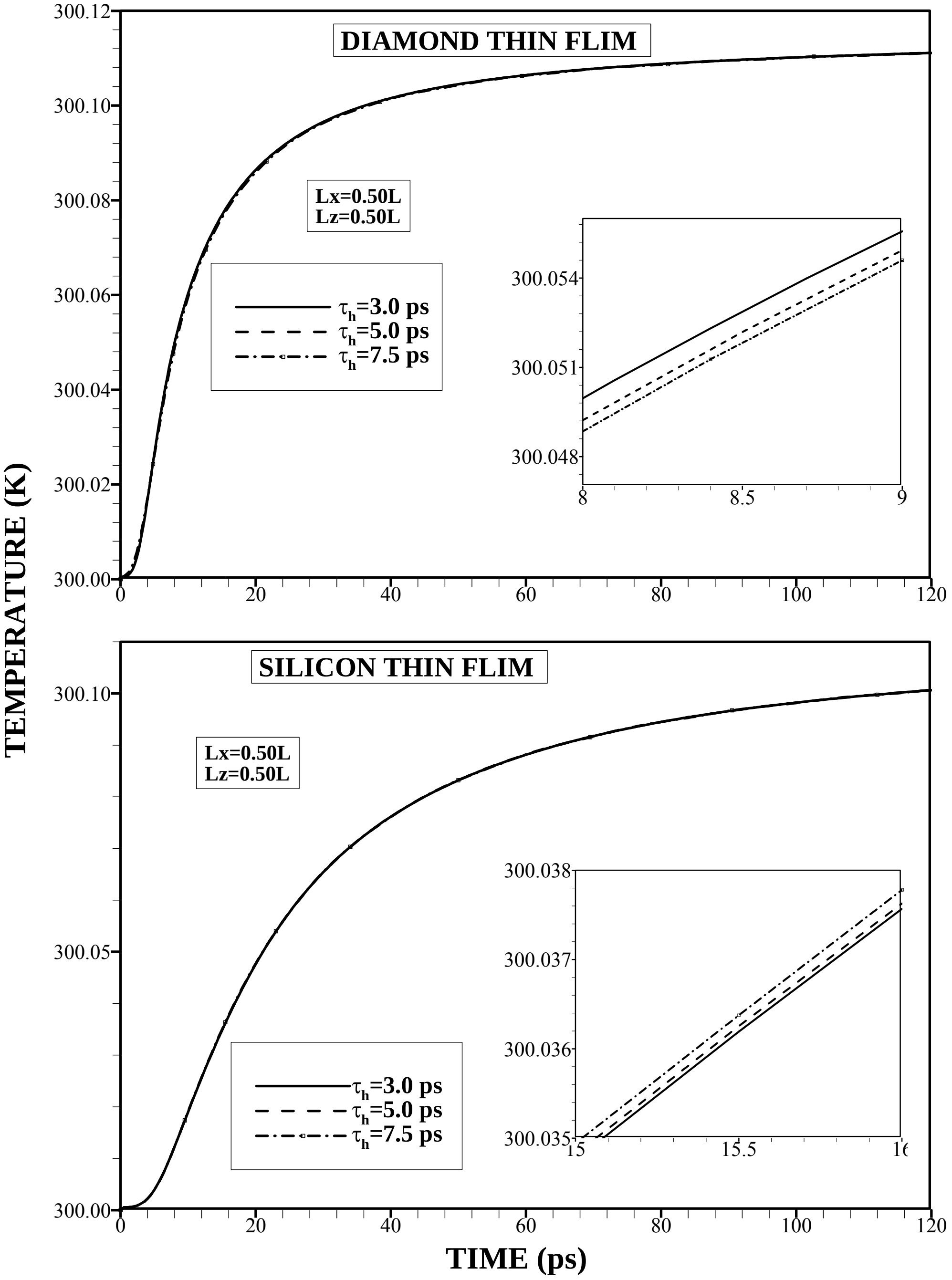

Figure 5.10 Temporal variation of equivalent equilibrium temperature at location Lx = 0.5L and Lz = 0.5L where L is the film width for three different pulse lengths of temperature oscillation at the film edge.

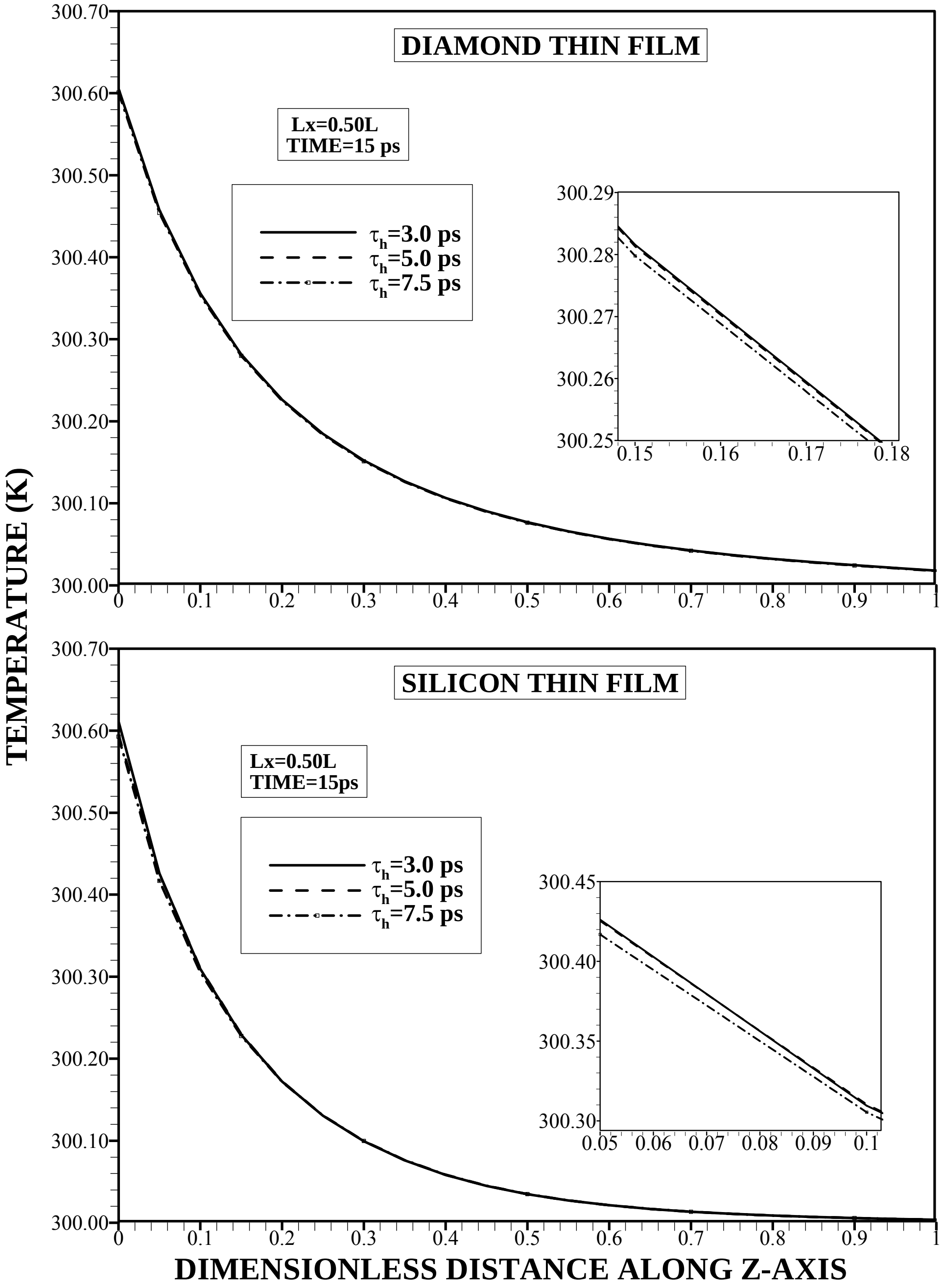

Figure 5.11 Equivalent equilibrium variation along the film width for heating duration of 15 ps and three different pulse lengths of temperature oscillation at the film edge. Lx = 0.5L, where L is the film width.

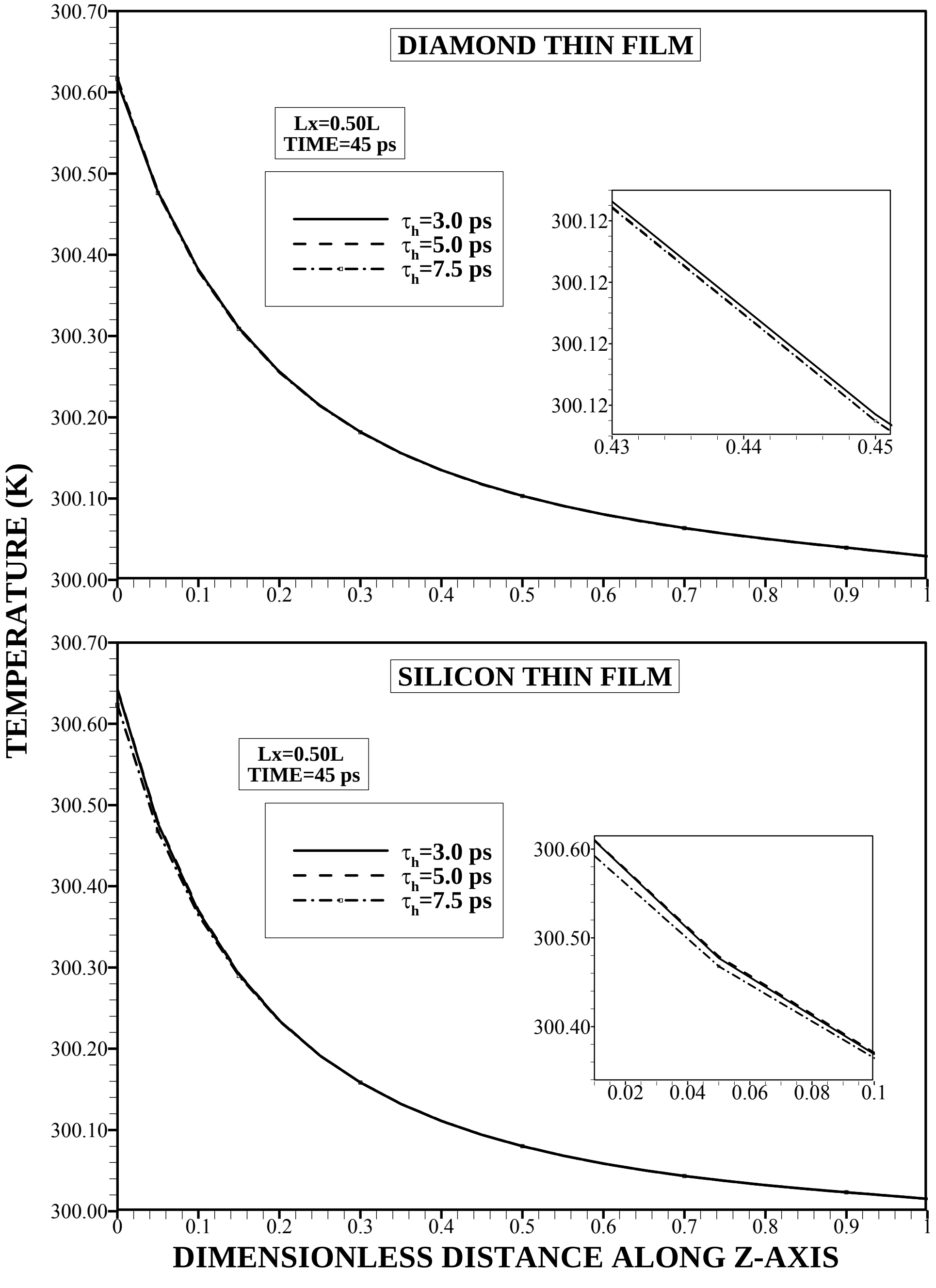

Figure 5.12 Equivalent equilibrium variation along the film width for heating duration of 45 ps and three different pulse lengths of temperature oscillation at the film edge. Lx = 0.5L, where L is the film width.

5.1.3 Transient Heat Transport Including the Effects of Pulse Duration of Heat Source in Silicon and Diamond Thin Films

The effect of temperature oscillation at the film edge on the phonon characteristics is examined in two-dimensional diamond and silicon films. Two different durations of temperature oscillations are incorporated in the analysis to examine the phonon characteristics in the film.

Figure 5.13 shows equivalent equilibrium temperature distribution along the dimensionless film width for different locations along the x-axis. Temperature along the silicon and diamond films is given in Figure 5.13 for the comparison reason. Dimensionless distance z = 0 corresponds to the high temperature edge where temperature oscillation is present and z = 1 is the low temperature edge where temperature is at 300 K. The small window in the picture shows the close view of temperature variation in the near region of the high temperature edge. Temperature jump occurs in the vicinity of the high temperature edge because of the emitted phonons from the high temperature edge, which do not undergo excessive scattering in this region. Temperature decay is sharp in the near region of the high temperature edge as compared to that corresponding to some distance away from the high temperature edge. This is because of the phonon intensity distribution in the film. In this case, phonon scattering in the film contributes to the film resistance, which is particularly true for the high frequency phonons. However, large wave length phonons show ballistic characteristics and do not suffer from scattering in the film. Their contribution to the film resistance becomes negligibly small. The slow decay of temperature towards the film width is associated with the emitted phonons, which undergo scattering and their intensity reduces with increasing film width. However, phonons emitted or reflected from the low temperature edge do not considerably contribute to the phonon intensity variation in the film. Therefore, equivalent equilibrium temperature remains low in the low temperature edge. The effect of heating cycle, which is the cycle related to high temperature oscillation at the high temperature edge, on temperature distribution is not significant along the film width. In this case, reduction in 75% of the cycle period does not alter temperature distribution in the film. This argument is true for diamond and silicon films. However, in the region close to the high temperature edge, temperature changes slightly with the frequency of temperature oscillation, which is more pronounced for the silicon film. Figure 5.14 shows dimensionless temperature variation for the heating period of 45 ps. Temperature behavior becomes identical for that is shown in Figure 5.13. Consequently, the effect of temperature oscillation, at high temperature edge, on temperature variation in the film is not significant with progressing heating time. The findings are true along the film width for silicon and diamond thin films.

Figure 5.15 and Figure 5.16 show temporal variation of equivalent temperature for diamond and silicon films and the location of $L_x = 0.5L$, where $L = 0.1\mu m$, in the films for different high temperature oscillation periods (Figure 3.7). Temperature variations in the diamond and the silicon film are shown for the comparison reason. Temperature rises rapidly in the early heating period and as the heating period increases it attains the quasi-steady increase. This behavior is particularly true for the diamond film. The rapid temperature increase is associated with the phonon intensity distribution in the early heating period. In this case, phonons transmitted from the high temperature edge suffer significantly from scattering and dispersion in the film. This, in turn, increases equivalent equilibrium temperature in the film. Since the acoustic speed of the phonons is much higher in diamond film than that of the silicon film, temperature increase becomes more rapid in the diamond film than that corresponding to the silicon film. However, as the heating period progresses, oscillation in temperature is observed, which is more pronounced in the silicon film. Since temperature pulsates at the film edge, the film resistance, due to the temporal behavior of the phonon intensity in the film, does not respond to this oscillation in the early heating period. This is associated with the ballistic phonons, which does not contribute to the phonon scattering in the film, which is particularly true for the diamond film (Figure 5.16). It should be noted that as the distance in the film gets close to the high temperature edge, the influence of ballistic phonons on the film resistance becomes significantly important; in which case, reducing the distance lowers the film resistance [56]. Therefore, as the increases away from the high temperature edge, temperature oscillation in the film reduces significantly, which can be observed when Figure 5.15 and Figure 5.16 are compared. This situation is more pronounced for the silicon film, which has lower acoustic wave speed than that of the diamond.

Figure 5.17 and Figure 5.18 show the temperature oscillation in the film with time at location $L_x = 0.5L$, where $L = 0.1\mu m$ for two heating periods and for two locations in films. Temperature variations in silicon and diamond films are also given for the comparison reason. The amplitude of temperature oscillation increases as the pulse period $\left(\tau_{cycle}\right)$ increases. It should be noted that increasing pulse period represents that the duration of high temperature at the edge remains long period of time during the heating process. Consequently, increasing the duration of high temperature at the film edge causes high amplitude temperature oscillation in the film. This is particularly true for the thin silicon film. Therefore, the rate of phonon emitted from the high temperature edge of the film increases with increasing heating duration at the film edge. The phonon scattering in the film causes temperature rise in the film. Moreover, temperature oscillation in the film does not follow exactly temperature oscillation at the film edge. This is associated with the rate of the phonons emitted from the high temperature edge and phonon scattering rate in the film. They are not harmonically in phase. In addition, the ballistic phonons do not contribute to temperature increase in the film despite they are generated at the high temperature edge of the film. The close examination of the temperature oscillation reveals that the film response to the temperature oscillation is similar to those observed for the diffusive heating [137]. This behavior is observed particularly location $\left(L_z = 0.05L\right)$ which is near more close to high temperature edge; therefore, the ballistic phonon contribution to the temperature oscillation becomes significant for the thin films. In the case of the location $L_z = 0.25L$, the film resistance gives rise a damping affect while suppressing the amplitude and modifying the frequency of temperature oscillation in the film (Figure 5.18). However, unlike the silicon film, increasing distance away from the high temperature edge influences the temperature oscillation in the diamond film. This is more pronounced for long temperature pulse period $\left(\tau_{cycle}\right)$ at the film edge.

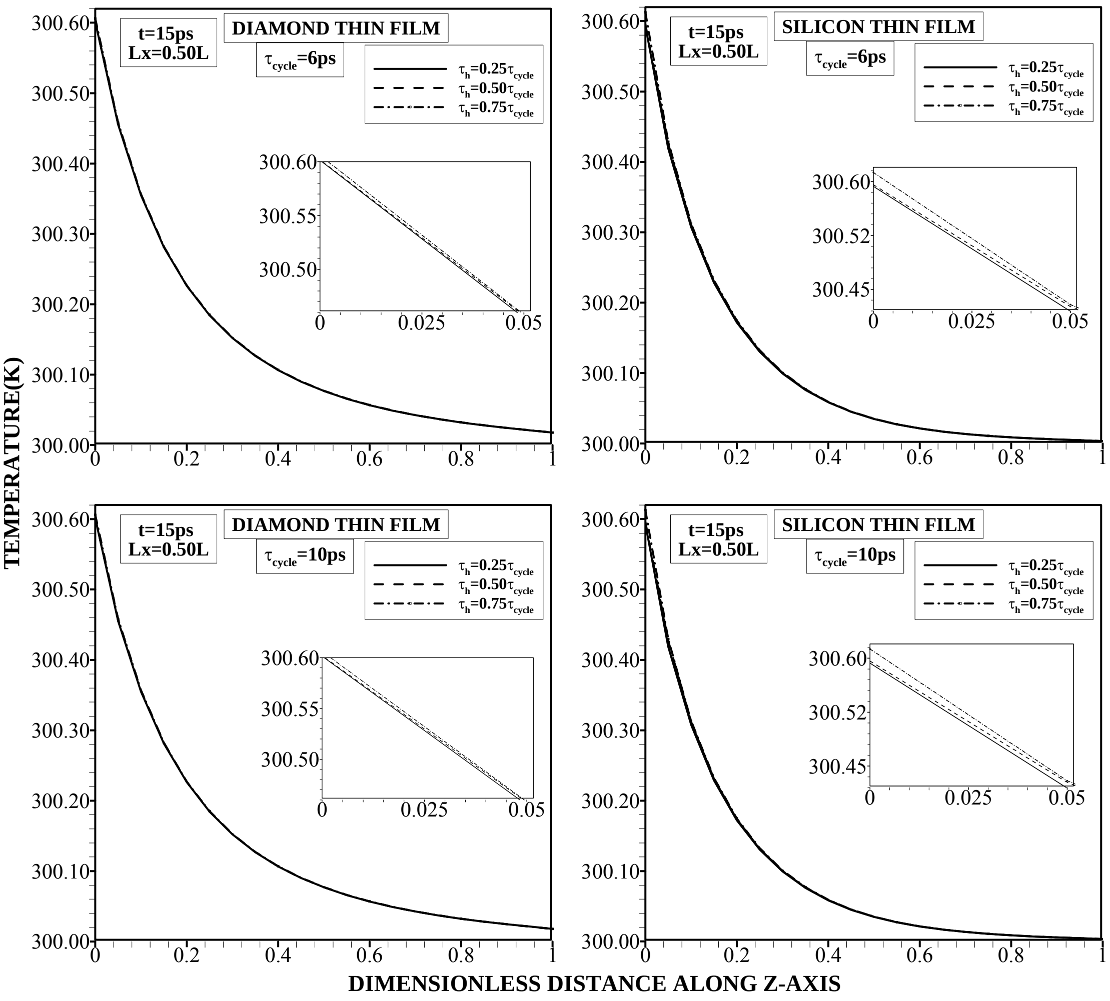

Figure 5.13 Equivalent equilibrium temperature along the film width for silicon and diamond films. $\tau_{cycle} = 6ps\ and\ 10ps$,t = 15 ps, and $L_x = 0.5L, where\ L = 0.1\mu m$.

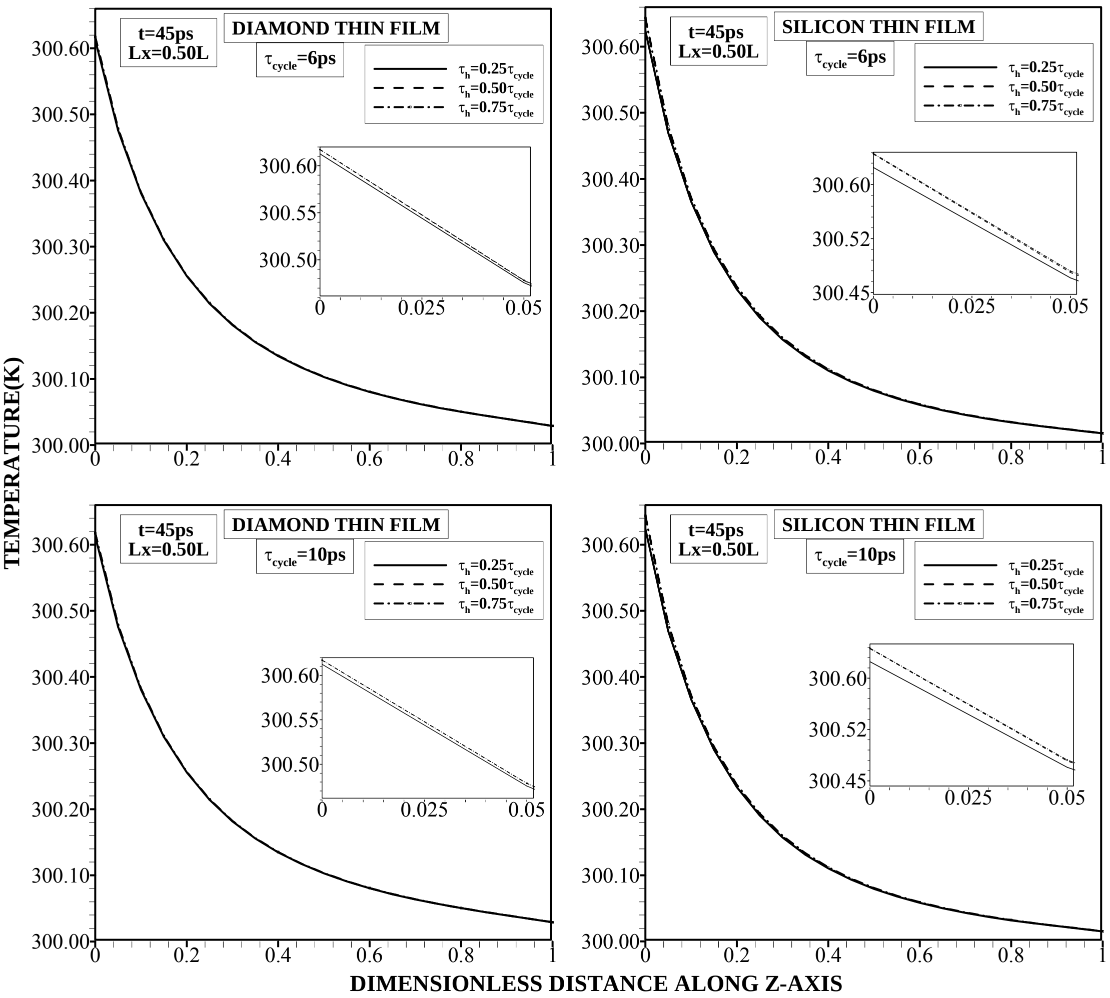

Figure 5.14 Equivalent equilibrium temperature along the film width for silicon and diamond films. $\tau_{cycle} = 6ps\ and\ 10ps$,t = 45 ps, and $L_x = 0.5L, where\ L = 0.1\mu m$.

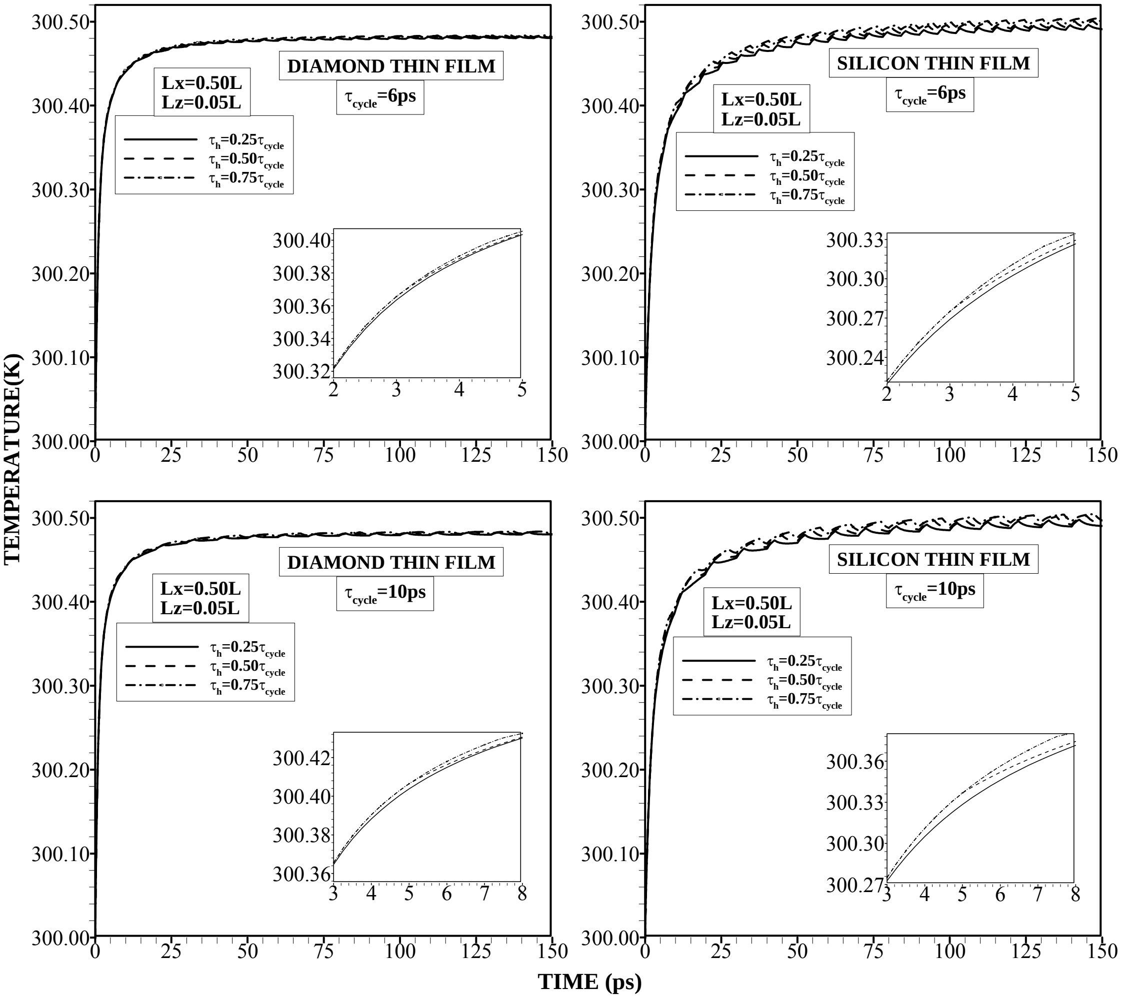

Figure 5.15 Temporal variation of equivalent equilibrium temperature for silicon and diamond films. $\tau_{cycle} = 6 ps\ and\ 10 ps$, $L_x = 0.5L\ and\ L_z = 0.05L, where\ L = 0.1\mu m$.

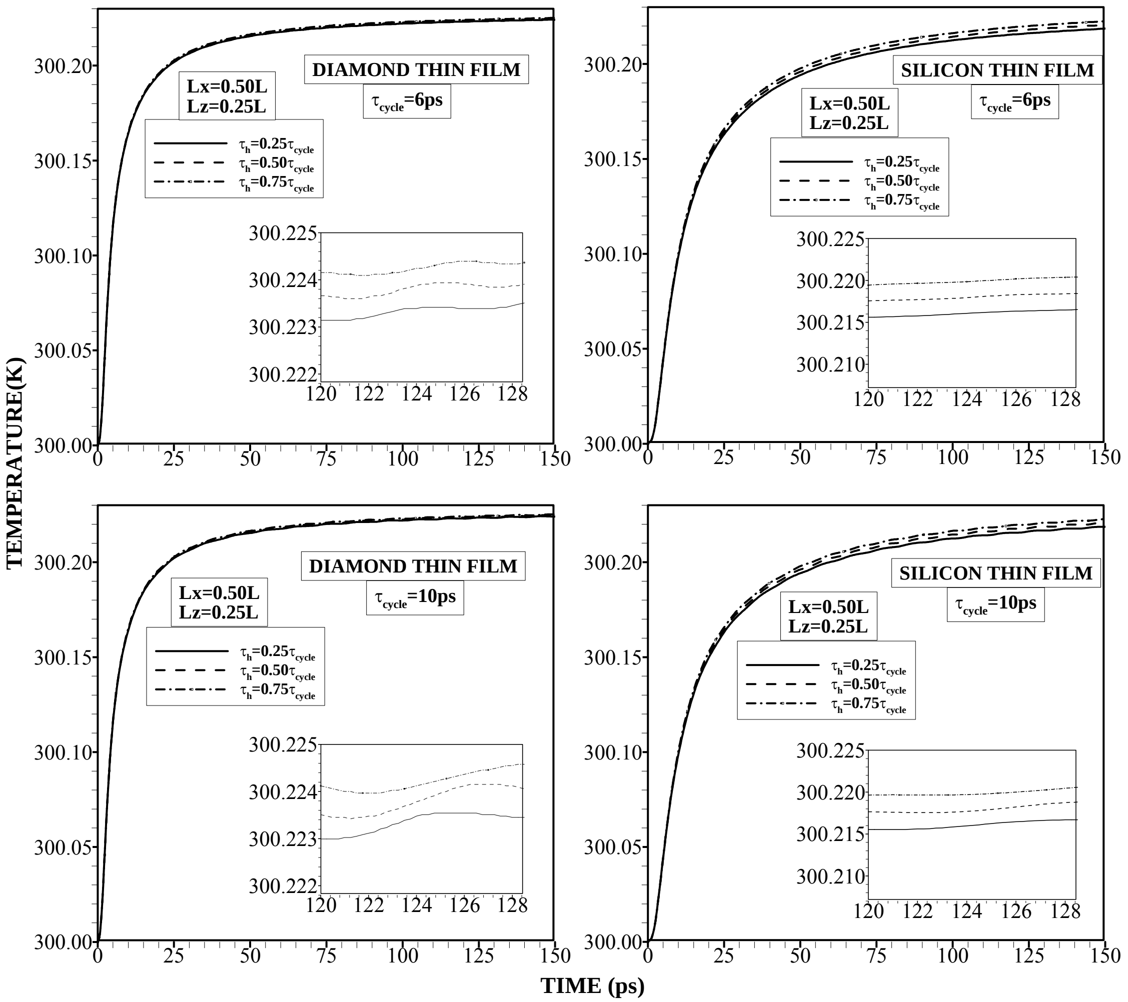

Figure 5.16 Temporal variation of equivalent equilibrium temperature for silicon and diamond films. $\tau_{cycle} = 6ps\ and\ 10ps$, $L_x = 0.5L\ and\ L_z = 0.25L, where\ L = 0.1\mu m$.

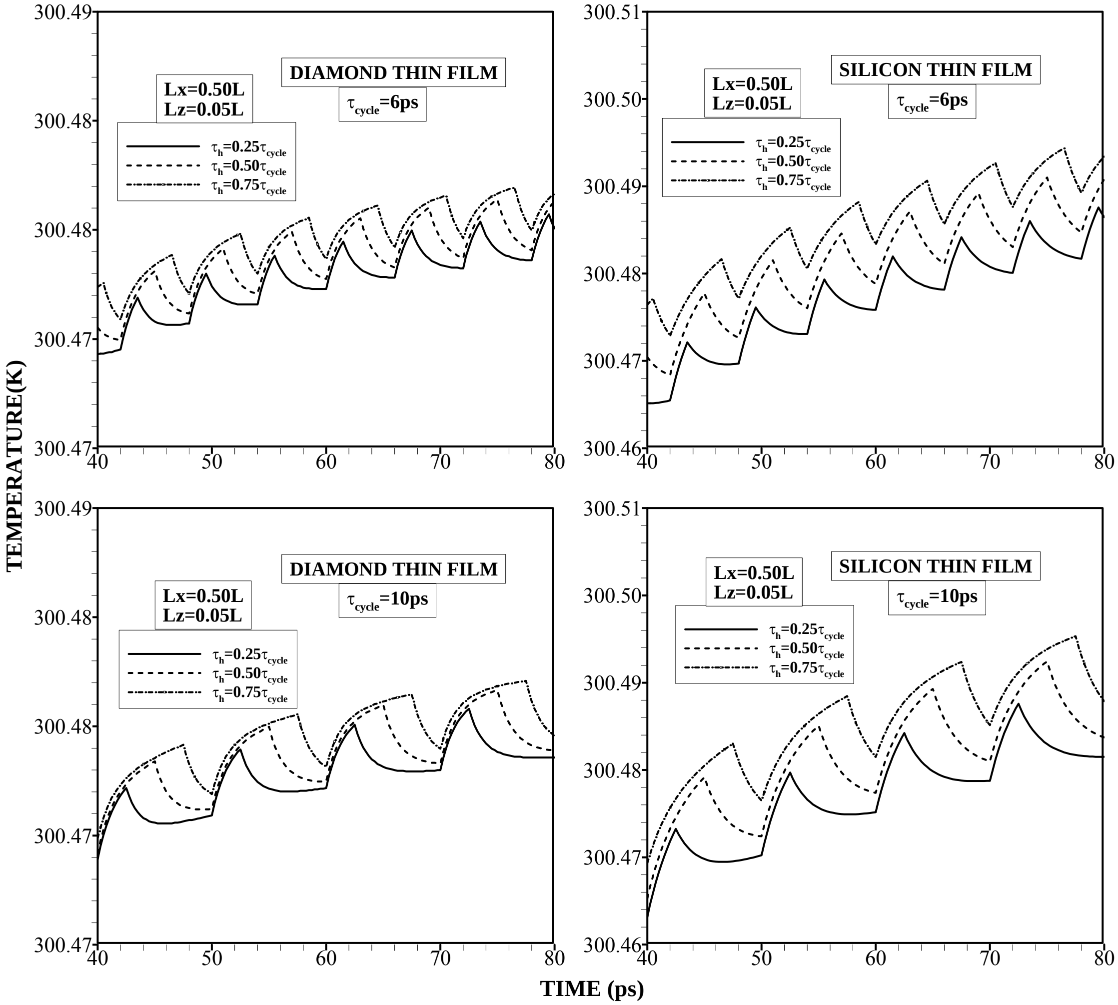

Figure 5.17 Close view of temporal variation of equivalent equilibrium temperature for silicon and diamond films. $\tau_{cycle} = 6ps\ and\ 10ps$, $L_x = 0.5L\ and\ L_z = 0.05L$, $where\ L = 0.1\mu m$.

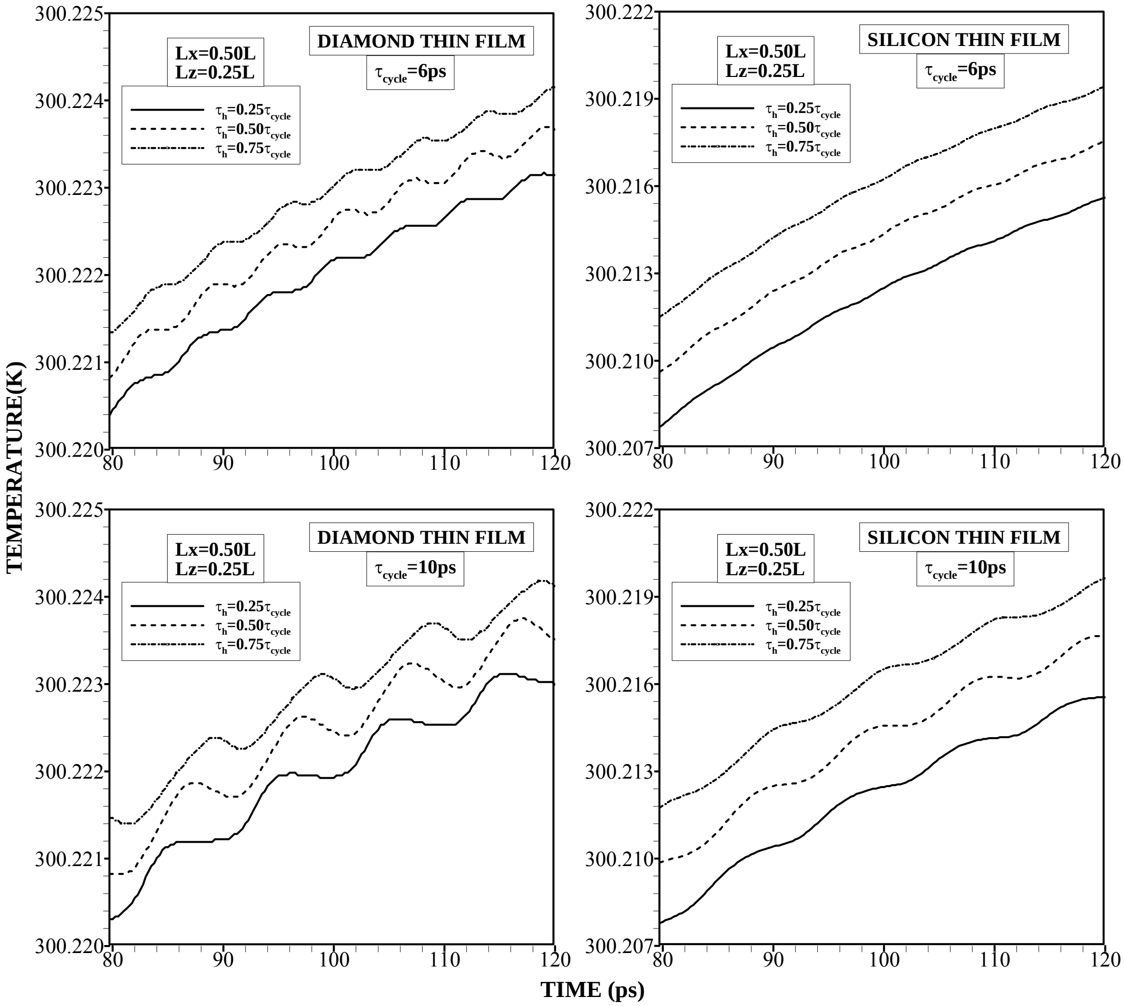

Figure 5.18 Close view of temporal variation of equivalent equilibrium temperature for silicon and diamond films. $\tau_{cycle} = 6ps\ and\ 10ps$, $L_x = 0.5L\ and\ L_z = 0.25L$, $where\ L = 0.1\mu m$.

5.1.4 Transient Heat Transport Including the Effects of Thickness and Temperature Oscillations in Diamond Thin Film

Phonon transport in a two-dimensional diamond film is considered and transport characteristics due to temperature pulsation at the film edge and film thickness are investigated. Equivalent equilibrium temperature is introduced to assess the contribution of ballistic phonons to energy transport across the film.

Figure 5.19 shows temporal variation of equivalent equilibrium temperature for two frequencies of temperature disturbance and four film thicknesses in the close region of the high temperature edge of the film ($x = 0.5L_x$ and $z = 0.05L_z$, where L_x is the film thickness and L_z is the film width). Temperature rises sharply in the early heating period because of the emitted phonons from the high temperature edge. Phonon scattering at the near region of the high temperature edge contributes to the film resistance; in which case, temperature increases sharply with progressing time in this region. Once temperature increase becomes gradual, temperature pulsation is observed, which appears as ripples on the temperature curve. Although amplitude of temperature oscillation is high at the film edge (Figure 3.7), temperature oscillation has low amplitude at the location where $x = 0.5L_x$ and $z = 0.05L_z$. Consequently, some of the emitted phonons have high frequencies and they do not undergo scattering in this region, which in turn do not contribute to temperature increase and temperature oscillations in this region. However, the reflected phonons from the low temperature edge of the film scatter in the film and contribute to temperature increase in this region. As the time progresses, the maximum amplitude of temperature ripples remains almost the same during the heating period, i.e. phonon transport attains quasi steady equilibrium with processing time. Temperature rippling appears to occur once the temperature equilibrium is established. This behavior is also observed in the previous study [137] when the diffusional transport took place during the heating cycle. Therefore, thin film response to temperature disturbance at the edge becomes similar to that observed during the diffusional heating. This behavior is more pronounced for thin film $\left(L_z = 0.01\mu m\right)$. As the film thickness increases, the amplitude of the ripples reduces and almost dies out for $L_z = 0.15\mu m$ film width. This indicates that influence of film thickness on temperature oscillation in the film is significant. This behavior can be explained in terms of reflected and emitted phonons from the low temperature edge. In the case of the thin film with $L_z = 0.01\mu m$, the reflected phonons cause bouncing in between the high and cold temperature edges while causing high rate of scattering in the film. This enhances equivalent equilibrium temperature and causes high amplitude rippling due to oscillatory excitation at the film edge. Moreover, temperature attains the highest value for $L_z = 0.01\mu m$, and then follows the other film thicknesses with ascending order. The ballistic phonons do not contribute to temperature increase and they do not suffer from the scattering in the film; however, reflected and emitted phonons from the low temperature edge have significant contribution to temperature increase in the film. This situation is also observed for the pulse frequency of 5 ps. The time shift (time lagging) between two consecutive temperature peaks in the ripple does not follow the time shift for temperature oscillation at high temperature edge. This observation is true for both frequencies of temperature oscillation at high temperature edge. This indicates that phonon scattering causes damping effect on the emitted and reflected phonons. This is more pronounced for the films with large thicknesses $\left(L_z \geq 0.1\mu m\right)$. Figure 5.20 shows temporal variation of equivalent equilibrium temperature for different film thicknesses and two frequencies of temperature oscillation at the film edge. The location is at $x = 0.5L_x$ and $z = 0.5L_z$ in the film, which corresponds to the mid-thickness and mid- width of the film. Temperature increases rapidly in the early heating period as similar to that shown in Figure 5.19. However, amplitude of temperature ripples is lower than that corresponding to Figure 5.19. This indicates that as the distance from the high temperature edge increases in the film, phonons attain relatively lower intensity in this region. Due to the phonon scattering, phonons loss some of their intensity before reaching at the mid thickness and mid-height of the film. This, in turn, lowers temperature rippling, which is more pounced for $0.01\mu m$ thick film. In addition, scattering of phonons contribute to damping of temperature ripples in this region.

Figure 5.21 shows variation of equivalent equilibrium temperature along the film width (z-axis) for different film thicknesses and two frequencies of temperature oscillation. It should be noted that x-axis location is the mid-thickness of the film $\left(x = 0.5L_x\right)$. The z-axis is normalized by the film width so that z-axis extends in between 0–1 for all the film widths. Temperature oscillation at the high temperature edge does not have significant effect on equivalent equilibrium temperature distribution in the film.

Temperature jump is observed at the high and low temperature edges, which is more pronounced at low temperature edge, particularly for the thin film $\left(L_x = 0.01\mu m\right)$. Temperature jump is associated with the emitted phonons from the edges; in which case, some of the phonons do not undergo scattering in the vicinity of the edges. The attainment of high temperature jump at the low temperature edge of the thin film is associated with the ballistic phonons. In this case, ballistic phonons do not contribute to film resistance through scattering. In this case, temperature decay becomes almost linear across the film width and only the phonons having smaller wavelengths than the film thickness suffer from the thermal resistance of the film. As the film thickness increases, equivalent equilibrium temperature reduces sharply in the region close to the high temperature edge and temperature decay becomes gradual as the distance along the film width increases towards the low temperature edge. This behavior is attributed to phonon intensity distribution in the film, which reduces with increasing depth because of the scattering. Since equivalent equilibrium temperature is associated with the average energy of all phonons around a local point and it is equivalent to the equilibrium temperature of phonons when they redistribute adiabatically to an equilibrium state, phonon intensity distribution in the film determines the behavior of equivalent equilibrium temperature. As the film thickness increases, equivalent equilibrium temperature decreases towards the low temperature edge. This is attributed to phonon scattering in the film; in which case, phonons uninterruptedly scatters along the film width and their intensity reduces due to the film resistance. This, in turn, lowers equivalent equilibrium temperature with increasing film width. Moreover, some of the ballistic phonons generated in the large film widths have larger wavelength than the film thickness. Consequently, their contribution to equivalent equilibrium temperature increase becomes smaller as compared to that corresponding to the relatively thinner films.

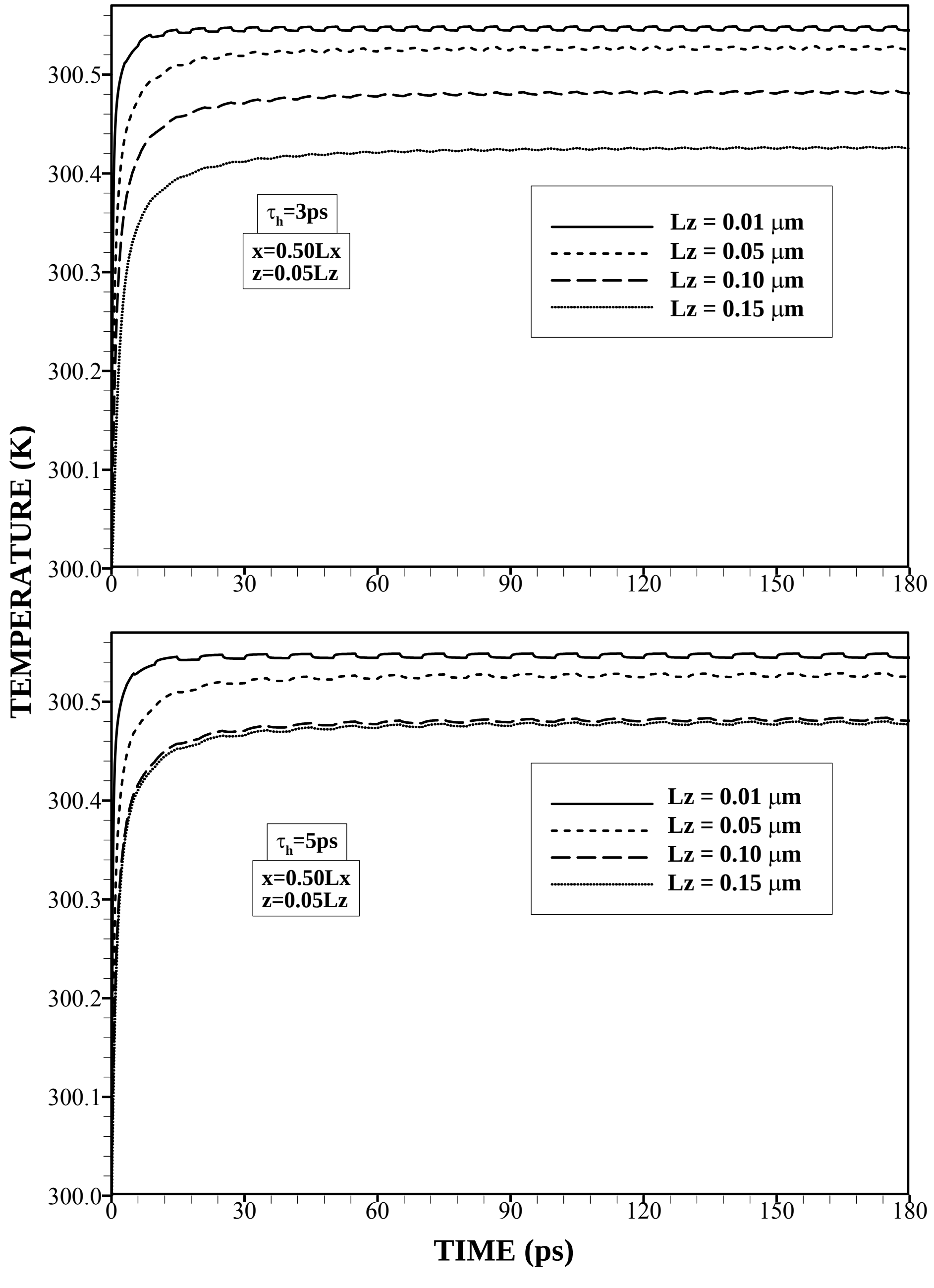

Figure 5.19 Temporal variation of equivalent equilibrium temperature for two frequencies of temperature oscillation and various film thicknesses. Temperature is located at $x = 0.5L_x$ and $z = 0.05L_z$ in the film.

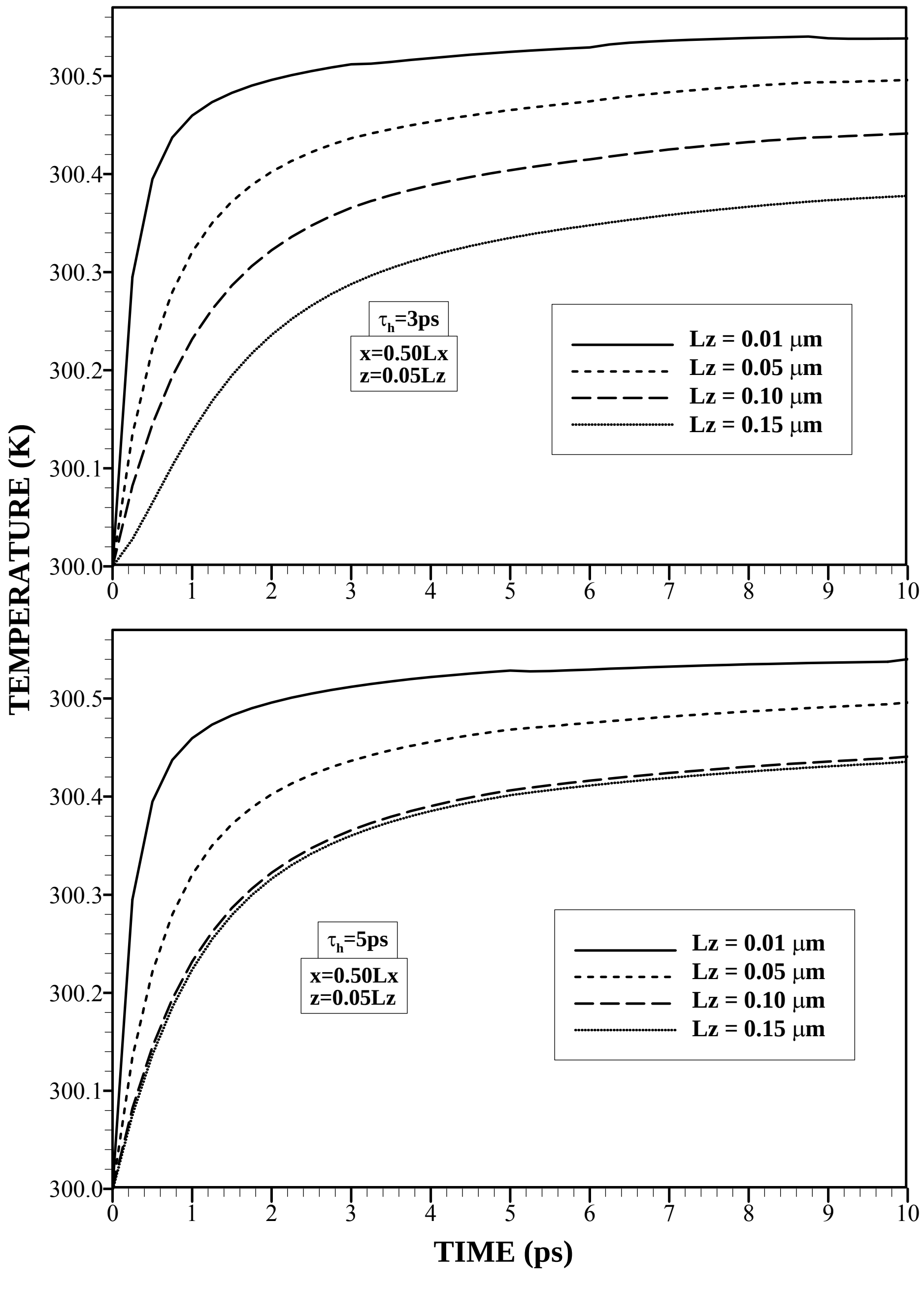

Figure 5.20 Temporal variation of equivalent equilibrium temperature for two frequencies of temperature oscillation and various film thicknesses. Temperature is located at $x = 0.5L_x$ and $z = 0.05L_z$ in the film.

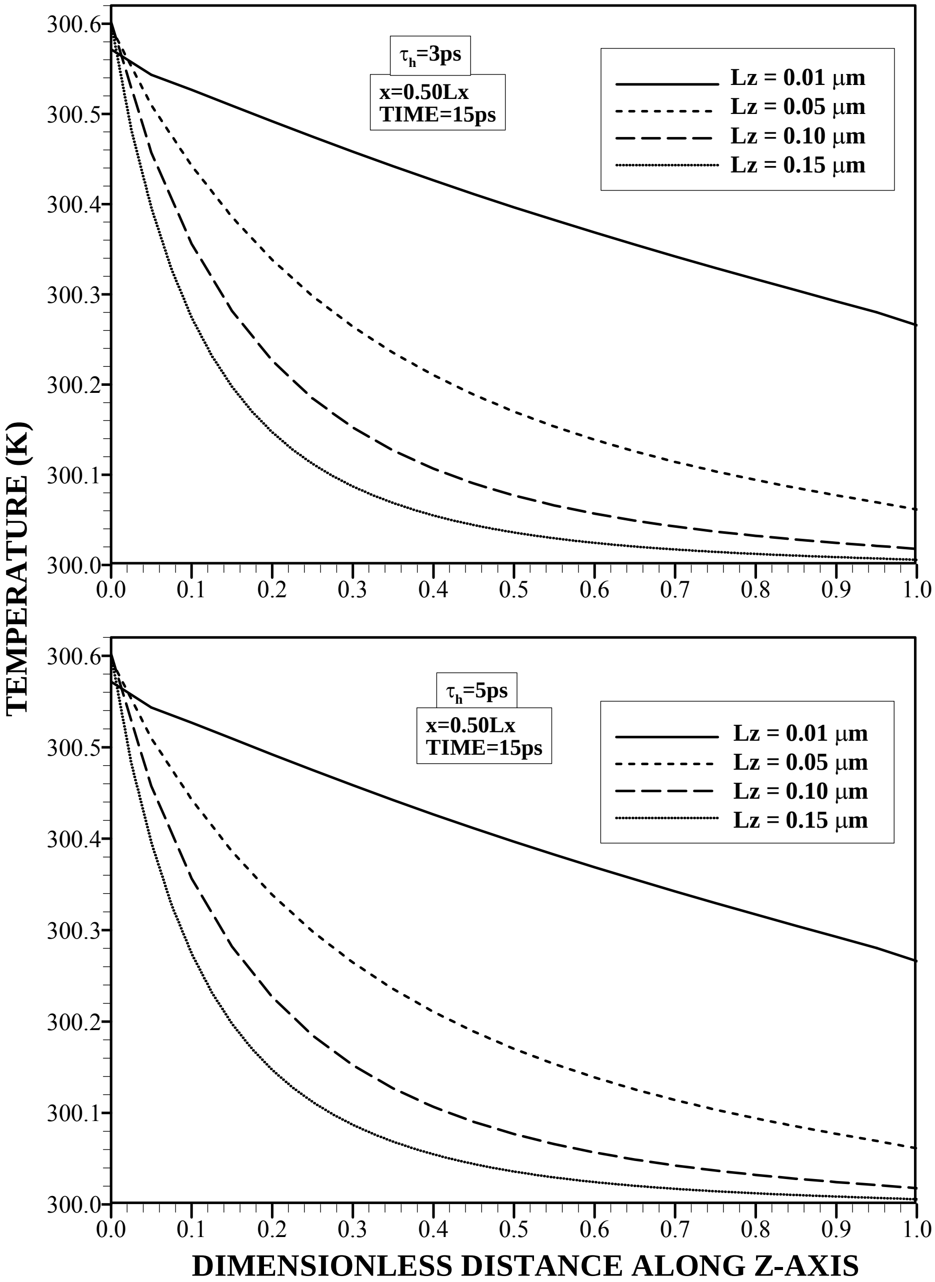

Figure 5.21 Equivalent equilibrium temperature variation along the film width for two frequencies of temperature oscillation and various film thicknesses. Temperature is presented for heating time t = 15 ps.

5.1.5 Transient Heat Transport Including the Effects of Heat Source Size and Temperature Oscillation in Silicon Thin Films

Phonon transport in a two-dimensional thin silicon film is considered and transient effects of temperature oscillation, at the film edge, on the transport characteristics are examined. The heat source size is varied to observe the effect of ballistic and quasi-ballistic phonons on the film resistance. Equivalent equilibrium temperature is introduced to assess the phonon intensity distribution in the film.

Figure 5.22 shows temporal variation of equivalent equilibrium temperature for different heat source sizes and two cycles of temperature oscillation. The location of equivalent equilibrium temperature is $L_x = 0.5L$ and $L_z = 0.05L$, where $L = 0.1\mu m$, and L_x is the distance along film thickness and L_z is along the film width (Figure 3.6). Temperature rises rapidly in the early heating period $(t \leq 10ps)$ and this increase becomes gradual with progressing heating duration in the close region of the high temperature edge (Figure 3.7). This is more pronounced for the case in which the heat source size is the largest. The rapid increase in temperature is associated with the phonon intensity distribution in the close region of the high temperature edge; in which case, phonons emitted from the high temperature edge undergo several scattering while causing temperature rise in this region. Acoustic phonons with the longitudinal and transverse polarization and wavelengths equal and less than $L_z = 0.05L$ contribute significantly to the phonon intensity distribution due to scattering in this region. In general, optical phonons have high frequencies and relatively low wavelengths and their contribution to phonon scattering is not significant in this region. The time required to attain 80% of equivalent equilibrium temperature is longer for the large heat source sizes $\left(w_s = L\right)$ and opposite is true for the small heat source size $\left(w_s = 0.25L\right)$. This is associated with the effect of heat source size on the phonon transport; in which case, increasing heat source size at the film edge allows more phonons emitted from high temperature edge of the film, which in turn, modifies the phonon scattering and the rate of temperature rise in the film. Consequently, temperature rise continuous until the quasi-steady condition yields, which becomes longer for the larger heat source size. However temperature oscillation is observed in the film with progressing time, which is more pronounced when equivalent equilibrium temperature rise attains almost quasi-steady. This behavior is also observed for the diffusional heating situation when the heat source is pulsated [137]. When comparing temporal variation of equivalent equilibrium temperature due to the cases of two cycles of temperature oscillation at the high temperature edge $\left(\tau_{cycle} = 6\,ps\ and\ 10\,ps\right)$, equivalent equilibrium temperature behaves almost similar for both cases. However temperature oscillation does not follow the frequency of temperature oscillation at the high temperature edge of the film. This situation can also be seen in Figure 5.23, in which temperature difference $\left(\Delta T = T_{\max} - T_{\min}\right)$ during one period of temperature oscillation) is given with heating time for two different cycles of temperature oscillation at the high temperature edge. Temperature difference $\left(\Delta T\right)$ increases with increasing heating time, which is more pronounced for the small heat source size. This behavior is attributed to the ballistic and quasi-ballistic behavior of phonons emitted from the high temperature source at the film edge. In this case, as the heat source size reduces, some of the emitted long wavelength phonons do not undergo scattering in the film and do not contributed to the temperature increase through equilibrium intensity increase in the film [139]. This results in a large amplitude oscillation in equivalent equilibrium temperature in the film during the heat source oscillation. Since the phonon transport in the thin film does not follow the Fourier heat diffusion, temperature difference varies with time and with the heat source size. As the period of heat source oscillation increases from 6 ps to 10 ps, temperature difference increases for all the heat source size at the film edge. Consequently, reduction in the heat source size increases temperature difference, which is more pronounced as the duration of the heat source oscillation increases. Figure 5.24 shows temporal variation of equivalent equilibrium temperature for two periods of temperature oscillation and various heat source sizes at the film edge. The temperature variation is plotted at a location $L_x = 0.5L$ and $L_z = 0.25L$, where $L = 0.1\mu m$, in the film. It is evident that temperature oscillation dies out at this location for all heating times. This indicates that temperature oscillation only appears in the close region of the high temperature edge where the heat source is located (Figure 3.6). As the distance in the film increases, phonon equilibrium intensity is re-distributed through the scattering in such a way that temporal response of the equilibrium phonon intensity distribution to heat source oscillation becomes steady.

Figure 5.25 shows equivalent equilibrium temperature along the normalized film width (z / L, where $L = 0.1\mu m$) for two heat source oscillation cycles and various values of the heat source size located at the high temperature edge. The heating duration is 15 ps and the location along the film thickness is $L_x = 0.5L$. It should be noted that z = 0 corresponds to the high temperature edge and z = 1 is located at the cold temperature edge. Temperature jump occurs at the high temperature edge boundary, where the heat source is located. This is associated with the boundary scattering at the interface. Temperature reduces sharply first in the near region of the high temperature edge and the decay becomes gradual as the distance increases along the film width towards the low temperature edge. The sharp decay of temperature is related to the phonon intensity distribution in the film; in which case, phonons emitted from the high temperature edge undergo scattering in the film and equilibrium phonon intensity re-distributed in the film at the heating period of 15 ps. Since phonon emission also takes place from the cold edges of the film, reflected phonons do not contribute to the phonon scattering in the film and the equilibrium intensity of phonons remain low. This, in turn, causes sharp decay of phonon intensity in the near region of the edge. In addition, cold temperature edge acts like a phonon sink lowering phonon intensity in the region of the cold temperature edge. Therefore, temperature decay becomes gradual in the region close to the cold edge of the film. However, temperature decay changes as the heat source size reduces; in which case, temperature attains lower values in the film for small heat source size as compared to that corresponding to the large heat source size. Temperature jump due to boundary scattering also remains large at the high temperature edge for the small size heat source. This behavior is attributed to the contribution of quasi-ballistic and ballistic effects of the phonon transport in the film. It was demonstrated earlier [139] that as the heat source size reduces the effect of the ballistic phonons on equilibrium phonon distribution becomes significant in the film. Similar observation is made in the film for the case of the small size heat source. Temperature difference becomes larger in the near region of the high temperature edge than that occurs in the region close to the low temperature edge. In this case, quasi-ballistic phonons emitted from the high temperature edge do not undergo scattering in the near region of the edge because of their long wavelengths. However, as the distance along the film width increases, some of these phonons having the wavelengths comparable to this distance in the film undergo scattering while enhancing the equilibrium phonon intensity distribution in this region. Therefore, temperature difference due to different sizes of the heat source at the high temperature edge becomes small. This behavior is also true for long heating duration, which is shown in Figure 5.26. However, increasing heating duration increases temperature in the film because of the equilibrium phonon intensity enhancement during the extend period of scattering of the emitted phonons from the high temperature edge.

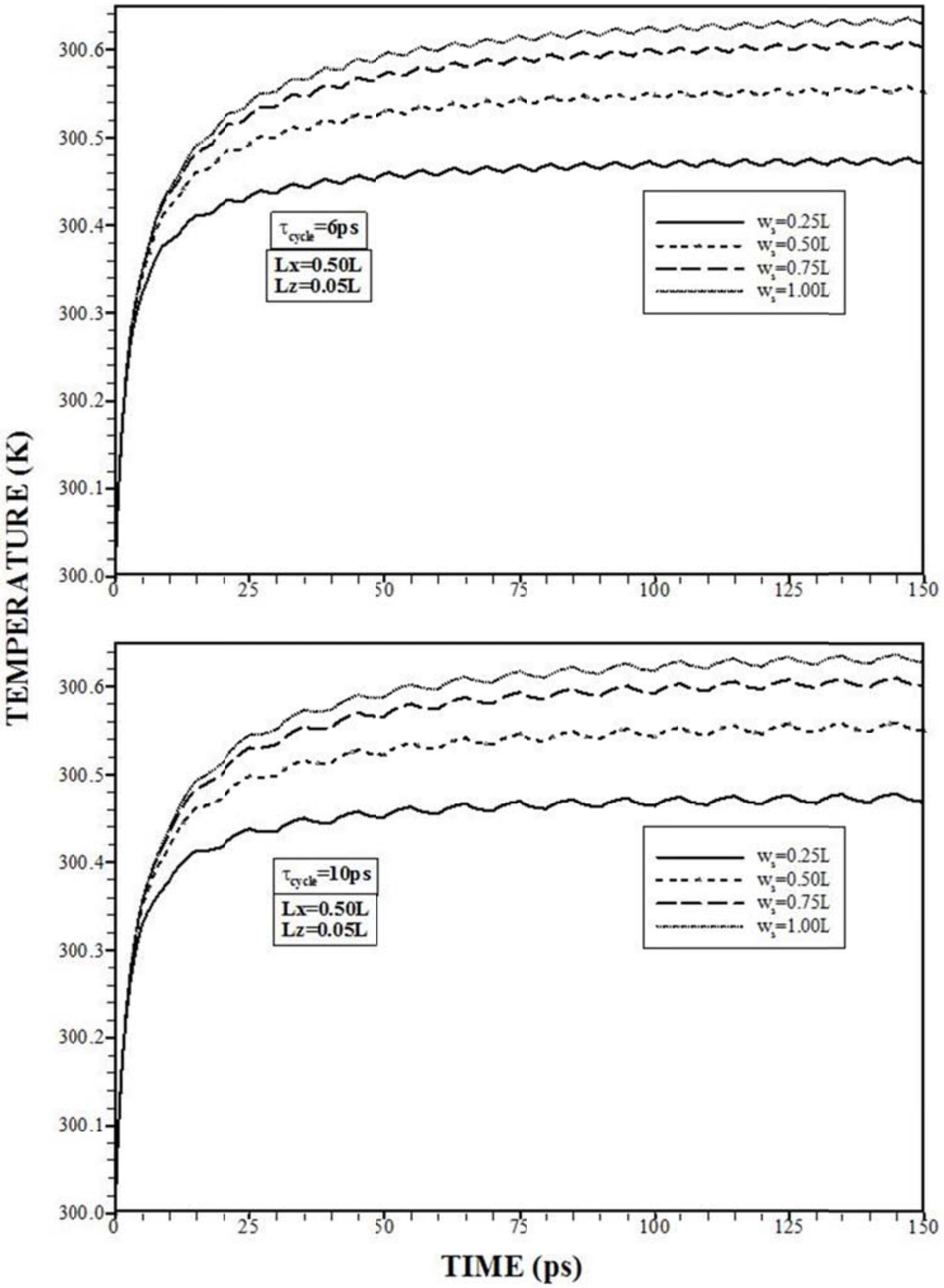

Figure 5.22 Temporal variation of equivalent equilibrium temperature for different heat source sizes and two cycles of temperature oscillation. The location in the film is $L_x = 0.5L$ and $L_z = 0.05L$, where $L = 0.1\mu m$.

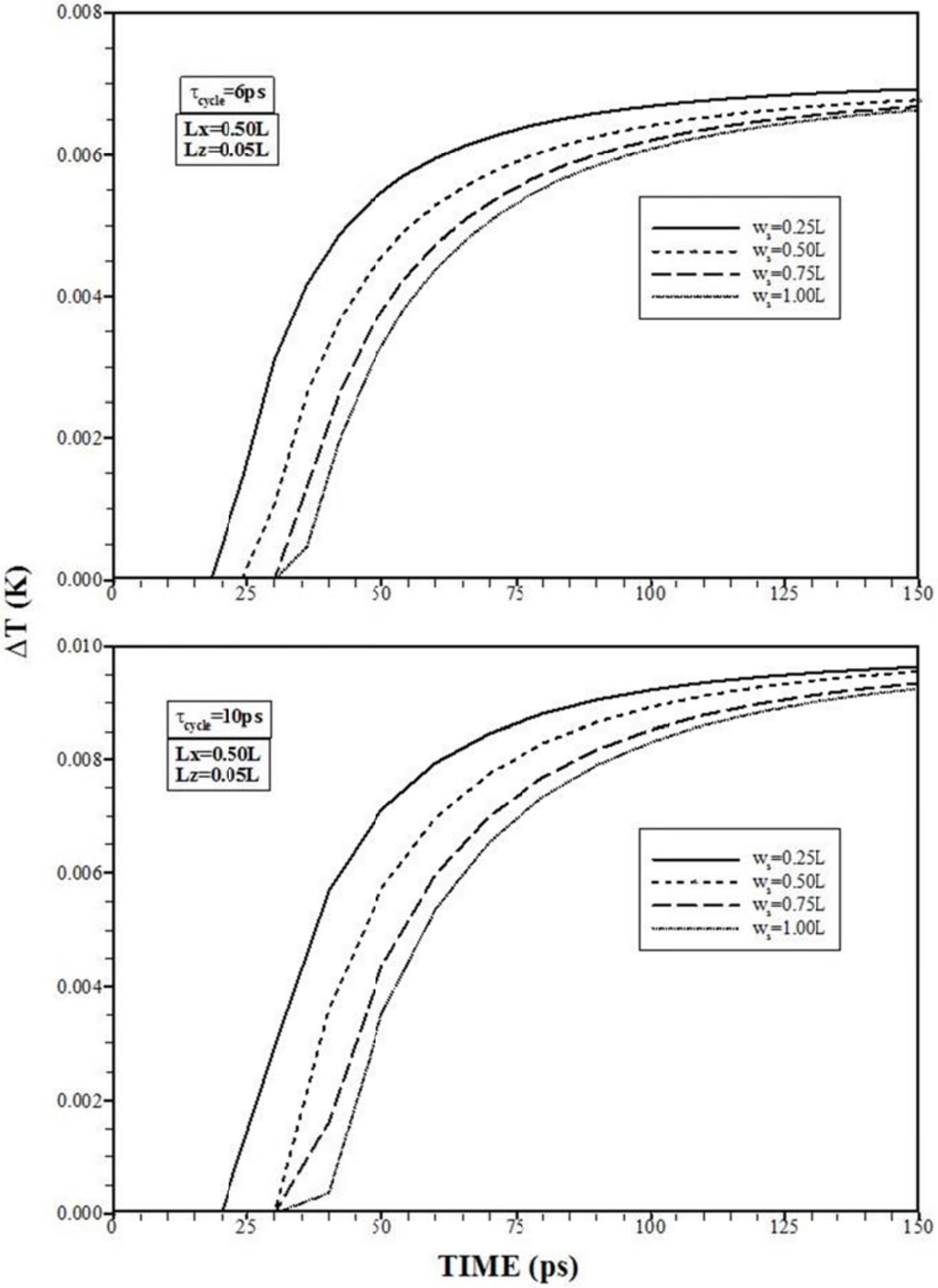

Figure 5.23 Temporal variation of equivalent equilibrium temperature difference due to two consecutive maximum and minimum temperature differences for different heat source sizes and two cycles of temperature oscillation.

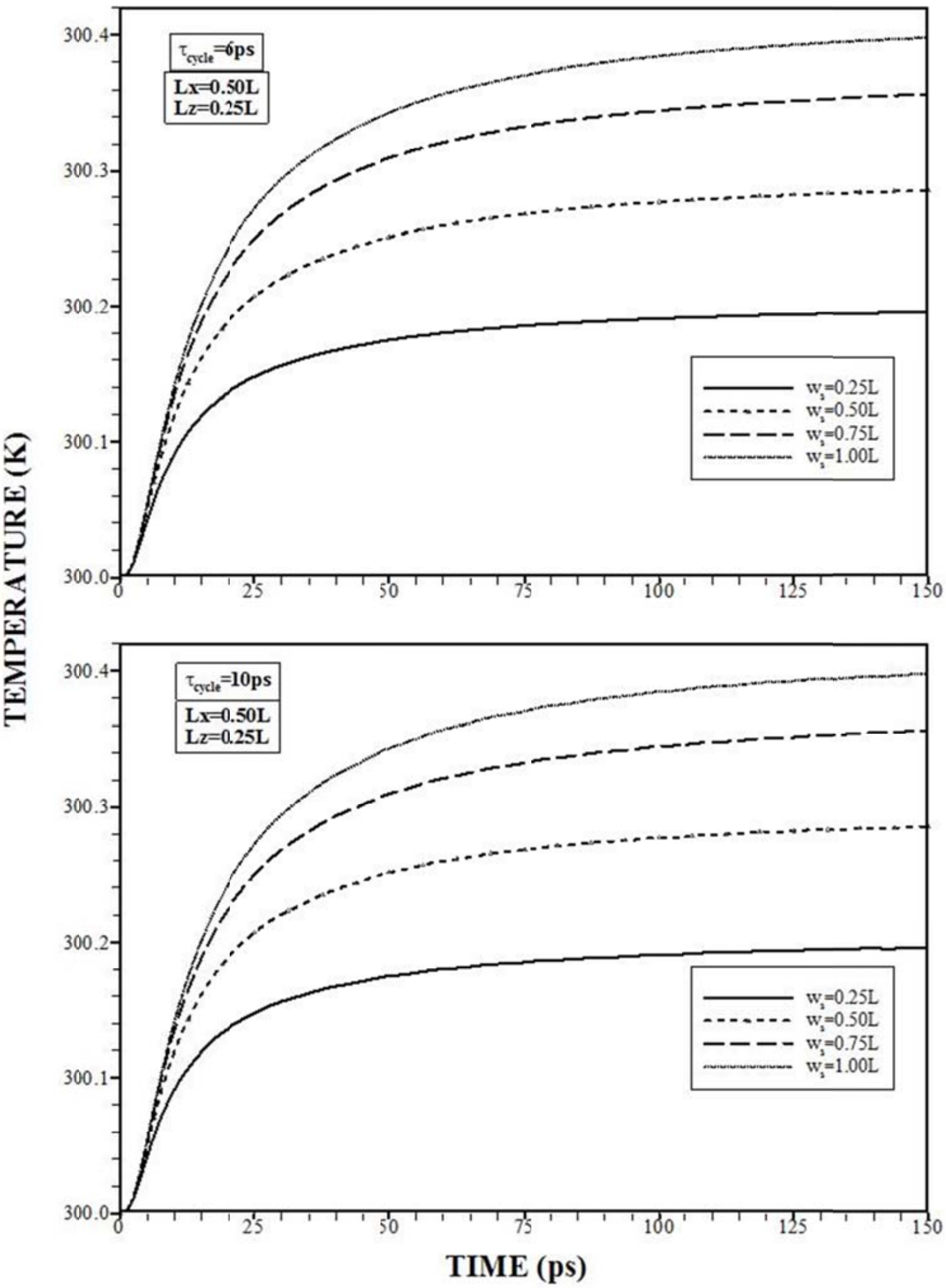

Figure 5.24 Temporal variation of equivalent equilibrium temperature for different heat source sizes and two cycles of temperature oscillation. The location in the film is $L_x = 0.5L$ and $L_z = 0.25L$, where $L = 0.1\mu m$.

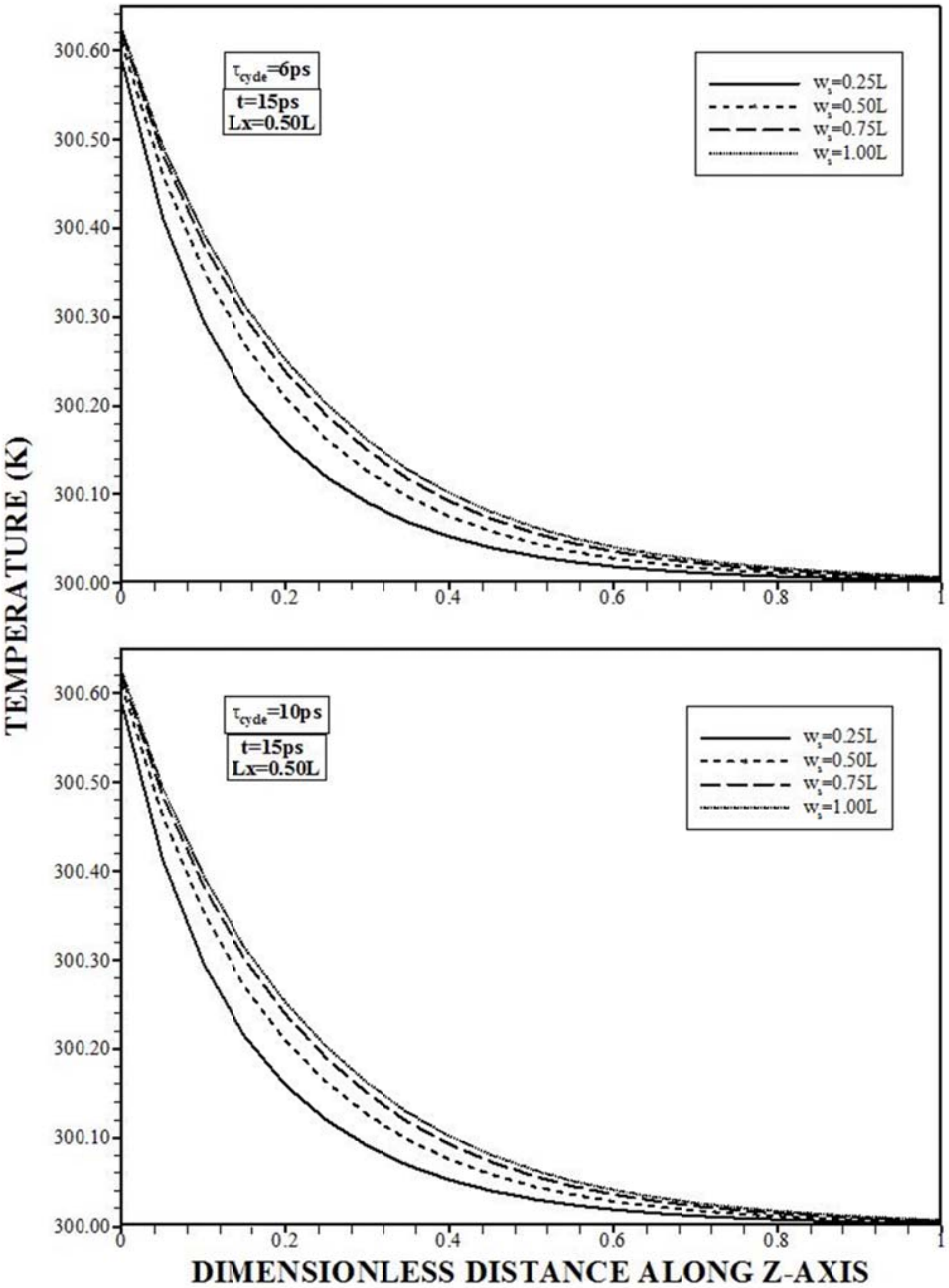

Figure 5.25 Equivalent equilibrium temperature variation along the film width for different heat source sizes and two cycles of temperature oscillation. The location in the film is $L_x = 0.5L$ and heating duration is 15 ps.

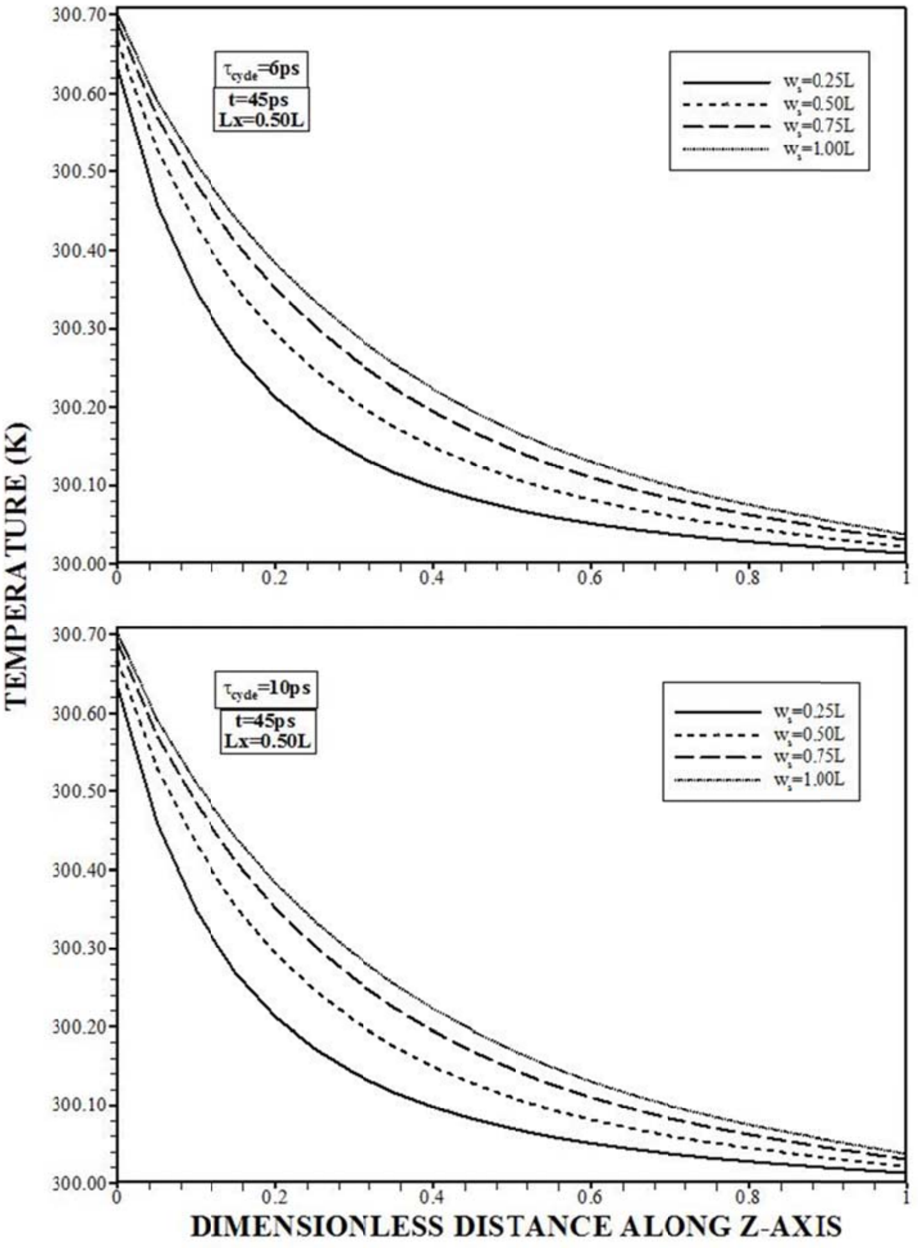

Figure 5.26 Equivalent equilibrium temperature variation along the film width for different heat source sizes and two cycles of temperature oscillation. The location in the film is $L_x = 0.5L$ and heating duration is 45 ps.

5.1.6 Transient Heat Transport in Silicon and Diamond Thin Film Pair Including the Thermal Boundary Resistance

Transient phonon transport across the two-dimensional silicon-diamond film pair is investigated incorporating the thermal boundary resistance at the film pair interface. Frequency dependent Boltzmann transport equation is incorporated and the cut-off mismatch model is adopted to formulate the thermal boundary resistance. The thermal boundary resistance predictions are compared with those obtained from the diffusive mismatch model.

Figure 5.27 shows temporal variation of the thermal boundary resistance across the silicon-diamond film pair obtained from the cut-off frequency and diffusive mismatch models while Figure 5.28 shows equivalent equilibrium temperature contours in the silicon and diamond film pair due to both thermal boundary resistance models. It should be noted that energy balance at the silicon-diamond interface is satisfied for the cut-off mismatch and diffusive mismatch models across the interface. The cut-off mismatch model relies on the previous formulation [108] for thermal boundary resistance across the thin film pair; in which case, the mismatch frequencies of all the acoustic branches of the phonons are considered to be forbidden to transfer from one film to another across the interface of the films pair. In general, the thermal boundary resistance (TBR) reduces with increasing heating period for both mismatch models introduced in the simulations. However, the rate of decrease in TBR becomes low after initial heating period $\left(\geq 50\ ps\right)$; in which case, almost quasi-steady behavior of TBR occurs after the initial heating duration. This behavior is associated with the phonon intensity distribution at the interface, which reaches almost quasi-steady state after the initial heating period is completed. Moreover, TBR resulted from the cut-off mismatch model has higher values than that obtained from the diffusive mismatch model. This is attributed to the consideration of the cut-off frequencies; in which case, only for those phonons having the allowable frequency range can possibly transfer to the diamond film, which is unlike the consideration made in the diffusive mismatch model. Therefore, the phonon intensity attains larger values for the cut-off frequency consideration at the silicon interface than that of the diffusive mismatch because of only phonons with allowable frequencies can possibly transmit to the diamond film while causing the high values of TBR at the silicon-diamond interface. TBR predicted using diffusive mismatch and cut-off mismatch models increases towards the film edges, which can be observed from Figure 5.29. In this case, the low temperature (300 K) boundary conditions implemented at the interface boundaries are responsible for the increase of TBR towards the edges of the interface. Moreover, the values of TBR predicted using the cut-off mismatch model predicts similar values for those reported in the open literature [119, 120]. This can be observed from Table 5.1, in which TBR values predicted from the present simulations and those obtained from the previous study [119, 120] are given.

Figure 5.30 shows the ratio of phonon intensities $\left(\eta_{LA}\right)$ due to longitudinal acoustic branches while Figure 5.31 shows the ratio of phonon intensities due to transverse acoustic branches $\left(\eta_{LA}\right)$ (the ratio is determined from $\eta_{LA/TA}=\dfrac{\left(I^{0}_{Si,LA/TA}\right)_{CMM}}{\left(I^{0}_{Si,LA/TA}\right)_{DMM}}$) along the silicon film width for different heating periods. The x-axis location is at the mid-thickness of the silicon film (Figure 3.8). In addition, the ratio represents phonon intensities corresponding to cut-off mismatch over the diffusive mismatch models. It should be noted that silicon film edge has the highest temperature (301 K) in the silicon-diamond film pair (Figure 3.8) and width represents the film size along the z-axis (Figure 3.8). The case of the ratio due to longitudinal acoustic branches $\left(\eta_{LA}\right)$ increases gradually along the film width, which is more pronounced at long heating periods. This is attributed to the amount of emitted phonons from the high temperature edge of the silicon film reaching at the interface, which increases with progressing time. Moreover, attainment of large intensity ratio towards the silicon film edge reveals that phonon intensity due to diffusive mismatch model attains lower values than that corresponding to cut-off mismatch model. This behavior can be explained in terms of the amount of phonons transferring from silicon interface to the diamond film. Since diffusive mismatch model predicts low thermal boundary resistance, the phonon transmittance across the silicon-diamond interface increases and the contribution of the reflected phonon intensities from the interface to the phonon intensity distribution becomes not significant in the silicon film, particularly in the region close to silicon film interface. In the case of the cut-off mismatch model, only phonons satisfying the frequency cut-off limit, due to frequency mismatch, can transfer to the diamond film and remaining phonons reflects from the silicon film interface. Consequently, the amount of phonon intensity transferring to the diamond film across the interface becomes less and those phonons reflected from the interface contributes to the phonon intensity enhancement in the silicon film, which is more pronounced in the close region of the film interface. As the distance approaches the silicon edge where temperature is high (301 K), the phonon intensity ratio approaches to about 1. This indicates that the reflected phonons from the interface do not significantly contribute to the phonon intensity distribution in the near region of the high temperature edge of the film. Hence, the amount of reflected phonons does not alter notably the phonon intensity in the region close to the high temperature edge. In the case of the transverse acoustic branches, the phonon intensity ratio $\left(\eta_{TA}\right)$, behaves similar to that presented in Figure 5.31 for the longitudinal acoustic braches. However, the ratio $\left(\eta_{TA}\right)$ is slightly lower than that of the longitudinal acoustic braches $\left(\eta_{LA}\right)$, provided that the differences are considerably small.

Figure 5.32 shows the ratio of phonon intensities due to longitudinal acoustic branches $\left(\eta_{LA}\right)$ while Figure 5.33 shows the ratio phonon intensities due to transverse acoustic branches (where the ratios are $\eta_{LA/TA} = \dfrac{\left(I^0_{Di,LA/TA}\right)_{CMM}}{\left(I^0_{Di,LA/TA}\right)_{DMM}}$) along the diamond film width for different heating periods. The x-axis location is the mid-thickness of the diamond film (Figure 3.8). The intensity ratio $\left(\eta_{LA}\right)$ is low at the interface of the diamond film and it increases towards to low temperature (300 K) edge of the film. Since phonon intensity transferred from the silicon film towards the diamond film is less for the cut-off mismatch model than that of the diffusive mismatch model, the intensity ratio

(η_{LA}) at the film interface becomes less than 1. As the film width increases towards the low temperature edge, the influence of the cut-off mismatch and diffusive mismatch models on the phonon transport becomes negligible because of the phonon scattering in the film. It should be noted that the low temperature edge acts like a phonon sink and phonons emitted from the low temperature edge does not contribute significantly to the phonon intensity distribution in the film. In the case of Figure 5.33, in which the phonon intensity ratio (η_{TA}), due to cut-off mismatch and diffusive mismatch for the transverse acoustic branches, is shown along the width of the diamond film, the behavior of the phonon intensity ratio (η_{LA}) is similar to that corresponding to the phonon intensity ratio (η_{LA}) due to the longitudinal acoustic phonons. In the early period, the ratio (η_{TA}) almost remains the same along the film width. However, as the heating period progresses, the ratio reduces, which is more pronounced for the heating period of 125 ps. This behavior is attributed to the amount of phonon intensity transfer from the silicon film to the diamond film through the interface. This amount reduces for the cut-off mismatch case, since the thermal boundary resistance attains higher values for the cut-off mismatch model than that of the diffusive mismatch model. Consequently, reduced phonon intensity transferred to the diamond film results in the reduced phonon intensity ratio at the diamond interface.

Figure 5.34 shows temporal behavior of the phonon intensity ratio (η_{LA}) due to cut-off mismatch and diffusive mismatch models for the longitudinal acoustic braches at the mid-height of the silicon film interface while Figure 5.35 shows the phonon intensity ratio (η_{TA}) for the transverse acoustic branches at the same location. The general form the phonon intensity ratio is $\eta_{LA/TA} = \frac{\left(I^0_{Si,LA/TA}\right)_{CMM}}{\left(I^0_{Si,LA/TA}\right)_{DMM}}$. The intensity ratio (η_{LA}) remains almost 1 in the early heating period and as the heating period progresses, the intensity ratio changes rapidly. The sudden increase in the intensity ratio indicates that phonons reaching at the silicon interface reflected at a higher rate for the cut-off mismatch case than that of the diffusive mismatch case. In this case, the reflected phonons contribute to the intensity enhancement at the silicon interface. However, as the time progresses further, the change in the ratio becomes gradual. This behavior is attributed to the temporal behavior of the phonon intensity distribution, which reaches almost quasi-steady state. Increasing the distance along the interface (*x*-axis) in the silicon film alters the change of the intensity ratio. In this case, in the region close to the edges of the interface (small *x*-values), the change of the intensity ratio becomes smaller than for those closer to the mid-height of the interface. This is associated with the low temperature (300 *K*) boundary conditions located at the edges of the silicon film. Therefore, phonon intensity reduces towards the edges of the interface, since the low temperature edges act like a phonon sink in the film. Consequently, reduced phonon intensity lowers the phonon intensity ratio in the region close to the edges. Nevertheless, the temporal behavior of the phonon intensity ratio is almost similar for all the locations along the silicon interface. In the case of Figure 5.35, in which phonon intensity ratio (η_{TA}) for the transverse acoustic branches is shown for the silicon film, temporal behavior of the phonon intensity ratio is similar to those shown in Figure 5.34. However, the values of the phonon intensity ratio for the transverse acoustic branches are slightly lower than that corresponding to the longitudinal branches. In addition, the phonon intensity variation at different locations along the interface is also similar to those shown in Figure 5.34. This indicates that the effect of cut-off mismatch model, incorporated in the simulations, on the phonon transport is the same as those of the longitudinal and transverse branches of the phonons.

Figure 5.36 shows temporal variation of the phonon intensity ratio $\left(\eta_{LA}\right)$ due to cut-off mismatch and diffusive mismatch models for the longitudinal acoustic braches at the mid-height of the diamond film interface while Figure 5.37 shows the intensity ratio $\left(\eta_{TA}\right)$ for the transverse acoustic branches at the same location. The phonon intensity ratio due to acoustic longitudinal branch $\left(\eta_{LA}\right)$ gradually reduces in the early heating period $\left(\leq 10\ ps\right)$ and as the heating period increases, the change in the phonon intensity ratio $\left(\eta_{LA}\right)$ becomes high. The gradual decrease of the phonon intensity ratio is attributed to the amount of phonon transferring from the silicon film to the diamond film across the interface, which is low during the early heating period. As the time progresses, the phonon intensity increases at the silicon interface and the amount of phonon intensity reflected from the interface towards the silicon film becomes large for the cut-off mismatch model. This gives rise to less amount of phonon transport to the diamond film as compared to that corresponding to the diffusive mismatch model. Therefore, the ratio of acoustic phonons of longitudinal branch $\left(\eta_{LA}\right)$, due to the diffusive mismatch and cut-off mismatch models, reduces sharply at the diamond interface, which is more pronounced at the mid-height of the interface. As similar to the silicon film, low temperature (300 *K*) boundaries are allocated at the edges of the diamond film. Hence, phonon intensity reduces in the region close to the low temperature edges; in which case, the effects of thermal boundary resistance models, incorporating the cut-off mismatch and diffusive mismatch, on the phonon transmittance to the diamond film becomes obvious. In the case of the phonon intensity ratio $\left(\eta_{TA}\right)$, due to acoustic transverse branches, temporal behavior as shown in Figure 5.37 is similar to that corresponding to the ratio of the longitudinal acoustic branch $\left(\eta_{LA}\right)$. In addition, the behavior of the ratio at different locations along the diamond interface is similar to that corresponding to the ratio shown in Figure 5.36.

Table 5.1. Thermal boundary resistance predicted from the present simulations using diffusive mismatch model (DMM) and cut-off mismatch model (CMM) and obtained from the previous studies [140], [141] .

THERMAL BOUNDARY RESISTANCE (m^2K/W)		
Current Simulation		Experimental Data [140], [141]
DMM	CMM	
2.18x10^{-10}	1.62x10^{-8}	3.3x10^{-8} [140]
		(1.7±0.5) x 10^{-8} [141]
		(1.3±0.6) x 10^{-8} [141]

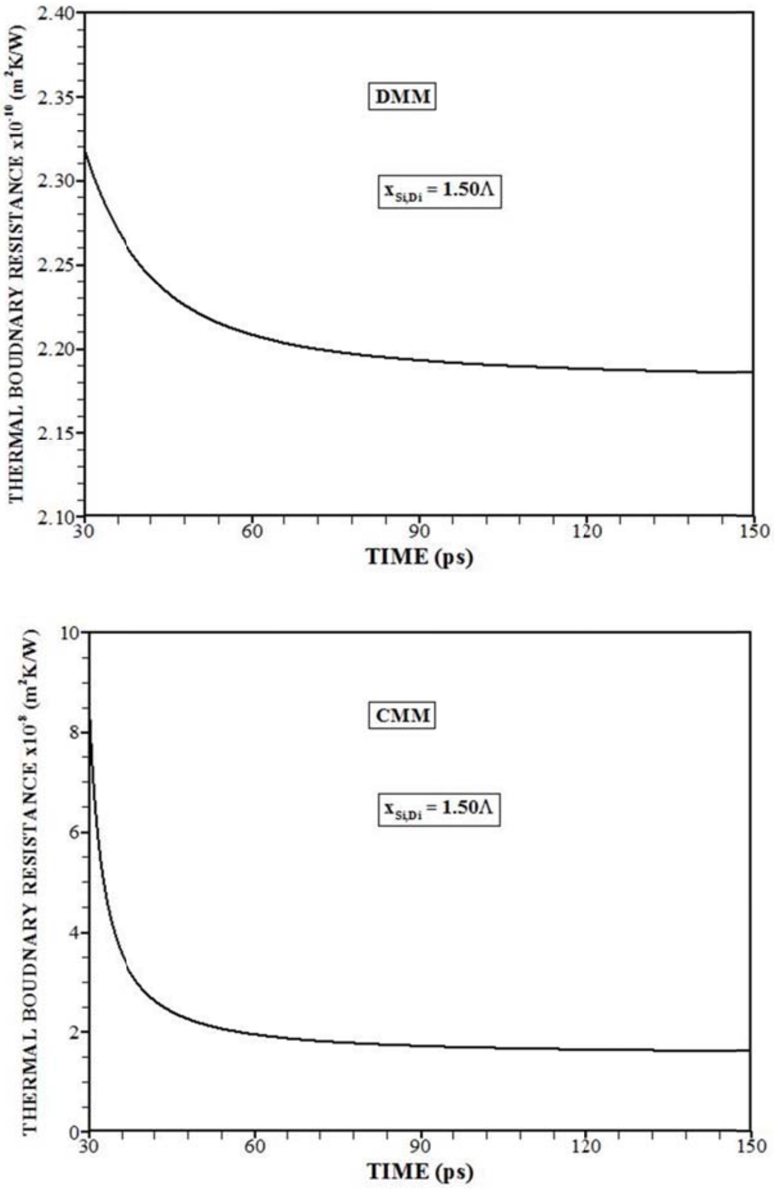

Figure 5.27 Temporal variation of thermal boundary resistance for diffusive mismatch and cut-off mismatch models for silicon-diamond film pair interface.

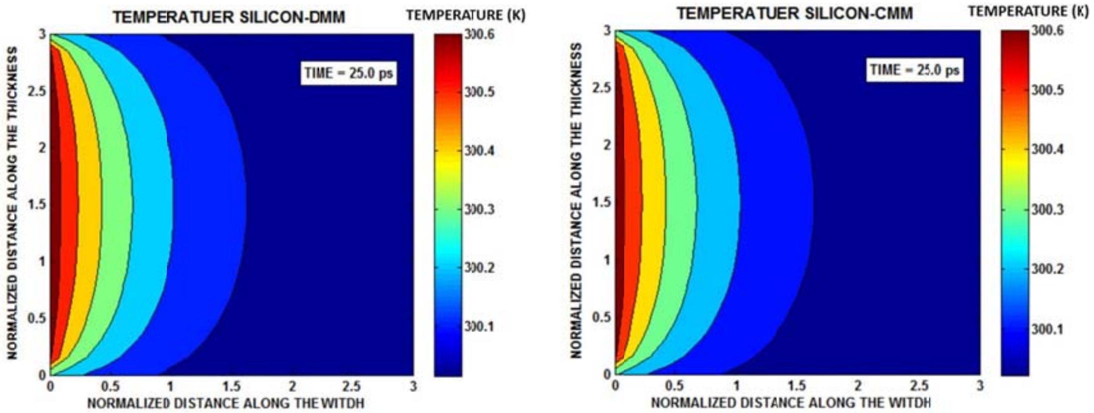

Silicon film – Diffusive Mismatch Model Silicon film – Cut-off Mismatch Model

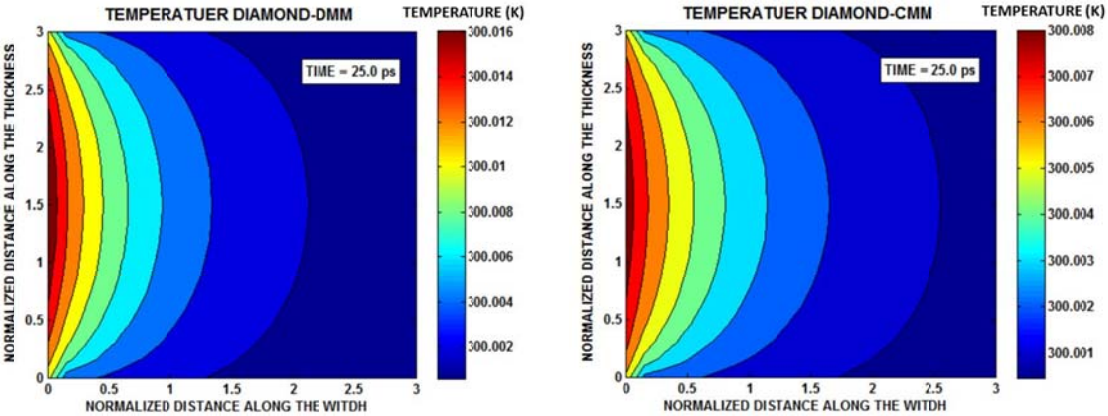

Diamond film – Diffusive Mismatch Model Diamond film – Cut-off Mismatch Model

Figure 5.28 Equivalent equilibrium temperature contours in the silicon and diamond films due to diffusive mismatch and cut-off mismatch models for 25 ps heating duration

.

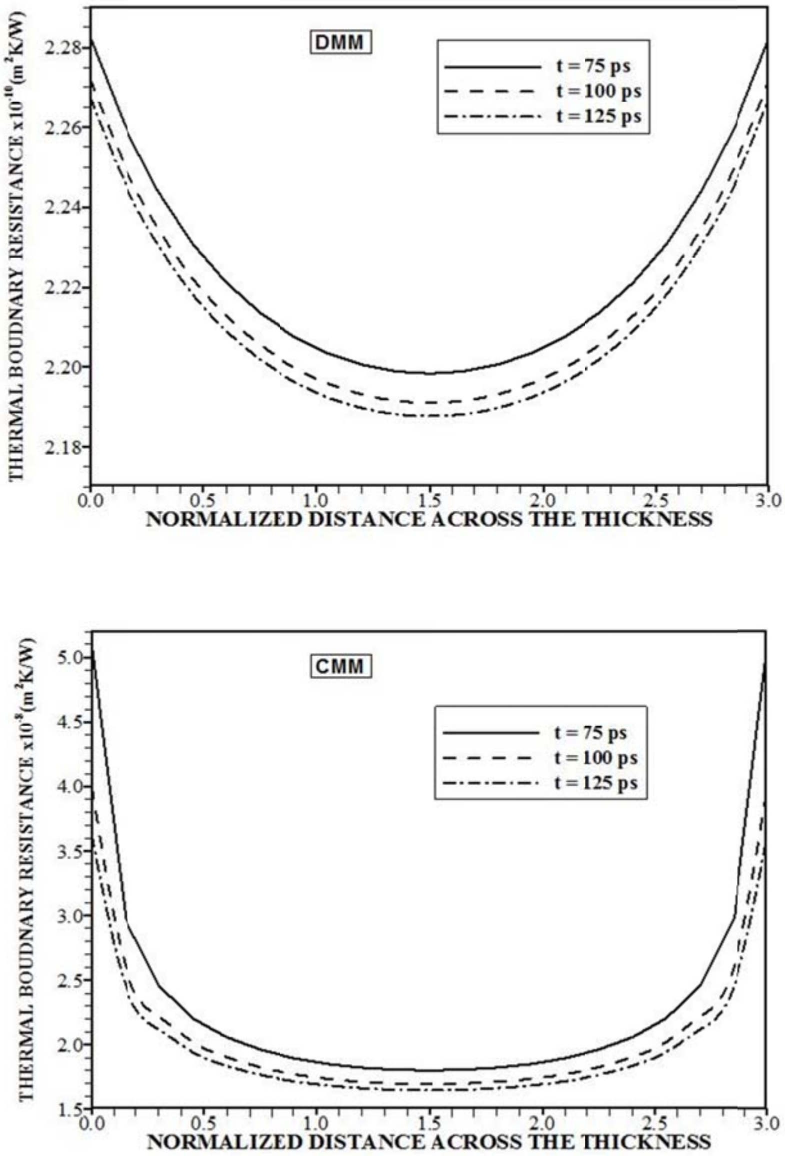

Figure 5.29 Thermal boundary resistance due to diffusive mismatch (DMM) and cut-off mismatch (CMM) models at the silicon-diamond film pair interface along the film thickness for different heating periods.

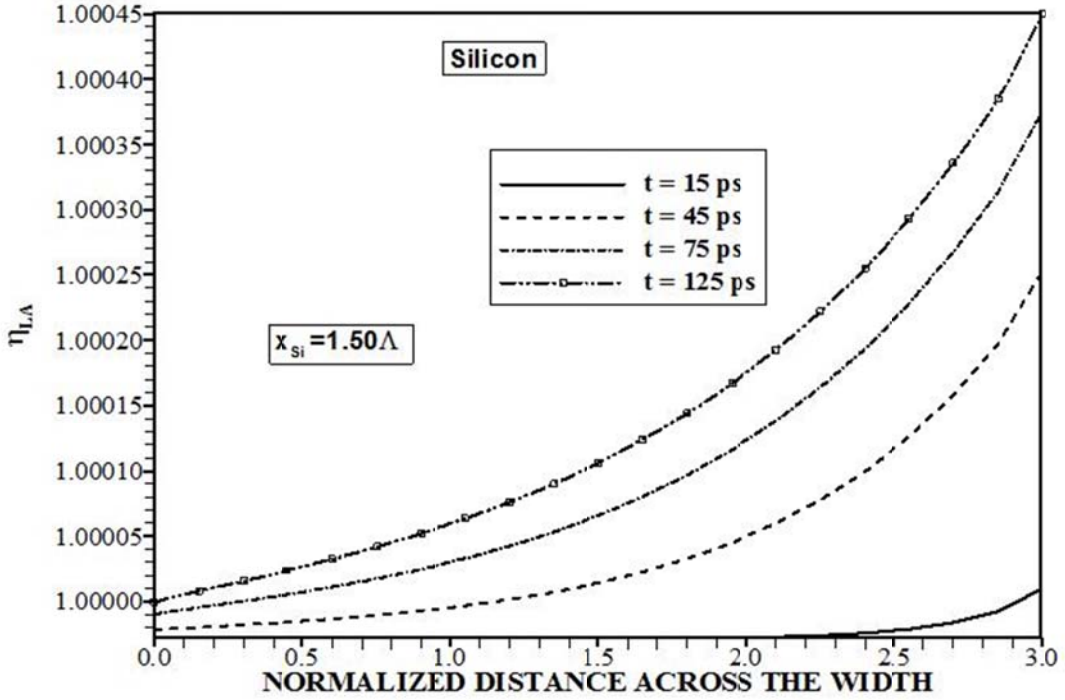

Figure 5.30 Ratio of phonon intensities due to longitudinal acoustic branches (η_{LA}) in silicon film for different heating periods. Ratio is determined from $\eta_{LA} = \frac{\left(I^0_{Si,LA}\right)_{CMM}}{\left(I^0_{Si,LA}\right)_{DMM}}$, where I^0 is the equilibrium phonon intensity.

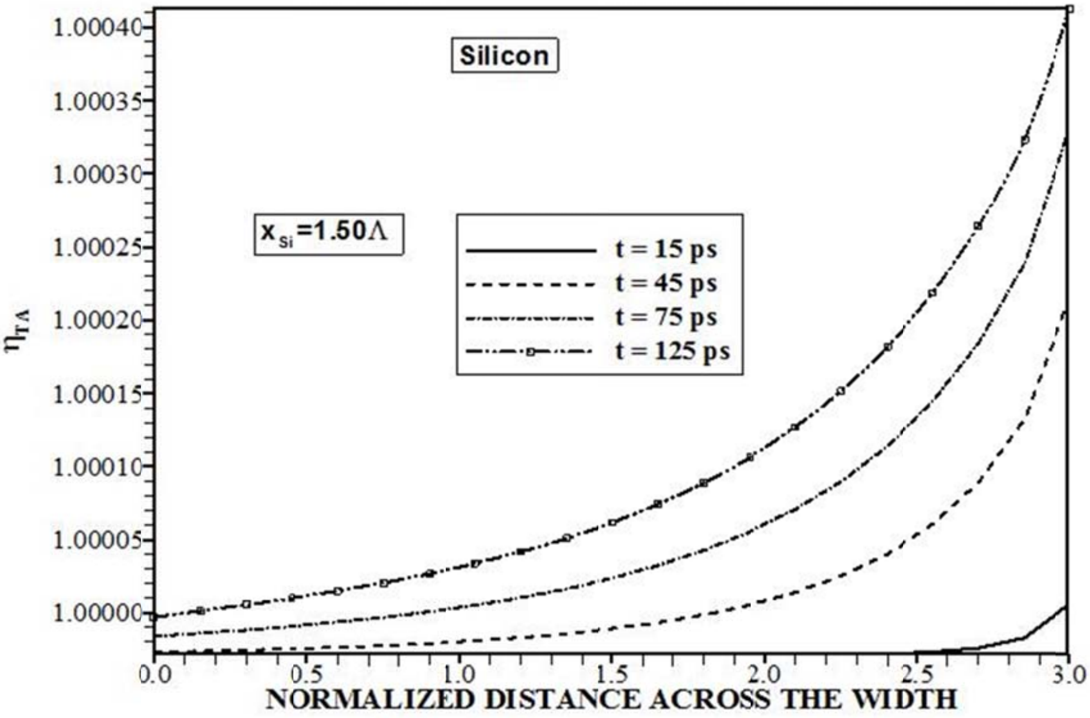

Figure 5.31 Ratio of phonon intensities due to transverse acoustic branches (η_{TA}) in silicon film for different heating periods. Ratio is determined from $\eta_{TA} = \frac{\left(I^0_{Si,TA}\right)_{CMM}}{\left(I^0_{Si,TA}\right)_{DMM}}$, where I^0 is the equilibrium phonon intensity.

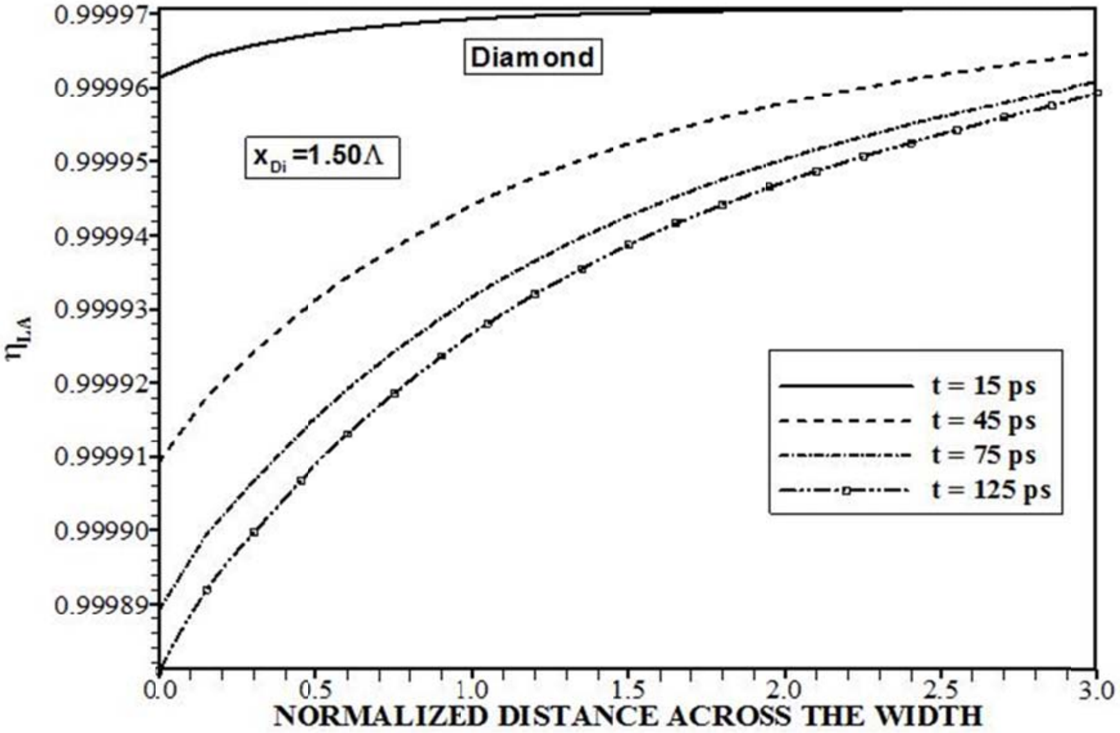

Figure 5.32 Ratio of phonon intensities due to longitudinal acoustic branches (η_{LA}) in diamond film for different heating periods. Ratio is determined from $\eta_{LA} = \frac{\left(I^0_{Si,LA}\right)_{CMM}}{\left(I^0_{Si,LA}\right)_{DMM}}$, where I^0 is the equilibrium phonon intensity.

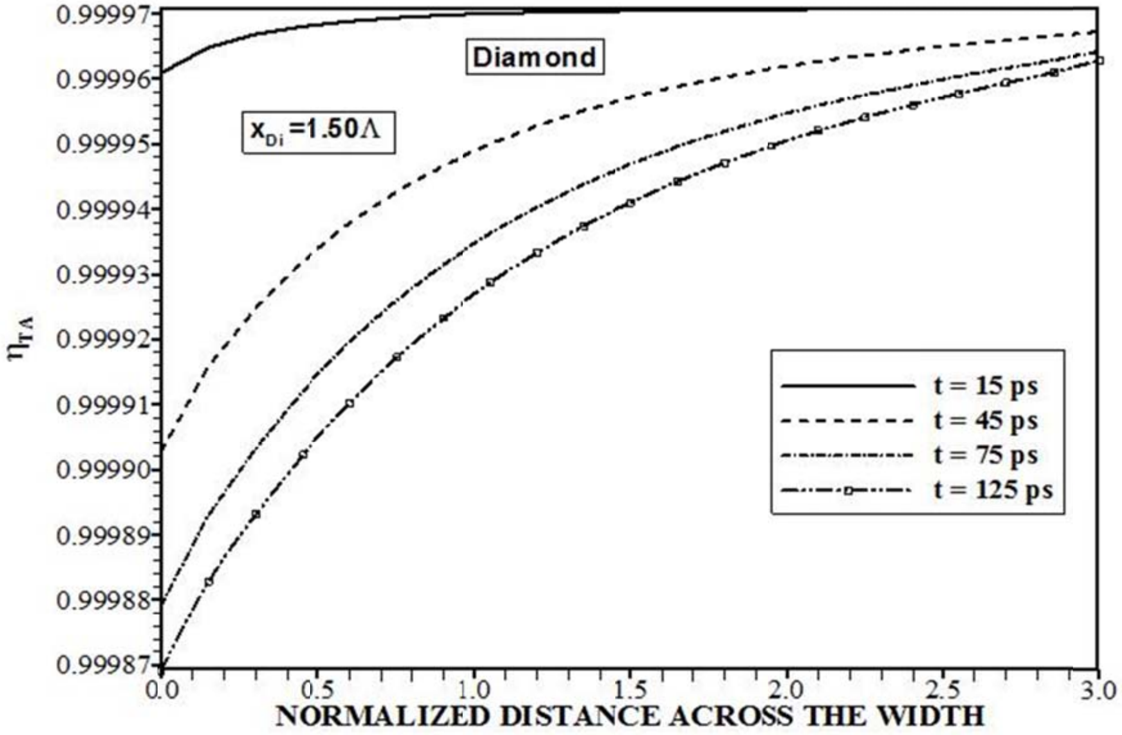

Figure 5.33 Ratio of phonon intensities due to transverse acoustic branches (η_{TA}) in diamond film for different heating periods. Ratio is determined from $\eta_{TA} = \frac{\left(I^0_{Si,TA}\right)_{CMM}}{\left(I^0_{Si,TA}\right)_{DMM}}$, where I^0 is the equilibrium phonon intensity.

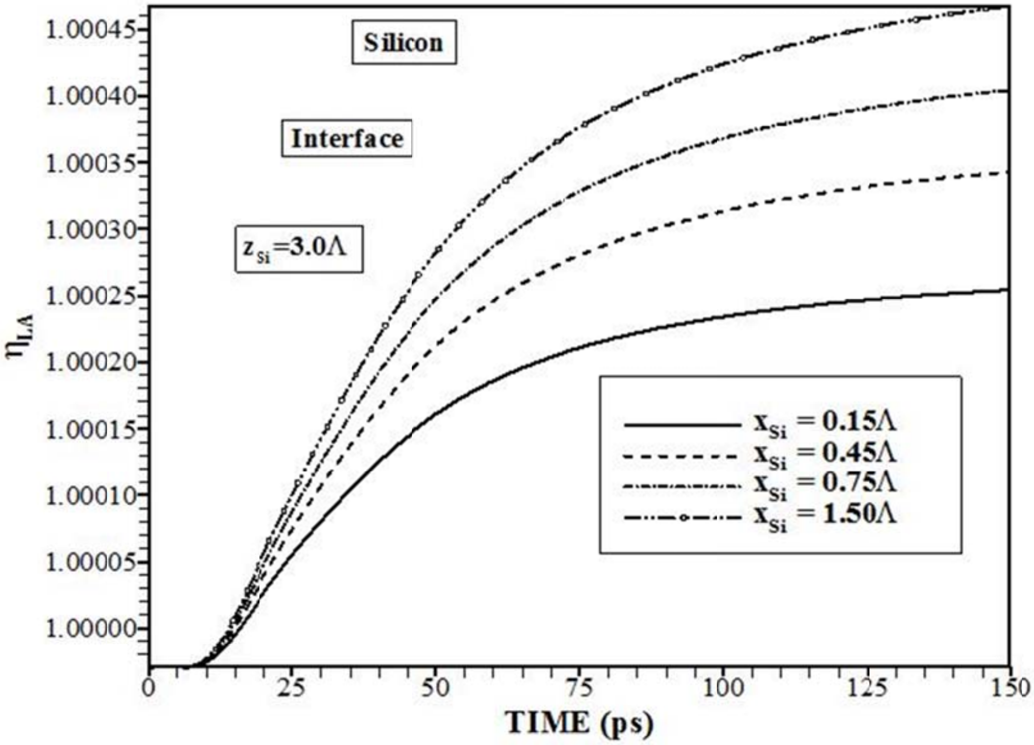

Figure 5.34 Temporal variation of ratio of phonon intensities due to longitudinal acoustic branches (η_{LA}) in silicon film for different heating periods. Ratio is determined from $\eta_{LA} = \frac{\left(I^0_{Si,LA}\right)_{CMM}}{\left(I^0_{Si,LA}\right)_{DMM}}$, where I^0 is the equilibrium phonon intensity.

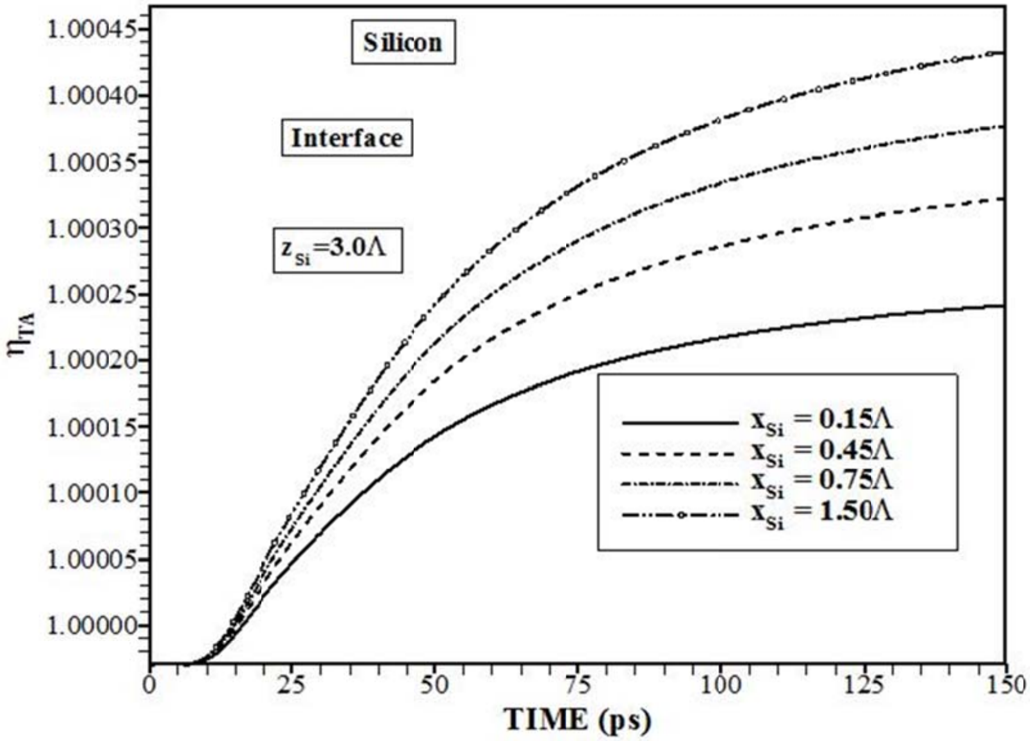

Figure 5.35 Temporal variation of ratio of phonon intensities due to transverse acoustic branches (η_{TA}) in silicon film for different heating periods. Ratio is determined from $\eta_{TA} = \frac{\left(I^0_{Si,TA}\right)_{CMM}}{\left(I^0_{Si,TA}\right)_{DMM}}$, where I^0 is the equilibrium phonon intensity.

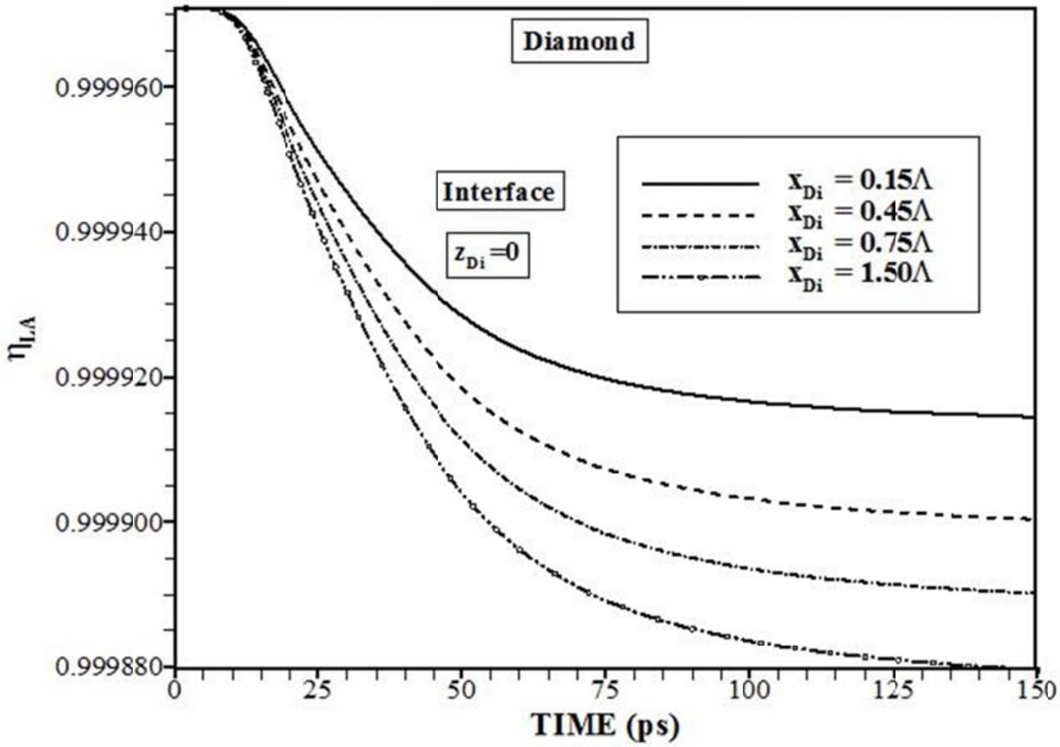

Figure 5.36 Temporal variation of ratio of phonon intensities due to longitudinal acoustic branches (η_{LA}) in diamond film for different heating periods. Ratio is determined from $\eta_{LA}=\frac{\left(I^{0}_{Si,LA}\right)_{CMM}}{\left(I^{0}_{Si,LA}\right)_{DMM}}$, where I^{0} is the equilibrium phonon intensity.

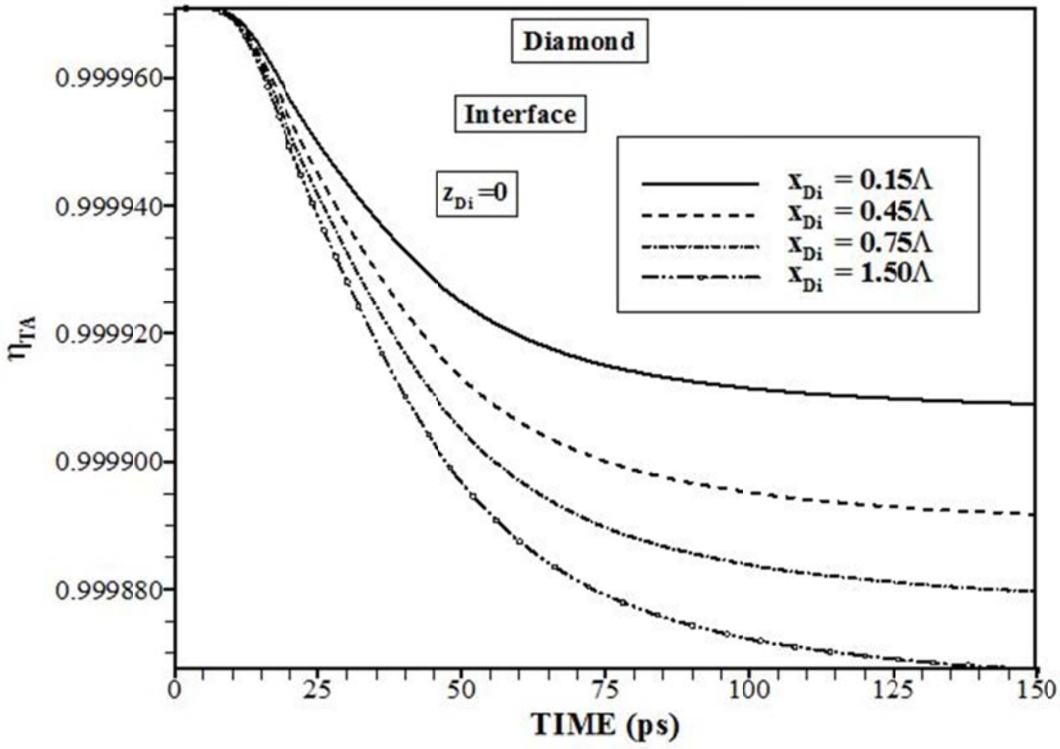

Figure 5.37 Temporal variation of ratio of phonon intensities due to transverse acoustic branches $\left(\eta_{TA}\right)$ in diamond film for different heating periods. Ratio is determined from $\eta_{TA}=\frac{\left(I^0_{Si,TA}\right)_{CMM}}{\left(I^0_{Si,TA}\right)_{DMM}}$, where I^0 is the equilibrium phonon intensity.

5.1.7 Transient Heat Transport Including Quantum Dot in Silicon Thin Films

Transient thermal energy transport in two-dimensional silicon with the presence of an aluminum dot is examined. Boltzmann transport equation is incorporated to predict the phonon intensity and equivalent equilibrium temperature in the film.

Figure 5.38 shows equivalent equilibrium temperature along the z-axis and x-axis location is at x = 3.7Λ, where Λ is the gray medium mean free path of silicon, for different heating durations while Figure 5.39 shows equivalent equilibrium temperature contours in the silicon film. It should be noted that the dispersion relations are incorporated in the analysis and phonon wavelengths vary for different modes and branches of phonons. On the other hand, the gray body consideration assumes a unique average mean free path. In the analysis, temperature of aluminum dot is considered to be uniform across its area, provided that temporal variation of temperature is assumed to vary exponentially in the aluminum dot, which is shown in

Figure 3.13. Moreover, x = 2.96 Λ corresponds to the edge of the aluminum dot in the film (Figure 3.11) and z = 0 is the low temperature edge of the silicon film. Equivalent equilibrium temperature reduces along the z-axis towards the low temperature edge of the silicon film. Since the quasi-ballistic phonons do not contribute to the film resistance, temperature decay becomes non-linear along the z-axis, which is more pronounced for the early heating periods. However, low temperature edge of the silicon film acts like a phonon sink and phonons reflected and emitted from the low temperature

edge do not contribute considerably to equivalent equilibrium temperature rise in the film. Since temperature increases exponentially with progressing time at the edge of the aluminum dot, phonons emitted from the aluminum-silicon interface towards the silicon film increases with progressing time. This in turn increases equivalent equilibrium temperature in the silicon film, particularly in the near region of the aluminum-silicon film interface. The boundary scattering at the aluminum-silicon interface also contributes to temperature jump at the interface; however, temperature jump reduces with progressing time at the silicon interface. This behavior is attributed to the increased rate of the phonon intensity transmitted from the aluminum interface towards the silicon interface with progressing time. Hence, temperature jump at the silicon interface reduces with an increasing rate as similar to temperature increase at the aluminum interface. Figure 5.40 shows equivalent equilibrium temperature along the x-axis at z-axis location of $z = 1.48\ \Lambda$, which is away from the aluminum dot in the silicon film (Figure 3.11) for the same heating periods shown in Figure 5.38. Since the symmetry reveals at the mid-height of the film width and across the film thickness, equivalent equilibrium temperature variation along the x-axis is shown at $z = 1.48\ \Lambda$. Equivalent equilibrium temperature profiles along the x-axis change slightly as compared those shown in Figure 5.38. This is attributed to the phonon intensity distribution in this region, which is away from the aluminum-silicon interface. Phonons undergo scattering prior to reaching at this region; consequently, equivalent equilibrium temperature shows relatively gradual decay along the x-axis, which is true for all the heating periods considered.

Figure 5.41 shows temporal variation of equivalent equilibrium temperature for different z-axis locations and x-axis location is the symmetry line. Equivalent equilibrium temperature increases rapidly during the early heating periods. This behavior is more pronounced in the close region of the aluminum dot in the silicon film. This is associated with the phonon intensity distribution in the early heating period, which increases rapidly with progressing time. The phonon scattering in the film enhances the film resistance and increases equivalent equilibrium temperature in the film. However, the rise of equivalent equilibrium temperature becomes gradual as the heating period progresses. This situation is mainly observed for the z-axis location z = 2.22 Λ, where it is close to the aluminum dot. Consequently, phonons emitted from the silicon interface towards to low temperature edge undergo high rate of scattering while increasing equivalent equilibrium temperature in this region. Since temperature at the aluminum dot edges is considered to increase exponentially (

Figure 3.13), the rise phonon intensity follows almost the rise of temperature at the aluminum dot interface. However, boundary scattering of transmitted phonons from the aluminum interface, lowers the phonon intensity in this region. Therefore, temporal variation of equivalent equilibrium temperature at the silicon interface does not follow exactly temperature at the aluminum dot interface. Nevertheless, the trend of sharp and gradual rises of temperature at the aluminum interface cause similar reflection on equivalent equilibrium temperature in the near region of the silicon film interface. Figure 5.42 shows temporal variation of equivalent equilibrium temperature for different x-axis location in the film and z-axis location is z = 1.48 Λ, which is away from the silicon-aluminum interface. Temporal behavior of temperature is similar to that is shown in Figure 5.41, provided that the values of temperature are lower in Figure 5.42 than those shown in Figure 5.41, which corresponds to the close region of the silicon interface. The attainment of low temperature is attributed to the scattering of emitted phonons from the aluminum-silicon interface prior to reaching at the distance away from the interface in the silicon film. In addition, the quasi-ballistic and ballistic phonons which do not contribute significantly to the film resistance and temperature increase in this region.

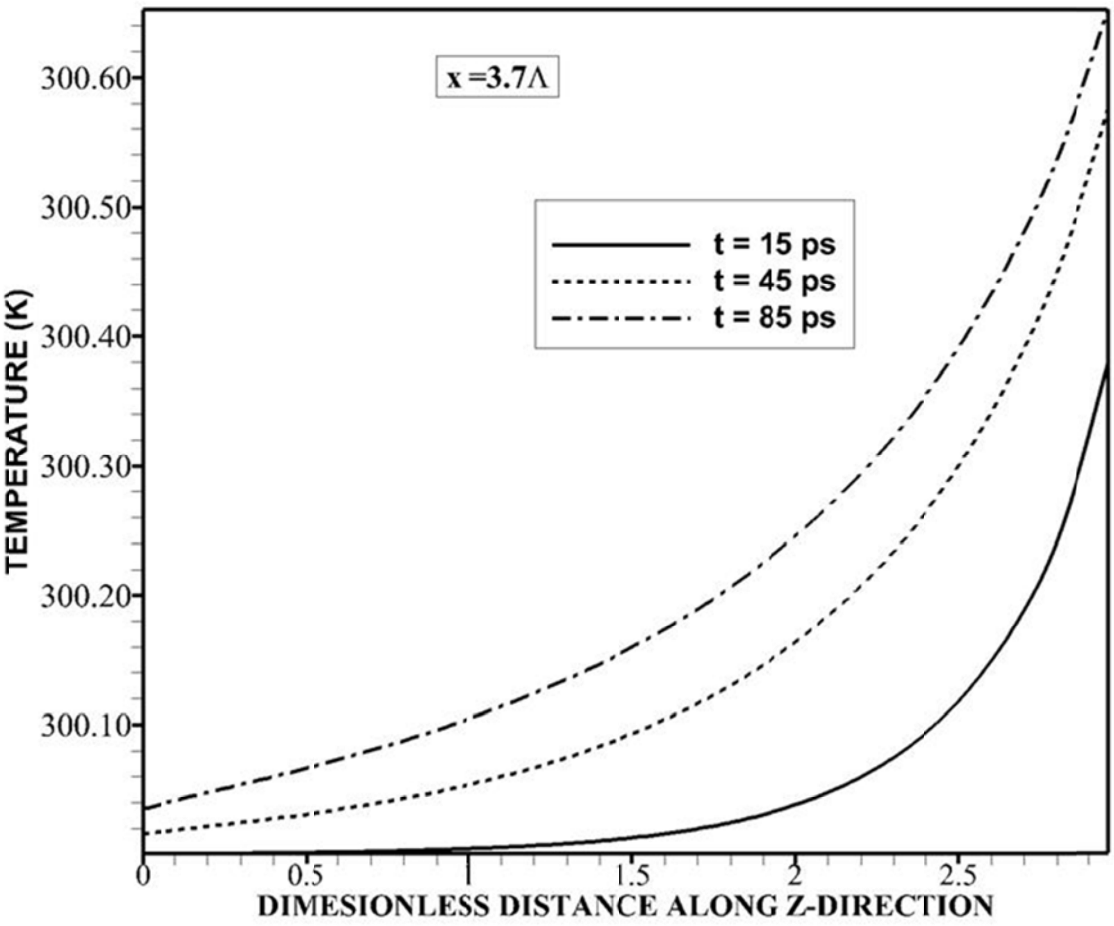

Figure 5.38 Equivalent equilibrium temperature along the z-axis for different heating periods. The x-axis location is x = 3.7 Λ. The x-axis is normalized with the averaged mean free path (Λ).

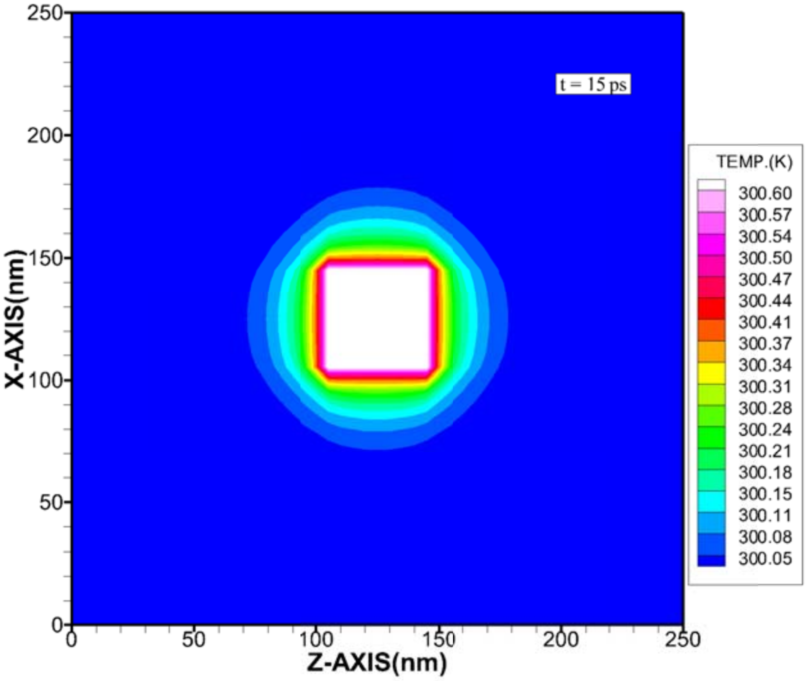

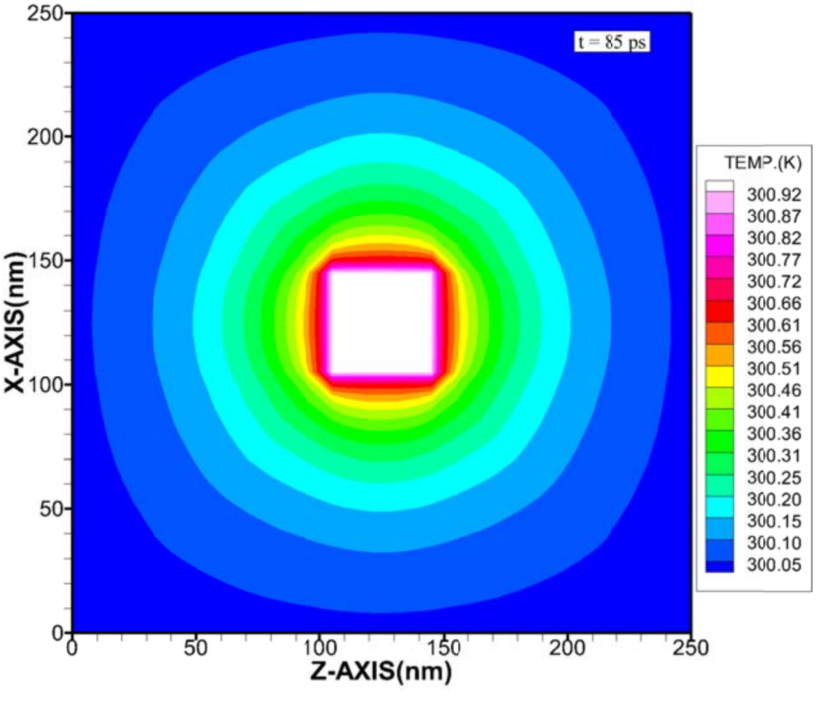

Figure 5.39 Equivalent equilibrium temperature contours in the silicon film for two heating periods.

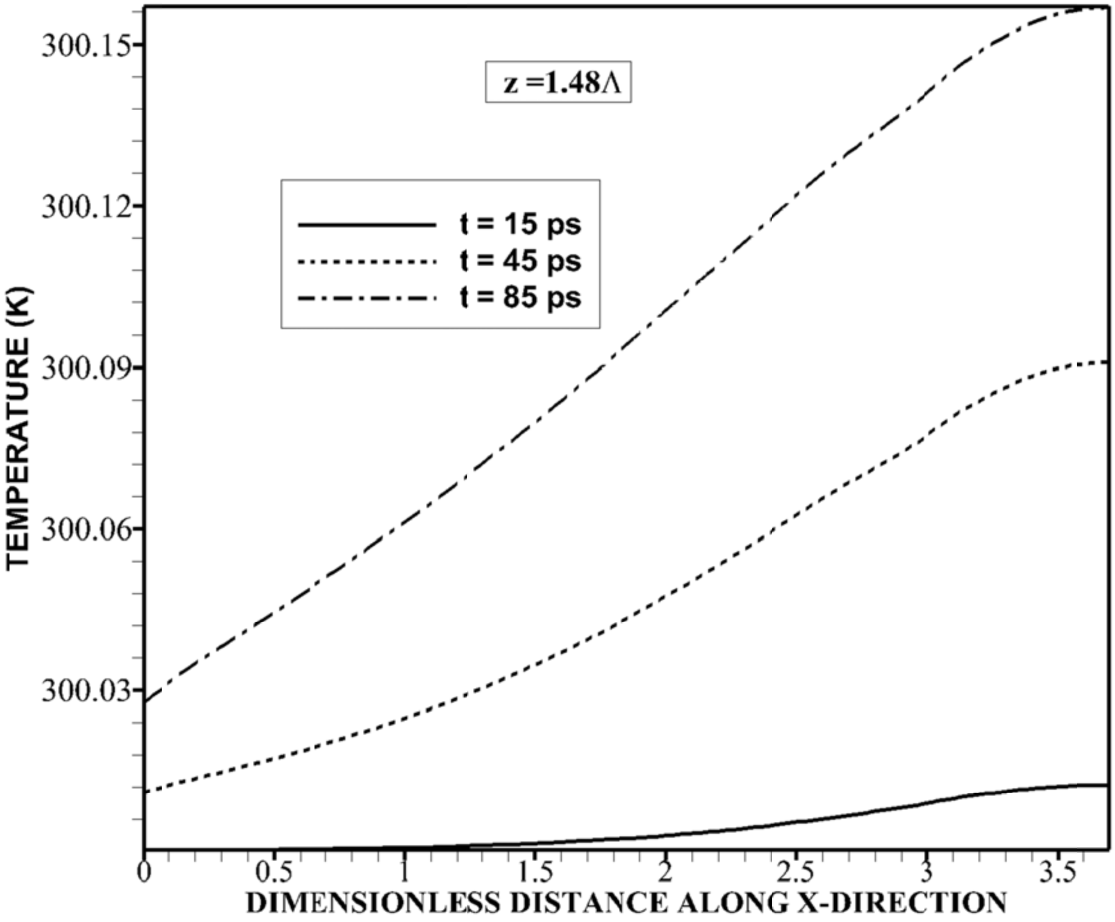

Figure 5.40 Equivalent equilibrium temperature along the x-axis for different heating periods. The z-axis location is z = 1.48 Λ. The x-axis is normalized with the averaged mean free path (Λ).

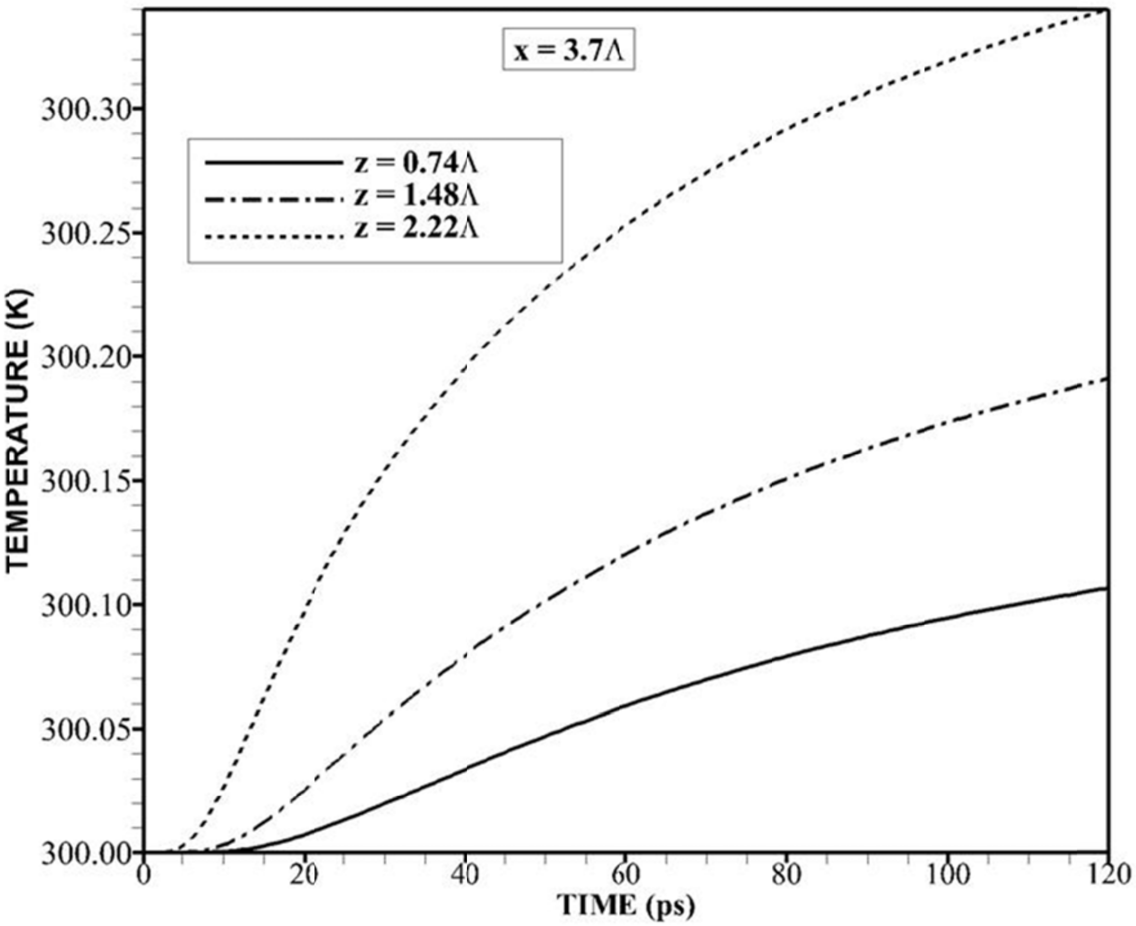

Figure 5.41 Temporal variation of equivalent equilibrium temperature for different z-axis locations. The axis location is x = 3.7Λ.

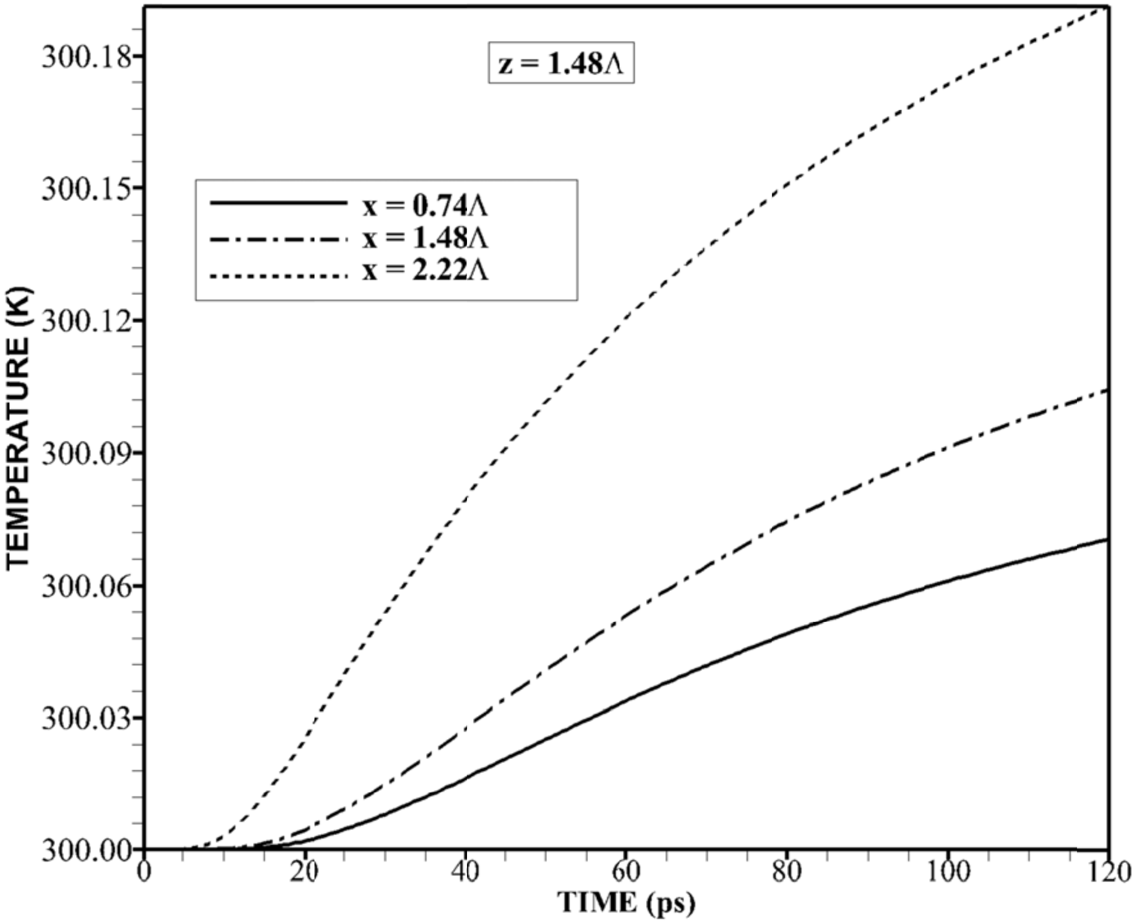

Figure 5.42 Temporal variation of equivalent equilibrium temperature for different x-axis locations. The z-axis location is z = 1.48Λ.

5.2 One Dimensional Dielectric Thin Films

In this section the results of case studies which are introduced in chapter 3 related to one dimensional dielectric thin films are presented. All the one dimensional cases are solved incorporating the EPRT along with the initial, boundary and interface conditions which discussed in chapter 3. The case studies are,

1. Steady State Heat Transport Including the Effect of Film Thickness on Entropy Generation Rate.
2. Transient Heat Transport Inculding the Effect of Minute Vacuum Gap in between the Films.

5.2.1 Steady State Heat Transport Including the Effect of Film Thickness on Entropy Generation Rate

Phonon transport in a thin silicon film is considered and entropy generation is investigated in the thin film. The effect of film thickness on entropy generation is computed due to temperature disturbance at the film edges. In order to assessment of phonon transport characteristics the following dimensionless parameters are introduced

Dimensionless Temperature

$$\textit{Dimensionless Temperature} = \frac{T(x) - T_{right}}{T_{left} - T_{right}} \tag{5.4}$$

Dimensionless Entropy Generation

$$\textit{Dimensionless Entropy Generation} = \frac{S_{gen}(x)}{S_{gen,max}} \tag{5.5}$$

Figure 5.43 shows dimensionless temperature predicted from the present study and obtained from the previous work [3]. It should be noted that boundary scattering results in temperature jump at the edges of the silicon film. The boundary scattering is associated with the emitted phonons and reflected phonons from film edges [3]. The findings revealed that both results are in good agreement. The difference between the results is considerably small, which is associated with the numerical round off errors.

Figure 5.44 shows normalized entropy generation in the silicon film for different film thicknesses. Entropy generation is obtained from frequency independent analysis; in which the film is assumed to have grey body characteristics. Entropy generation reduces sharply in the region of the high temperature edge where temperature attains high values. It should be noted that phonon emitted from the high temperature edge undergo scattering in the near region of the film edge because of the film resistance. This, in turn, reduces phonon intensity considerable in this region. In addition, phonons emitted from the low temperature edge scatters in the film. This contributes to phonon intensity variation in this region. As the distance from the high temperature edge increases towards the low temperature edge, entropy generation reduces sharply. This is observed for all film thicknesses. This behavior is attributed to phonon scattering in this region; in which case, phonon intensity decay becomes rather gradual in this region as compared to the region close to the high temperature edge. In addition, reflected phonons from the low temperature edge do not contribute significantly to phonon intensity distribution through the scattering in this region, which is particularly true for the thick films

$(thickness \geq 0.5\mu m)$. When comparing entropy generation due to the film thicknesses, decay of entropy is sharper for thick films. This is attributed to redistribution of phonon intensity in the film because of the emitted and reflected phonons from the film edges. Phonons emitted from the high and low temperature edges suffer from scattering with in the film. The rate of phonon scattering is high in the region of the high temperature and it becomes gradual in the region away from the high temperature edge. The reflected phonons from the low temperature edge may not have significant contribution to phonon intensity in the region close to the high temperature edge; however, their contribution at some distance away from the high temperature edge is considerable. This, in turn, modifies the phonon scattering and entropy generation in the film.

Figure 5.45 shows normalized entropy generation along the film thickness for different thicknesses. The results are obtained for the solution of the frequency dependent radiative energy transport equation. The boundary conditions are set to be the same for the data presented in Figure 5.44. Entropy generation shows almost similar behavior along the film thickness to that shown in Figure 5.44. It should be noted that the magnitude of entropy is smaller for frequency dependent case than that of the frequency independent case (Figure 5.46). Entropy reduces sharply and the reduction becomes gradual in the region next to the high temperature edge provided that the decay is sharper for frequency independent solution of radiative phonon transport equation (Figure 5.44) than that of the frequency dependent case. The attainment of slow decay of entropy in the near region of the high temperature edge is associated with the emitted phonons from the high temperature edge. However, as the film thickness increases, entropy generation becomes sharper in the film for the frequency dependent solution of the phonon radiative transport equation. This observation differs from that obtained for the frequency independent solution. The total entropy generation with film thickness is shown in Figure 5.46 for frequency dependent and independent cases. The total entropy generation rate is determined by integration from the equation (3.47) and equation (3.52) for frequency dependent and frequency independent cases respectively. Increasing film thickness increases entropy generation in the film; however, the rate of increase is higher for thinner films $\left(thickness \leq 0.5 \mu m \right)$. This situation is true for both frequency dependent and independent cases. It should be noted that increasing film thickness enhances the film resistance due to the phonon scattering in the film; consequently, entropy generation increases. Entropy generation due to frequency dependent case attains lower values than that corresponding to frequency independent case. This behavior is associated with the effect of the ballistic phonons, which do not undergo scattering in the film and, therefore, do not contribute to the heat generation in the film. Consequently, entropy generation rate is not influenced by the ballistic phonons. This, in turn, results in less entropy generation in the film for frequency dependent case than that of the independent case. The total entropy generation attains almost twice for the frequency independent case as compared to that corresponding to the frequency dependent case. Therefore, thermodynamic irreversibility is highly dependent on the phonon frequency in terms of the entropy generation in the film, which is influenced by the film thickness.

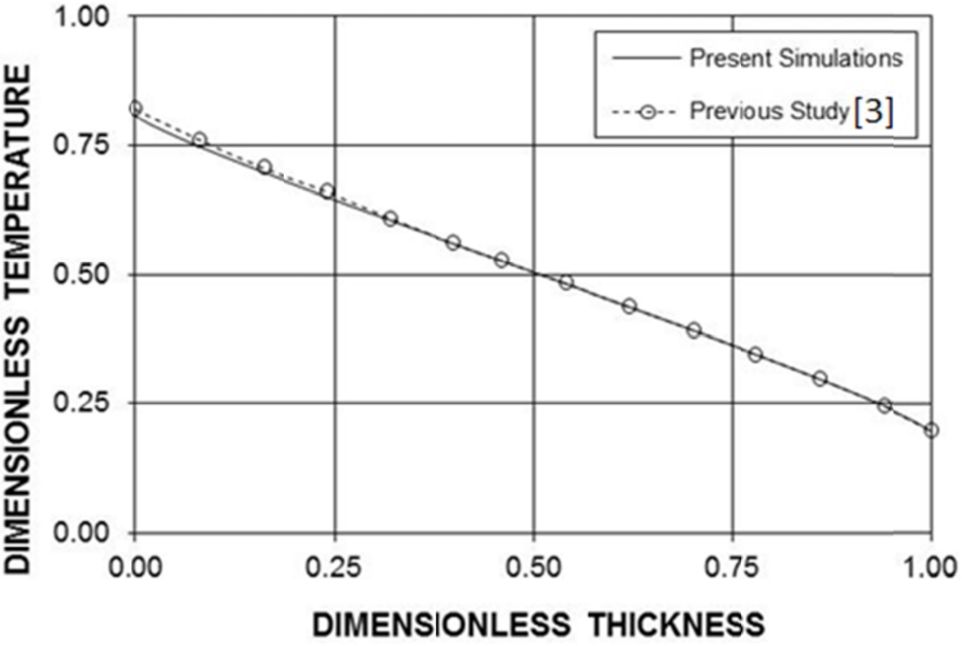

Figure 5.43 Comparison of normalized temperature along the film thickness predicted from the present study and obtained from the previous study [3].

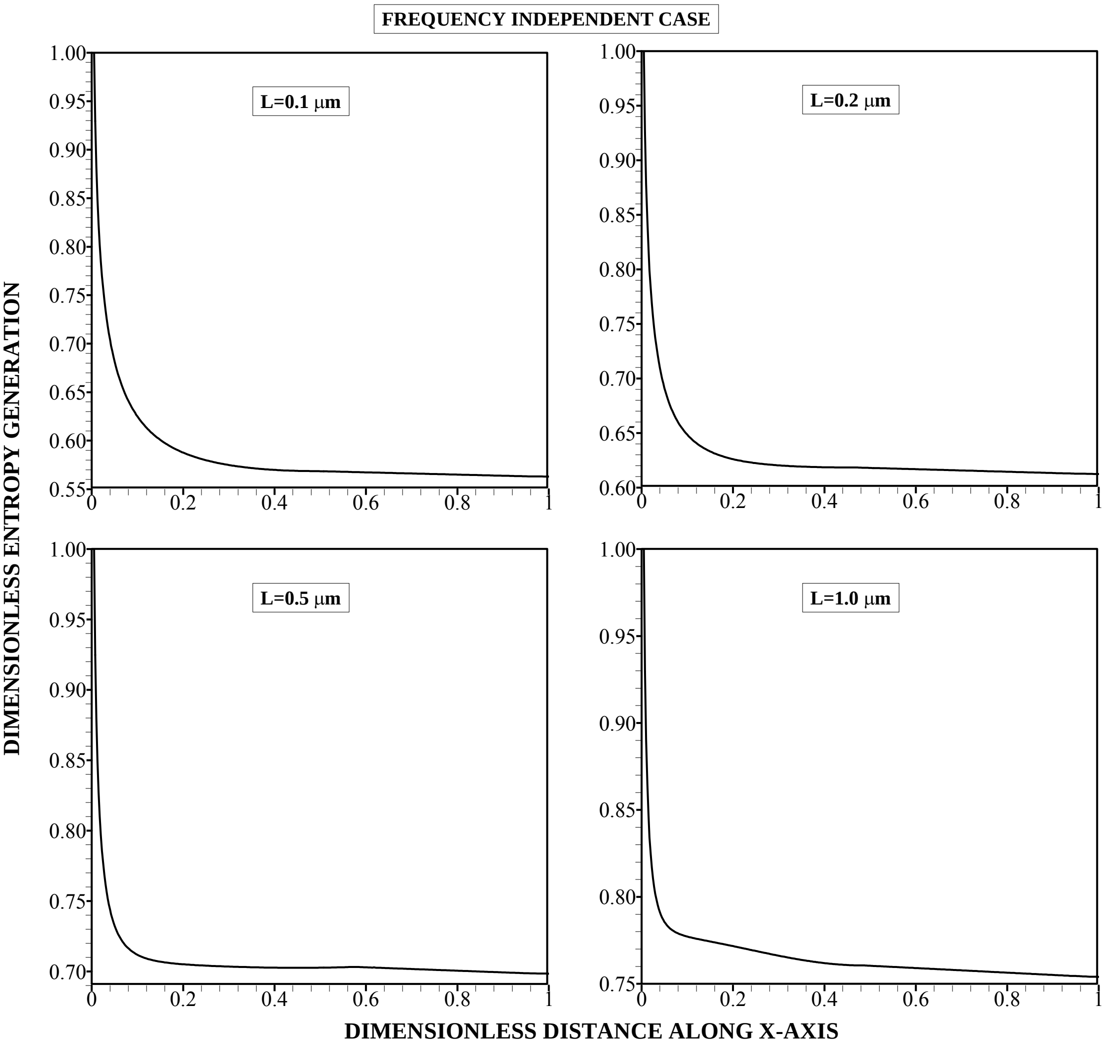

Figure 5.44 Normalized entropy generation along the normalized film thickness for different film thicknesses. The predictions are obtained for frequency independent case.

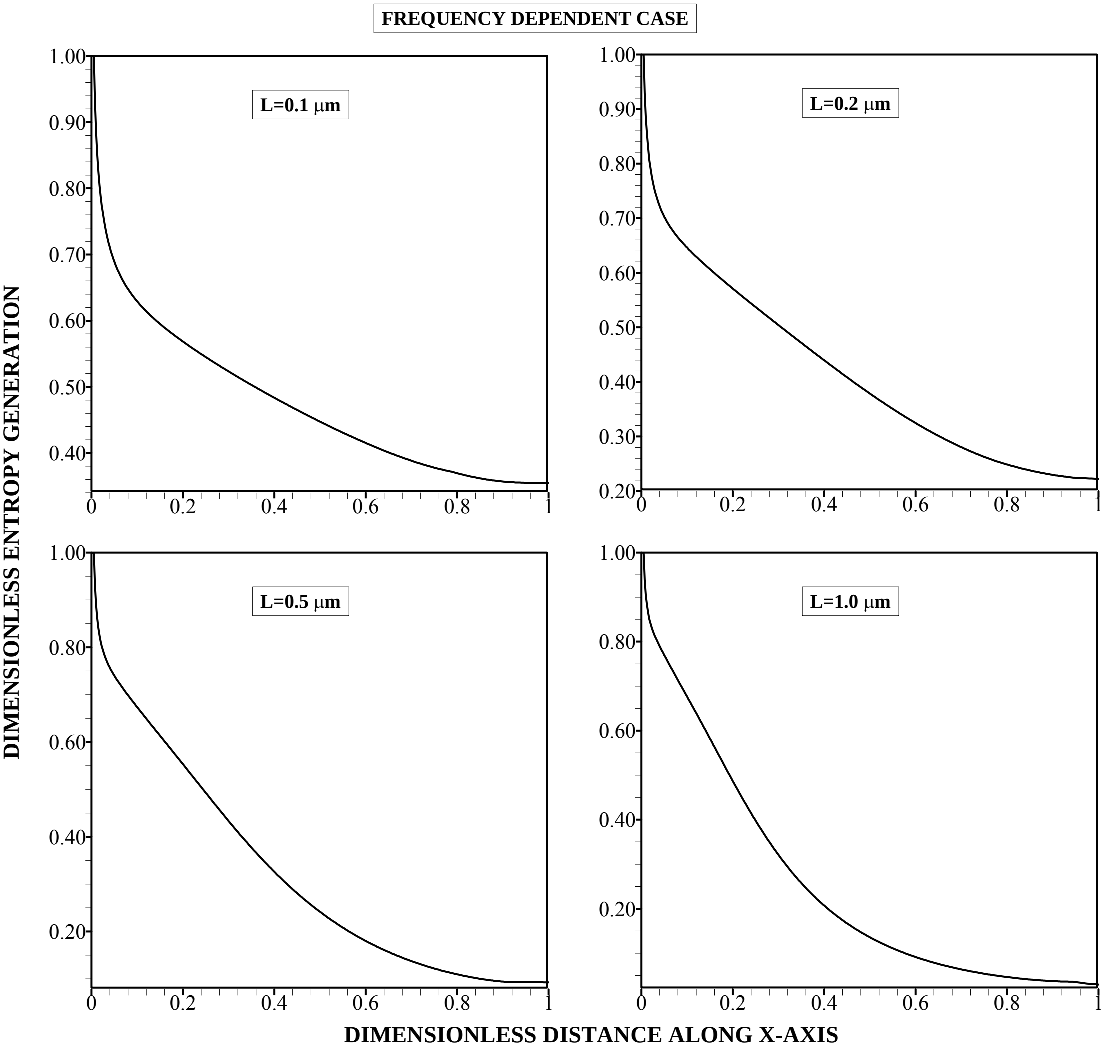

Figure 5.45 Normalized entropy generation along the normalized film thickness for different film thicknesses. The predictions are obtained for frequency dependent case.

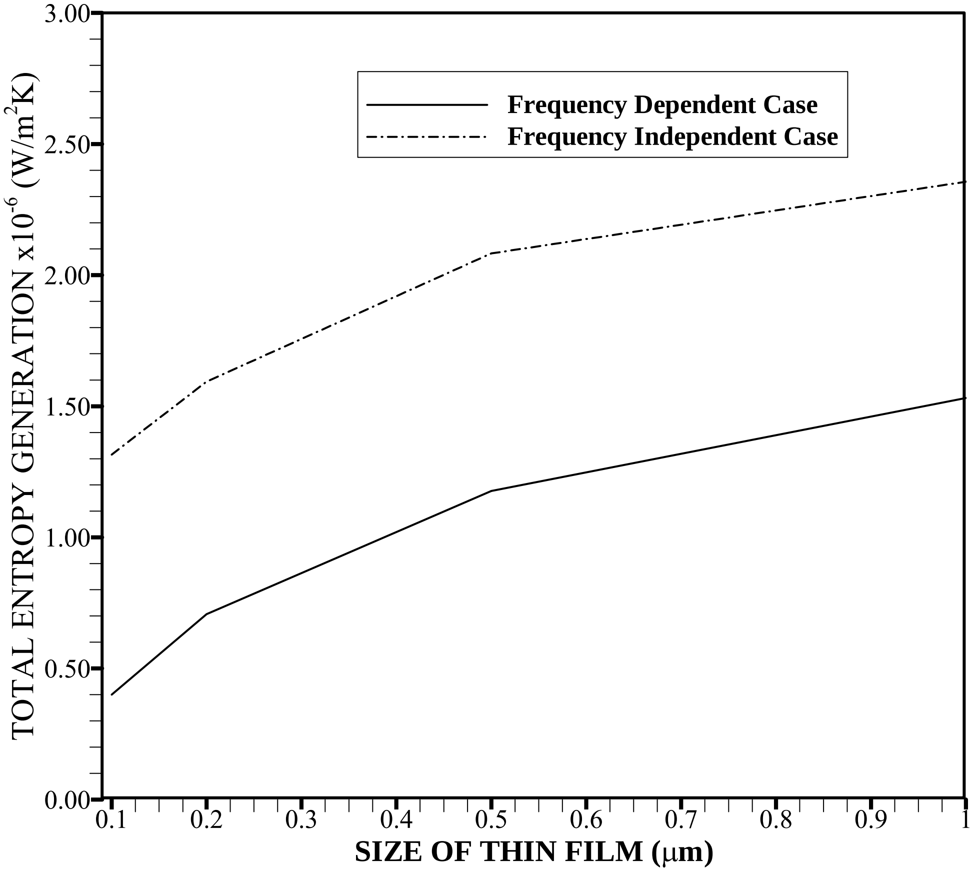

Figure 5.46 Total entropy generation with the film thicknesses for frequency dependent and frequency independent cases.

5.2.2 Transient Heat Transport Including the Effect of Minute Vacuum Gap in between the Films

Phonon transport across the silicon thin films pair with presence of the gap in between them is considered. Frequency dependent Boltzmann equation is solved numerically to determine transient phonon intensity distribution in the films pair. Equivalent equilibrium temperature is introduced to assess the phonon transport characteristics. Equivalent equilibrium temperature is defined anywhere in the thin silicon film pair and it is the analog of the thermodynamic temperature defined in the diffusive limit in any medium. It represents the average energy of all phonons around a local point and it is equivalent to the equilibrium temperature of phonons when they redistribute adiabatically to an equilibrium state.

In order to assessment of effective thermal conductivity $\left(k_{eff.}\right)$, the Fourier analogy is incorporated. Heat flux, which calculated from steady state Boltzmann transport equation across the films pair, multiplied with the total length of both sections and divided by temperature difference across physical domain. To demonstrate the phonon transport characteristics, the dimensionless temperature is introduced which is given by,

$$Dimensionless\,Temperature = \frac{T_{A,B}(x,t) - T_{Low}}{T_{High} - T_{Low}} \tag{5.6}$$

where, $T_{High} = 301\,K$ and $T_{Low} = 300\,K$. It should be noted that the dimensionless temperature is defined to provide the values in between 0 and 1.

Figure 5.47 shows the thermal conductivity data predicted and reported in the previous study [142]. To validate the code developed for the frequency dependent phonon transport in the silicon film, the simulation conditions are changed according to the experimental conditions reported [142]. Thermal conductivity predicted agrees well with the data obtained from the previous study [142]. Some small discrepancies between the predictions and the experimental data are attributed to the numerical errors associated with the simulations, which is estimated in the order of 1% and the experimental errors. Nevertheless, the discrepancies are negligibly small.

Figure 5.48 shows dimensionless temperature along the film pairs and the gap for 100 ps heating duration. In addition, equivalent equilibrium temperature with no gap in between the films pair is shown for the comparison purposes. Temperature jump is evident at the edges of the films in the films pair because of the boundary scattering taking place at the edges. Since the boundary scattering remains the same at the high temperature edge of the film, temperature jump remains almost the same for all gap sizes in between the silicon films pair. It should be noted that the reflected phonons from the first film edge due to their small wavelength (smaller than the gap size) contributes to the temperature jump at the high temperature film edge; however, their contribution is not significantly high to resemble a large temperature jump at the high temperature edge due to differences in the gap size. Phonons emitted from the high temperature edge undergo scattering in the film and cause equivalent equilibrium temperature increase prior to reaching at the film interface. Phonons with large wavelengths (larger than the gap size) can possibly be transmitted to the second film. However, some of those phonons contribute to the boundary scattering at the gap edge, which adds to temperature jump at the film pair interface. Consequently, reflected phonons and those phonons having smaller wavelengths than the gap size contributes to the boundary scattering at the interface. This results in varying temperature jump with the gap size. In this case, increasing gap size causes large temperature jump at the first film interface due to the attainment of high phonon intensity at the edge. High phonon intensity results in increased equivalent equilibrium temperature at the first film edge. Due to the consideration of radiation heat transfer (Casimir limit) from the first film edge to the second film edge across the gap contributes to temperature increase at the second film edge. However, phonons transmitted have significant effect on equivalent equilibrium temperature increase at the second film edge because of the boundary scattering in this region. Although increasing gap size causes attainment of high equivalent equilibrium temperature at the first film edge, the rate of phonons transmitted to the second film becomes small. This, in turn, results in small temperature rise at the second film edge despite the amount of heat transferred via radiation is high at the large gap size. This behavior reveals that equivalent equilibrium temperature increase is mainly because of those phonons transmitted to the second film rather than the net radiation heat transfer taking place between the film edges across the gap. Temperature jump at the film pair disappears for the case of the continuous film consideration (no gap case). In the case of the late heating period (500 ps), temperature jump at the high temperature edge of the film varies for different gap sizes. This situation is seen in Figure 5.49, in which dimensionless equivalent equilibrium temperature is shown along the film thickness for the heating period of 500 ps. The effect of the gap size on temperature jump with progressing heating duration is associated with the amount of phonon scattered at the high temperature edge, which increases with progressing time. In addition, the contribution of phonons reflected from the interface edge of the first film to amount of phonons scattered at the high temperature edge increases with progressing heating time.

Figure 5.50 shows temporal variation of equivalent equilibrium temperature at the interface of the first silicon film the first film edge $\left(x_A = 3\Lambda\right)$ for different values of gap sizes (where, Λ is the mean free path of silicon corresponding to gray medium). The continuous silicon film (zero gap size) as the same size of the film pair is also shown for the comparison reason. Equivalent equilibrium temperature rises rapidly in the early heating period, which is more pronounced for the large gap sizes. In this case, increasing gap size enhances the rate of temperature increase at the first film interface. This behavior is attributed to amount of phonons, which are reflected from the interface due to their shorter wavelengths than that of the gap size. As the heating time progresses, the amount of phonons emitted from the high temperature edge of the first film increases despite some of the phonons under go scattering in the film prior to reaching at the first film interface. In this case, mainly short wavelength phonons undergo scattering in the film prior to reaching at the film edge; therefore, phonons having large wavelengths or comparable to the gap size reaches the interface. Once the gap size becomes small most of the phonons can possibly transmitted to the second silicon film without significantly contributing to the boundary scattering at the first film interface. Consequently, equivalent equilibrium temperature due to phonon scattering at the interface attains low values. The time to reach quasi-steady value of equivalent equilibrium temperature increases as the film gap increases. Hence, phonons with short wavelengths and reflected from the first film interface causes phonon scattering at the near region of the interface, which in turn alters the time to reach quasi-steady behavior of equivalent equilibrium temperature at the film interface. Moreover, quasi-ballistic and ballistic phonons do not significantly contribute to the boundary scattering at the interface, provided that phonons reaching the interface without scattering having the wavelengths shorter than the gap size, contribute to the boundary scattering at the first film interface. This also influences the time taken to reach quasi-steady behavior of phonon transport across the interface of the films pair. However, at the second film interface $\left(x_B = 0\right)$, temporal behavior of equivalent equilibrium temperature becomes almost opposite to those occurred at the first film interface. This can be seen from Figure 5.51, in which temporal variation of equivalent equilibrium temperature at the second film interface is shown for different gap sizes. In this case, the rate of rise of equivalent temperature is highest for no gap conditions and then follows the small gap sizes. This is attributed to amount of phonons transferring to the second film interface. Reducing the gap size increases the amount of transmitted phonons to the second film interface, which enhances the rate of equivalent equilibrium temperature in this region. Although equivalent equilibrium temperature attains high values at the first film interface for the large gap sizes, net radiation heat transfer due to Casimir limit does not significantly effects equivalent equilibrium temperature increase at the second film interface for the large gap sizes. Therefore, those phonons transmitted to the second film interface has significant effect on the rate of equivalent equilibrium temperature increase at the second film interface.

Figure 5.52 shows equivalent equilibrium temperature difference at the edges of the first film interface $\left(x_A = 3\Lambda\right)$ and second film interface $\left(x_B = 0\right)$ at the heating duration of 2000 ps. It should be noted that equivalent equilibrium temperature attains almost quasi-steady state at the interfaces of the film pair after 2000 ps of heating duration. Increasing gap size at the film interface increases the temperature difference, which is more pronounced for the large gap sizes. In the case of small gap sizes $\left(L_{Gap} / \Lambda \leq 0.025\right)$, variation of temperature difference is almost linear with increasing gap size. However as the gap size increases further, this variation becomes almost in a non-linear form. Consequently, phonon transmittance and net radiative heating at the edges of the films pair become complex, in terms of the phonon scattering at the interface boundaries, for the large gap sizes. Although the effect of net radiative heating on equivalent equilibrium temperature variation at the interfaces of the film edges is not significant, this effect may become important when the gap size becomes large. This is due to the fact that equivalent equilibrium temperature increases at the first film edge with increasing film gap size while altering the net radiation heat transfer across the gap in the interface of the films pair. In addition, attainment of high values of equivalent equilibrium temperature at the first film edge and low values of temperature at the second film edge due to the large gap sizes enhance the temperature differences for the large gap sizes. Consequently, high rate of reflected phonons from the first film interface and low rate of phonon transmittance at the second film interface modify equivalent equilibrium temperature rise at both interfaces, which is more pronounced for the large gap sizes. The ballistic phonons transmitted across the interface suppresses temperature rise at the first film interface, which in turn lowers the equivalent equilibrium temperature difference across the gap in the films pair.

Figure 5.53 shows the thermal conductivity ratio $\left(k_{eff} / \mathrm{k}_{\mathrm{Bulk}}\right)$, where k_{eff} is the thermal conductivity of the film pair and k_{Bulk} is the thermal conductivity of the bulk silicon) with the dimensionless gap size. It should be noted that k_{eff} is obtained from the steady state solution of the Boltzmann transport equation across the films pair. The thermal conductivity ratio reduces with increasing gap size, since the k_{Bulk} remains the same, k_{eff} reduces with increasing gap size. This is attributed to the temperature variation at the film edges across gap size; in which case, temperature difference between the first film edge and the second film edge increases with increasing gap size. This, in turn, suppresses the heat transfer across the film pair, particularly towards the second film. In addition, those phonons with large wavelengths can possibly transfer to the second film across the gap. Since these phonons resembles only fraction of the total phonons emitted from the high temperature edge of the first film, phonon energy transport into the second film becomes small. However, thermal energy transfer from the first film edge to the second film edge via radiation (Casimir limit) does alter temperature at the second film edge. Consequently, the presence of gap resembles the thermal boundary resistance in between the thin films. However, changing the gap size within the film pair, thermal conductivity can be reduced significantly, which can be an interest for the thermal insulation applications.

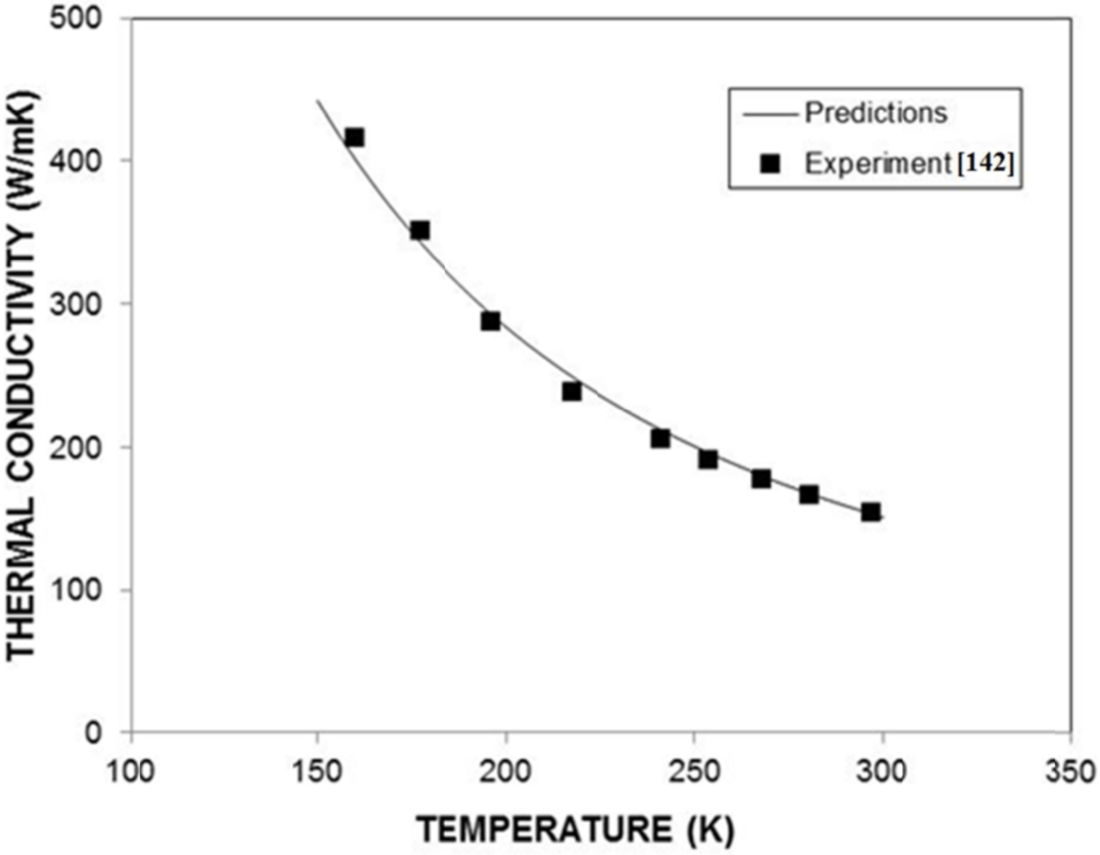

Figure 5.47 Thermal conductivity predicted and obtained from the previous study [142].

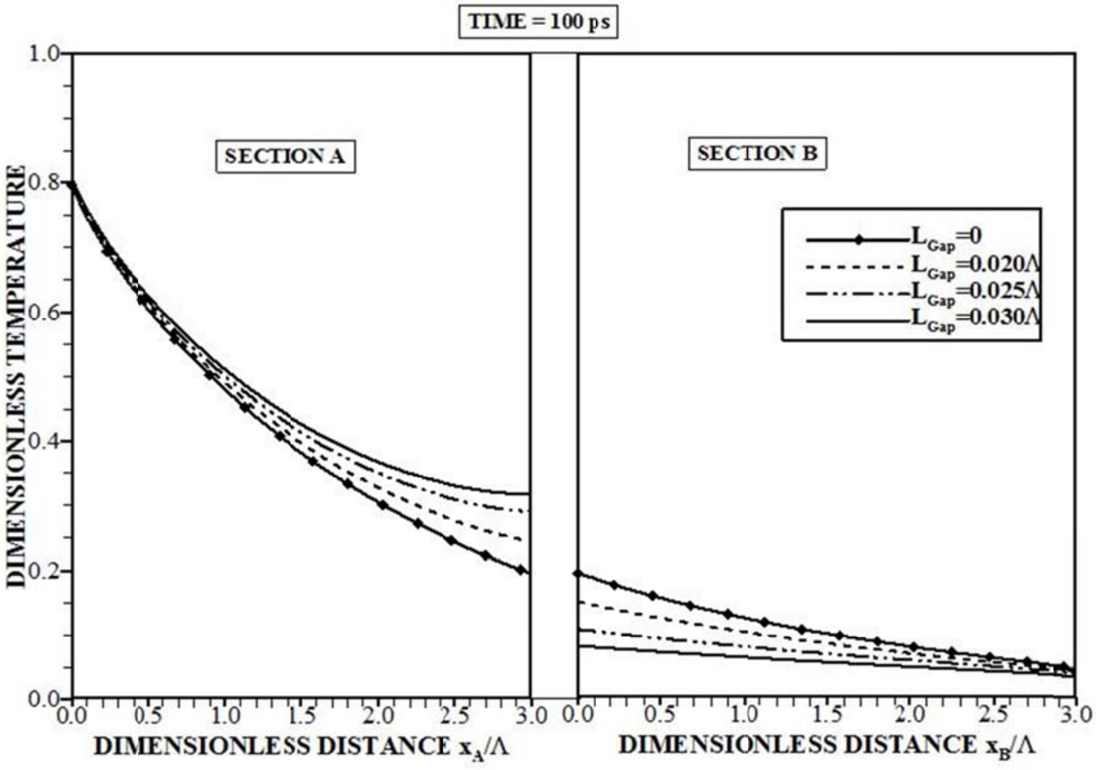

Figure 5.48 Equivalent equilibrium temperature along the thickness of films pair for heating duration of 100 ps. Section *A* represents the first film and section *B* is the second film. The gap is located in between two films. Λ is the mean free path of silicon corresponding to gray medium.

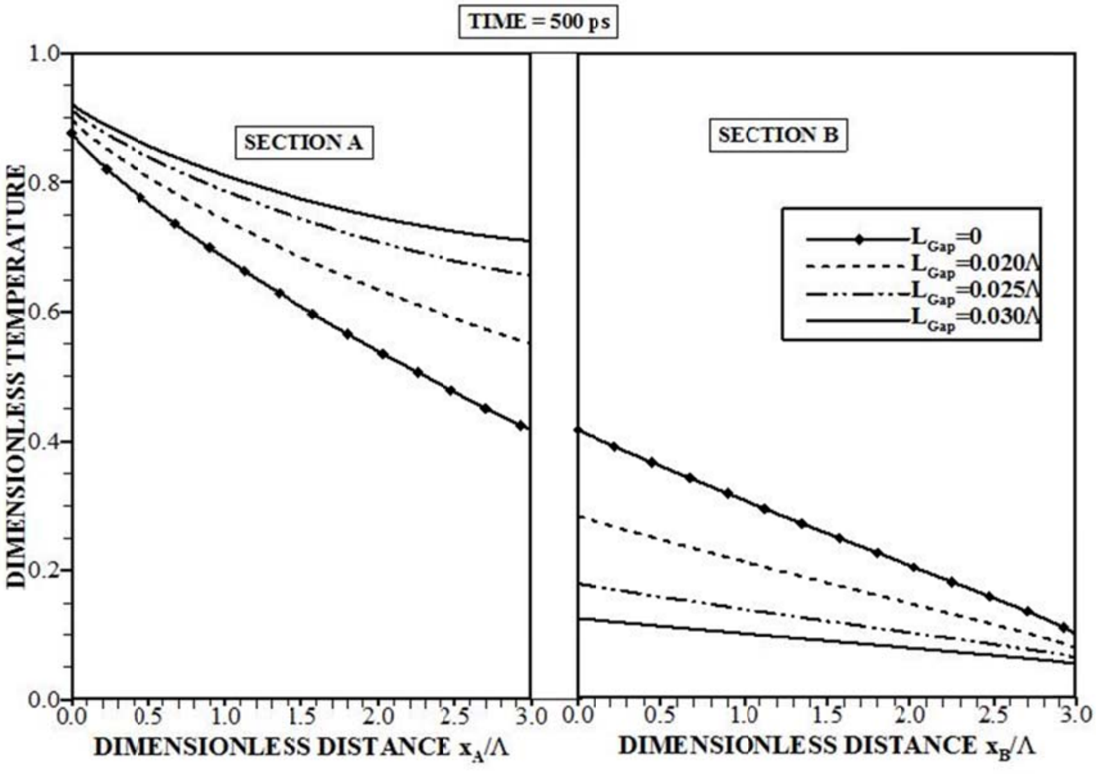

Figure 5.49 Equivalent equilibrium temperature along the thickness of films pair for heating duration of 500 ps. Section A represents the first film and section B is the second film. The gap is located in between two films. Λ is the mean free path of silicon corresponding to gray medium.

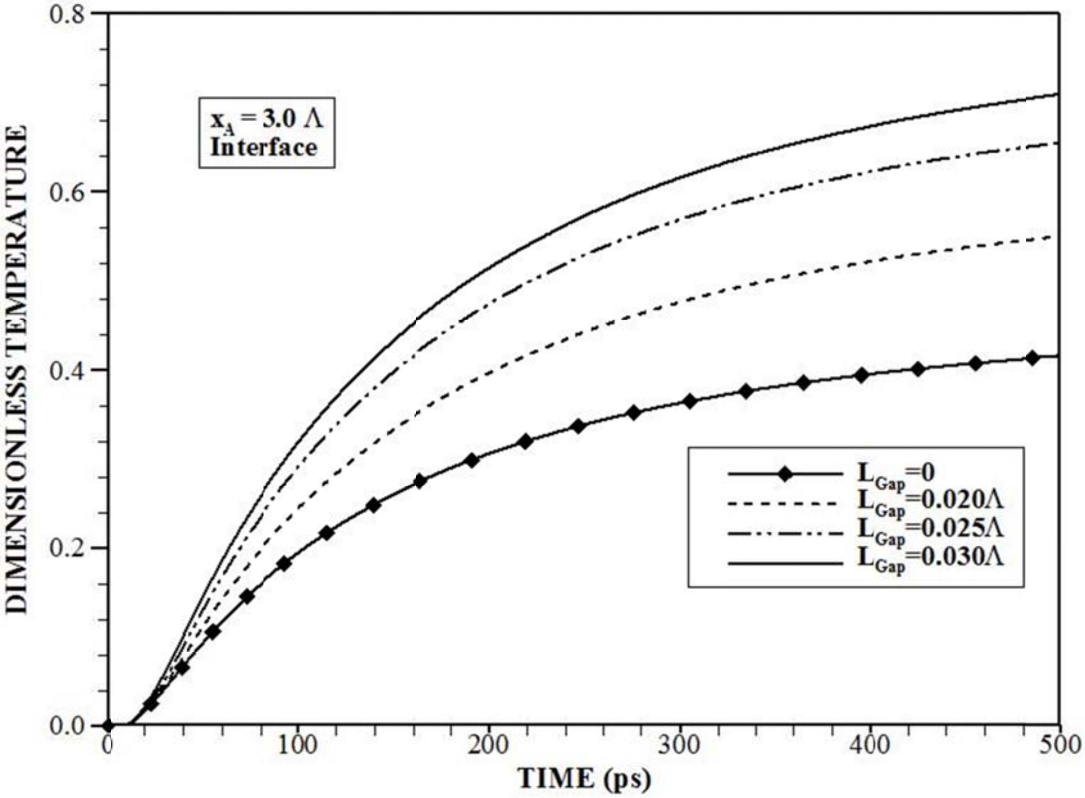

Figure 5.50 Temporal variation of dimensionless equivalent equilibrium temperature $\left(\dfrac{T_A - T_{Low}}{T_{High} - T_{Low}}\right)$ at the first film edge $\left(x_A = 3\Lambda\right)$ for different values of gap sizes. Λ is the mean free path of silicon corresponding to gray medium.

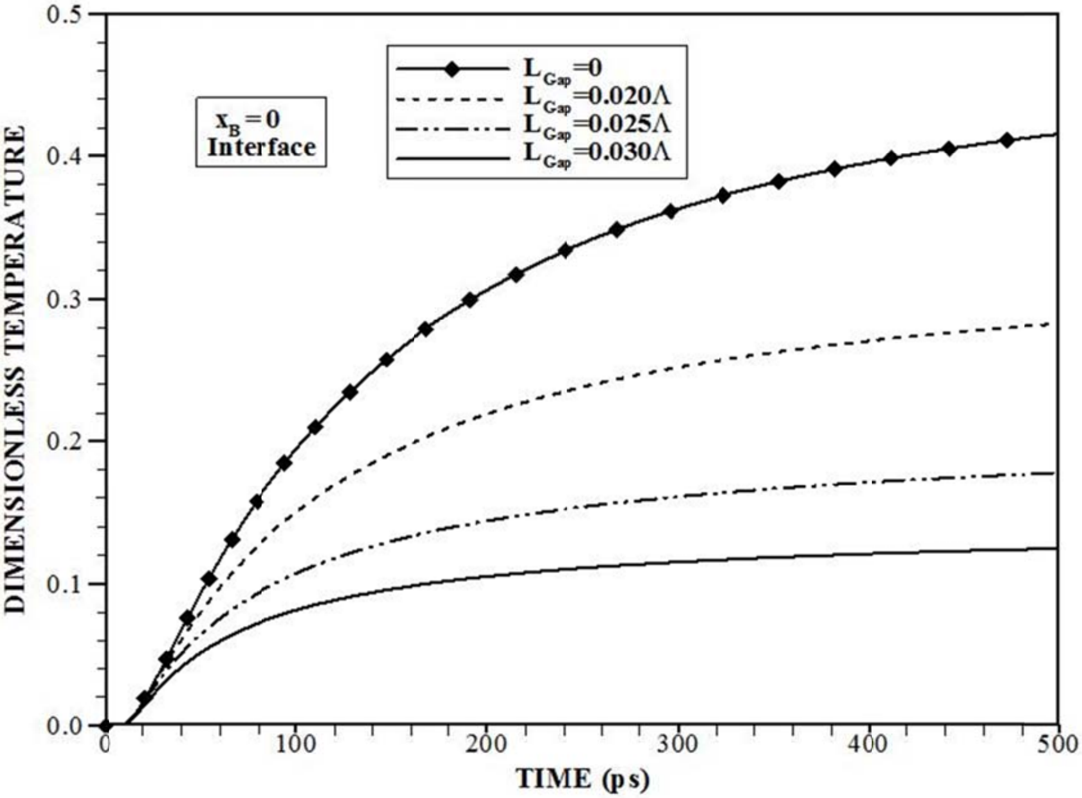

Figure 5.51 Temporal variation of dimensionless equivalent equilibrium temperature $\left(\frac{T_A - T_{Low}}{T_{High} - T_{Low}}\right)$ at the second film edge $\left(x_B = 0\right)$ for different values of gap sizes. Λ is the mean free path of silicon corresponding to gray medium.

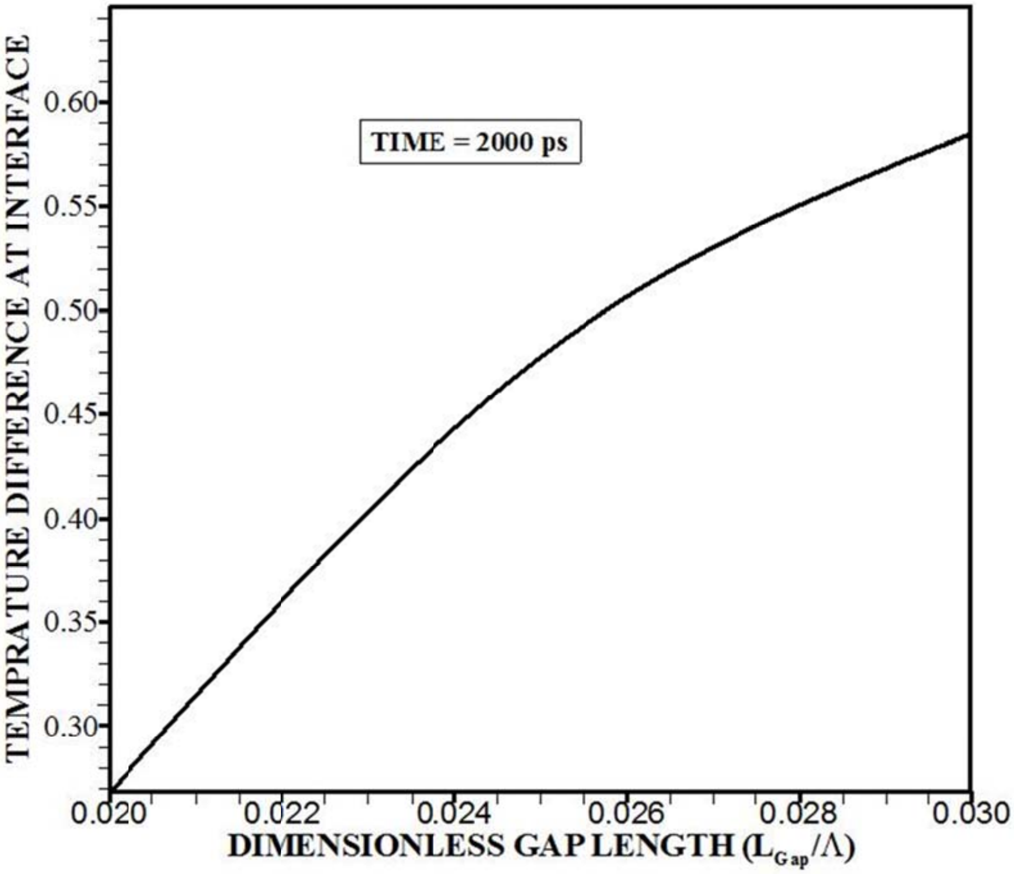

Figure 5.52 Equivalent equilibrium temperature difference between the first film edge $(x_A = 3\Lambda)$ and the second film edge $(x_B = 0)$ with dimensionless gap length (L_{Gap}/Λ, where L_{Gap} is the gap size in between the films and Λ is the mean free path of silicon corresponding to gray medium.).

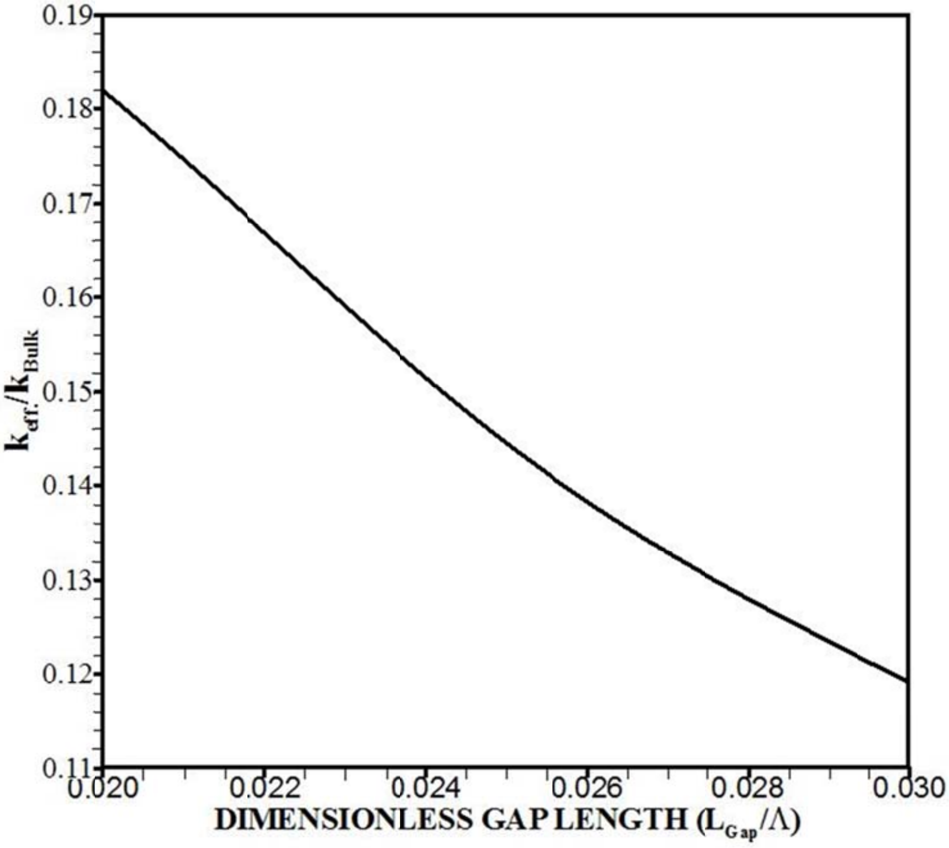

Figure 5.53 Thermal conductivity ratio (k_{eff}/k_{Bulk}) with dimensionless gap length (L_{Gap}/Λ, where L_{Gap} is the gap size in between the films and Λ is the mean free path of silicon in gray medium).

5.3 One Dimensional Metallic Thin Films

In this section the results of case studies which are introduced in chapter 3 related to one dimensional metallic thin films are presented. All the one dimensional cases are solved incorporating the EPRT along with the initial, and boundary and interface conditions which discussed in chapter 3. The case studies are,

1. Transient Analysis of Heat Transport Characteristics in Aluminum Thin Films.
2. Effect of Thermal Oscillation on Heat Transport Charaterstics in Aluminum Thin Films.
3. Effect of Thermal Oscillation and Film Thickness on Heat Transport Charaterstics in Aluminum Thin Film.

5.3.1 Transient Heat Transport in Aluminum Thin Films

Energy transport in aluminum thin film is considered due to the temperature disturbance across the film. The transient solution of the frequency dependent phonon radiative transport equation is simulated for various film thicknesses. Equivalent equilibrium temperature is introduced to assess the transport characteristics in the film. Temperature predictions are compared with those obtained from the frequency independent solution of radiative phonon transport equation and from the two-equation model. In the diffusion limit, the frequency independent solution is demonstrated to reduce to modified form of the two-equation model. In order to assessment of energy transport characteristics in lattice and electron sub systems the following dimensionless parameter is introduced,

$$Dimensionless\,Temperature = \frac{T_{p,e}(x,t) - T_{right}}{T_{left} - T_{right}} \tag{5.7}$$

where $T_{p,e}(x,t)$ is the lattice site or electron temperature in the film, T_{right} is low temperature at the right edge of the film, and T_{left} is high temperature at the left edge of the film (Figure 3.17).

Figure 5.54 shows dimensionless steady state phonon temperature along the film length for different film thicknesses., Temperature curves are obtained from the solution of the radiative transport equation for the frequency dependent and the independent cases, and from the two equation model. Temperature distribution obtained from the frequency dependent and the frequency independent solutions of the radiative phonon transport equation are closer than that of the solution of the two-equation model. However, temperature difference between the frequency dependent and independent cases is higher in the region close to the high temperature edge as compared to the low temperature edge. This is attributed to the effect of emitted quasi-ballistic phonons from the high temperature edge, which do not undergo scattering in the near region of the high temperature edge. Therefore, contribution of the quasi ballistic phonons to phonon intensity increase towards the low temperature edge increases phonon temperature in this region. Temperature jump in the vicinity of the film edges is observed for the solution of the radiative phonon transport equation. However, temperature jump does not take place for the solution of the two-equation model. As the film thickness increases, the difference between temperature profiles due to the solution of the phonon radiate transport and the two-equation model increases. This is attributed to the consideration of the hyperbolic conduction equation in the two-equation model [16]. Since phonon temperature is mainly governed by the phonon intensity distribution in the lattice system, phonon temperature distribution is governed by the phonon scattering rate in the film and the presence of the quasi-ballistic phonons. When comparing phonon temperature distributions due to frequency dependent and independent cases, temperature corresponding to the frequency dependent case attains lower values than that of the frequency independent case. This behavior is associated with the phonon scattering in the film; in which case, ballistic phonons, due to frequency dependent case, do not contribute to the phonon scattering because of the film resistance in the film.

Figure 5.55 shows normalized lattice site temperature predicted from frequency dependent and frequency independent cases for four different film thicknesses and the heating period of 30 ps while Figure 5.56 shows counter plots of temperature for the different cases considered in the simulations. The axial location is at x = Lx/4, where Lx is the film thickness. In general, the behavior of temperature predictions due to frequency independent and independent solution of the radiative transport equation demonstrates similar behavior, which is more pronounced for the thin film $L_x = 0.25L$ $\left(where\ L = 0.1\mu m\right)$. This is attributed to the emitted phonons from the high temperature edge, which results in temperature jump at the interface of the film edge while modifying the phonon intensity distribution in the film, particularly in the near region of the high temperature edge. In the case of thicker films $\left(L_x \geq L\right)$, phonons undergo several scattering in the film prior to reaching at the low temperature edge, which modifies the phonon intensity distribution in the film. Since the grey body assumption is incorporated in the frequency independent solution, as the film thickness increases phonon transport approaches to the diffusional transport. Moreover, temperature jump is smaller for the frequency independent case than that of the frequency dependent case. This is because of the consideration of the ballistic phonons, which are emitted from the film edges. Since phonon transport in the film is initiated by the emitted phonons from the high temperature edge, regardless of the frequency dependence, the radiative phonon transport results in temperature jump at the interface of the film edge. In the case of the frequency dependent solution, ballistic phonons contribute significantly to energy transport across the film without suffering from the scattering. Therefore, phonon intensity distribution changes considerably in the film for the frequency dependent consideration of the radiative transport. This behavior is observed for all the film thicknesses considered in the simulations. The effect of film thickness is significant on temperature distribution; in which case, temperature difference due to the cases considered become large in the region of the high temperature edge and they become small in the region close to the low temperature edge. However, temperature difference becomes small almost in all the regions of $L_x = 2L$ thick film for all the cases considered. As the heating period progresses, this situation changes, which can be observed from Figure 5.57 in which normalized temperature variation along the normalized film length is shown for the heating period of 90 ps. In general, the frequency dependent solution predicts lower temperature in the film than those corresponding to other cases. Normalized temperature remains high for the solution of the two-equation model for all the film thicknesses. Consequently, as the heating period increases, energy transport deviates from the diffusional transport and phonon transport characteristics are modified by the ballistic phonons, which is more pronounced for the small film thickness $L_x = 0.25L$.

Figure 5.58 shows normalized electron temperature along the film length for different film thicknesses and the heating period of 30 ps. It should be noted that normalized temperature is obtained from the frequency independent solutions of the radiative transport equation. However, in lattice sub-system radiative transport equation is solved for frequency dependent and independent cases. Therefore, the frequency dependent represents electron temperature corresponding to the frequency dependent solution of phonon temperature in the lattice sub-system. The behavior of electron temperature along the film thickness is the same for the solution of the frequency dependent and the independent cases, provided that electron temperature attains higher values for the frequency independent solution of the radiative transport equation. Since the insulated boundary condition at the film edges is considered for the electron sub-system, electron energy gain occurs from the thermal communication of electron and lattice sub-systems through the electron-phonon coupling, i.e. phonon energy transfer to electrons increases electron temperature in the film. Therefore, high temperature phonons, due to the frequency independent case, gives rise to high electron temperature in the lattice sub-system. As the film thickness increases, the difference between electron temperatures, due to the frequency dependent and the independent solutions of the radiative transport, becomes small. This is attributed to the close values of phonon temperatures due to both cases (Figure 5.55). Although radiative transport equation is solved after considering the grey body for the electron sub-system, frequency dependence of the phonon transport in the lattice system affects electron temperature variation in the film. Figure 5.59 shows normalized electron temperature along the film length for different film thicknesses and the heating duration of 90 ps. Temperature predictions from the frequency dependent and the independent solutions of radiative transport are similar to those in Figure 5.58 Electron temperature decay becomes sharp in the film as the film thickness increases. This is attributed to phonon temperature variation in the film; consequently, sharp decay of phonon temperature causes sharp decay of electron temperature in the film.

Figure 5.60 shows temporal variation of normalized phonon temperature in the near region of the high temperature edge for different film thicknesses. Phonon temperature rises rapidly in the early heating period and it becomes gradual as the heating period progresses. This is more pronounced for the frequency independent case. The sharp rise of temperature is associated with the scattering of phonons in the near region of the high temperature edge. In this case, phonons emitted from the high temperature edge undergo scattering because of the film resistance. However, temperature rise is faster for the frequency independent case as compared to its counterpart corresponding to the frequency dependent case. This is associated with the assumption of grey body in the frequency independent solution of the radiative transport, which accommodates the entire phonons scattering with in the film and the film resistance increases the phonon temperature in this region. In the case of frequency dependent solution of the radiative transport equation, ballistic phonons do not undergo scattering in the film and do not contribute to phonon intensity variation in the film. Consequently, their contribution to phonon temperature rise is negligible. As the time progresses further, quasi-steady radiative transport takes place and temperature increase becomes almost steady with progressing time. As the film thickness increases, the time to reach the quasi-steady behavior extends significantly, which is more pronounced the large film thickness $\left(L_x = 2L\right)$. In addition, the rise of phonon temperature in the film becomes gradual as the film thickness increases. This behavior is attributed to the film resistance; in which case, phonons emitted from the high temperature edge of the film also reflects from the low temperature edge of the film. This modifies the phonon intensity distribution in the film as the film thickness changes. This behavior is also associated with the effect of ballistic phonons on the phonon intensity distribution in the film. Since the ballistic phonons have the wavelengths comparable to the film thickness; therefore, for thin films the number of the ballistic phonons is larger than that of the thick films. This, in turn, increases the amount of scattered phonons in the film while modifying the phonon intensity in the film.

Figure 5.61 shows temporal variation of normalized electron temperature at the location $x = L_x / 4$ for different film thicknesses. The temporal behavior electron temperature is similar to that is shown in Figure 5.60 for the phonon temperature. The rise of electron temperature in the early heating period is high and it becomes gradual as the heating period progresses. Increasing film thickness modifies the temporal behavior of electron temperature in the film. It should be noted that the insulated boundary is considered for the electron sub-system; in which case electron gradients are set to be zero at the edges of the film. Consequently, energy transport from the lattice system to electron sub-system through the electron-phonon coupling causes electron temperature variation in the film. In this case, high phonon temperature results in high electron temperature in the film, which is more pronounced for the solution of the frequency independent radiation transport equation. The non-linear behavior of the phonon intensity distribution in the film results in non-linear behavior of electron temperature in the film.

Figure 5.62 shows thermal conductivity of the film obtained from the frequency dependent and the independent solutions of the phonon radiative transport equation. Thermal conductivity reduces with decreasing film thickness, which is in agreement with the previous finding [56]. The frequency dependent solution of the radiative transport equation predicts lower thermal conductivity as compared to its counterpart obtained from the frequency independent solution of the radiative transport equation. This behavior is attributed to the presence of the ballistic phonons, which do not contribute to the phonon scattering in the film, which is consistent with the previous study [71]. Moreover, thermal conductivity for the frequency dependent case reduces almost half of the value of that obtained from the frequency independent case. Therefore, frequency dependence of the phonon transport is critically important to assess the characteristics of the thin aluminum film.

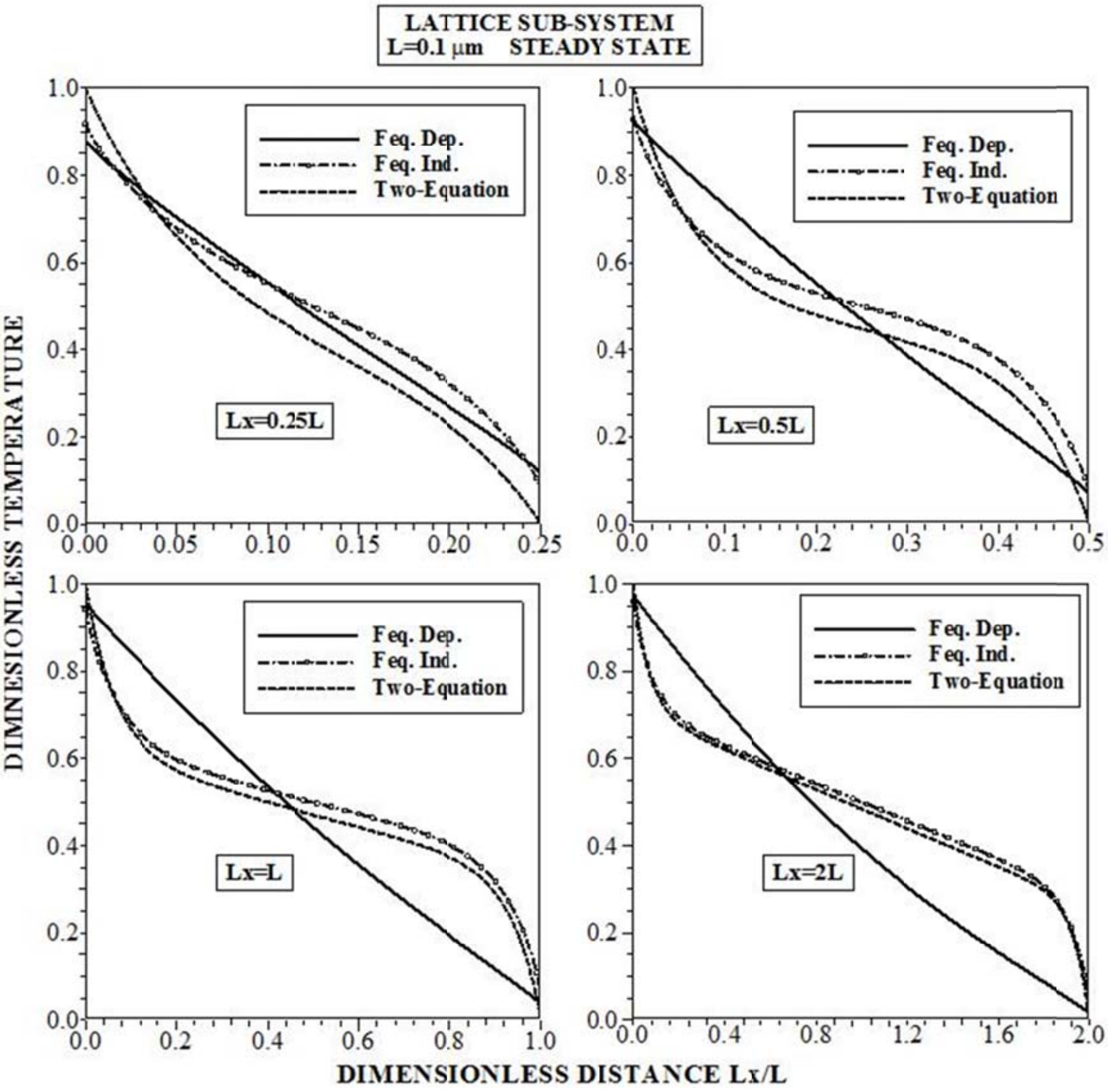

Figure 5.54 Dimensionless temperature distribution in the lattice sub-system for different film thicknesses. Temperatures are presented for steady state solutions due to the frequency dependent and the frequency independent solutions of the radiative transport equation, and the solution of the two-equation model.

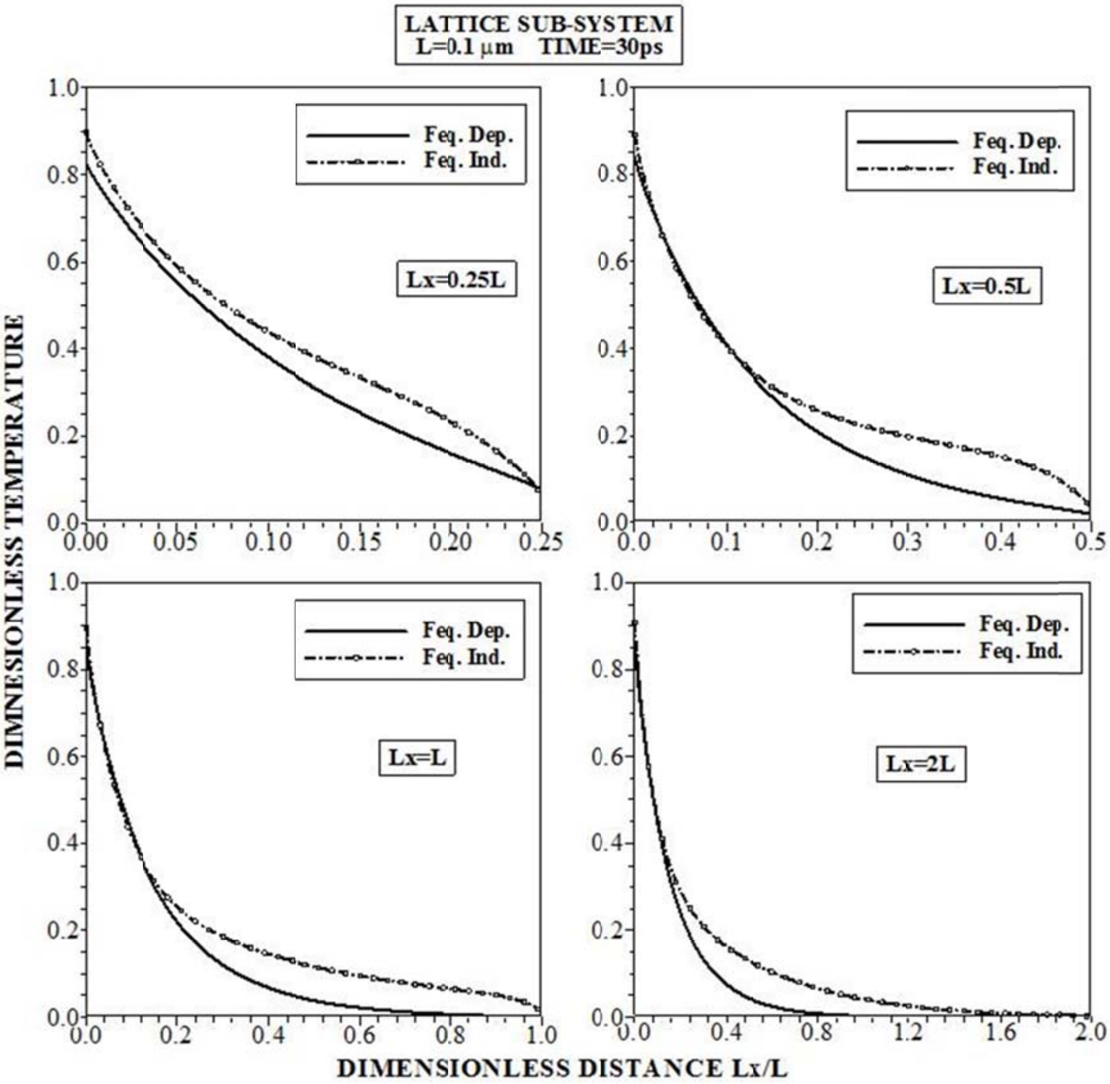

Figure 5.55 Dimensionless temperature distribution along the film length in the lattice sub-system for different film thicknesses and 30 ps of the heating duration. The solutions are presented for the frequency dependent and the frequency independent solutions of the radiative transport equation.

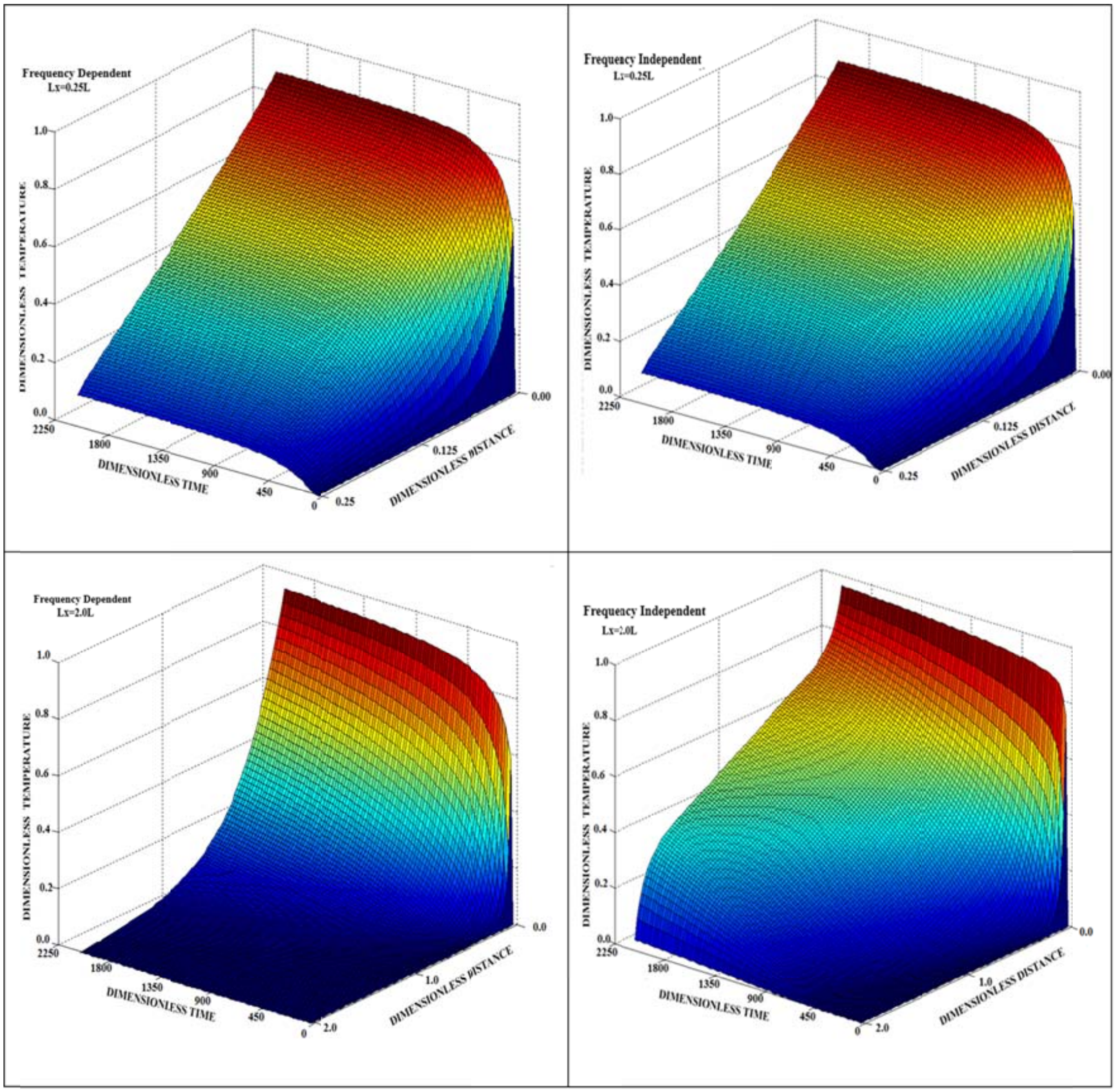

Figure 5.56 Surface plot of dimensionless equivalent equilibrium temperature with dimensionless length and dimensionless time for different film thicknesses. Distance is normalized through the film thickness $\mathit{Dimensionless}\ \mathrm{Distance} = x / Lx$, and tine is normalized by $\mathit{Dimensionless\ Time} = t / \tau$ where $\tau = Ce / G$ and $\tau = 8.94\mathrm{x}10^{-14}\ s$.

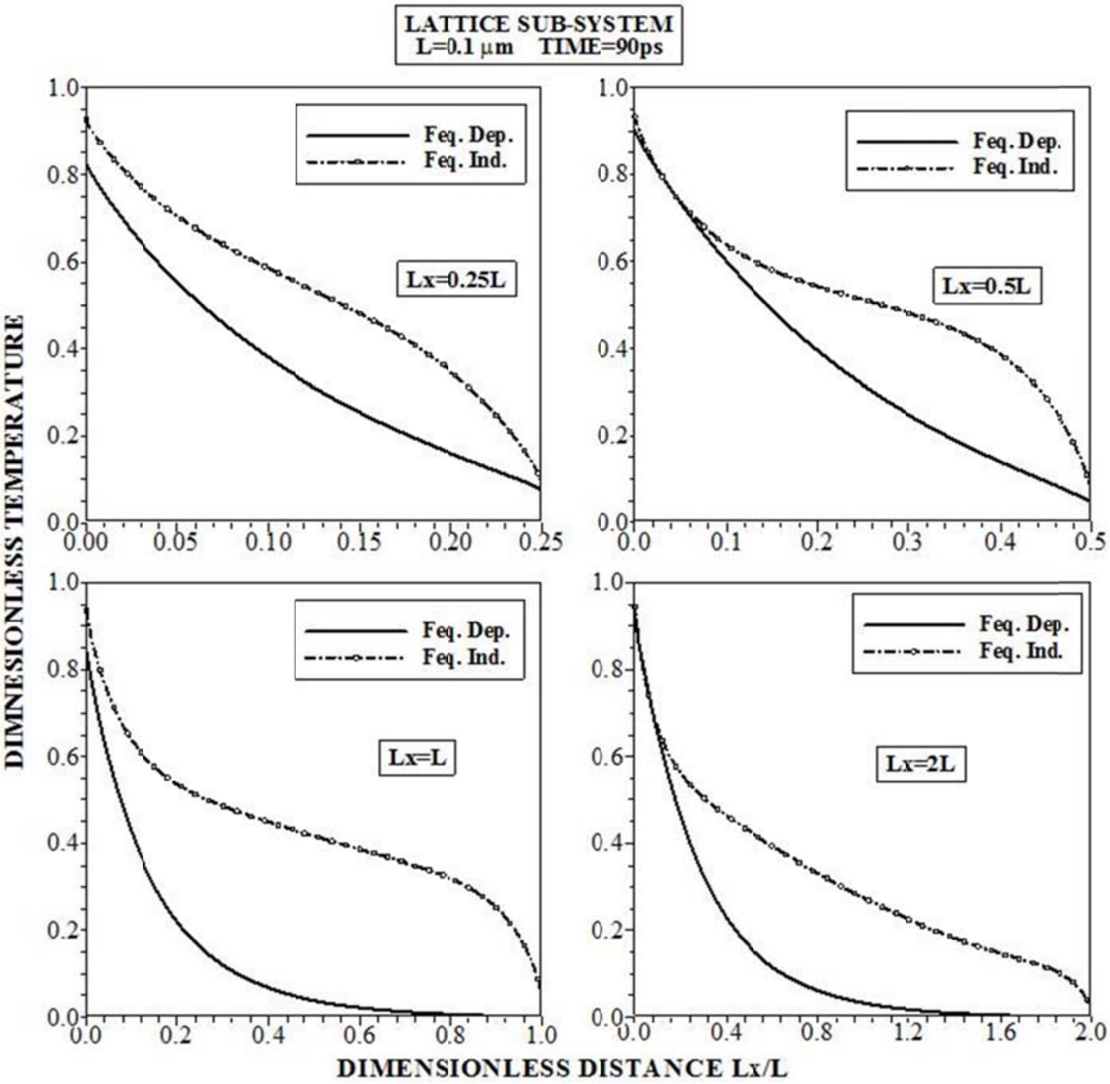

Figure 5.57 Dimensionless temperature distribution along the film length in the lattice sub-system for different film thicknesses and 90 ps of the heating duration. The solutions are presented for the frequency dependent and the frequency independent solutions of the radiative transport equation.

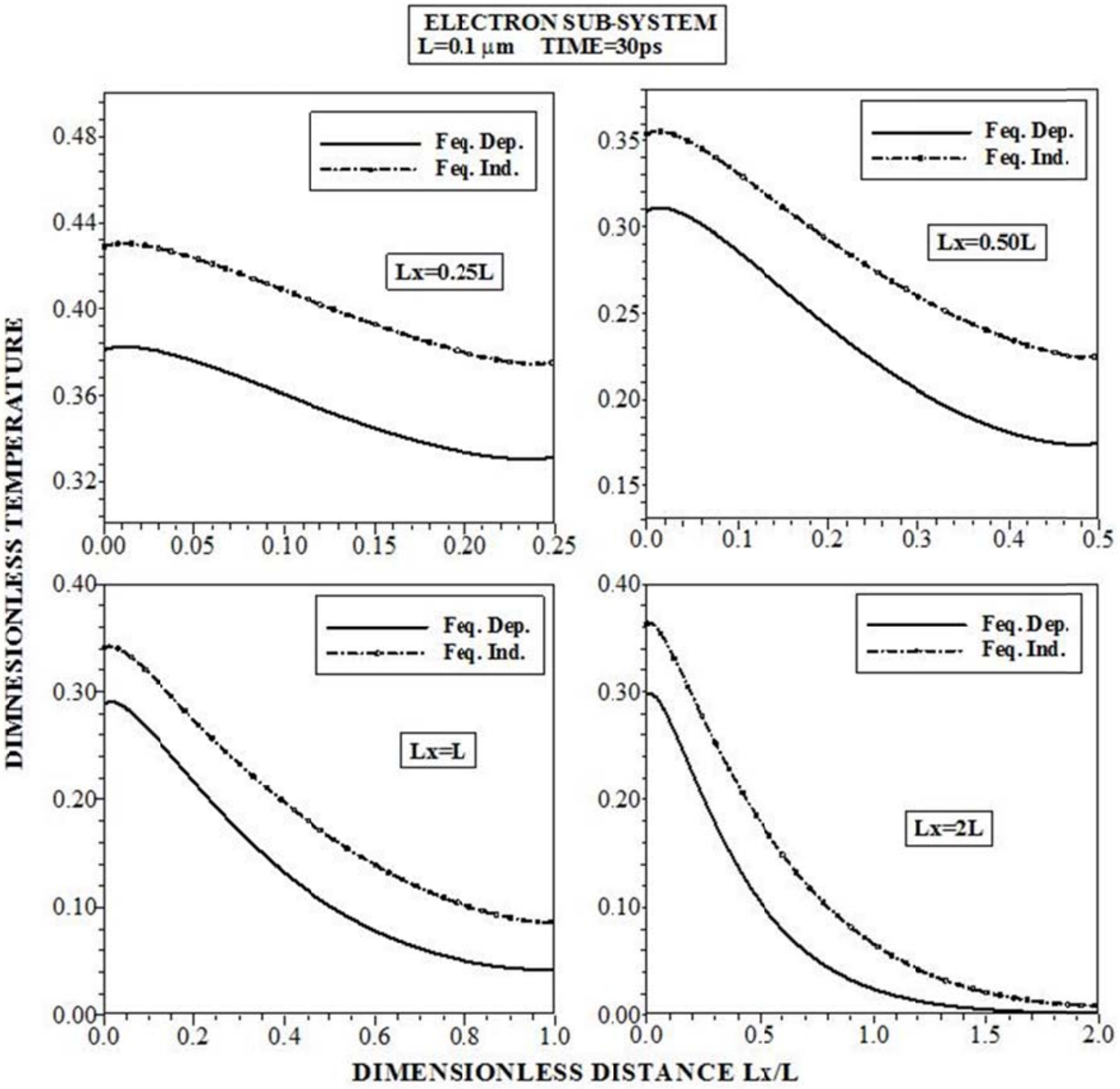

Figure 5.58 Dimensionless temperature distribution along the film length in the electron sub-system for different film thicknesses and 30 ps of the heating duration. The solutions are presented for the frequency dependent and the frequency independent solutions of the radiative transport equation.

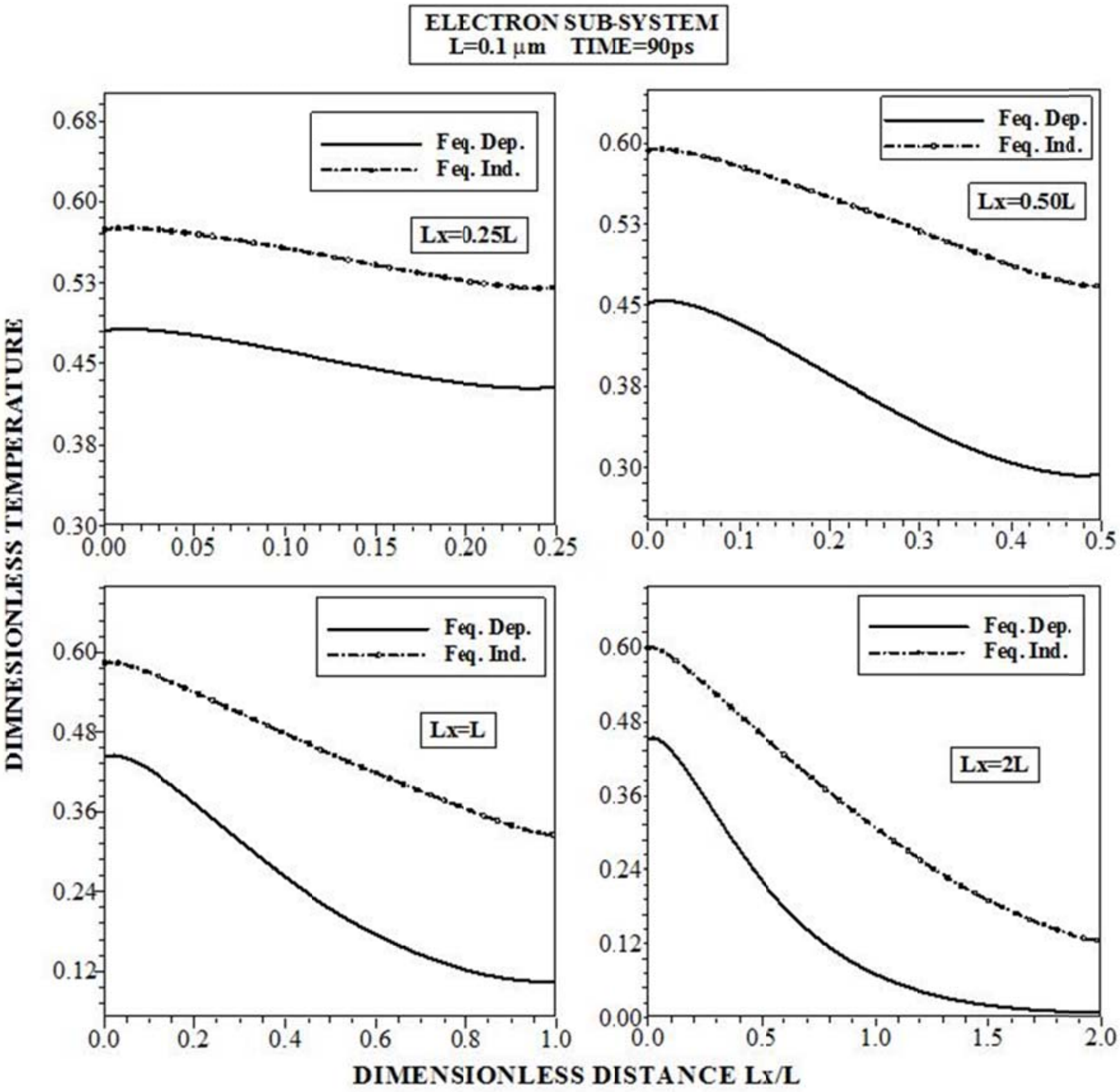

Figure 5.59 Dimensionless temperature distribution along the film length in the electron sub-system for different film thicknesses and 90 ps of the heating duration. The solutions are presented for the frequency dependent and the frequency independent solutions of the radiative transport equation.

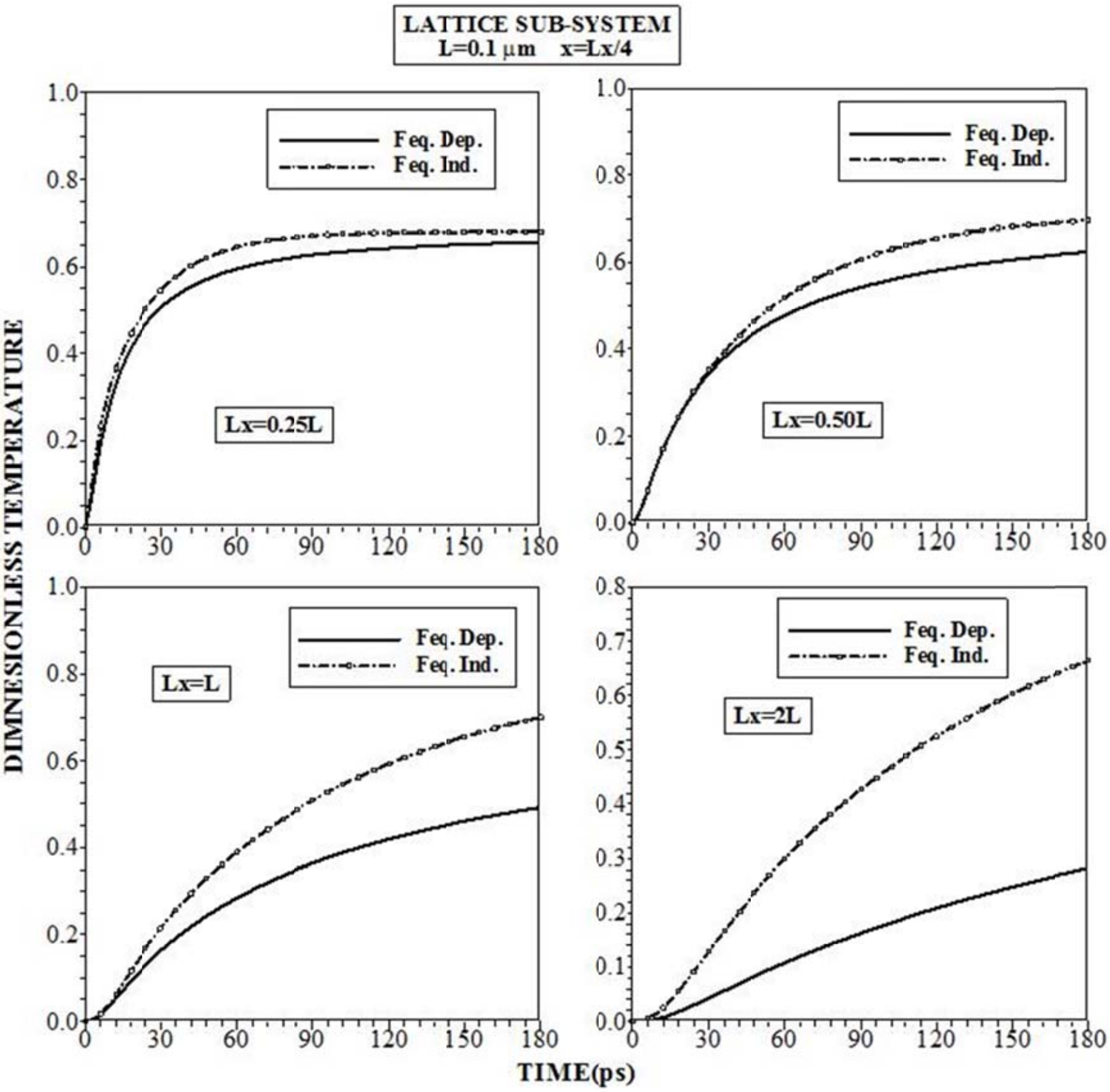

Figure 5.60 Temporal variation of dimensionless temperature distribution in the lattice sub-system for different film thicknesses and x-axis location is x = Lx/4, where Lx is the film thickness. The solutions are presented for the frequency dependent and the frequency independent solutions of the radiative transport equation.

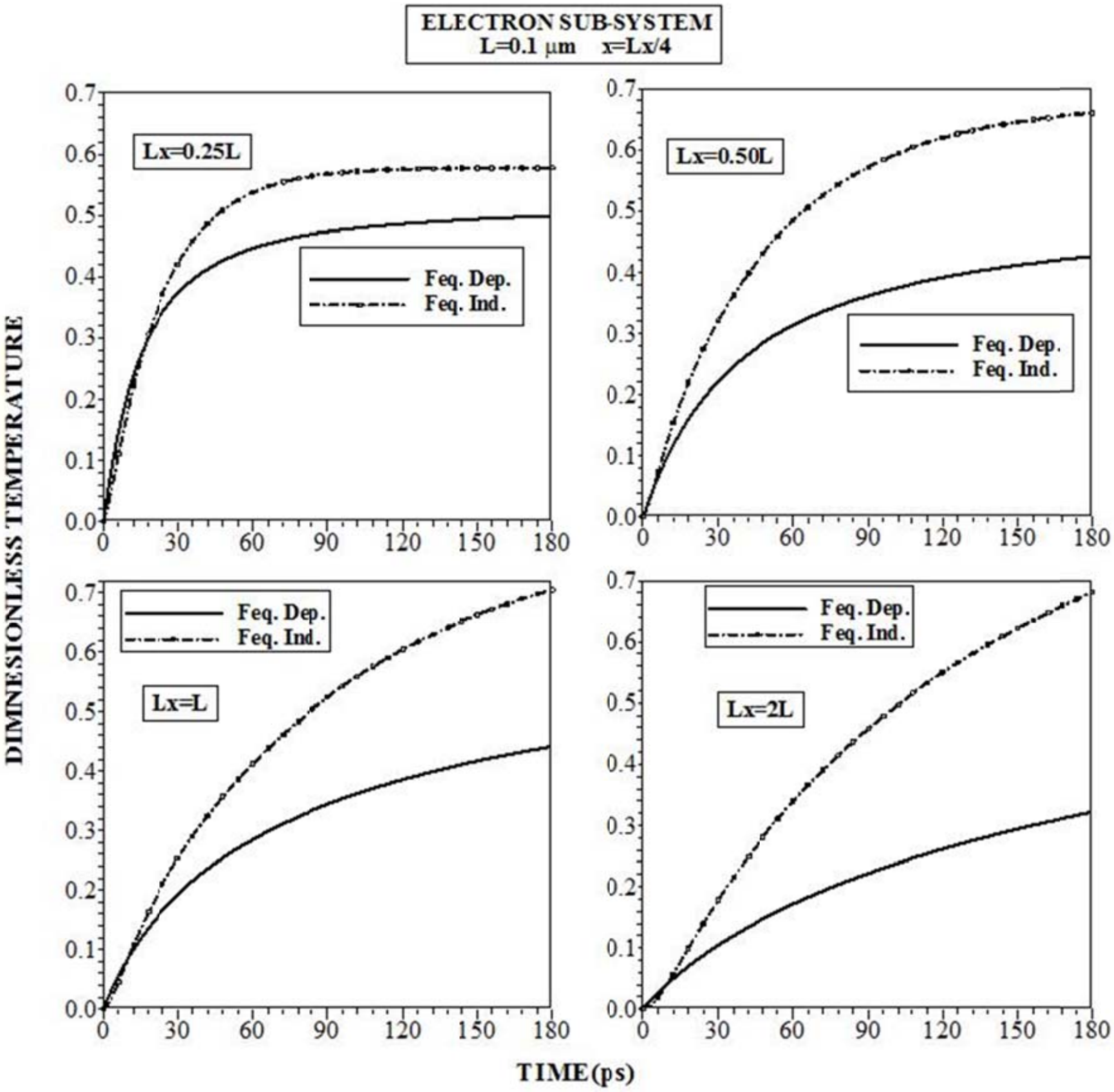

Figure 5.61 Temporal variation of dimensionless temperature distribution in the electron sub-system for different film thicknesses and x-axis location is x = Lx/4, where Lx is the film thickness. The solutions are presented for the frequency dependent and the frequency independent solutions of the radiative transport equation.

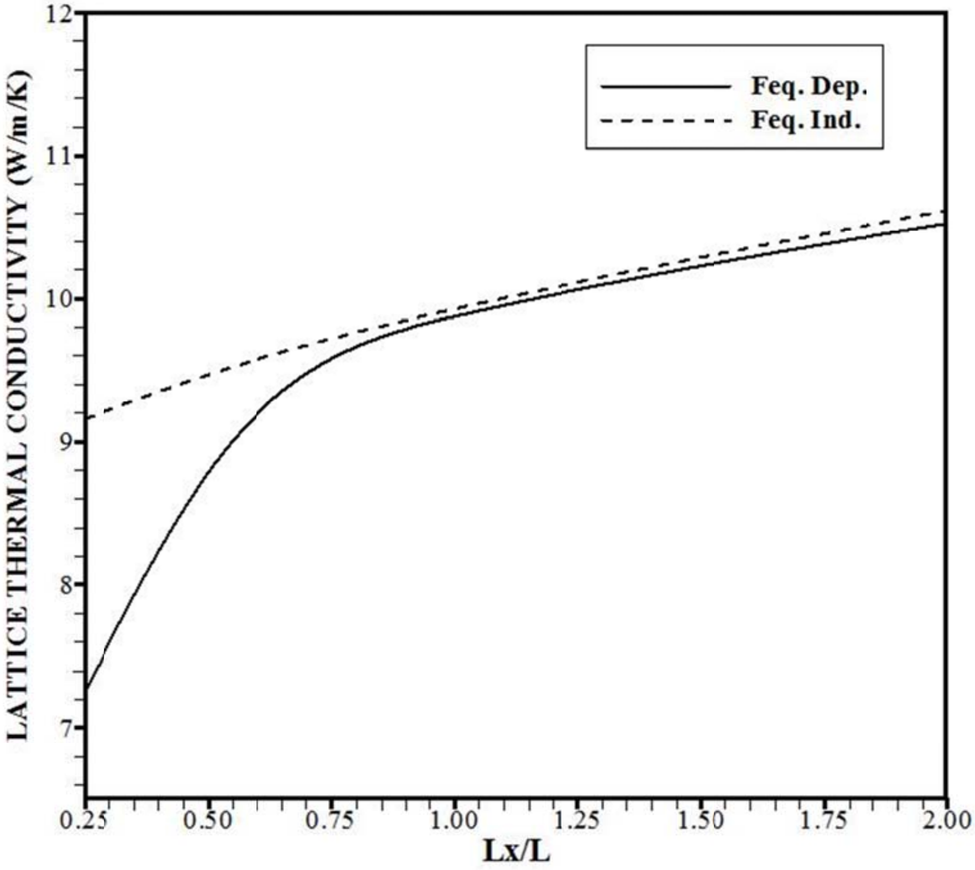

Figure 5.62 Lattice thermal conductivity with normalized film thickness. Lx represents the film thickness and L = 0.1 μm. The solutions are presented for the frequency dependent and the frequency independent solutions of the radiative transport equation.

5.3.2 Transient Heat Transport Including the Effect of Thermal Oscillation in Aluminum Thin Film

Energy transfer in the aluminum thin film, due to temperature disturbance at the film edges, is examined using the frequency dependent and frequency independent transient phonon transport considerations. Equivalent equilibrium temperature is introduced to assess the rate of phonon transport in the film. The solution of modified two-equation model is obtained to compare with the predictions of frequency dependent Boltzmann equation for the steady heating situation. In order to assessment of energy transport characteristics in lattice and electron sub systems the following dimensionless parameter is introduced,

$$Dimensionless\,Temperature = \frac{T_{p,e}(x,t) - T_{right}}{T_{left} - T_{right}} \tag{5.8}$$

where $T_{p,e}(x,t)$ is the lattice site or electron temperature in the film, T_{right} is low temperature at the right edge of the film, and T_{left} is high temperature at the left edge of the film.

Figure 5.63 shows dimensionless equivalent equilibrium temperature, along the film thickness obtained for frequency dependent, frequency independent and modified two-equation models for the steady state heating case. Equivalent equilibrium temperature predicted from frequency independent and modified two equation models behave similar along the film thickness; however, frequency dependent solution of the radiative transport equation results in different behavior of equivalent equilibrium temperature. Since the phonon transport is formulated using the hyperbolic heat equation incorporating the electron-phonon coupling, no temperature jump occurs at the edges of the film. Because of boundary scattering, the emitted phonons from the edges result in temperature jump at the edges of the film. Since the effects of quasi-ballistic and ballistic phonons are not incorporated in both the two-equation and frequency independent solution of the radiative transport equation, equilibrium equivalent temperature behaves similar, except temperature at the film edges. The use of phonon branches through the dispersion relations alters the group velocity and phonon relaxation time in the film. Consequently, phonons having the wavelengths comparable and larger than the film thickness, does not significantly contribute to the phonon scattering in the film. This in turn lowers equivalent equilibrium temperature in the film. This behavior is more pronounced for the thin film. As the film thickness increases, frequency dependent and independent solutions of the radiative transport equation result in similar behavior of equivalent equilibrium temperature. However, equivalent equilibrium temperature due to two-equation model is similar to the that obtained from the diffusive limit [16]; in which case, parabolic decay is observed in temperature with increasing film thickness. In addition, temperature jump due to boundary scattering at the film edges reduces considerably with increasing film thickness, which is more pronounced for the frequency independent solution of the radiative transport equation. This behavior is attributed to the behavior of the phonons emitted from the film edges, which contributes significantly to the film resistance through boundary scattering.

Figure 5.64 shows dimensionless equivalent equilibrium temperature along the film thickness in the lattice sub-system for different temperature oscillations (Figure 3.7) at the film edge and the frequency dependent and independent solutions of the phonon radiative transport equation. Figure 5.65 and Figure 5.66 show 3-dimensional surface of equivalent equilibrium temperature variation with time and film thickness. The total heating period is 8 ps and the film thickness (*L*) is $L = 0.1 \mu m$. It should be noted that τ_h represents the duration of the high temperature pulse (301 *K*, Figure 3.7). Equivalent equilibrium temperature increases to reach its peak value in the near region of the high temperature edge of the film. The location of the peak temperature differs for frequency dependent and independent cases; in which case, the location of peak temperature becomes closer to the film edge as compared to that of the frequency independent case. Moreover, the behavior of equivalent equilibrium temperature is different than that is observed for the silicon film [56]. This is associated with the thermal communication of the electron and phonon sub-systems during the heating period and boundary scattering of phonons at the high temperature edge. Therefore, electron-phonon coupling between both sub-systems suppresses temperature increase at the high temperature edge of the film. Consequently, some of the phonons emitted from the high temperature edge is transferred to electron sub-system through electron phonon coupling while electron temperature attains high values in this region (Figure 5.65). In addition, boundary scattering due to different modes of the phonons emitted from the high temperature edge results in large temperature jump at the high temperature edge. In the case of frequency dependent simulations, some of the phonons with large wavelengths do not undergo scattering in the near region of the high temperature edge of the film. This, in turn, causes the change of the location of the temperature peak in the film. In addition, the quasi-ballistic and ballistic phonons do not contribute to the film resistance; therefore, the maximum value of equivalent equilibrium temperature remains lower than that corresponding to the frequency independent case. This behavior is true for all the periods of temperature oscillations $\left(\tau_{cycle}\right)$ incorporated in the simulations. As the distance increases along the thickness of the film towards the low temperature edge, temperature difference between the frequency dependent and independent solutions becomes large. This behavior is attributed to the phonon intensity distribution in the lattice sub-system. In addition, electron-phonon coupling contributes to the temperature difference, since electron temperature differences between both solutions reduce as the distance along the film thickness increases towards the low temperature edge.

Figure 5.67 shows electron temperature distribution in the film for frequency dependent and frequency independent solutions of the phonon radiative transport equation and different periods of temperature oscillation at the film edge as similar to those shown in Figure 5.64 for heating duration of 8 ps. Electron temperature remains high in the close region of the high temperature film edge and it reduces sharply as the distance along the film thickness increases towards the low temperature edge. Electrons gain energy from the lattice site through electron-phonon coupling and electron excess energy increase becomes high in the region where the phonon intensity is high in the film. Consequently, electron temperature behavior almost follows the lattice site phonon behavior in the film, provided that the magnitude of electron temperature remains less than phonon temperature in the surface region. Electron temperature corresponding to frequency dependent solution of lattice phonons results in lower temperature than that of frequency independent solution. This behavior is related to phonon temperature in the lattice sub-system, which is lower for frequency dependent solution. Consequently, energy transport from lattice sub-system to electron sub-system, through electron-phonon coupling, remains low for the case of the frequency dependent solution.

Figure 5.68 shows temporal behavior of equivalent equilibrium temperature in the lattice sub-system for frequency dependent and independent solutions of the radiative phonon transport equation and different periods of temperature oscillation at the film edge. It should be noted that the location is $x = 0.05L$, where $L = 0.1\mu m$, in the film. In general, temperature increase is sharp in the early heating period and it becomes gradual as the heating period progresses. This is associated with the phonon scattering in the film, which increases with progressing time. Oscillation of equivalent equilibrium temperature occurs with progressing time and the amplitude of temperature oscillation is higher for the frequency independent case than that of frequency depend solution of phonon radiative transport equation. Since the location, where temporal behavior of temperature is shown in the figure, is close to the high temperature edge, the amplitude of temperature oscillation remains high. However, the period of temperature oscillation in the film does not follow the period of oscillation at the film edge. In this case, period of temperature oscillation in the film remains higher than that corresponding to the film edge. This is more pronounced as the period of oscillation at the film edge increases. The differences in the period of temperature oscillations are related to the scattering of the emitted phonons from the high temperature edge. The scattering of phonons modify the phonon intensity distribution in the near region of the high temperature edge. This, in turn, alters the equilibrium phonon intensity distribution over the wave numbers (k). Consequently, re-distribution of the equilibrium phonon intensity distribution causes the changes of temporal response of the film resistance to the temperature oscillation at the film edge. However, phonons reflected from the low temperature edge (I^-, reflected phonon intensity) also contributes to phonon scattering in the near region of the high temperature edge; however, this effect is not significantly high [136]. The reduced amplitude of temperature oscillation for the frequency dependent case is attributed to the quasi-ballistic and ballistic phonons behavior, which do not contributed to temperature variation in the film. However, as the location in the film changes to $x = 0.1L$, where $L = 0.1\mu m$, amplitude of temperature oscillation changes in the film. This situation can be observed from Figure 5.69, in which temporal variation of temperature is shown for frequency dependent and independent solutions of phonon radiative transport equation at $x = 0.1L$. Therefore, temporal behavior of temperature in the lattice sub-system changes significantly with increasing distance along the film thickness. In this case, phonon intensity distribution changes significantly through scattering while modifying the thermal response of the film resistance to temperature oscillation at the film edge. This behavior is more pronounced for small period of temperature oscillation at the film edge; in which case, the amplitude of temperature oscillation at $x = 0.1L$ reduces significantly. Figure 5.70 shows temporal variation of electron temperature for frequency dependent and independent solutions of phonon radiative transport equation and different periods of temperature oscillation at the film edge. The location, where temperature oscillation is shown in Figure 5.70, is at $x = 0.05L$. Electron temperature behaves similar to those shown for phonon temperature in Figure 5.68. However, the rise and decay of temperature oscillation differs along the consecutive oscillations unlike the case observed for phonon temperature. This is associated with the energy transfer from the lattice sub-system to the electron sub-system through electron-phonon coupling, which shows non-linear behavior with time. The amplitude of temperature oscillation increases with increasing period of temperature oscillation at the film edge as similar to the temporal response of phonon temperature as shown in Figure 5.68.

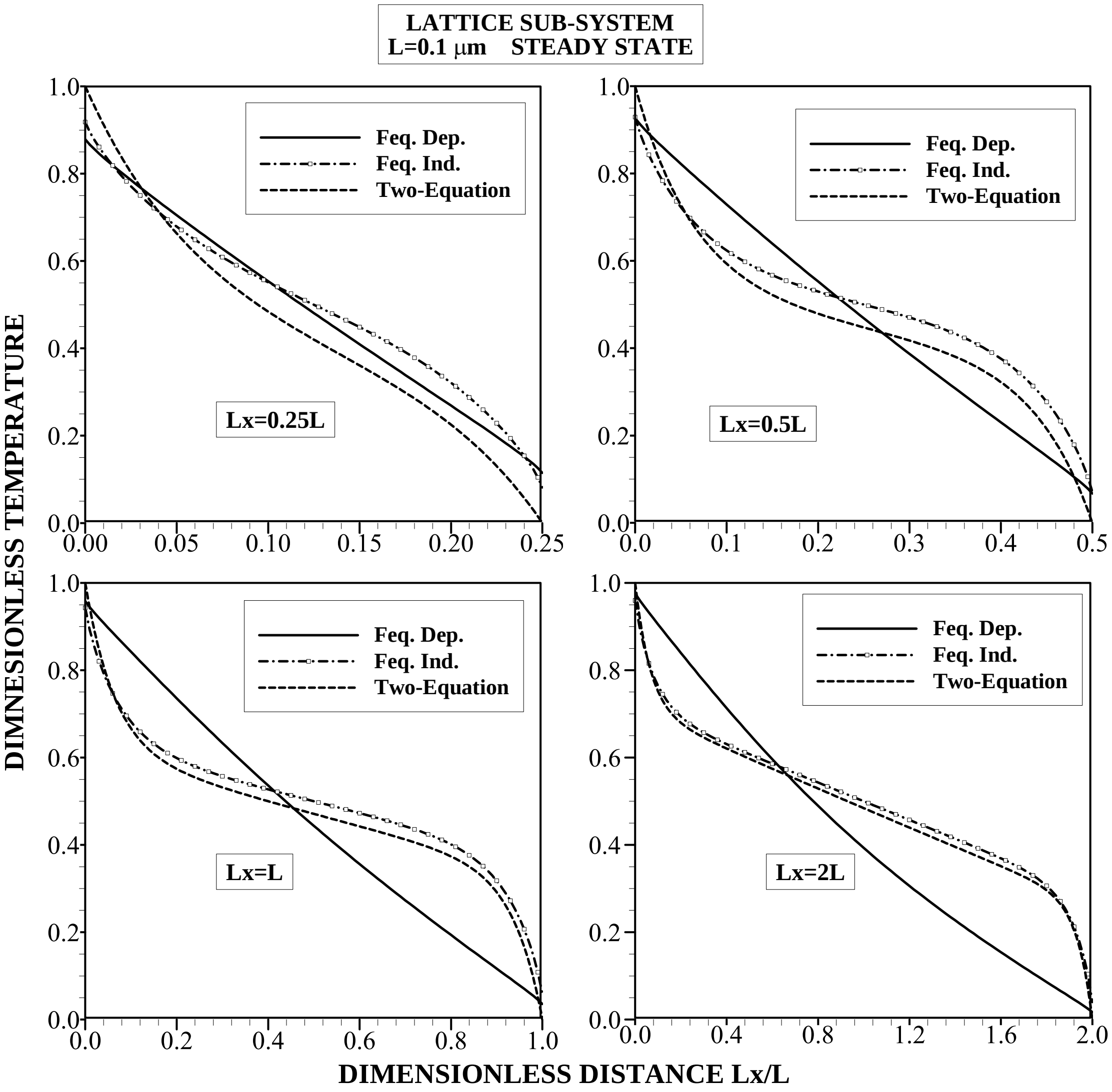

Figure 5.63 Comparison of dimensionless temperature due the frequency dependent, frequency independent solutions of phonon radiative transport equation and modified two-equation model.

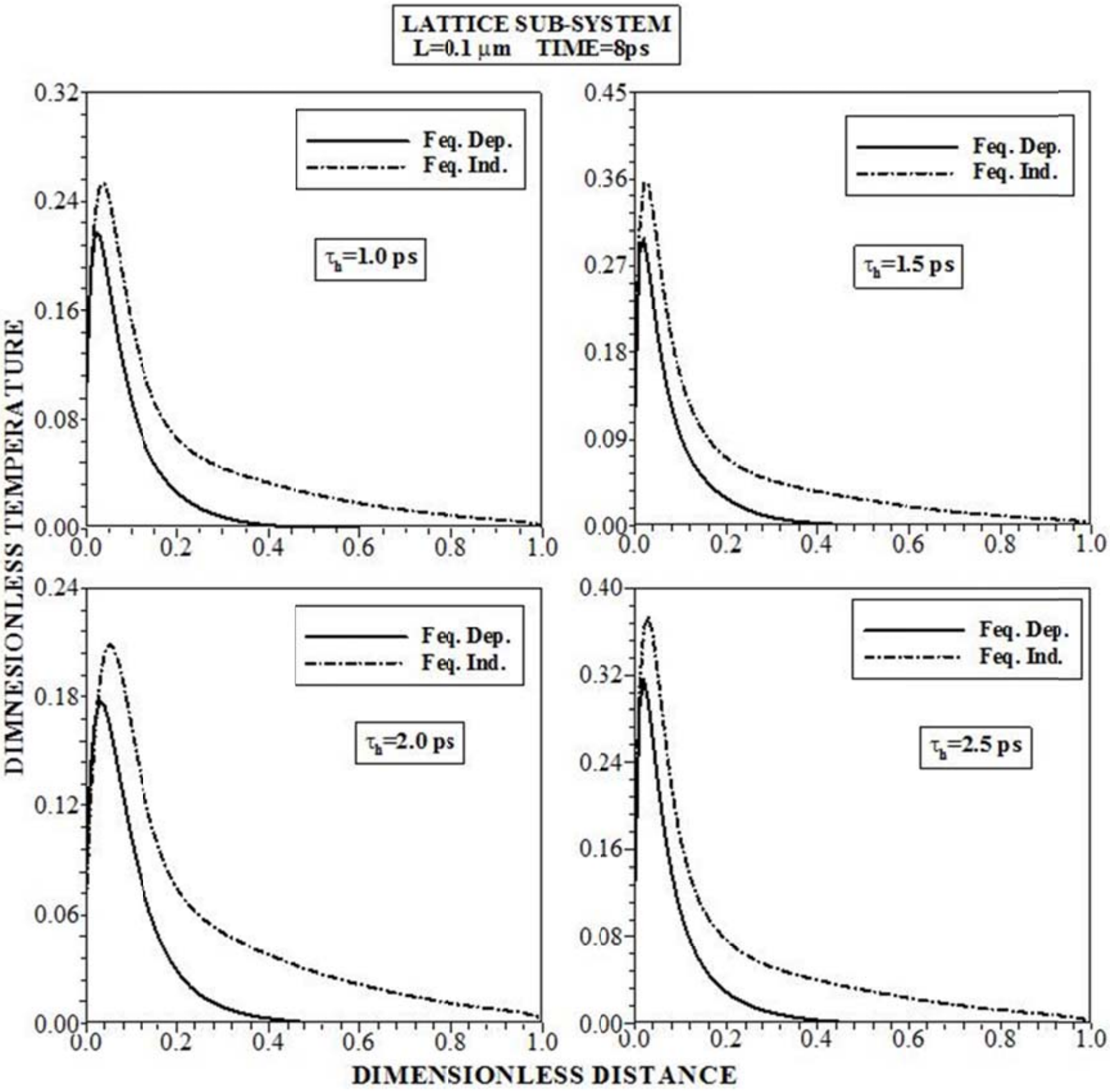

Figure 5.64 Dimensionless equivalent equilibrium temperature, in the lattice sub-system, along the film thickness for the frequency dependent and independent solutions of phonon radiative transport equation for different duration of high temperature in the temperature oscillation and heating duration of 8 ps.

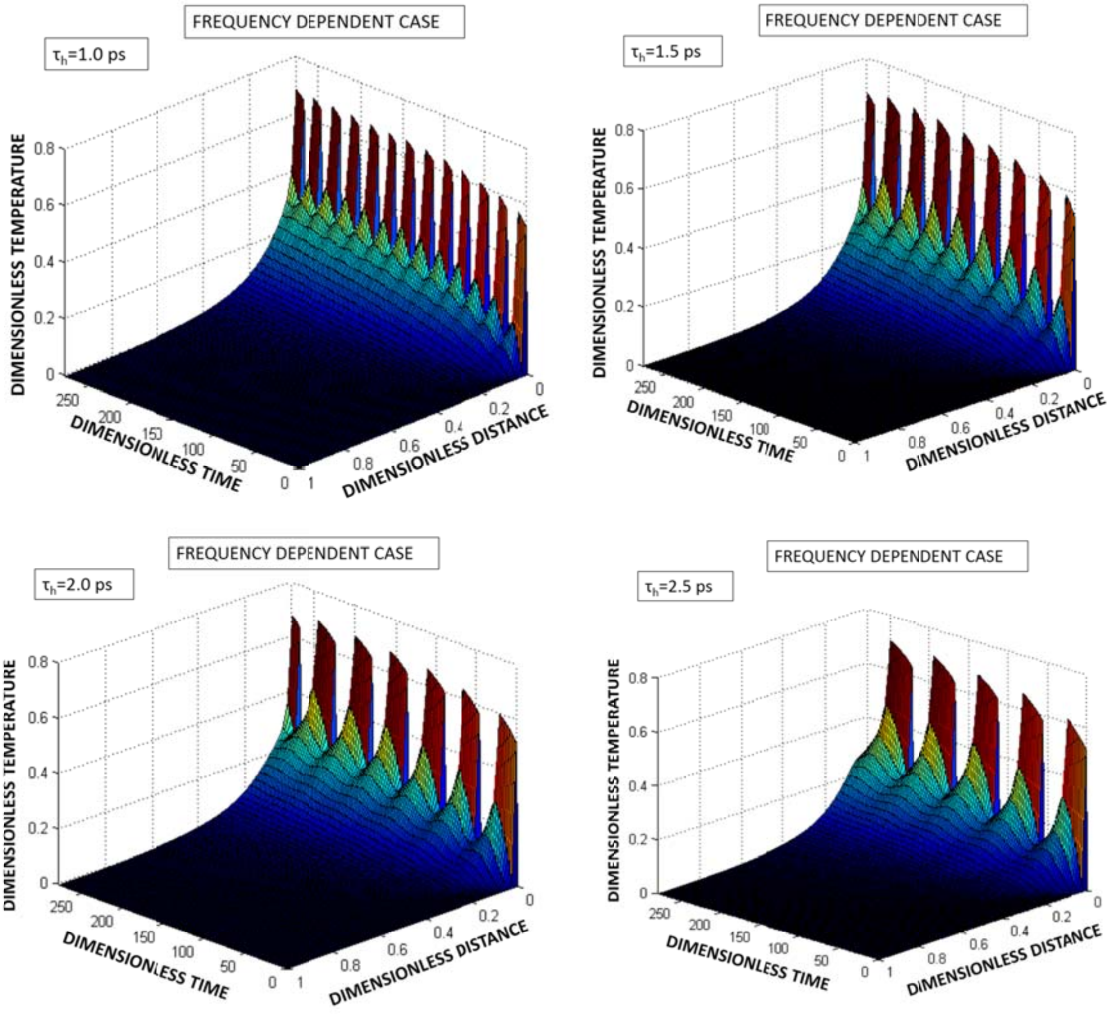

Figure 5.65 3-dimensional view of equivalent equilibrium temperature, obtained from frequency dependent solution of radiative transport equation, with time and distance along the film thickness for different duration of high temperature in temperature oscillation at the film edge. $Dimensionless\ Time = t/\tau_d$ where $\tau_d = C_e/G$ and $\tau_d = 8.94\text{x}10^{-14}\ s$.

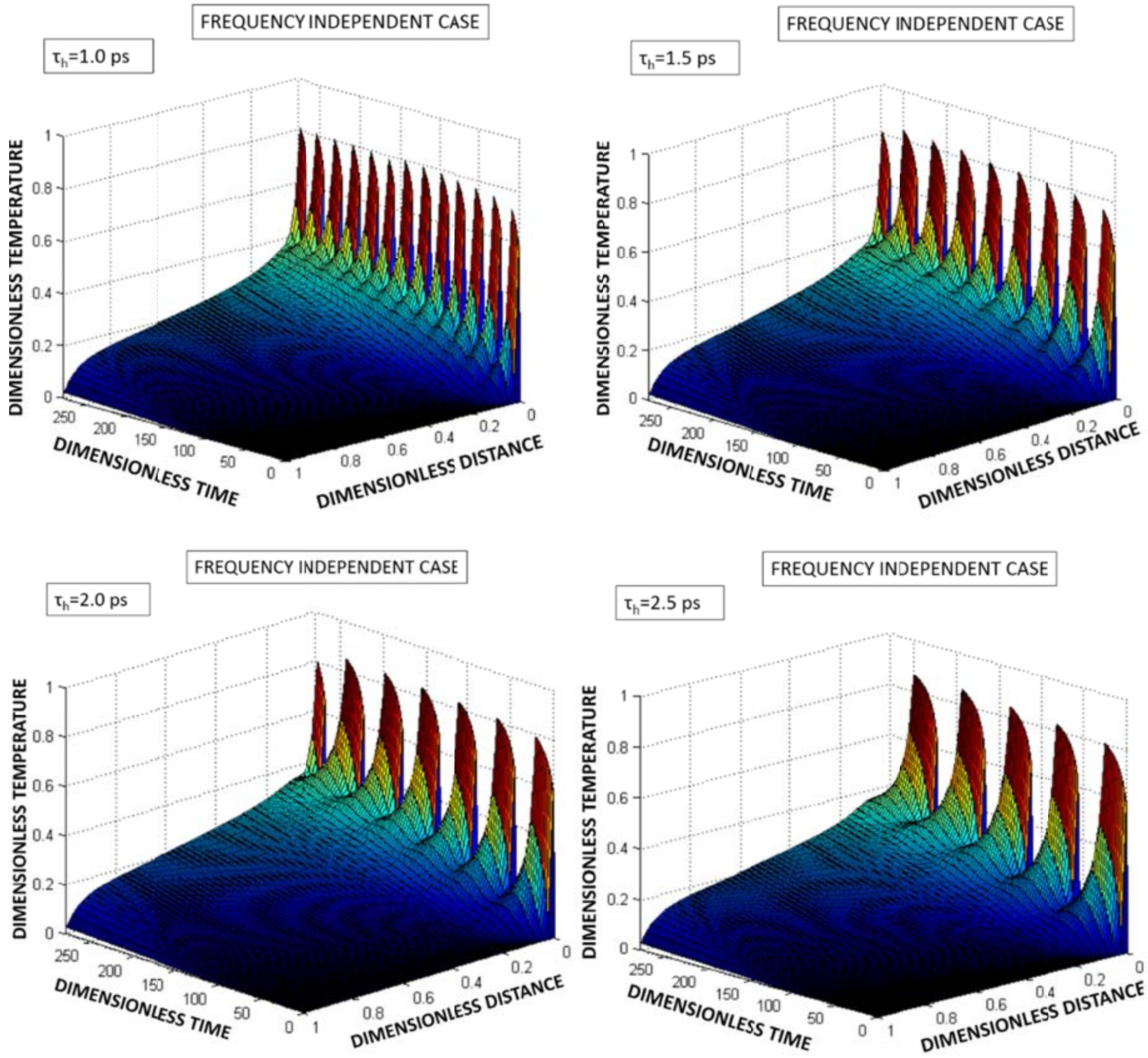

Figure 5.66 3-dimensional view of equivalent equilibrium temperature, obtained from frequency independent solution of radiative transport equation, with time and distance along the film thickness for different duration of high temperature in temperature oscillation at the film edge. $\mathit{Dimensionless\ Time} = t / \tau_d$ where $\tau_d = C_e / G$ and $\tau_d = 8.94\text{x}10^{-14}\ s$.

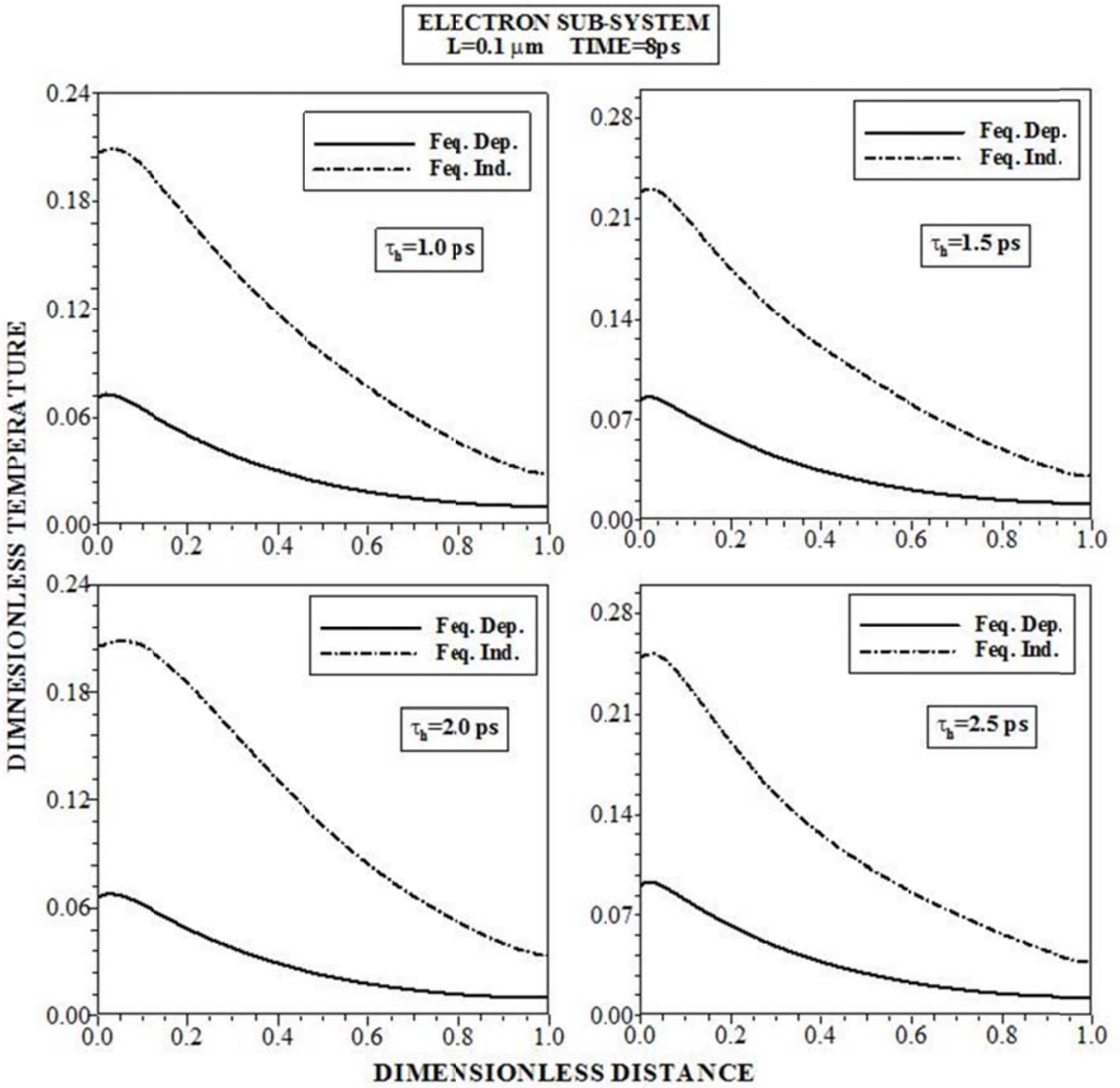

Figure 5.67 Dimensionless temperature, in the electron sub-system, along the film thickness for the frequency dependent and independent solutions of phonon radiative transport equation for different duration of high temperature in the temperature oscillation and heating duration of 8 ps.

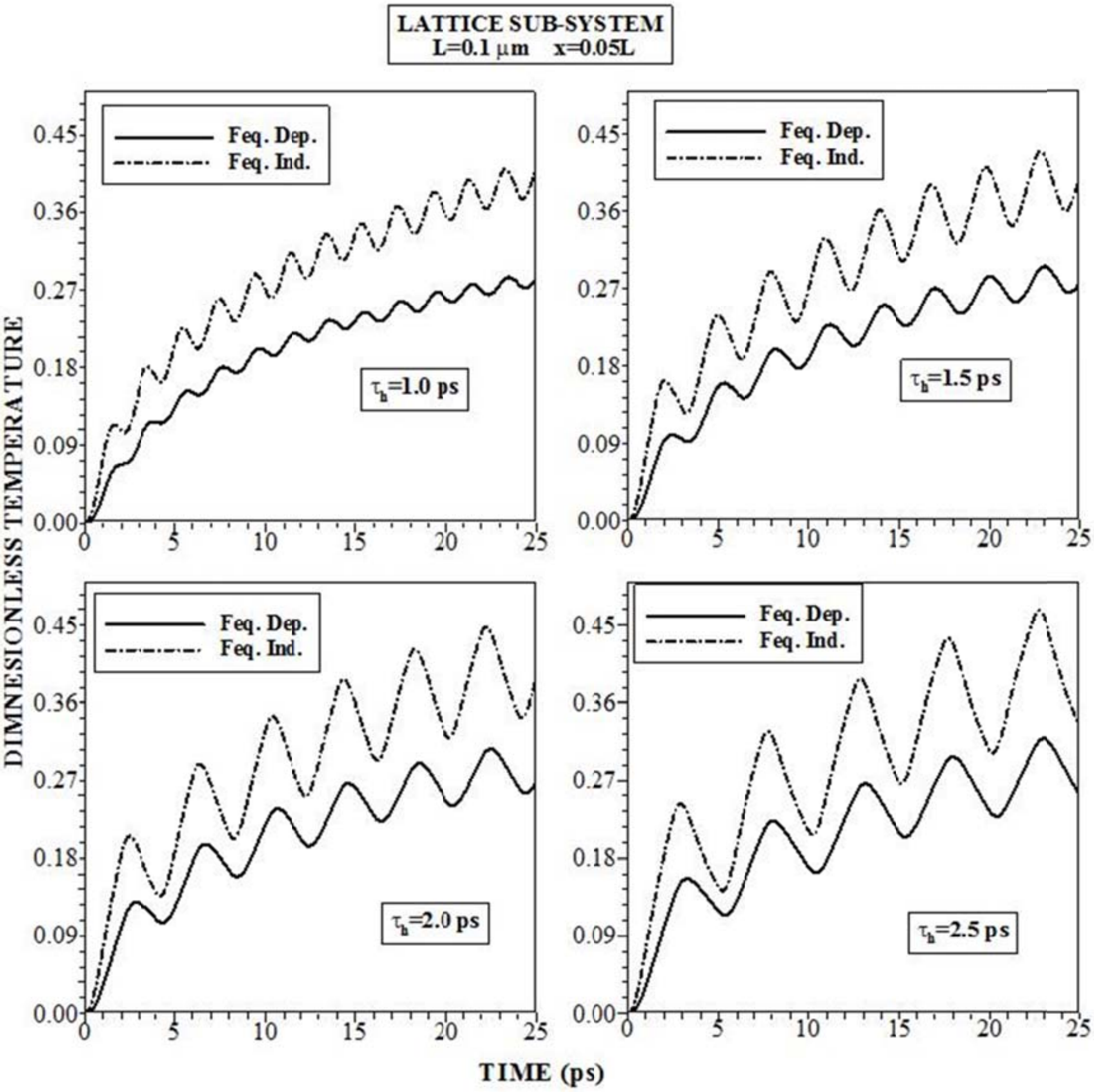

Figure 5.68 Temporal variation of dimensionless temperature, in the lattice sub-system, for the frequency dependent and independent solutions of phonon radiative transport equation for different duration of high temperature (τ_h) in the temperature oscillation and heating duration of 8 ps. The location is x = 0.05L (L = 0.1μm) in the film.

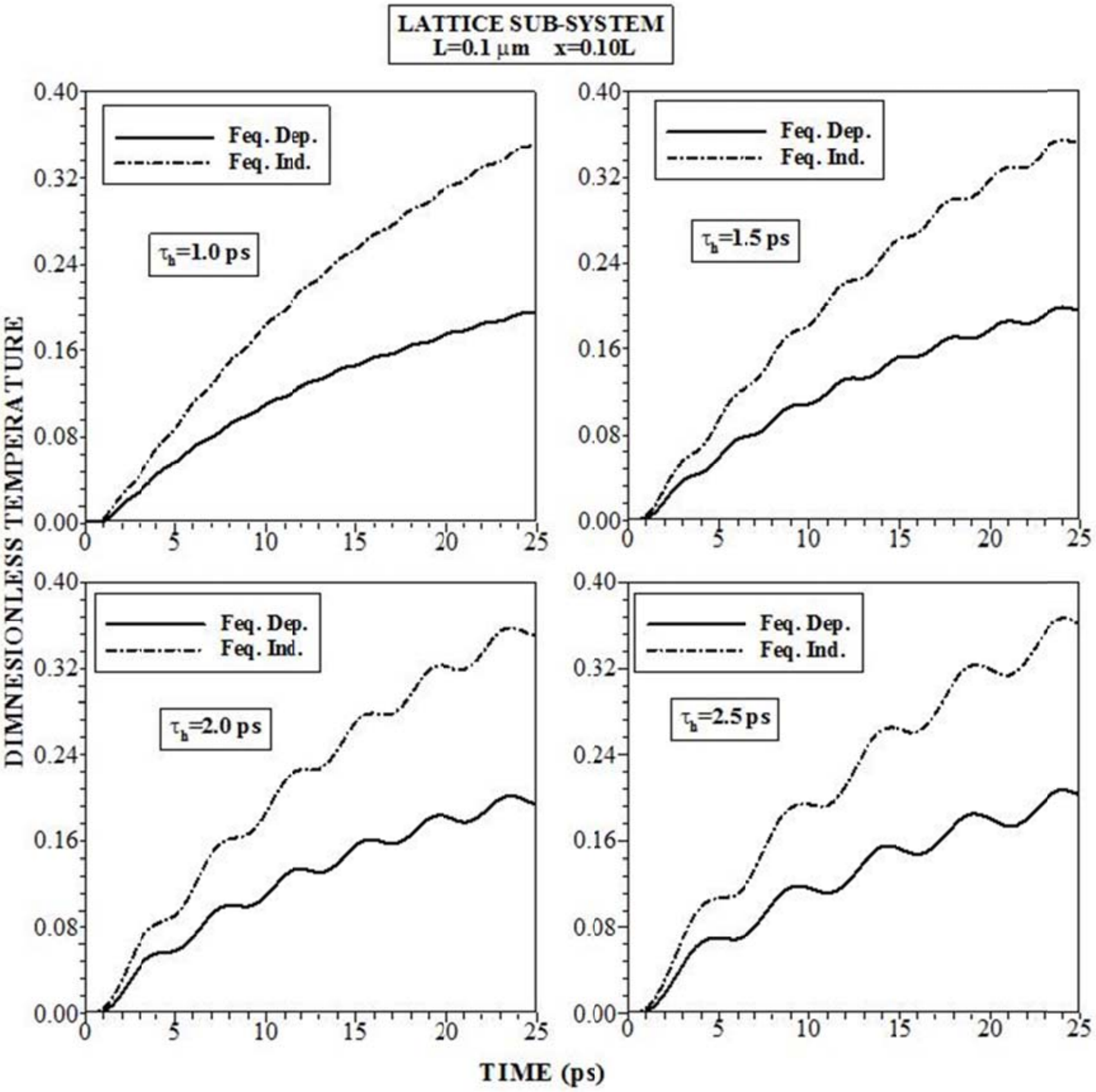

Figure 5.69 Temporal variation of dimensionless temperature, in the lattice sub-system, for the frequency dependent and independent solutions of phonon radiative transport equation for different duration of high temperature (τ_h) in the temperature oscillation and heating duration of 8 ps. The location is x = 0.1L (L = 0.1μm) in the film.

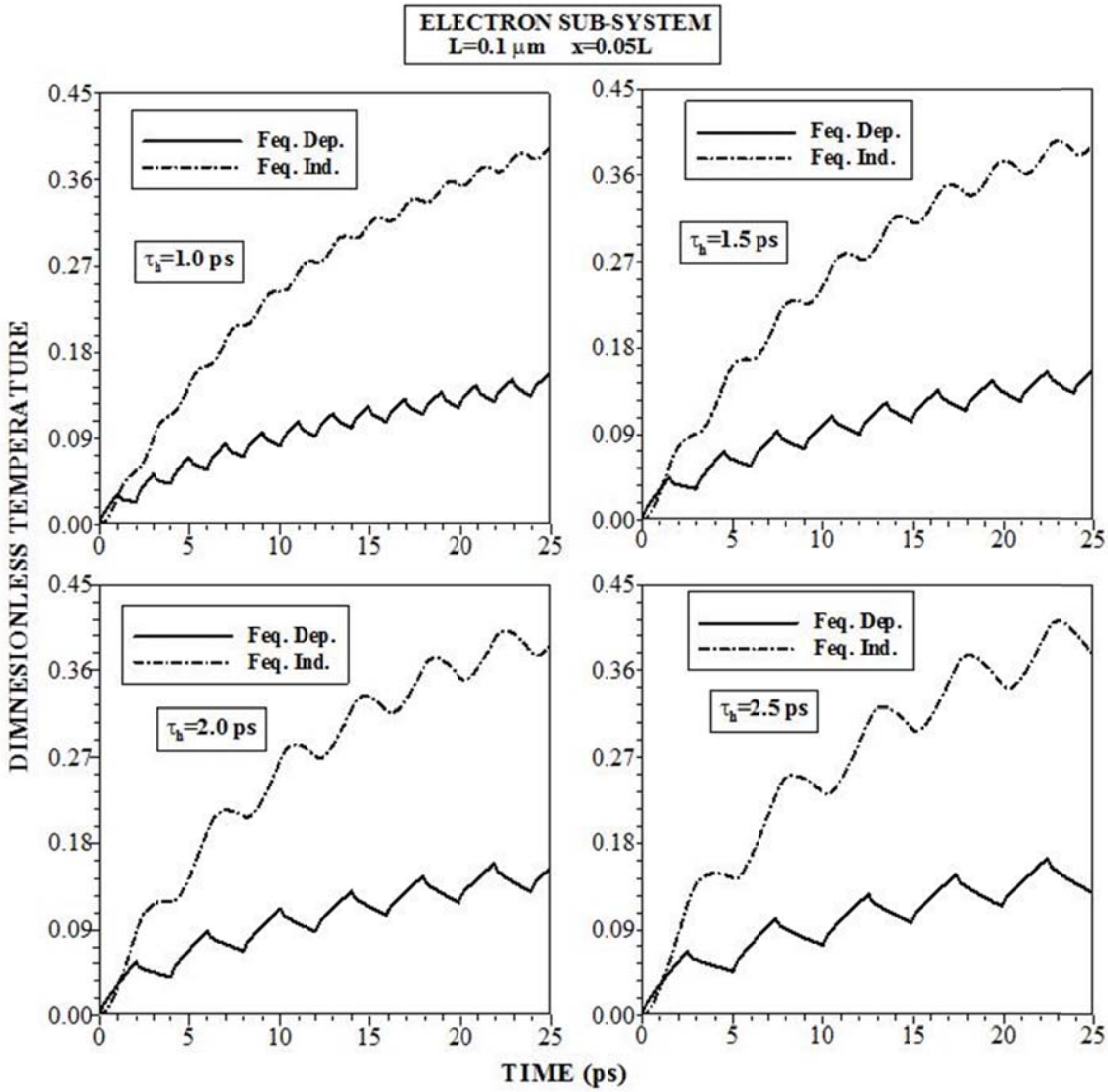

Figure 5.70 Temporal variation of dimensionless temperature, in the electron sub-system, for the frequency dependent and independent solutions of phonon radiative transport equation for different duration of high temperature (τ_h) in the temperature oscillation and heating duration of 8 ps. The location is x = 0.05L (L = 0.1μm) in the film.

5.3.3 Transient Heat Transport Including the Effects of Thermal Oscillation and Film Thickness in Aluminum Thin Film

Phonon transport characteristics are investigated in a thin aluminum film. Transient frequency dependent radiative phonon transport equation is solved for the lattice and the electron sub-systems. The effect of film thickness on the phonon transport characteristics due to temperature oscillation at the film edge is examined. In order to assessment of energy transport characteristics in lattice and electron sub systems the following dimensionless parameter is introduced,

$$Dimensionless\,Temperature = \frac{T_{p,e}(x,t) - T_{right}}{T_{left} - T_{right}} \tag{5.9}$$

where $T_{p,e}(x,t)$ is the lattice site or electron temperature in the film, T_{right} is low temperature at the right edge of the film, and T_{left} is high temperature at the left edge of the film that is 301 *K*.

Figure 5.71 shows dimensionless equivalent equilibrium temperature with the dimensionless film thickness is shown (x/L_x, where L_x is the film thickness) in the lattice sub-system for two heating periods of temperature oscillation (Figure 3.7) at the left edge of the film. The heating time is 8 ps and $L = 0.1 \mu m$. It should be noted that frequency dependent and independent solutions of phonon radiative transport equation are given for the comparison reason. Dimensionless temperature increases to reach its maximum in the region close to the high temperature edge. Attainment of low temperature in the vicinity of the film edge is because of the boundary scattering of the emitted phonons from the high temperature edge. This, in turn, generates temperature jump at the film edge. However, the attainment of high temperature in the near region of the film edge is related to the scattering of phonons in this region, which contributes to the film resistance in this region. As the film thickness increases, the value of the peak temperature reduces in the film. This behavior is true for both solutions of phonon radiate transport equation due to frequency dependent and frequency independent cases. This behavior is attributed to the dimensionless distance in the film. In this case, reducing film thickness lowers the actual value of x in the film, since x / L_x remains constant in the figure. Consequently, for small film thicknesses, the location of temperature becomes close to the high temperature edge, which in turn, results in higher temperature for the thinner films. Dimensionless temperature reduces sharply first and as the dimensionless distance increases towards the low temperature edge where $x / L_x = 1$, the reduction becomes gradual. The emitted phonons from the high temperature edge undergo scattering and contribute to the film resistance while increasing temperature in the film. In addition, phonons reflected from the low temperature edge also contribute to phonon scattering in the film; however, phonon intensity emitted from the low temperature edge is smaller than that emitted from the high temperature edge. Therefore, the effect of reflected and emitted phonons from the low temperature edge on the equilibrium phonon intensity increase is not considerably high in the film. When comparing the heating duration of temperature oscillation $\left(\tau_h\right)$ at the high temperature of the film edge, dimensionless temperature increases slightly for long heating period (high value of τ_h). Since temperature oscillation is defined through the function $T_{Left}(t) = \begin{cases} 301\,K(0 < t < \tau_h) \\ 300\,K(otherwise) \end{cases}$ and $T_{Right}(t) = 300K$, the amount of phonon emission from the high temperature edge increases for the longer duration of τ_h. This, in turn, increases scattering rate in the film while enhancing dimensionless temperature in the near region of the film. Moreover, when comparing the peak value of dimensionless temperature due to frequency dependent and frequency independent solutions of phonon radiative transport equation, the peak dimensionless temperature remains higher for the frequency independent solutions than that of the frequency dependent solutions, which is particularly true for the small film thicknesses. In this case, ballistic and quasi-ballistic phonons do not undergo scattering in the film and does not contribute to temperature increase in the film despite the fact that they contribute to energy transport across the film. When the phonon wavelengths become comparable or greater than the film thickness, they do not suffer from scattering in the film. The similar arguments are true for the longer heating period which is shown in Figure 5.72. However, dimensionless temperature behavior changes across the film thickness; in which case, emitted and reflected phonon intensities from both edges of the film undergo scattering and normalize the equilibrium intensity in the film in such a way that the peak temperature in the close region of the high temperature edge replaces with the smooth decay of temperature in this region.

Figure 5.73 shows dimensionless temperature distribution along the dimensionless distance in the electron sub-system for different two heating periods of temperature oscillation at the high temperature film edge and frequency dependent and independent solutions of the phonon radiative transport equation. The heating duration is similar to that shown in Figure 5.71. Electron temperature does not follow phonon temperature in the lattice sub-system despite energy exchange takes place via electron-phonon coupling during thermal communications of both sub-systems. Electron temperature remains higher for the smaller thicknesses than that corresponding to larger film thicknesses. This is attributed to the location where temperature is obtained, in which case, locations in the film $\left(x / L_x\right)$ become close to the high temperature edge. Dimensionless electron temperature increases as the heating period $\left(\tau_h\right)$ increases. This is attributed to the long duration of thermal communications of both sub-systems. Since phonon temperature is higher in the lattice sub-system than electron temperature, energy transfer takes place from phonon sub-system to the electron sub-system. Consequently, with long heating periods, temperature increases in the electron sub-system. When comparing temperature distributions obtained from frequency dependent and frequency independent solutions of phonon radiative transport equation in the lattice sub-system, electron temperature remains high for frequency independent solution of phonon radiative transport equation in the lattice sub-system. It should be noted that the dispersion relations are available for the lattice sub-system and relation time is very short in the electron sub-system; therefore, the frequency dependent solution of phonon radiative transport equation is introduced for the phonon sub-system only. Hence, the frequency independent solution of phonon radiative transport equation is obtained for the electron sub-system. However, change in dimensionless temperature in the electron sub-system due to frequency dependent and independent cases is associated with the differences in dimensionless temperature in the lattice sub-system due to both solutions. Consequently, frequency dependent solution of phonon radiative transport equation in the lattice sub-system is responsible for temperature difference in the electron sub-system. In the case of long heating period $\left(\tau_h = 2.5ps\right)$ of temperature oscillation, dimensional electron temperature does not alter from that of the short heating pulse period $\left(\tau_h = 1.5ps\right)$. Figure 5.74 shows electron temperature variation along the dimensionless distance for various film thicknesses and two different heating periods $\left(\tau_h\right)$ of temperature oscillation at the high temperature edge. The heating duration in Figure 5.74 is 22 ps. Dimensionless electron temperature behavior differs from that is shown in Figure 5.73. This is associated with the long heating duration; in which case, thermal communication between the electron and lattice sub-systems is responsible for this difference during the long heating period.

Figure 5.75 shows temporal variation of dimensionless temperature in the phonon sub-system for different film thicknesses and two heating periods of temperature oscillation at the high temperature film edge. The location in the film is $x = 0.05L_x$ and temperature distributions due to frequency dependent and frequency independent solutions of phonon radiative transport equation are given for the comparison reason. Figure 5.76 shows the surface plot of dimensionless phonon temperature distribution in the lattice sub-system. Since the phonons emitted from high temperature edge are forced to oscillate due to temperature oscillation at high temperature edge, dimensionless equivalent equilibrium temperature oscillates with time. However, oscillation of equivalent equilibrium temperature does not follow exactly temperature oscillation at the film edge. This behavior is attributed to the emitted phonon frequencies; in which case, not all the emitted phonon frequencies have harmonics with temperature oscillation at the high temperature film edge. The magnitude of dimensionless temperature oscillation is larger for thin films than those of thick films. In this case, emitted phonons from high temperature edge undergo scattering in the film while contributing to temperature increase, which in turn increases dimensionless temperature in the thin film. However, as the film thickness increases, the amplitude of dimensionless equivalent equilibrium temperature oscillation reduces. Consequently, increasing film thickness creates a damping effect on equivalent equilibrium temperature oscillation in the film. This is more pronounced for the frequency dependent solution of phonon radiative transport equation. Moreover, increasing film thickness influences the location of dimensionless peak equivalent equilibrium temperature in the film; in which case, increasing film thickness results in peak temperature to move away from the high temperature film edge $\left(x / L_x = 0\right)$. When comparing the frequency dependent and independent solutions of the phonon radiative transport equation, it is evident that magnitude of dimensionless temperature reduces for frequency dependent case. Since quasi-ballistic and ballistic phonons do not undergo scattering in the film, their contribution becomes negligible to temperature increase in the film. Moreover, increasing heating period $\left(\tau_h\right)$ of temperature oscillation at the high temperature edge increases the period of dimensionless equivalent equilibrium temperature oscillation in the film. However, the period of dimensionless equivalent equilibrium temperature oscillation is different than that of the heating period of temperature oscillation at the high temperature edge of the film. As the location in the film changes, temporal behavior of dimensionless temperature changes. This situation is observed from Figure 5.77, in which temporal behavior of dimensionless temperature is shown at location $x = 0.1L_x$. In this case, amplitude of dimensionless temperature reduces considerably with increasing film thickness, which is more pronounced for the frequency dependent solution of the phonon radiative transport equation.

Figure 5.78 shows temporal behavior of dimensionless temperature in the electron sub-system for different film thicknesses and two different heating periods (τ_h) of temperature oscillation at the film edge. Figure 5.79 shows three-dimensional plot of electron temperature variation. Dimensionless temperature in the electron sub-system oscillates similarly with temperature oscillation in the lattice sub-system. However, temperature variation in each oscillation cycle does not follow the behavior of temperature oscillation in the lattice sub-system. This is attributed to the thermal communications of both sub-systems through electron-phonon coupling. In this case, temporal behavior of energy transport during the thermal communications of both sub-systems modifies temporal behavior of electron temperature, i.e., electron temperature rise and fall in each oscillation cycle becomes sharper than that corresponding to phonon temperature in the lattice sub-system. As the heating period of temperature oscillation at the film edge increases $\left(\tau_h = 2.5ps\right)$, the magnitude of electron temperature oscillation increases. This is associated with the energy transfer from the lattice sub-system to the electron sub-system. Since the heating duration is long and phonon temperature in the lattice sub-system attains larger values than that in the electron sub-system, energy transfer towards the electron sub-system modifies electron temperature. When comparing electron temperatures obtained from the frequency dependent and frequency independent solutions of phonon radiative transport equation, it is evident that electron temperature remains high for the frequency independent case and the effect of film thickness on electron temperature rise is negligibly small. This is because of the low phonon temperature in the lattice sub-system for the frequency dependent case (Figure 5.75). Consequently, energy transfer from the lattice sub-system to the electron sub-system becomes small during thermal communications of both sub-systems while resulting in low electron temperature. The effect film thickness on electron temperature becomes less significant for the frequency independent case. This is attributed to the effect of ballistic and quasi-ballistic phonons on the transport characteristics, in which case, this effect is only accounted in the frequency dependent solution of phonon radiative transport.

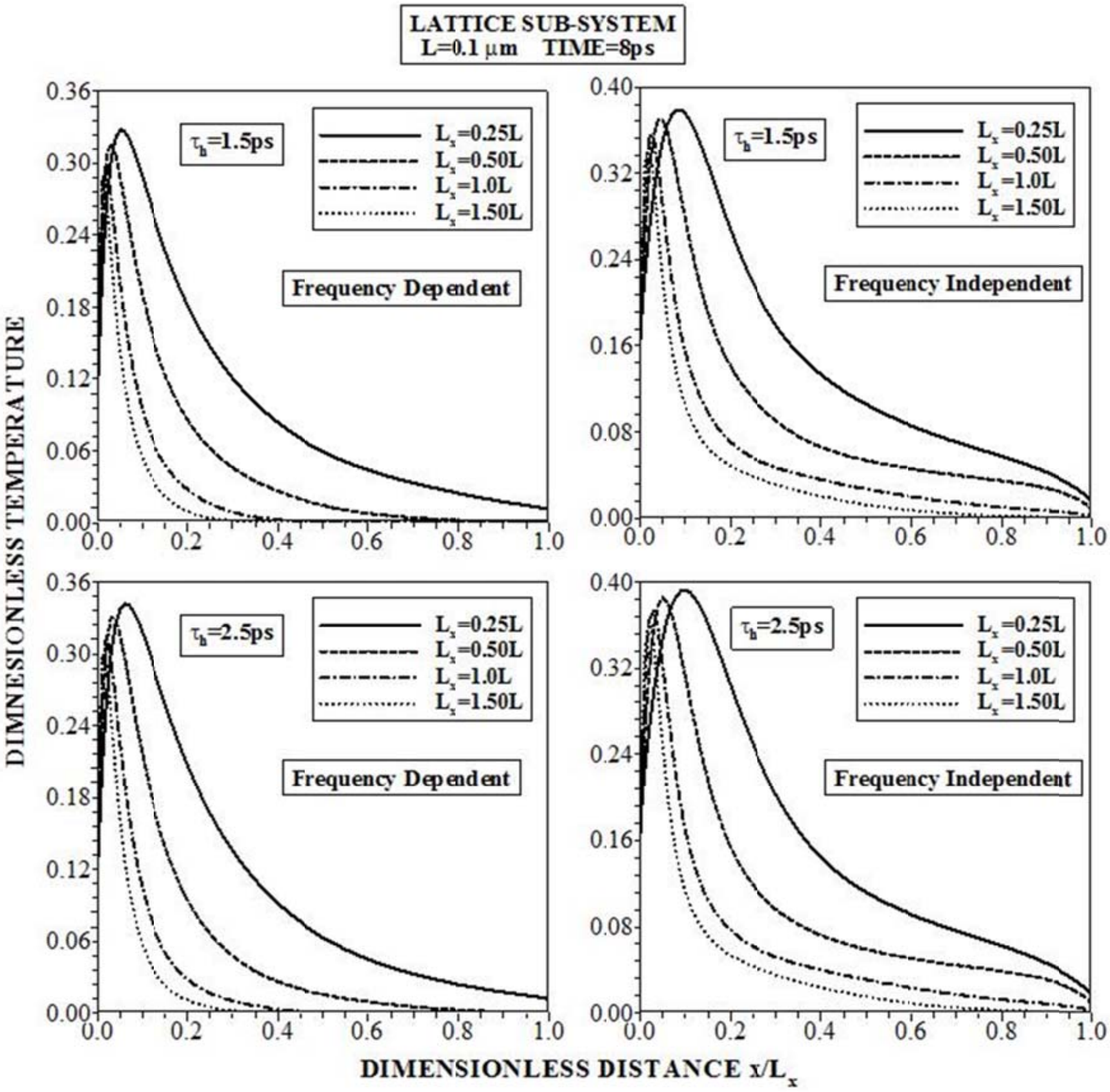

Figure 5.71 Dimensionless equivalent equilibrium temperature in the lattice sub-system for different film thicknesses and frequency dependent and independent solutions of phonon radiative transport equation. Heating time is 8 ps.

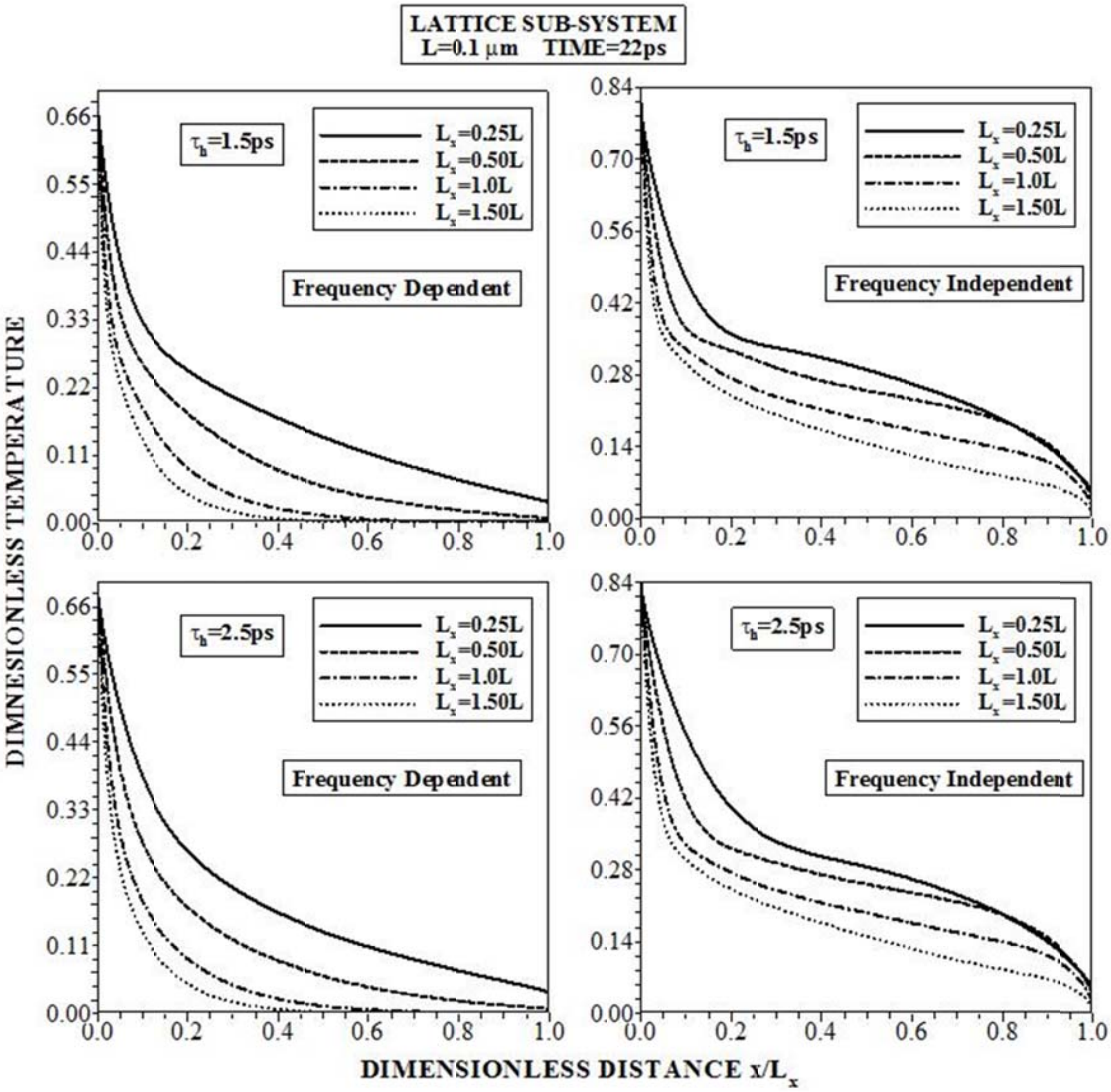

Figure 5.72 Dimensionless equivalent equilibrium temperature in the lattice sub-system for different film thicknesses and frequency dependent and independent solutions of phonon radiative transport equation. Heating time is 22 ps.

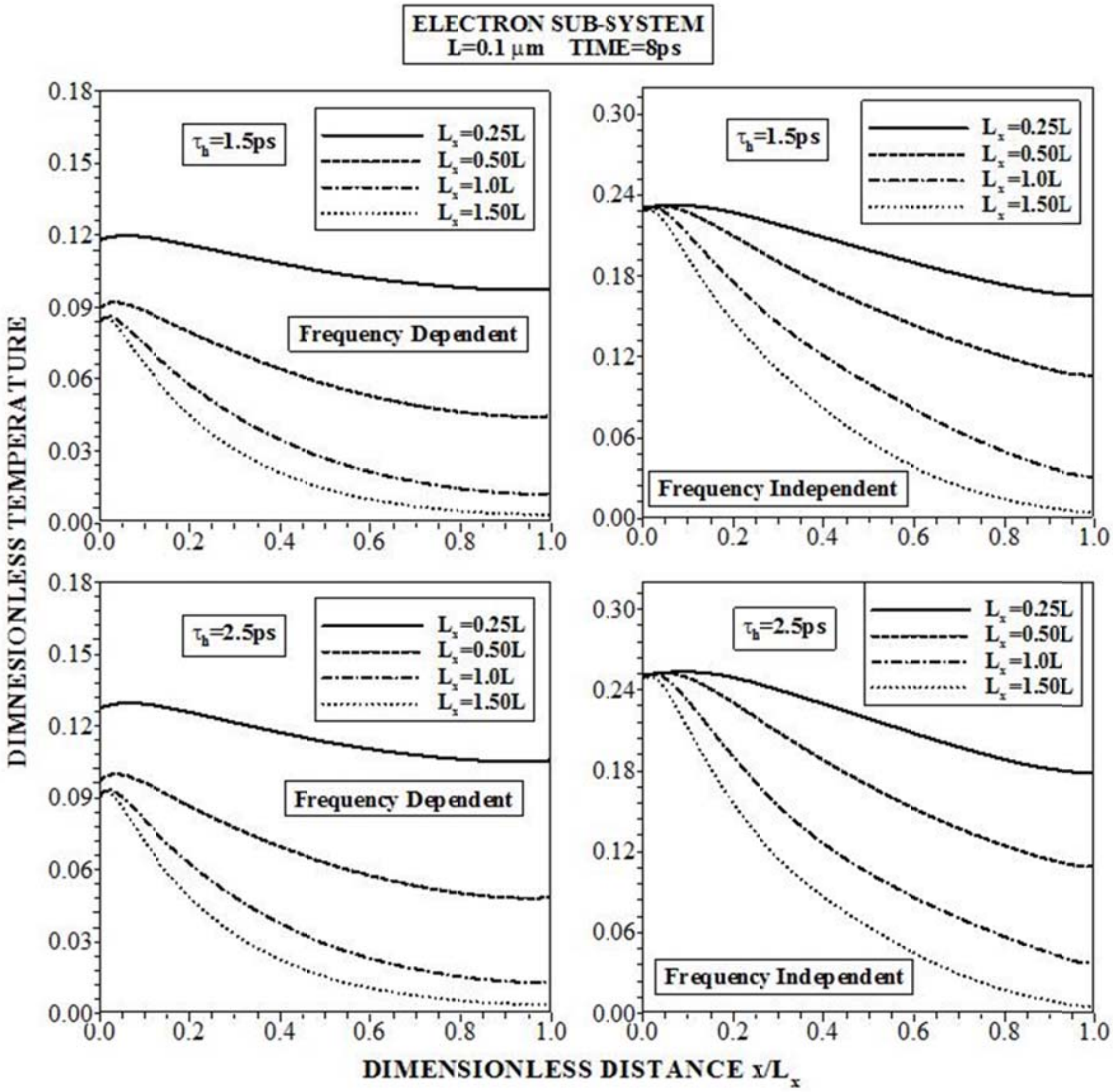

Figure 5.73 Dimensionless temperature in the electron sub-system for different film thicknesses and frequency dependent and independent solutions of phonon radiative transport equation. Heating time is 8 ps.

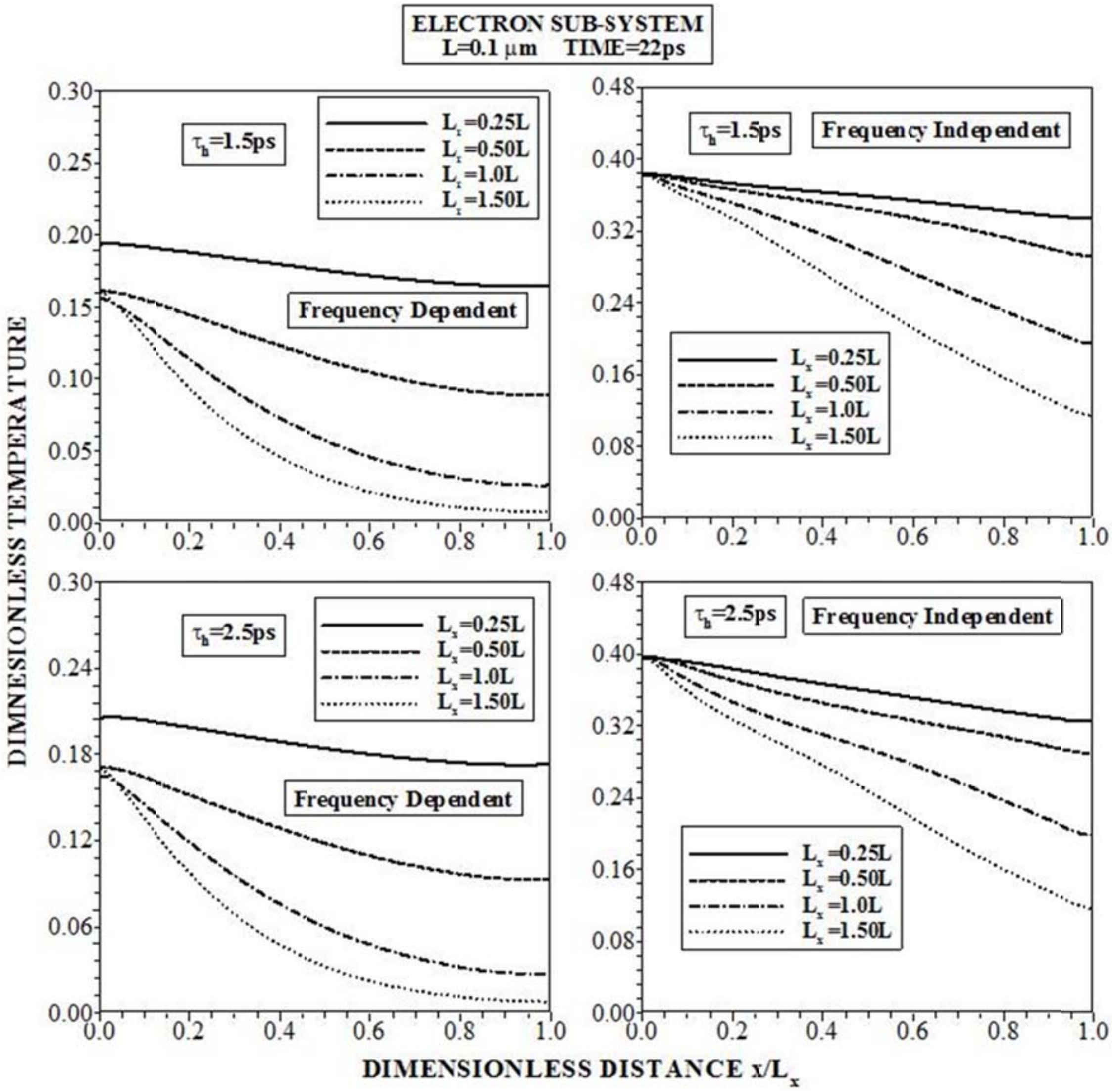

Figure 5.74 Dimensionless temperature in the electron sub-system for different film thicknesses and frequency dependent and independent solutions of phonon radiative transport equation. Heating time is 22 ps.

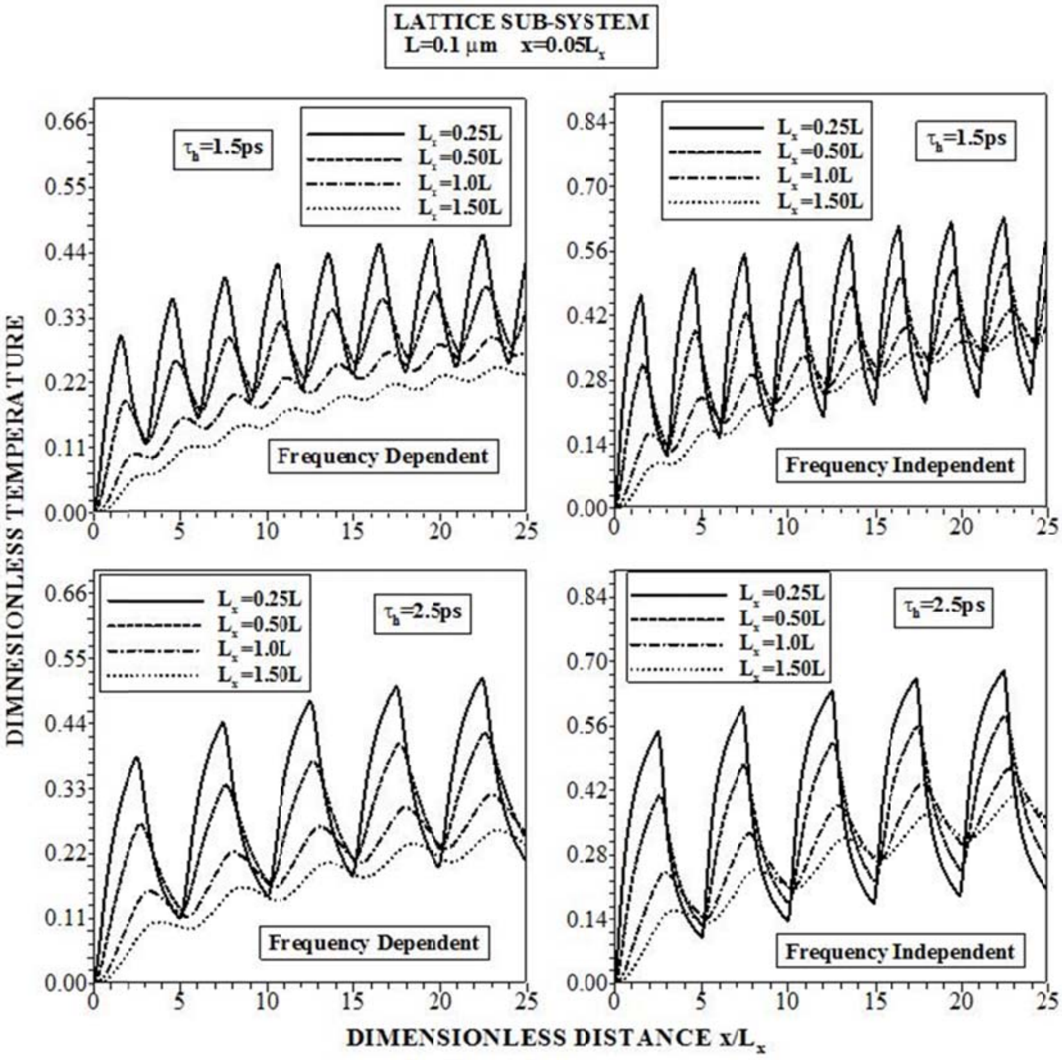

Figure 5.75 Temporal variation of dimensionless equivalent equilibrium temperature in the lattice sub-system for different film thicknesses and frequency dependent and independent solutions of phonon radiative transport equation. Location is x = 0.05Lx, where Lx is the film thickness.

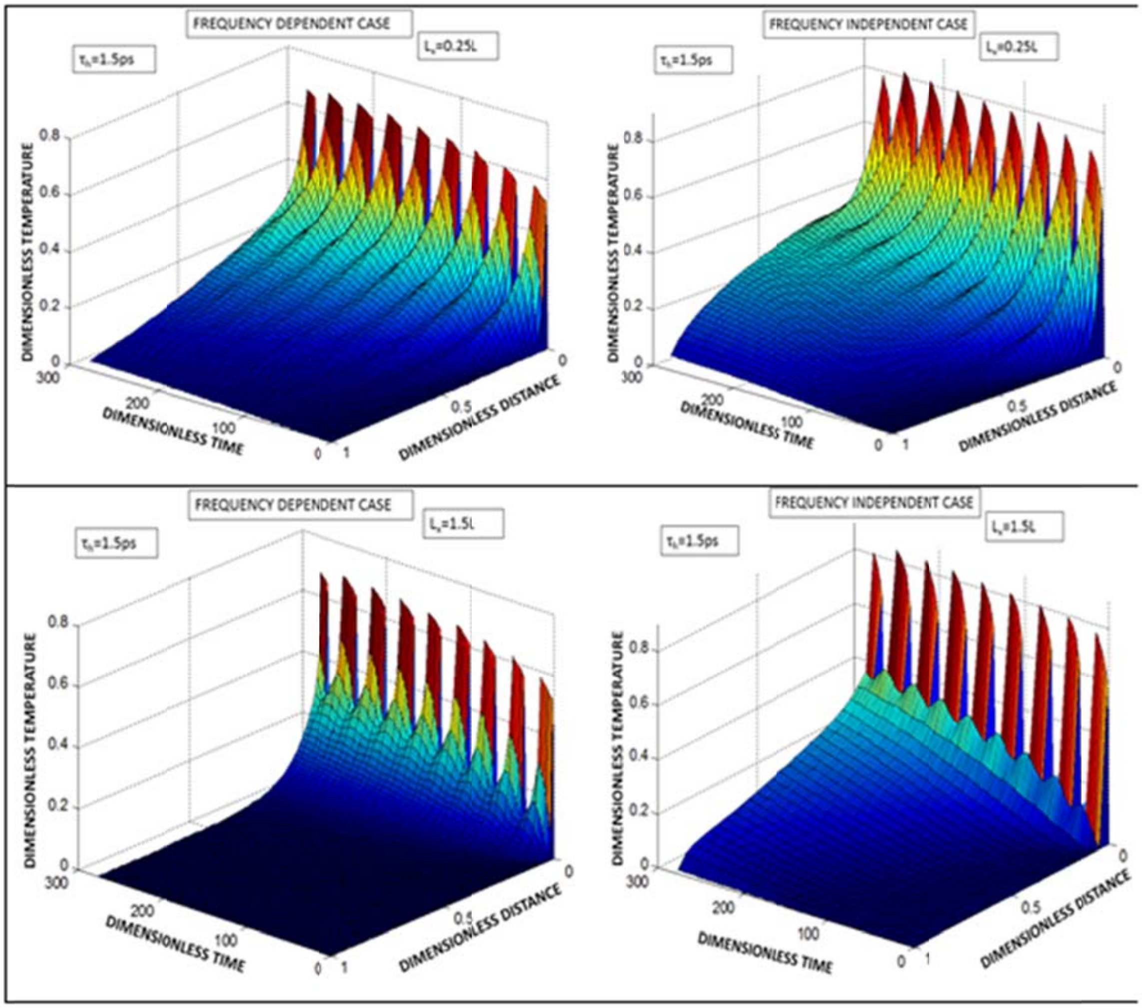

Figure 5.76 Surface plot of dimensionless equivalent equilibrium temperature, in the lattice sub-system for different film thicknesses and frequency dependent and independent solutions of phonon radiative transport equation. $Dimensionless\ Time = t/\tau_d$ where $\tau_d = C_e/G$ and $\tau_d = 8.94\text{x}10^{-14}\ s$.

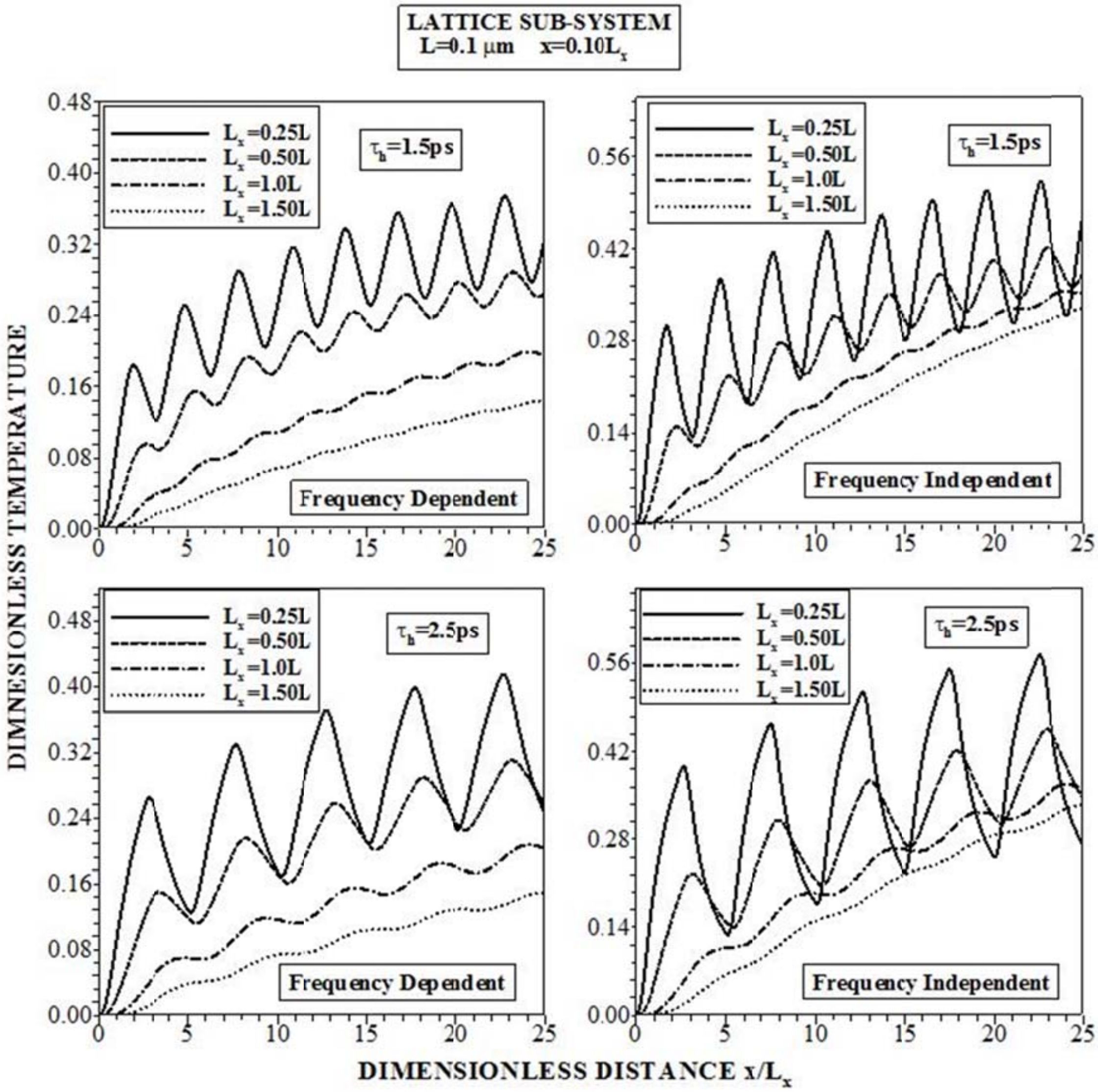

Figure 5.77 Temporal variation of dimensionless equivalent equilibrium in the lattice sub-system for different film thicknesses and frequency dependent and independent solutions of phonon radiative transport equation. Location is x = 0.1Lx, where Lx is the film thickness.

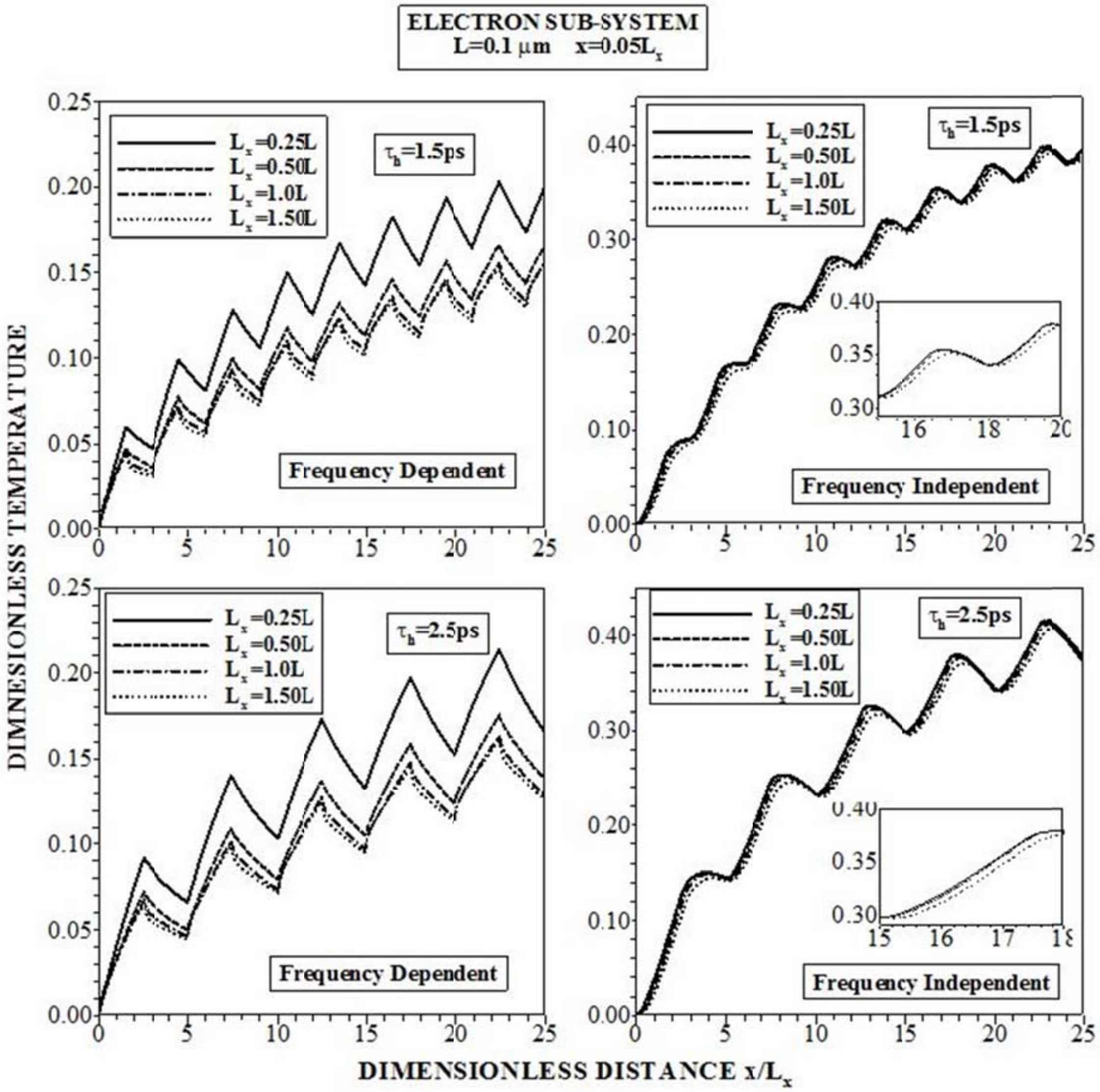

Figure 5.78 Temporal variation of electron temperature in the lattice sub-system for different film thicknesses and frequency dependent and independent solutions of phonon radiative transport equation. Location is x = 0.05Lx, where Lx is the film thickness.

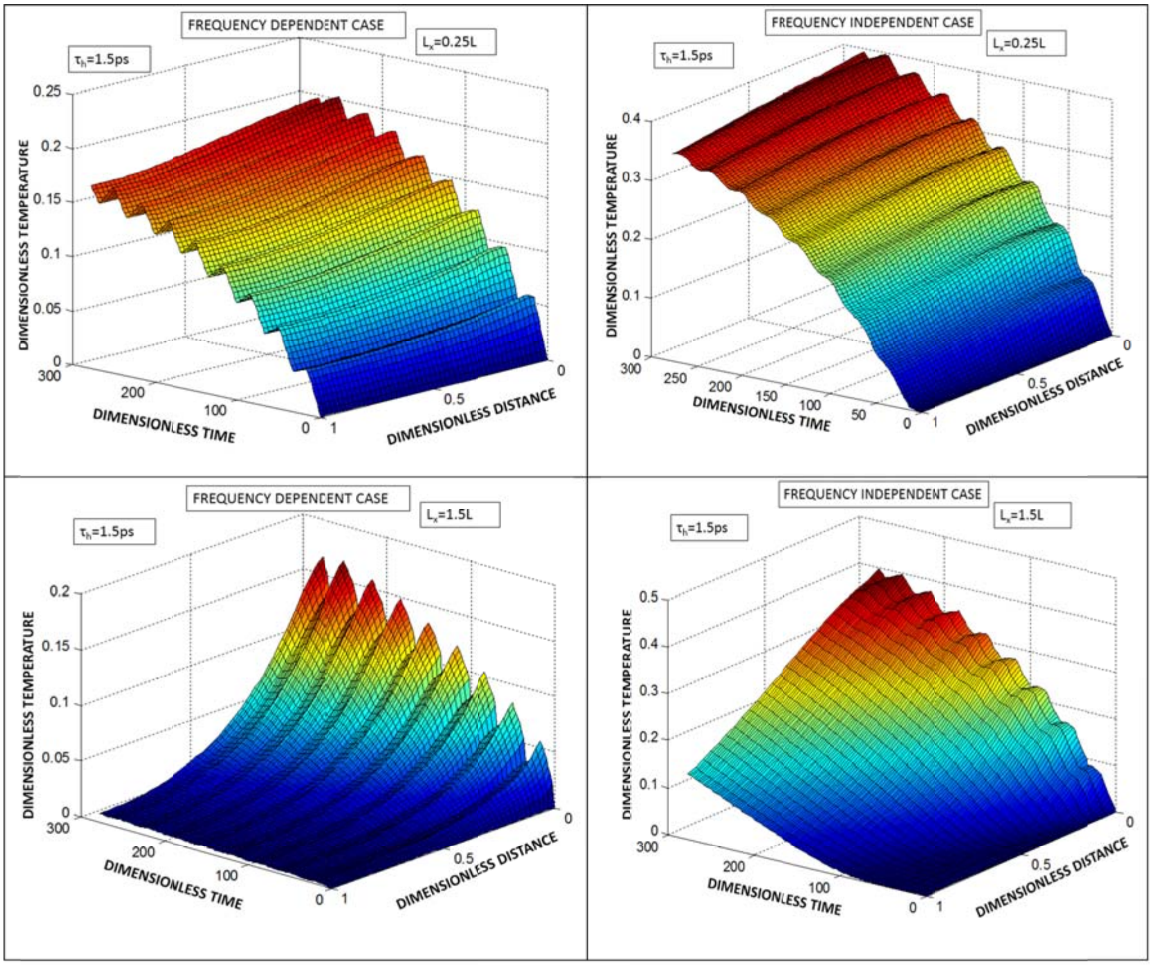

Figure 5.79 Surface plot of dimensionless electron temperature in the lattice sub-system for different film thicknesses and frequency dependent and independent solutions of phonon radiative transport equation $Dimensionless\ Time = t / \tau_d$ where $\tau_d = C_e / G$ and $\tau_d = 8.94\text{x}10^{-14}\ s$.

CHAPTER 6

CONCLUSIONS

This chapter presents the conclusions obtained from of all case studies, introduced and discussed in chapter 3. The conclusions consist of three sub-sections. Section 1 covers the conclusions derived from dimensional dielectric case studies while section 2 and section 3 represent the conclusions of thermal transport in one dimensional dielectric and metallic cases respectively.

6.1 Two Dimensional Dielectric Thin Films

6.1.1 Steady State Heat Transport Including the Effects of Heat Source Size and Silicon Film Dimension

Phonon transport in two-dimensional thin silicon film is considered and the frequency dependent Boltzmann equation is incorporated to formulate the phonon transport in the film. The influence of ballistic phonons on the film resistance is assessed through introducing varying film thickness and heat source size in the analysis. Numerical solution of the Boltzmann equation is presented with the appropriate boundary conditions. To evaluate the phonon resistance, due to scattering in the film, equivalent equilibrium temperature is introduced and the effective thermal conductivity of the film is determined. It is found that the ballistic phonons contributes significantly to the phonon transport in the thinner film $\left(L = 0.1\,\mu m\right)$; in which case, thermal resistance of the film to the phonon transport reduces while lowering the effective thermal conductivity of the film. The size of the heat source influences the distribution of equivalent equilibrium temperature in the film. In this case, small heat source size at the film edge results in attainment of relatively lower peak temperature along the center line of the film than that of the large heat source size. Therefore, the effect of heat source size on the phonon transport is similar to that corresponding to the effect of the film thickness. The coupling effect of the film thickness and the heat source size on the phonon transport is not very significant in the film; in which case, the behavior of effective thermal conductivity with the heat source size becomes similar for both film thicknesses ($L = 0.1\,\mu m$ and $L = 1.0\,\mu m$). Effective thermal conductivity reduces sharply with reducing heat source size; however, this reduction takes place at a lower degree as compared that corresponding to the reduction due to the film thickness.

6.1.2 Transient Heat Transport Including the Effect of Temperature Oscillation in Silicon and Diamond Thin Films

Transient thermal response of thin silicon and diamond films is investigated due to temperature oscillation at the film edge. Frequency dependent Boltzmann equation is solved numerically in two-dimensional thin film. Temperature oscillation (pulsation) is introduced at one edge of the film and the simulation is repeated for different pulse lengths of temperature oscillation. The study is extended to include the silicon and the diamond films. Temperature predictions are validated with the findings of the previous study. It is found that temperature predictions agree well with the previous findings. Time lagging (time difference between the maximum and minimum temperatures, due to temperature oscillation at the film edge, during two consecutive oscillations) occurs in equivalent equilibrium temperature in the near region of the film edge. The frequency of equilibrium equivalent temperature does not match the frequency of temperature oscillation at the film edge, which is more pronounced for the silicon film. In this case, time lagging remains larger than the pulse length of temperature oscillation at the film edge. The amplitude of the time lagging (difference between the maximum and the minimum temperature in equivalent equilibrium temperature during two consecutive oscillations) is small during the early heating period; however, it becomes large in the late heating period. In this case, equivalent equilibrium temperature demonstrates diffusive behavior in the close region of the film as similar to those observed for the diffusive limit. This behavior is associated with the ineffective contribution of the inphase phonons (inphase with the frequency of temperature oscillation at the film edge) to the phonon scattering in the film. As the distance increases along the film width, the amplitude of the time lagging reduces and the influence of temperature oscillation (at the film edge) on equivalent equilibrium temperature becomes negligibly small.

6.1.3 Transient Heat Transport Including the Effects of Pulse Duration of Heat Source in Silicon and Diamond Thin Films

Phonon transport in the silicon and the diamond thin films is considered. The frequency dependent solution of radiative phonon transport equation is presented for two-dimensional film. Temperature oscillation at one edge of the film is incorporated to assess the film thermal response to temperature oscillations. The heating period of temperature oscillation is varied to examine its effects on equivalent equilibrium temperature in the film. The study is extended to include the variation of transport characteristics at different locations in the film when temperature oscillation is introduced at one edge of the film. The numerical method using the discrete ordinate method is introduced to solve the governing phonon transport equation with the appropriate boundary conditions. It is found that equivalent equilibrium temperature rise is rapid in the early heating period, which is more pronounced for the diamond film. Increasing the distance from the high temperature edge slightly alters temperature rise in the film because of the influence of the ballistic phonons, which becomes significant when the distance reduces. Temperature oscillation results in oscillation of equivalent equilibrium temperature in the film. This behavior is observed during the late heating periods, which is more pronounced for the silicon film. Oscillation of equivalent equilibrium temperature does not follow exactly temperature oscillation at the film edge. This is attributed to the out of phase behavior of the film resistance and temperature oscillation at the film edge. The amplitude of equivalent equilibrium temperature oscillation reduces as the film thickness increases. This is mainly associated with the ballistic phonons, which do not contribute to the film resistance through scattering in the film. As the distance from the high temperature edge increases, oscillation of equivalent equilibrium temperature becomes more visible for the diamond film than that corresponding to the silicon film. In this case, increasing temperature pulse $\left(\tau_{cycle}\right)$ amplifies the amplitude of equilibrium equivalent temperature oscillation.

6.1.4 Transient Heat Transport Including the Effects of Thickness and Temperature Oscillation in Diamond Thin Film

Influence of temperature disturbance and film thickness on phonon transport in a diamond film is examined. Transient analysis of phonon transport in a two-dimensional thin film including the frequency dependence is presented. Since the resulting radiative transport equation is in integro-differential form, a numerical scheme employing discrete ordinate method is used to solve the transport equation. High frequency temperature oscillation is applied at one edge of the two-dimensional film while the other edges are kept at low temperature (300 *K*). To assess the phonon transport characteristics, equivalent equilibrium temperature is introduced and its behavior is examined along the film width and the film thickness. The numerical code is modified to validate with the previous results presented in the open literature. It is found that the present predictions agree well with the findings of the previous study. Temperature oscillation at the film edge has significant effect on equivalent equilibrium temperature behavior. This is particularly true for the thin film (Lz = 0.01 μm); in which case, ballistic phonons do not undergo scattering in the film and temperature oscillation at the film edge results in ripples on the temperature curve. The magnitude of ripples reduces as the film width increases. The time shift between the maximum and minimum amplitude of the ripples does not follow the time shift between two consecutive oscillations of temperature at the film edge. This behavior indicates that the damping of temperature oscillation takes place in the film, which is more pronounced with increasing film width. Similar behavior is also observed for the diffusive transport in the films. Temperature jump at the low temperature edge increases as the film thickness reduces, which is attributed to the presence of ballistic phonons. Equivalent equilibrium temperature decays almost linearly along the film width indicating the occurrence of the quasi-steady transport at the earlier periods as compared to those corresponding to larger film width. In this case, temperature decay is sharp in the close region of the high temperature edge and as the distance increases towards the low temperature edge, temperature decay becomes gradual, which is more pronounced for the thick films of $Lz \geq 0.1\mu\text{m}$.

6.1.5 Transient Heat Transport Including the Effects of Heat Source Size and Temperature Oscillation in Silicon Thin Film

Phonon transport in a two-dimensional silicon thin film is considered and transient effects of temperature oscillation, at the high temperature edge of the film, on equilibrium phonon intensity distribution are examined in the film. The frequency dependent of phonon transport is incorporated in the analysis to assess the influence of heat source size, located at the high temperature edge, on the transport characteristic. A numerical solution of the Boltzmann equation is introduced and the discrete ordinate method is incorporated to discretize the governing transport equation with the appropriate boundary conditions. Equivalent equilibrium temperature is accommodated to account for the equilibrium phonon intensity distribution in the film. It is found that equivalent equilibrium temperature rises rapidly in the early heating period, particularly in the near region of the high temperature edge; however, temperature rise becomes gradual as the heating period progresses. This behavior is associated with the scattering of the phonons emitted from the high temperature edge in the film. Although temperature oscillation is considered at the high temperature edge of the film, equivalent equilibrium temperature rises smoothly in the early heating periods in the near region of the high temperature edge. On the other hand, equivalent equilibrium temperature oscillates during the late heating periods in this region. This behavior is attributed to the temporal behavior of equilibrium phonon temperature distribution in the film. As the distance increases towards the mid-section of the film, temperature oscillation diminishes and quasi-steady rise of equivalent equilibrium temperature is observed. Frequency and the amplitude of equivalent equilibrium temperature oscillation do not follow the oscillation characteristics of temperature at the high temperature edge. The maximum value of equivalent equilibrium temperature decreases in the film as the heat source size reduces, which is attributed to quasi-ballistic and ballistic phonons behavior of emitted phonons in the film.

6.1.6 Transient Heat Transport in Silicon and Diamond Thin Films Pair Including the Thermal Boundary Resistance

Phonon transport across the silicon and diamond thin films is investigated incorporating the thermal boundary resistance. Frequency dependent Boltzmann transport equation is solved numerically to predict the phonon intensity distribution in the film pair. Diffusive mismatch and cut-off mismatch models are introduced to model the thermal boundary resistance across the interface of the silicon and diamond thin films. In order to assess the characteristics of the thermal boundary resistance, a transient analysis is of the phonon intensity ratio is introduced for the acoustic longitudinal and acoustic transverse branches of phonon transport. The phonon intensity ratio represents the phonon intensities due to diffusive mismatch model over the phonon intensities due to cut-off mismatch model with in the silicon and diamond films. The cut-off mismatch models relies on the frequency mismatch between the silicon and diamond films for all branches; in which case, phonons having frequencies less than the cut-off frequency can be transmitted to the diamond film across the interface and for those phonons larger frequency can be reflected from the interface towards the silicon film, provided that the emitted, transmitted, and reflected phonons satisfy the energy balance at the interface. It is found that thermal boundary resistance attains low values in the early heating period because of the amount of phonons at the interface, which is small. As the heating time progresses, thermal boundary resistance attains almost steady value. Thermal boundary resistance attains lower values for the diffusive mismatch model than that corresponding to the cut-off mismatch model. This is attributed to the amount of phonons transmitted across the silicon-diamond interface. Since phonons having frequencies less than the cut-off mismatch can possibly transmit to the diamond film, the amount of phonons transmitted across the interface becomes less in the case of cut-off mismatch model. The predictions of thermal boundary resistance using the cut-off mismatch model agrees well with those reported in the open literature. The ratio of the phonon intensity due to cut-off mismatch and diffusive mismatch models remains greater than 1 at the interface for the acoustic branches. The ratio of phonon intensity reduces towards the edges of the interface because of the low temperature boundaries located at the edges of the interface.

6.1.7 Transient Heat Transport Including Quantum Dot in Silicon Thin Film

Transient phonon transport in a two-dimensional silicon film with presence of an aluminum dot is studied. Frequency dependent Boltzmann equation is solved numerically to predict phonon intensity distribution in the film. Exponential temperature variation is assumed at the aluminum interface to observe the temporal response of phonon intensity distribution in the film. To assess the phonon transport characteristics, equivalent equilibrium temperature is introduced in the film. Equivalent equilibrium temperature is defined anywhere in the thin silicon films pair and it corresponds to the average energy of all phonons around a local point, which is equivalent to the equilibrium temperature of phonons when they redistribute adiabatically to an equilibrium state. The computer code developed is verified with the thermal conductivity data presented in the open literature. It is found that thermal conductivity predictions agree well with the data presented in the open literature. Phonon intensity distribution in the close region of the aluminum dot attains high values despite the presence of quasi-ballistic and ballistic phonons in the silicon film. Temporal variation of equivalent equilibrium temperature follows almost temperature distribution at the interface of the aluminum dot. In the early heating period, the rise of equivalent equilibrium temperature is high and as the heating time progresses it becomes gradual, which is more pronounced in the close region of the silicon interface. Temperature jump reduces at the silicon film interface with progressing time. The behavior of equivalent equilibrium temperature provides useful information on the phonon characteristics when the quantum dot is present in the two-dimensional thin silicon film. The present study may guide the researchers to obtain the maximum benefit of the transport characteristics by altering the film or the dot sizes.

6.2 One Dimensional Dielectric Thin Films

6.2.1 Steady State Heat Transport Including the Effect of Film Thickness on Entropy Generation Rate

Phonon transport in silicon thin film is considered and entropy generation is examined because of temperature disturbance at the film edges. The solution of radiative transport equation is presented for frequency depended and frequency independent phonon transport across the thin film. A numerical scheme incorporating the discrete ordinate method is used to simulate the governing equations. The numerical code developed is validated through the results of the previous study. It is found that temperature profile predicted from the numerical code agrees well with its counterpart obtained from the previous study. Entropy generation is high in the region close to the high temperature edge for all the film thicknesses considered in the present study. Entropy generation decreases sharply in the region next to the near region of the high temperature edge and it becomes gradual as the distance increases along the film thickness. This is more pronounced as the film thickness increases. This behavior is associated with the emitted and reflected phonons from the edges of the film; in which case, phonon scattering in the film modifies the phonon intensity distribution and reduces the phonon intensity in the film, especially after certain distance away from the high temperature edge. Frequency dependent consideration of the phonon transport results in less total entropy generation that corresponding to the frequency independent case. This is associated with the ballistic phonons, which are emitted from the edges of the film. In this case, the ballistic phonons do not undergo scattering in the film and do not contribute to the film resistance; therefore, their contribution to energy transport across the film is significant, but entropy generation becomes negligible.

6.2.2 Transient Heat Transport Including the Effect of Gap in between the Films

Phonon transport across thin silicon films pair with presence of gap is examined. To assess the phonon transport characteristics across the gap within the film pair, equivalent equilibrium temperature is introduced. Equivalent equilibrium temperature is defined anywhere in the thin silicon films pair and it corresponds to the average energy of all phonons around a local point, which is equivalent to the equilibrium temperature of phonons when they redistribute adiabatically to an equilibrium state. The transient solution of frequency dependent Boltzmann equation is presented and the phonon intensity distribution in the films pair is predicted numerically in accordance with the relevant boundary conditions. Since the gap size between the films pair is small (Casimir limit), radiative energy transport in between the edges of the films pair across the gap is incorporated together with phonon transmission and reflection at the edges of the gap within the films while satisfying the energy conservation. In order to validate the computer code developed for the phonon transport in the films pair, thermal conductivity data reported in the open literature are predicted. It is found that thermal conductivity data predicted agrees well with the experimental data reported in the open literature. The presence of the gap in between the films pair modifies the phonon transport characteristics significantly. In this case, difference between equivalent equilibrium temperatures across the gap increases with increasing gap size. This behavior is attributed to the amount of phonons transmitted from the first film edge to the second film edge across the gap. The gap size enlargement results in phonon intensity increase at the first film edge. This is because of the consideration that only those phonons having wavelengths larger than the gap size can possibly transmit to the second film interface. This, intern, increases the phonon intensity at the film edge while causing attainment of large values of equivalent equilibrium temperature at the interface. Although increase in temperature at the first film edge results in increased rate of radiation heat transfer from the first film edge to second film edge across the gap, temperature at the second film edge remains low. This is associated with the amount of phonon transmittance from first film edge to the second film edge, which becomes low with increasing gap size.

Consequently, the amount of phonon transmittance to the second film edge has more effect on the temperature difference across the gap than the net radiation heat transfer due to Casimir limit consideration. Thermal conductivity of the films pair $\left(k_{eff}\right)$ reduces with increasing gap size because of small rate of thermal energy transfer to the second film. The thermal conductivity ratios predicted in this study may guide the researchers to obtain the maximum benefit by altering the gap size.

6.3 One Dimensional Metallic Thin Films

6.3.1 Transient Heat Transport in Aluminum Thin Films

Phonon transport in the aluminum thin film is investigated due to temperature disturbance at the film edges and the energy equation incorporating the radiative phonon transport is introduced in the analysis. Transient and the frequency dependent solution of the radiative phonon transport is considered in the lattice system and the grey body assumption is employed in the electron sub-system to formulate the governing energy equations. The frequency independent solution of the radiative transport equation is also incorporated to compare the energy transfer in the thin film. Equivalent equilibrium temperature is introduced to assess the transport characteristics of the film. The solution of two-equation model is accommodated to compare the steady state solution of the frequency dependent and the independent solutions of the radiative transport equation. The numerical code developed is validated trough the temperature data presented in the previous study. It is found that the findings of the numerical code agree well with the previous results obtained for temperature distribution in the thin film. Equivalent equilibrium temperature predicted from the solution of the radiative phonon transport does not agree with its counterpart obtained from the two-equation model. Temperature predictions from the frequency dependent solution of the transport equation are lower than that corresponding to the frequency independent case. This behavior is attributed to the effect of the ballistic phonons on the phonon transport characteristics; in which case, ballistic phonons do not undergo scattering in the film and their effect on the phonon intensity distribution is negligible. Increasing film thickness alters temperature distribution in the lattice sub-system. Since electron energy in the electron sub-system depends on the energy transfer from the lattice sub-system through electron-phonon coupling, phonon intensity significantly influences electron temperature distribution in the film. Equivalent equilibrium temperature increases rapidly in the region close to the high temperature edge of the film during the early heating period and as the time progresses, temperature increase becomes gradual. The attainment of the quasi-steady temperature in the film takes place earlier for the thin film $\left(Lx = 0.25L\right)$ as compared to the thick film $\left(Lx = 2L\right)$. Thermal conductivity predicted from the frequency dependent solution of the radiative transport equation is less than that corresponding to the frequency independent case. In this case, ballistic phonons do not contribute to the film resistance while lowering the film thermal conductivity. Consequently, transport characteristics of the aluminum thin film depends on the phonon characteristics in the film; in which case, radiative phonon transport incorporating the frequency dependent solution provides the useful information.

6.3.2 Transient Heat Transport Including the Effect of Thermal Oscillation in Aluminum Thin Film

Energy transport, due to temperature disturbance at the film edges, is examined in a thin aluminum film. Temperature oscillation is considered at the film edge and the thermal response of the film resistance is predicted for various periods of temperature oscillation. Since thermal separation between the electron and the lattice sub-systems takes place in the film, temporal response of temperature in both sub-systems is analyzed. The frequency dependent and frequency independent solutions of phonon radiative transport equation are obtained numerically and resulting phonon intensity distribution is assessed through behavior of equivalent equilibrium temperature in the film. The dispersion relations are incorporated in the frequency dependent solution of phonon radiative transport equation. The behavior of equivalent equilibrium temperature in the lattice sub-system obtained from the solution of phonon transport equation and the two-equation model is compared for the steady state heating situation across the film thickness. It is found that the behavior of phonon temperature obtained from the frequency independent solution of phonon transport equation and the two-equation model are closer than that corresponding to frequency dependent solution of phonon transport equation, which is more pronounced for small film thickness Lx=0.25L, where L=0.1µm. This behavior is associated with the effect of quasi-ballistic and ballistic phonons on the transport characteristics; in which case, phonon temperature rise in the film reduces considerably for thin films. The differences in phonon temperature due to different models become small with increasing film thickness. Temperature oscillation at the edge of the film results in similar temperature oscillation in the electron and the lattice sub-systems. This is more pronounced at the location close to the high temperature edge. The amplitude and period of temperature oscillation do not follow those corresponding to oscillation at the high temperature edge of the film. This behavior is associated with the re-distribution of equilibrium phonon intensity after phonon scattering in this region. As the period of temperature oscillation increases at the film edge, the magnitude of equivalent equilibrium temperature oscillation increases; however, as the location changes away from the high temperature edge, the magnitude of temperature oscillation in the film reduces. Electron temperature behaves similar to phonon temperature in the film. Electron temperature corresponding to frequency dependent of phonon radiative transport equation attains lower values than that of frequency independent case in the film.

6.3.3 Transient Heat Transport Including the Effects of Thermal Oscillation and Film Thickness in Aluminum Thin Film

Energy transfer in an aluminum thin film is considered due to temperature disturbance at the film edges. Temperature oscillation is introduced at high temperature edge of the film and thermal response of the film is examined accordingly. Transient frequency dependent and independent solutions of phonon radiative transport equation are obtained numerically for various film thicknesses. Two different heating periods of temperature oscillation are incorporated in the simulations. Since the relaxation time of electron sub-system is short and dispersion relations do not exist, frequency independent form of phonon radiative transport equation is adopted to formulate temperature rise in the electron sub-system. Electron-phonon coupling is incorporated in the energy equation to account for thermal communications of the electron and the lattice sub-systems during the energy transport. Equivalent equilibrium temperature is introduced to assess phonon characteristics in the film. Dispersion relations are used to formulate phonon transport in the lattice sub-system of the aluminum film for the frequency dependent solution of phonon radiative transport equation. It is found that temperature pulsation at high temperature edge of the film results in similar pulsation in the region close to the high temperature edge of the film. This is more pronounced as the film thickness reduces; however, period and amplitude of oscillation of equivalent equilibrium temperature differ from that of temperature oscillation at the film edge. Ballistic and quasi-ballistic phonons influence temperature distribution in the film. In this case, frequency dependent solution of phonon radiative transport equation results in lower temperatures in the lattice sub-system as compared to those corresponding to frequency independent solution. Temperature in the electron sub-system highly depends on temperature distribution in the lattice sub-system because of the energy exchange through the electron-phonon coupling parameter. Temperature oscillation in the electron sub-system is different than temperature oscillation in the lattice sub-system.

6.4 Future Work

In this dissertation, investigation of energy transport characteristics in dielectric and metallic thin films are carried out for different heating situations and boundary condition. The following topics are suggested for the future study of the current work covering micro and nano-scale heat transport.

- The energy transport charateristics in various films geometery Including a triangular geometry.
- The EPRT can be incorporated to investigate the energy transport characteristics inside the quantum dot.
- The effect of minute gap located in between dielectric and metallic thin film pair, on thermal transport characteristics can be investigated.
- Frequency dependent EPRT can be extended to include the two dimensional metallic films.

REFERENCES

[1] L. Wang, “Generalized Fourier law,” *Int. J. Heat Mass Transf.*, vol. 37, no. 17, pp. 2627–2634, 1994.

[2] G. Atefi, A. Bahrami, and M. R. Talaee, “Analytical solution of dual phase lagging heat conduction in a hollow sphere with time-dependent heat flux,” *New Asp. Fluid Mech. Heat Transf. Environ.*, vol. 1, pp. 114–126, 2010.

[3] A. Majumdar, “Microscale heat conduction in dielectric thin films,” *J. Heat Transf.*, vol. 115, no. 1, pp. 7–16, 1993.

[4] J.-P. Mulet, K. Joulain, R. Carminati, and J.-J. Greffet, “Enhanced radiative heat transfer at nanometric distances,” *Microscale Thermophys. Eng.*, vol. 6, no. 3, pp. 209–222, 2002.

[5] C. J. Fu and Z. M. Zhang, “Nanoscale radiation heat transfer for silicon at different doping levels,” *Int. J. Heat Mass Transf.*, vol. 49, no. 9–10, pp. 1703–1718, May 2006.

[6] G. Chen, *Nanoscale Energy Transport and Conversion*. Oxford University Press, 2005.

[7] C. V. D. R. Anderson, “Thermal Heat Transport Characterization for Macroscale, Microscale, and Nanoscale Heat Conduction,” The University of Minnesota, 2008.

[8] D. Y. Tzou, “Thermal shock phenomena under high-rate response in solids,” *Annu. Rev. Heat Transf.*, vol. 4, pp. 111–185, 1992.

[9] C. Cattaneo, “A form of heat conduction equation which eliminates the paradox of instantaneous propagation,” *Compte Rendus*, vol. 247, pp. 431–433, 1958.

[10] P. Vernotte, “Les paradoxes de la theorie continue de l’equation de la chaleur,” *Compte Rendus*, vol. 246, pp. 3154–3155, 1958.

[11] D. Y. Tzou, “Unified field approach for heat conduction from macro- to micro-scales,” *J. Heat Transfer*, vol. 117, no. 1, pp. 8–16, 1995.

[12] T.-W. Tsai, Y.-M. Lee, and Y.-H. Liao, “Analysis of microscale heat transfer and ultrafast thermoelasticity in a multi-layered metal film,” in *Proceedings of the ASME Summer Heat Transfer Conference 2009, HT2009*, 2009, vol. 2, pp. 87–95.

[13] B. S. Yilbas, “Validity of Fourier theory of radiation heating of metals,” *Res Mech.*, vol. 24, no. 4, pp. 377–382, 1988.

[14] B. S. Yilbas, “Heating of metals at a free surface by laser irradiation an electron kinetic theory approach,” *Int. J. Engng Sci.*, vol. 24, no. 8, pp. 1325–1334, 1986.

[15] B. S. Yilbas, “Electron kinetic theory approach - one- and three-dimensional heating with pulsed laser,” *Int. J. Heat Mass Transf.*, vol. 44, no. 10, pp. 1925–1936, 2001.

[16] B. S. Yilbas, “Improved formulation of electron kinetic theory approach for laser ultra-short-pulse heating,” *Int. J. Heat Mass Transf.*, vol. 49, no. 13–14, pp. 2227–2238, 2006.

[17] B. S. Yilbas, “Electron kinetic theory approach for picosecond laser pulse heating,” *Numer. Heat Transf. Part A Appl.*, vol. 39, no. 8, pp. 823–845, 2001.

[18] L. De Broglie, “Recherches sur la Theorie des Quanta,” *Ann. Phys. (Paris).*, vol. 3, 1925.

[19] E. Schrödinger, “Quantisation as a Problem of Characteristic Values,” *Ann. Phys.*, vol. 79, pp. 361–376,489–529, 1926.

[20] R. K. Kawakami, E. Rotenberg, H. J. Choi, E. J. Escorcia-Aparicio, M. O. Bowen, J. H. Wolfe, E. Arenholz, Z. D. Zhang, N. V. Smith, and Z. Q. Qiu, “Quantum-well states in copper thin films,” vol. 398, no. 6723, pp. 132–134, Mar. 1999.

[21] R. L. Liboff, *Kinetic Theory*, 2nd ed. New York: Willey, 1998.

[22] D. Y. Tzou, “Lagging behavior in ultrafast laser heating,” in *American Society of Mechanical Engineers, Heat Transfer Division*, 1995, vol. 304, no. 2, p. 139.

[23] M. Chen, J. M. Nash, and C. E. Patton, “A numerical study of nonlinear Schrödinger equation solutions for microwave solitons in magnetic thin films,” *J. Appl. Phys.*, vol. 73, no. 8, p. 3906, Apr. 1993.

[24] H. Wong and V. A. Gritsenko, “Defects in silicon oxynitride gate dielectric films,” *Microelectron. Reliab.*, vol. 42, no. 4–5, pp. 597–605, Apr. 2002.

[25] D. G. Cahill, W. K. Ford, K. E. Goodson, G. D. Mahan, A. Majumdar, H. J. Maris, R. Merlin, and S. R. Phillpot, “Nanoscale thermal transport,” *J. Appl. Phys.*, vol. 93, no. 2, p. 793, Dec. 2003.

[26] S. Bin Mansoor, “Absorption of Light Waves and Energy Transport in Thin Silicon Film in Relation to Photovoltaic Applications,” KFUPM, 2010.

[27] J. M. Ziman, *Electrons and Phonons: The Theory of Transport Phenomena in Solids*. London: Oxford University Press, 1960.

[28] Y. Joshi, M. Tiwari, and G. Verma, “Role of Four-Phonon Processes in the Lattice Thermal Conductivity of Silicon from 300 to 1300°K,” *Phys. Rev. B*, vol. 1, no. 2, pp. 642–646, Jan. 1970.

[29] L. D. Landau and E. M. Lifshitz, *Quantum mechanics*. Pergamon, 1977.

[30] C. Kittel, *Introduction to Solid State Physics*, 6th ed. Willey, 1986.

[31] W. G. Vincenti, *Introduction to Physical Gas Dynamics*. Florida: Robert E. Krieger, 1966.

[32] M. G. Holland, “Analysis of lattice thermal conductivity,” *Physical Review*, vol. 132, no. 6. pp. 2461–2471, 1963.

[33] S. Bin Mansoor and B. S. Yilbas, “Phonon radiative transport in silicon–aluminum thin films: Frequency dependent case,” *Int. J. Therm. Sci.*, vol. 57, pp. 54–62, Jul. 2012.

[34] G. Chen, “Heat transport in the perpendicular direction of superlattices and periodic thin-film structures,” *Am. Soc. Mech. Eng. Dyn. Syst. Control Div. DSC*, vol. 59, pp. 13–24, 1996.

[35] B. S. Yilbas, a. Y. Al-Dweik, and S. Bin Mansour, “Analytical solution of hyperbolic heat conduction equation in relation to laser short-pulse heating,” *Phys. B Condens. Matter*, vol. 406, no. 8, pp. 1550–1555, Apr. 2011.

[36] D. L. Nika and A. a Balandin, “Two-dimensional phonon transport in graphene.,” *J. Phys. Condens. Matter*, vol. 24, no. 23, Jun. 2012.

[37] C. Jeong, S. Datta, and M. Lundstrom, “Thermal conductivity of bulk and thin-film silicon: A Landauer approach,” *J. Appl. Phys.*, vol. 111, no. 9, 2012.

[38] Y. Ju and G. Cha, “Impact of micro/nanoscale heat transfer in silicon substrates on thermal interface resistance characterization,” in *ASME International Mechanical Engineering Congress and Exposition, Proceedings*, 2009, vol. 13, no. PART B, pp. 1277–1281.

[39] D. Donadio and G. Galli, “Temperature dependence of the thermal conductivity of thin silicon nanowires.,” *Nano Lett.*, vol. 10, no. 3, pp. 847–51, Mar. 2010.

[40] Q. Hao, G. Chen, and M.-S. Jeng, “Frequency-dependent Monte Carlo simulations of phonon transport in two-dimensional porous silicon with aligned pores,” *J. Appl. Phys.*, vol. 106, no. 11, 2009.

[41] B. T. Wong, M. Francoeur, and M. Pinar Mengüç, “A Monte Carlo simulation for phonon transport within silicon structures at nanoscales with heat generation,” *Int. J. Heat Mass Transf.*, vol. 54, no. 9–10, pp. 1825–1838, Apr. 2011.

[42] C. Dames, B. Poudel, W. Z. Wang, J. Y. Huang, Z. F. Ren, Y. Sun, J. I. Oh, C. Opeil, M. J. Naughton, and G. Chen, “Low-dimensional phonon specific heat of titanium dioxide nanotubes,” *Appl. Phys. Lett.*, vol. 87, no. 3, p. 031901, 2005.

[43] G. Chen and M. Neagu, “Thermal conductivity and heat transfer in superlattices,” *Appl. Phys. Lett.*, vol. 71, no. 19, p. 2761, 1997.

[44] J. Xu, Y. Gan, D. Zhang, and X. Li, “Microscale boiling heat transfer in a micro-timescale at high heat fluxes,” *J. Micromechanics Microengineering*, vol. 15, no. 2, pp. 362–376, Feb. 2005.

[45] M. Avci and O. Aydin, “Second-law analysis of heat and fluid flow in microscale geometries,” *Int. J. Exergy*, vol. 4, no. 3, p. 286, 2007.

[46] H. Chu, S. Lin, and C. Lin, “Non-Fourier heat conduction with radiation in an absorbing , emitting , and isotropically scattering medium,” vol. 73, pp. 571–582, 2002.

[47] S. Pisipati, C. Chen, J. Geer, B. Sammakia, and B. T. Murray, “Multiscale thermal device modeling using diffusion in the Boltzmann Transport Equation,” *Int. J. Heat Mass Transf.*, vol. 64, pp. 286–303, Sep. 2013.

[48] G. Chen, “Nanoscale Heat Transfer and Nanostructured Thermoelectrics,” *IEEE Trans. Components Packag. Technol.*, vol. 29, no. 2, pp. 238–246, 2006.

[49] H. Xiang, P.-X. Jiang, and Q.-X. Liu, “Non-equilibrium molecular dynamics study of nanoscale thermal contact resistance,” *Mol. Simul.*, vol. 34, no. 7, pp. 679–687, 2008.

[50] Y. Bayazitoglu and G. Tunc, “Extended Slip Boundary Conditions for Microscale Heat Transfer,” *J. Thermophys. Heat Transf.*, vol. 16, no. 3, pp. 472–475, Jul. 2002.

[51] B. S. Yilbas and S. Bin Mansoor, “Phonon transport in two-dimensional silicon thin film: influence of film width and boundary conditions on temperature distribution,” *Eur. Phys. J. B*, vol. 85, no. 7, p. 243, Jul. 2012.

[52] A. Lervik, F. Bresme, and S. Kjelstrup, “Heat transfer in soft nanoscale interfaces: the influence of interface curvature,” *Soft Matter*, vol. 5, no. 12, p. 2407, 2009.

[53] S. Srinivasan, R. S. Miller, and E. Marotta, “Parallel computation of the Boltzmann transport equation for microscale heat transfer in multilayered thin films,” *Numer. Heat Transf. Part B Fundam.*, vol. 46, no. 1, pp. 31–58, Jul. 2004.

[54] S. Shen, A. Narayanaswamy, and G. Chen, “Surface phonon polaritons mediated energy transfer between nanoscale gaps.,” *Nano Lett.*, vol. 9, no. 8, pp. 2909–13, Aug. 2009.

[55] S. Lefèvre, S. Volz, and P.-O. Chapuis, “Nanoscale heat transfer at contact between a hot tip and a substrate,” *Int. J. Heat Mass Transf.*, vol. 49, no. 1–2, pp. 251–258, Jan. 2006.

[56] B. S. Yilbas and S. Bin Mansoor, “Phonon Transport in Thin Film: Ballistic Phonon Contribution to Energy Transport,” *Numer. Heat Transf. Part A Appl.*, vol. 64, no. 10, pp. 800–819, Nov. 2013.

[57] M. Bunzendahl, X. Y. Yu, G. Chen, and P. Hui, “Thermal diffusivity of free-standing diamond thin-film,” in *American Society of Mechanical Engineers, Heat Transfer Division, (Publication) HTD*, 1996, vol. 323, no. 1, pp. 131–135.

[58] X. W. Wang, H. Lee, Y. C. Lan, G. H. Zhu, G. Joshi, D. Z. Wang, J. Yang, a. J. Muto, M. Y. Tang, J. Klatsky, S. Song, M. S. Dresselhaus, G. Chen, and Z. F. Ren, “Enhanced thermoelectric figure of merit in nanostructured n-type silicon germanium bulk alloy,” *Appl. Phys. Lett.*, vol. 93, no. 19, p. 193121, 2008.

[59] F.-C. Chou, J. R. Lukes, and C.-L. Tien, “Heat transfer enhancement by fins in the microscale regime,” in *ASME International Mechanical Engineering Congress and Exposition*, 1998, pp. 165–172.

[60] G. Balasubramanian, S. Banerjee, and I. K. Puri, “Interfacial thermal resistance in nanoscale heat transfer,” in *ASME International Mechanical Engineering Congress and Exposition, Proceedings*, 2009, vol. 10, no. PART B, pp. 969–973.

[61] T. Kalisik and P. Majumdar, “A thermal conductivity model for micro-nanoscale,” *IEEE Trans. Components Packag. Technol.*, vol. 30, no. 4, pp. 1199–1207, 2006.

[62] C. Fu and Z. M. Zhang, “Prediction of nanoscale radiative heat transfer between silicon and silicon or another material,” in *Proceedings of the ASME Heat Transfer/Fluids Engineering Summer Conference 2004, HT/FED 2004*, 2004, vol. 4, pp. 381–385.

[63] C. L. Tien and G. Chen, “Challenges in Microscale Conductive and Radiative Heat Transfer,” *J. Heat Transfer*, vol. 116, no. 4, pp. 799–807, Nov. 1994.

[64] B. S. Yilbas and S. Bin Mansoor, “Phonon transport and equivalent equilibrium temperature in thin silicon films,” *J. Non-Equilibrium Thermodyn.*, vol. 38, no. 2, pp. 153–174, 2013.

[65] A. Majumdar, “Microscale heat conduction in dielectric thin films,” in *American Society of Mechanical Engineers, Heat Transfer Division.Thin-Film Heat Transfer - Properties and Processing, Winter Annual Meeting of the American Society of Mechanical Engineers*, 1991, pp. 33–42.

[66] J. W. Gao, R. T. Zheng, H. Ohtani, D. S. Zhu, and G. Chen, “Experimental investigation of heat conduction mechanisms in nanofluids. Clue on clustering.,” *Nano Lett.*, vol. 9, no. 12, pp. 4128–32, Dec. 2009.

[67] S. Bin Mansoor and B. S. Yilbas, “Phonon transport in silicon–silicon and silicon–diamond thin films: Consideration of thermal boundary resistance at interface,” *Phys. B Condens. Matter*, vol. 406, no. 11, pp. 2186–2195, May 2011.

[68] a. McGaughey and M. Kaviany, “Quantitative validation of the Boltzmann transport equation phonon thermal conductivity model under the single-mode relaxation time approximation,” *Phys. Rev. B*, vol. 69, no. 9, p. 094303, Mar. 2004.

[69] W. Dai and R. Nassar, “A compact finite-differnce scheme for solving a one-dimensional heat transport equation at the microscale,” *J. Comput. Appl. Math.*, vol. 132, pp. 431–441, 2001.

[70] S. V. J. Narumanchi, J. Y. Murthy, and C. H. Amon, “Submicron Heat Transport Model in Silicon Accounting for Phonon Dispersion and Polarization,” *J. Heat Transfer*, vol. 126, no. 6, p. 946, 2004.

[71] B. S. Yilbas and S. Bin Mansoor, “Logistic characteristics of phonon transport in silicon thin film: the S-curve,” *Phys. B Condens. Matter*, vol. 426, pp. 79–84, Oct. 2013.

[72] A. A. Joshi and A. Majumdar, “Transient ballistic and diffusive phonon heat transport in thin films,” *J. Appl. Phys.*, vol. 74, no. 1, p. 31, 1993.

[73] J. Che, T. Çağın, W. Deng, and W. a. Goddard, “Thermal conductivity of diamond and related materials from molecular dynamics simulations,” *J. Chem. Phys.*, vol. 113, no. 16, p. 6888, 2000.

[74] Y. S. Ju, “Phonon heat transport in silicon nanostructures,” *Appl. Phys. Lett.*, vol. 87, no. 15, p. 153106, 2005.

[75] S. V. J. Narumanchi, J. Y. Murthy, and C. H. Amon, “Comparison of Different Phonon Transport Models for Predicting Heat Conduction in Silicon-on-Insulator Transistors,” *J. Heat Transfer*, vol. 127, no. 7, p. 713, 2005.

[76] R. a. Escobar and C. H. Amon, “Influence of Phonon Dispersion on Transient Thermal Response of Silicon-on-Insulator Transistors Under Self-Heating Conditions,” *J. Heat Transfer*, vol. 129, no. 7, p. 790, 2007.

[77] M. Rashidi-Huyeh, S. Volz, and B. Palpant, “Non-Fourier heat transport in metal-dielectric core-shell nanoparticles under ultrafast laser pulse excitation,” *Phys. Rev. B*, vol. 78, no. 12, p. 125408, Sep. 2008.

[78] Y. Chen, M. Chu, L. Wang, X. Bao, Y. Lin, and J. Shen, “First-principles study on the structural, phonon, and thermodynamic properties of the ternary carbides in Ti-Al-C system,” *Phys. Status Solidi*, vol. 208, no. 8, pp. 1879–1884, Aug. 2011.

[79] K. Etessam-yazdani, S. Member, Y. Yang, and M. Asheghi, “Ballistic Phonon Transport and Self-Heating Effects in Strained-Silicon Transistors,” vol. 29, no. 2, pp. 254–260, 2006.

[80] B. A. Shakouri, “Nanoscale Thermal Transport and Microrefrigerators on a Chip,” in *Proceedings of the IEEE*, 2006, pp. 1613 – 1638.

[81] B. Thouy, J. P. Mazellier, J. C. Barbé, and G. Le Carval, “Phonon Transport in Electronic Devices : From Diffusive to Ballistic Regime,” in *Simulation of Semiconductor Processes and Devices, 2008. SISPAD*, 2008, no. 4, pp. 7–10.

[82] M. Asheghi, K. Kurabayashi, R. Kasnavi, and K. E. Goodson, "Thermal conduction in doped single-crystal silicon films," *J. Appl. Phys.*, vol. 91, no. 8, p. 5079, 2002.

[83] S. Sinha and K. E. Goodson, "Review : Multiscale Thermal Modeling in Nanoelectronics," *Int. J. Multiscale Comput. Eng.*, vol. 3, no. 1, pp. 107–133, 2005.

[84] R. Alkhairy, "Green ' s Function Solution for the Dual-Phase-Lag Heat Equation," *Appl. Math.*, vol. 2012, no. October, pp. 1170–1178, 2012.

[85] J. a. Pascual-Gutiérrez, J. Y. Murthy, and R. Viskanta, "Thermal conductivity and phonon transport properties of silicon using perturbation theory and the environment-dependent interatomic potential," *J. Appl. Phys.*, vol. 106, no. 6, p. 063532, 2009.

[86] H. Karamitaheri, N. Neophytou, and H. Kosina, "Ballistic phonon transport in ultra-thin silicon layers: Effects of confinement and orientation," *J. Appl. Phys.*, vol. 113, no. 20, p. 204305, 2013.

[87] T. W. Brown and E. Hensel, "Statistical phonon transport model for multiscale simulation of thermal transport in silicon: Part I – Presentation of the model," *Int. J. Heat Mass Transf.*, vol. 55, no. 25–26, pp. 7444–7452, Dec. 2012.

[88] T. W. Brown and E. Hensel, "Statistical phonon transport model for multiscale simulation of thermal transport in silicon: Part II – Model verification and validation," *Int. J. Heat Mass Transf.*, vol. 55, no. 25–26, pp. 7453–7459, Dec. 2012.

[89] T. Yamada, S. Hamian, B. Sundén, K. Park, and M. Faghri, "Diffusive-ballistic heat transport in thin films using energy conserving dissipative particle dynamics," *Int. J. Heat Mass Transf.*, vol. 61, pp. 287–292, Jun. 2013.

[90] B. S. Yilbas and S. Bin Mansoor, "Transient Effects of Phonon Transport in Two-Dimensional Silicon Film," *Numer. Heat Transf. Part A Appl.*, vol. 62, no. 9, pp. 742–760, Nov. 2012.

[91] I. I. Kuleyev, I. G. Kuleyev, S. M. Bakharev, and a. V. Inyushkin, "Features of phonon transport in silicon rods and thin plates in the boundary scattering regime. The effect of phonon focusing at low temperatures," *Phys. B Condens. Matter*, vol. 416, pp. 81–87, May 2013.

[92] L.-C. Liu and M.-J. Huang, “Thermal conductivity modeling of micro- and nanoporous silicon,” *Int. J. Therm. Sci.*, vol. 49, no. 9, pp. 1547–1554, Sep. 2010.

[93] A. Pattamatta, “Modeling thermal resistance in carbon nanotube contacts,” *Int. J. Therm. Sci.*, vol. 49, no. 9, pp. 1485–1492, Sep. 2010.

[94] T. C. Clancy, S. J. V. Frankland, J. a. Hinkley, and T. S. Gates, “Multiscale modeling of thermal conductivity of polymer/carbon nanocomposites,” *Int. J. Therm. Sci.*, vol. 49, no. 9, pp. 1555–1560, Sep. 2010.

[95] T. T. Lam and E. Fong, “Heat diffusion vs. wave propagation in solids subjected to exponentially-decaying heat source: Analytical solution,” *Int. J. Therm. Sci.*, vol. 50, no. 11, pp. 2104–2116, Nov. 2011.

[96] N. Donmezer and S. Graham, “A multiscale thermal modeling approach for ballistic and diffusive heat transport in two dimensional domains,” *Int. J. Therm. Sci.*, vol. 76, pp. 235–244, Feb. 2014.

[97] H.-F. Lee, S. Kumar, and M. a. Haque, “Role of mechanical strain on thermal conductivity of nanoscale aluminum films,” *Acta Mater.*, vol. 58, no. 20, pp. 6619–6627, Dec. 2010.

[98] H. S. Sim, S. H. Lee, and K. G. Kang, “Femtosecond pulse laser interactions with thin silicon films and crater formation considering optical phonons and wave interference,” *Microsyst. Technol.*, vol. 14, no. 9–11, pp. 1439–1446, Jan. 2008.

[99] W. Ma, H. Wang, X. Zhang, and W. Wang, “Study of the Electron–Phonon Relaxation in Thin Metal Films Using Transient Thermoreflectance Technique,” *Int. J. Thermophys.*, vol. 34, no. 12, pp. 2400–2415, Aug. 2011.

[100] M. Xu and Q. Cheng, “Temperature Enhancement Through Interaction of Thermal Waves for Phonon Transport in Silicon Thin Films,” *Int. J. Thermophys.*, vol. 34, no. 2, pp. 306–321, Feb. 2013.

[101] L. Cheng, M. Xu, and L. Wang, “From Boltzmann transport equation to single-phase-lagging heat conduction,” *Int. J. Heat Mass Transf.*, vol. 51, no. 25–26, pp. 6018–6023, Dec. 2008.

[102] M. Xu and L. Wang, “Dual-phase-lagging heat conduction based on Boltzmann transport equation,” *Int. J. Heat Mass Transf.*, vol. 48, no. 25–26, pp. 5616–5624, Dec. 2005.

[103] J. Fang and L. Pilon, “Scaling laws for thermal conductivity of crystalline nanoporous silicon based on molecular dynamics simulations,” *J. Appl. Phys.*, vol. 110, no. 6, p. 064305, 2011.

[104] T. Wang, “Solution of the phonon boltzmann transport equation employing rigorous implementation of phonon conservation rules,” in *ASME 2006 International Mechanical Engineering Congress and Exposition*, 2006, pp. 1–9.

[105] C. Hua and A. J. Minnich, “Transport regimes in quasiballistic heat conduction,” *Phys. Rev. B*, vol. 89, no. 9, p. 094302, Mar. 2014.

[106] D. P. Sellan, J. E. Turney, a. J. H. McGaughey, and C. H. Amon, “Cross-plane phonon transport in thin films,” *J. Appl. Phys.*, vol. 108, no. 11, p. 113524, 2010.

[107] J. E. Turney, a. J. H. McGaughey, and C. H. Amon, “In-plane phonon transport in thin films,” *J. Appl. Phys.*, vol. 107, no. 2, p. 024317, 2010.

[108] A. J. Minnich, G. Chen, S. Mansoor, and B. S. Yilbas, “Quasiballistic heat transfer studied using the frequency-dependent Boltzmann transport equation,” *Phys. Rev. B*, vol. 84, no. 23, p. 235207, Dec. 2011.

[109] B. T. Wong, M. Francoeur, V. N.-S. Bong, and M. P. Mengüç, “Coupling of near-field thermal radiative heating and phonon Monte Carlo simulation: Assessment of temperature gradient in n-doped silicon thin film,” *J. Quant. Spectrosc. Radiat. Transf.*, vol. 143, pp. 46–55, Aug. 2014.

[110] A. Bulusu and D. G. Walker, “One-dimensional thin-film phonon transport with generation,” *Microelectronics J.*, vol. 39, no. 7, pp. 950–956, 2008.

[111] Z. L. Wang, H. T. Mu, J. G. Liang, and D. W. Tang, “Thermal boundary resistance and temperature dependent phonon conduction in CNT array multilayer structure,” *Int. J. Therm. Sci.*, vol. 74, pp. 53–62, Dec. 2013.

[112] R. Guo and B. Huang, “Thermal transport in nanoporous Si: Anisotropy and junction effects,” *Int. J. Heat Mass Transf.*, vol. 77, pp. 131–139, Oct. 2014.

[113] R. Prasher, “Thermal boundary resistance of nanocomposites,” *Int. J. Heat Mass Transf.*, vol. 48, no. 23–24, pp. 4942–4952, Nov. 2005.

[114] D. Y. Tzou, “Nonlocal behavior in phonon transport,” *Int. J. Heat Mass Transf.*, vol. 54, no. 1–3, pp. 475–481, Jan. 2011.

[115] S. Hida, T. Hori, T. Shiga, J. Elliott, and J. Shiomi, “Thermal resistance and phonon scattering at the interface between carbon nanotube and amorphous polyethylene,” *Int. J. Heat Mass Transf.*, vol. 67, pp. 1024–1029, Dec. 2013.

[116] Z. Wang, X. Tian, J. Liang, J. Zhu, D. Tang, and K. Xu, “Prediction and measurement of thermal transport across interfaces between semiconductor and adjacent layers,” *Int. J. Therm. Sci.*, vol. 79, pp. 266–275, May 2014.

[117] Z. Liang and H.-L. Tsai, “Reduction of solid–solid thermal boundary resistance by inserting an interlayer,” *Int. J. Heat Mass Transf.*, vol. 55, no. 11–12, pp. 2999–3007, May 2012.

[118] M. Barisik and A. Beskok, “Temperature dependence of thermal resistance at the water/silicon interface,” *Int. J. Therm. Sci.*, vol. 77, pp. 47–54, Mar. 2014.

[119] Y. Dong, B.-Y. Cao, and Z.-Y. Guo, “Size dependent thermal conductivity of Si nanosystems based on phonon gas dynamics,” *Phys. E Low-dimensional Syst. Nanostructures*, vol. 56, pp. 256–262, Feb. 2014.

[120] W.-X. Zhou, K.-Q. Chen, L.-M. Tang, and L.-J. Yao, “Phonon thermal transport in InAs nanowires with different size and growth directions,” *Phys. Lett. A*, vol. 377, no. 43, pp. 3144–3147, Dec. 2013.

[121] Y.-C. Hua and B.-Y. Cao, “Phonon ballistic-diffusive heat conduction in silicon nanofilms by Monte Carlo simulations,” *Int. J. Heat Mass Transf.*, vol. 78, pp. 755–759, Nov. 2014.

[122] R. J. Stevens, L. V. Zhigilei, and P. M. Norris, “Effects of temperature and disorder on thermal boundary conductance at solid–solid interfaces: Nonequilibrium molecular dynamics simulations,” *Int. J. Heat Mass Transf.*, vol. 50, no. 19–20, pp. 3977–3989, Sep. 2007.

[123] C. Chen, J. Geer, and B. Sammakia, “Sub-continuum thermal transport modeling using diffusion in the Lattice Boltzmann Transport Equation,” *Int. J. Heat Mass Transf.*, vol. 79, pp. 666–675, Dec. 2014.

[124] B. S. Yilbas and S. B. Mansoor, “Phonon Transport in Two-Dimensional Silicon–Diamond Film Pair,” *J. Thermophys. Heat Transf.*, vol. 27, no. 3, pp. 465–473, Jul. 2013.

[125] H. B. G. Casimir, “Note on the conduction of heat in crystals,” *Physica*, vol. 5, no. 6, pp. 495–500, Jun. 1938.

[126] E. T. Swartz and R. O. Pohl, “Thermal boundary resistance,” *Reviews of Modern Physics*, vol. 61, no. 3. pp. 605–668, 1989.

[127] N. W. Arhcroft and N. D. Mermin, *Solid State Physics*. Harcourt College Publihers, 1976.

[128] M. F. Modest, *Radiative heat transfer*. New York: McGraw Hill, 1993.

[129] M. Kaviany, *Heat Transfer Physics*. Cambridge University Press, 2008.

[130] B. N. Brockhouse, “Lattice Vibrations in Silicon and Germanium,” *Phys. Rev. Lett.*, vol. 2, no. 6, pp. 256–258, Mar. 1959.

[131] a. Ward, D. Broido, D. Stewart, and G. Deinzer, “Ab initio theory of the lattice thermal conductivity in diamond,” *Phys. Rev. B*, vol. 80, no. 12, p. 125203, Sep. 2009.

[132] M. Planck , Masius, Morton,,, *The theory of heat radiation,*. Philadelphia: P. Blakiston’s Son & Co., 1914.

[133] B. S. Yilbas and S. B. Mansoor, “Lattice Phonon and Electron Temperatures in Silicon-Aluminum Thin Films Pair: Comparison of Boltzmann Equation and Modified Two-Equation Model,” *Transp. Theory Stat. Phys.*, vol. 42, no. 1, pp. 21–39, 2013.

[134] R. Stedman and G. Nilsson, “Dispersion relations for phonons in aluminum at 80 and 300 K,” *Phys. Rev.*, vol. 145, no. 2, pp. 492–500, 1966.

[135] A. C. Bouley, N. S. Mohan, and D. H. Damon, “The Lattice Thermal Conductivity of Copper and Aluminum Alloys at Low Temperatures,” *Therm. Conduct.*, vol. 14, pp. 81–88, 1976.

[136] B. S. Yilbas and S. Mansoor, Bin, “Frequency dependent phonon transport in two-dimensional silicon and diamond films,” *Mod. Phys. Lett. B*, vol. 26, no. 17, p. 1250104, Jul. 2012.

[137] B. S. Yilbas, S. Z. Shuja, and S. M. A. Khan, “Laser repetitive pulse heating of tool surface,” *Opt. Laser Technol.*, vol. 43, no. 4, pp. 754–761, Jun. 2011.

[138] G. Chen, “Thermal conductivity and ballistic-phonon transport in the cross-plane direction of superlattices,” *Physical Review B - Condensed Matter and Materials Physics*, vol. 57, no. 23. pp. 14958–14973, 1998.

[139] B. S. Yilbas and S. Bin Mansoor, “Influence of Heat Source Size on Phonon Transport in Thin Silicon Film,” *Transp. Theory Stat. Phys.*, vol. 42, no. 2–3, pp. 65–84, 2014.

[140] K. E. Goodson, O. W. Käding, M. Rösler, and R. Zachai, “Experimental investigation of thermal conduction normal to diamond-silicon boundaries,” *J. Appl. Phys.*, vol. 77, no. 4, p. 1385, 1995.

[141] K. E. Goodson, O. W. Kading, M. Rosler, and R. Zachi, “Thermal conduction normal to diamond-silicon boundaries,” *Appl. Phys. Lett.*, vol. 66, no. 23, pp. 3134–3136, 1995.

[142] M. Asheghi, Y. K. Leung, S. S. Wong, and K. E. Goodson, “Phonon-boundary scattering in thin silicon layers,” *Appl. Phys. Lett.*, vol. 71, no. 13, p. 1798, 1997.

VITAE

Name	Haider Ali
Nationality	Pakistani
Date of Birth	September 19, 1986
Email	haider.ali32@yahoo.com haiali@kfupm.edu.sa
Address	KFUPM P. O. Box 8602, King Fahd University of Petroleum and Mineral, Dhahran-31261, Saudi Arabia
Academic Background	M. Eng. (Mechanical Engineering) 2011 NED University of Engineering & Technology, Karachi, Pakistan. B.E. (Mechanical Engineering) 2008 NED University of Engineering & Technology, Karachi, Pakistan.

Publications

1. **Ali H.**, Yilbas B.S., Influence of heat source size and film thickness on phonon transport in a two-dimensional thin film, Journal of Non-Equilibrium Thermodynamics, Vol. 39 (2), pp. 79-9, 2014.
2. **Ali H.**, Yilbas B.S., Entropy generation in silicon thin film: influence of film thickness on entropy generation rate, Journal of Non-Equilibrium Thermodynamics, Vol. 39 (3), pp. 147-158, 2014.
3. **Ali H.**, Yilbas B.S., Effect of temperature oscillation on thermal characteristics of an aluminum thin film, Applied Physics A, Vol. 117(4), pp. 2143–2158, 2014.